UNIVERSITÀ DEGLI STUDI DI ROMA "LA SAPIENZA"

Dipartimento di Scienza e Tecnica dell'Informazione e della Comunicazione

DOTTORATO DI RICERCA IN TELERILEVAMENTO (XVII CICLO)

OPTICAL PROPERTIES AND RADIATIVE EFFECTS OF TROPOSPHERIC AEROSOLS AND OZONE IN THE CENTRAL MEDITERRANEAN

Relatore: Prof. Giorgio Fiocco

Coordinatore: Prof. Giovanni Picardi

Esaminatori: Prof. Giorgio Fiocco
Prof. Carlo Ulivieri
Dr. Marco Cacciani

The research carried out during the PhD program has had the aim to characterize the radiative field in the Southern sector of the Central Mediterranean, particularly in the ultraviolet (280-400 nm) and visible (400-700 nm) spectral intervals, to identify the role played by ozone and tropospheric aerosols. This study is based on measurements performed by ground-based, airborne and space-borne instruments, and on their interpretation by means of an accurate radiative transfer model; this approach has the advantage of a more detailed description of atmospheric properties than what could be obtained by a single technique among those cited above.

Aerosols have the potential to change the radiative balance, producing either a warming or a cooling, under clear sky conditions, thus representing a not negligible climate factor. Among all the different types of atmospheric aerosols, desert dust is of primary importance, since it has a large impact on solar radiation through scattering and absorption processes. The optical properties of the different aerosol types reaching the measuring site of the island of Lampedusa, in the Central Mediterranean, have been derived and the radiative impact of the aerosols have been studied.

Desidero ringraziare il prof. Giorgio Fiocco sotto la cui supervisione ho svolto
il lavoro di ricerca del dottorato.
Un ringraziamento particolare va a Giorgio di Sarra, una guida insostituibile e paziente
nel cammino di studio degli ultimi anni, e Giandomenico Pace, interlocutore instancabile
(nonché autore delle foto fatte a Lampedusa).
Grazie infine a tutto il gruppo CLIM-OSS dell'ENEA, guidato da Massimo Frezzotti,
per avermi assicurato un ambiente di lavoro sereno e stimolante.

SUMMARY

INTRODUCTION

The research carried out during the PhD program has had the aim to characterize the radiative field in the Southern sector of the Central Mediterranean, particularly in the ultraviolet (280-400 nm) and visible (400-700 nm) spectral intervals, to identify the role played by ozone and tropospheric aerosols. This study is based on measurements performed by ground-based, airborne and space-borne instruments, and on their interpretation by means of an accurate radiative transfer model; this approach has the advantage of a more detailed description of atmospheric properties than what could be obtained by a single technique among those cited above. In particular, the radiative transfer model allows to reconstruct the atmospheric vertical structure and composition and to reproduce the scattering and absorption processes governing the transmission of solar radiation through the Earth's atmosphere; moreover, the model offers the possibility to study the dependence of the solar radiation on the geophysical parameters that influence it, like solar position, gas, clouds, aerosols, surface albedo, altitude, pressure, temperature.

Ground-based measurements of solar and sky radiation are best suited to reliably and continuously derive the detailed aerosol optical properties: but as they are limited to key locations, they do not provide global coverage. On the other hand, instruments placed on space-borne platforms offer the advantage of a global coverage, but they often require a large number of assumptions for the derivation of aerosol properties. Validation of aerosol information in so-called "closure" experiments is therefore of crucial importance.

In this work the impact of ozone and aerosol on the UV radiation will be studied: the total ozone and aerosol amounts will be taken into account, as well as their vertical distributions. Moreover, the effects of aerosol on the solar radiation will be examined.

The solar ultraviolet (UV) radiation has a relevant impact on biological systems: among the principal effects on humans and animals there are genetic mutations, skin cancer, and cataract, while on plants UV-induced modifications regard the leaves' dimension and growth rate and, as a consequence, the photosynthetic activity. Hence, the need for accurate measurement of spectral UV, which has historically been a difficult task; the fact that irradiance varies by many orders of magnitude over a relatively short wavelength range (290-320 nm) requires that useful instruments have a wide dynamic range and a high degree of spectral purity and accuracy.

UV radiation is essentially regulated by O_2 and O_3: the presence of these two gases in the stratosphere results in the absorption of nearly all solar radiation below 280 nm. Solar UV-B radiation (280-320 nm) is significantly absorbed by atmospheric ozone, whereas only a small fraction (less than 3%) of UV-A radiation (320-400 nm) is absorbed by ozone. Above about 310 nm clouds and aerosols are the main factors affecting UV radiation.

If a major concern regarding a decrease in stratospheric ozone is the consequential increase of UV-B radiation passing through the atmosphere and reaching the Earth's surface, on the other hand the role of aerosols is largely uncertain.

Aerosols have the potential to change the radiative balance, producing either a warming or a cooling, under clear sky conditions, thus representing a not negligible climate factor. Aerosol particles have two main effects on the atmospheric radiative budget: a direct one, through absorption and scattering, and an indirect one, since they can act as condensation nuclei for cloud droplets, thereby influencing the cloud properties and their radiative characteristics and lifetime. The concentration, shape, size distribution, refractive index and vertical distribution of the atmospheric aerosols are highly variable, both in time and space; some of these quantities (especially the microphysical properties) are generally not well known, and difficult to be measured.
Among all the different types of atmospheric aerosols, desert dust is of primary importance first of all because its potential source areas cover about one third of the terrestrial surface; a further aspect which renders the desert aerosol one of the most prominent aerosol types is the long-range atmospheric transport: the dust particles are captured by the wind at the surface, are raised to considerable tropospheric altitudes by the strong convective regimes that develop over the desert, and may be transported to large distances by the winds. Finally, desert dust has a large impact on solar radiation through scattering and absorption processes. Dust is a mixture of various minerals, whose optical constants depend on dust origin, mobilization properties, physical and chemical transformation during transport in the atmosphere, as well as on the aggregation status of the minerals. According to the Intergovernmental Panel on Climate Change [*IPCC*, 2001] the global, annual mean direct radiative forcing for the mineral dust aerosol of anthropic origin (i.e. the perturbation to the irradiance levels due to the presence of these particles) is estimated to range between –0.6 and +0.4 W m^{-2}; the level of scientific understanding is however defined "very low", since estimates of the aerosol direct radiative forcing are affected by uncertainties deriving from an inadequate knowledge of the aerosol composition and associated optical properties. Thus, efforts are needed to improve our knowledge of the atmospheric aerosol properties.
Sokolik and Toon [1996] estimated that, although the key quantities which influence the direct radiative forcing are affected by a wide range of uncertainties, the forcing due to mineral aerosol near dust source areas is comparable to the forcings observed for clouds.
In the Mediterranean basin the transport of mineral dust from the Sahara desert is rather common and is modulated by the synoptic meteorological conditions. The strong impact of the Saharan dust on the radiative balance and the solar irradiance reaching sea and land surface can also influence evaporative fluxes an, on a basin-wide scale, its hydrological budget [*Gilman and Garrett*, 1994].
The Mediterranean Sea is an almost completely closed basin, being connected to the Atlantic Ocean through the narrow Gibraltar strait. Its morphologic characteristics have important consequences on airmasses and atmospheric circulation at the regional scale: the Mediterranean sea is an important heat reservoir and source of moisture for surrounding land areas; it represents an important source of energy and moisture for cyclone development and its complex land topography plays a crucial role in steering air flow. Because of its latitude, the Mediterranean Sea is located in a transitional zone where mid-latitude and tropical variability are both important. The Southern part of the region is mostly under the influence of the descending branch of the Hadley cell, while the Northern part is more linked to the mid-latitude variability, characterized by the North Atlantic Oscillation (NAO) and other mid-latitude teleconnection patterns.

It follows that the study of climate variability of the Mediterranean basin, which can be due to several causes, like internal atmospheric dynamics, variations in external forcing and the ocean-atmosphere coupling, requires a particular attention.
The focus of this research is the role that tropospheric aerosols and ozone can have as factors exerting a forcing on the radiative balance of the Central Mediterranean region.

The measuring site is the Laboratory for Climate Observations, established since 1998 by the National Agency for New Technologies, Energy and Environment (ENEA) at the island of Lampedusa (35.5° N, 12.6° E); several atmospheric parameters (greenhouse gas concentrations, measured since 1992, meteorological parameters, total ozone, aerosol optical depth, spectral ultraviolet irradiance, solar radiation) are monitored to study their long-term evolution. The aerosol lidar from the University of Rome "La Sapienza" deployed at ENEA station measures vertical distributions of tropospheric aerosols since 2002.
Lampedusa represents a very interesting site for atmospheric studies for many reasons:

- in the Central Mediterranean, approximately 100 km east of Tunisia and 150 km South of Sicily, far from pollution sources, Lampedusa is an excellent site for measurements of background levels of greenhouse gases (carbon dioxide, methane, etc.), also because the island is rather rocky and poor in vegetation, whose presence affects the CO_2 behaviour;
- the island is characterized by large variability of aerosol properties and optical depth. Part of the time it is reached by airmasses from Europe, mainly carrying continental/polluted aerosols, and part of the time exposed to air from Africa, especially in spring/early summer. African air masses often carry high amounts of desert aerosol, which significantly affect the radiation fluxes;
- the island is small (approximately 20 km^2) and there are no large islands or continental areas within a radius of about 120 km (see Figure 1); Lampedusa represents just a small perturbation in satellites' field of view, almost totally occupied by the sea, where the inversion of satellite data are more reliable due to a homogeneous low reflectivity: thus the island is particularly suitable for validation of satellite observations; moreover, cloudless sky is very often found at Lampedusa (mainly in the period May-September).

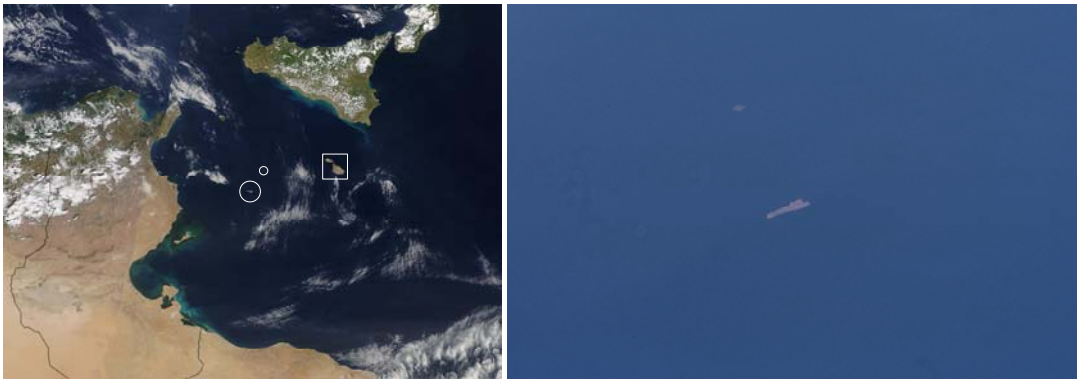

Figure 1. Lampedusa island (circle) as seen from the Moderate Resolution Imaging Spectroradiometer, MODIS, (left) and from the International Space Station in 2001 (right, picture ISS002-338-30 is courtesy of Earth Sciences and Image Analysis Laboratory, NASA Johnson Space Center). The small island of Linosa (small circle) is visible North of Lampedusa and Malta (square) to the Northeast.

In Chapter 1 of this thesis the interaction of the solar radiation with the atmosphere will be discussed. It will be shown how the various geophysical parameters, like ozone, aerosols, clouds and surface albedo interact with solar radiation, and the radiative transfer equation governing the transmission of sunlight will be derived. The general features of the radiative transfer model will be given.
Chapter 2 is devoted to the descriptions of the ground-based, air-borne and space-borne instruments, whose measurements have been used in the subsequent analysis.
Chapter 3 is dedicated to the presentation of the UVSPEC model used to reproduce the measurements performed by the various instruments and to calculate the aerosol radiative forcing.
The core of the research presented in this thesis will be described in Chapters 4 and 5. Chapter 4 concerns the retrieval of aerosol optical properties and estimate of the aerosol radiative forcing at the surface and at the top of the atmosphere. This topic has been developed through the derivation of the aerosol properties and of their direct radiative forcing at the surface and at the top of the atmosphere (TOA) during the Photochemical Activity and solar Ultraviolet Radiation modulation factors (PAUR II) campaign, through the estimate of direct radiative forcing of Saharan dust in the Mediterranean from ground-based measurements and Multi-angle Imaging Spectro-Radiometer (MISR) space-borne observations, and through the derivation of the single scattering albedo for the main aerosol types detected at Lampedusa from the Multifilter Rotating Shadowband Radiometer (MFRSR) measurements performed from July 2001 to September 2003.
In Chapter 5 the influence of aerosol and ozone vertical distribution on radiation levels are examined, and the radiative forcing at the surface, in the troposphere, and at the top of the atmosphere are estimated. These topics have been explored studying the influence of the aerosol and ozone vertical distributions on the actinic flux profiles in the lower troposphere measured during the PAUR II campaign and studying the influence of the vertical profile of Saharan dust on the visible direct radiative forcing at the surface and at the TOA in days with different aerosol loadings.
It is worth noting that the ground-based measurements used in the analyses in Chapters 4 and 5 refer to different time periods and that contemporary surface, airborne and spaceborne data were not available in any of the examined periods. Nevertheless, it will be shown that some analyses require the knowledge of a large number of atmospheric parameters, while general information can be extracted from a limited set of observations.
Finally, concluding final remarks will be given, together with an outlook of possible future work.

CHAPTER 1

THE SOLAR RADIATION - ATMOSPHERE INTERACTION: THEORETICAL BASIS

1.1. COMPOSITION AND STRUCTURE OF THE EARTH'S ATMOSPHERE

The Earth's atmosphere is a mixture of a multitude of chemical constituents. The most abundant of them are nitrogen N_2 (78% by volume) and oxygen O_2 (21%). These gases, as well as the noble gases (argon, neon, helium, krypton, xenon), possess very long lifetimes against chemical destruction and, hence, are relatively well mixed throughout the entire homosphere (region below approximately 90 km altitude). Minor constituents with variable mixing ratios, such as H_2O, CO_2, CH_4, H_2, N_2O, CO, O_3, and many others, also play an important role despite their low concentration: they influence the transmission of solar and terrestrial radiation in the atmosphere and are therefore linked to the physical climate system; they are key components of biogeochemical cycles; in addition, they determine the "oxidizing capacity" of the atmosphere and, hence, the atmospheric lifetime of biogenic and anthropogenic trace gases. Figure 1.1.1 shows an approximate distribution with altitude of the mixing ratio of main chemical constituents.

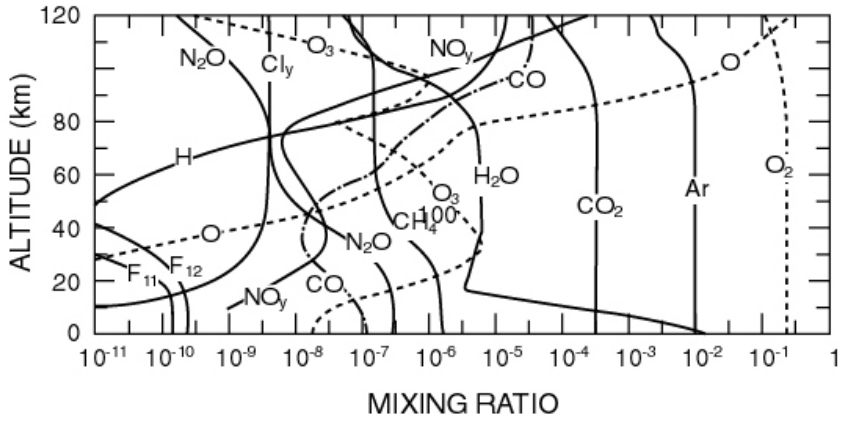

Figure 1.1.1. Typical vertical distribution of the mixing ratio of chemical constituents in the atmosphere. Some lines are shown as dashes for clarity ($F_{11} = CFCl_3$ and $F_{12} = CF_2Cl_2$).

The atmosphere is generally described in terms of layers characterized by specific vertical temperature gradients. The troposphere, which extends from the surface to the tropopause at the approximate altitude of 18 km in the tropics, 12 km at midlatitudes, and 6 to 8 km near the poles, is characterized by a decrease of the mean temperature with increasing altitude; this layer, which contains about 85-90% of the atmospheric mass, is often dynamically unstable with rapid vertical exchanges of energy and mass being associated with convective activity. Above the troposphere, the atmosphere becomes very stable, as the vertical temperature gradient reverses in the stratosphere. This layer, which extends up to 50 km (the stratopause), contains 90% of the atmospheric ozone. The layer between 50 and 90 km altitude is called the mesosphere and its upper limit the mesopause. In this latter region, the temperature again decreases with height. Above 85-90 km, in the region called the thermosphere, the temperature increases to reach maximum values that are strongly dependent on the level of solar activity. Vertical exchanges associated with dynamical mixing become insignificant, but molecular diffusion becomes an important process that produces gravitational separation of species according to their molecular or atomic weight.
Variations of temperature, pressure and density are much larger in vertical directions than in horizontal. Figure 1.1.2 shows the temperature profiles of the standard atmospheric models often used in radiative transfer calculations. "Standard U.S. 1976 atmosphere" is representative of the global mean atmospheric conditions, while "Midlatitude atmosphere" is for latitudes between 30 and 60°.

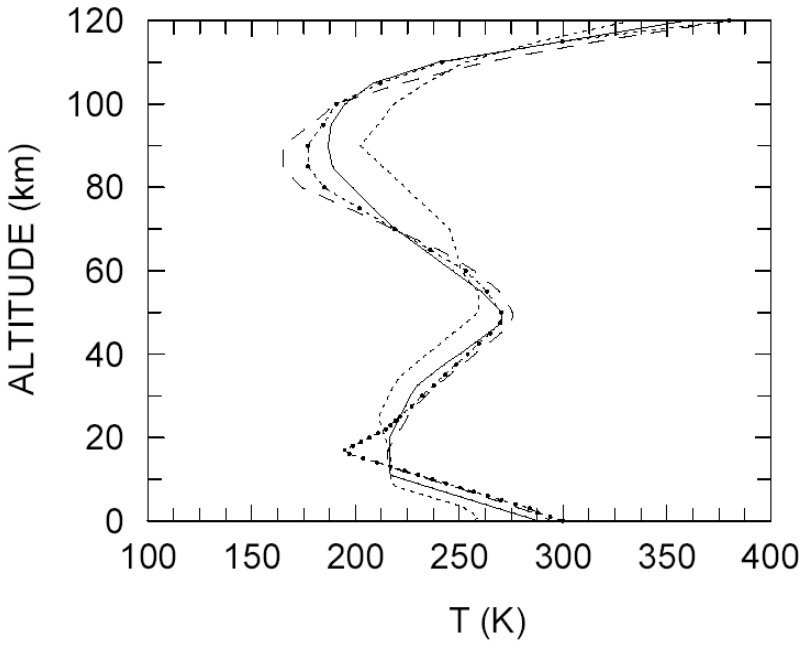

Figure 1.1.2. Vertical temperature profiles for the Standard U.S. (solid line), the Midlatitude summer (dashed line), Subartic summer (dotted line), and Tropical (dotted with symbol) atmosphere [*Anderson et al.*, 1986].

The air pressure varies with altitude according to the law of hydrostatic balance, which states that the pressure at any height in the atmosphere is equal to the total weight of the gas above that level.
The hydrostatic equation expresses the pressure p as a function of the height z

$$\frac{dp(z)}{dz} = -\rho(z)g \qquad (1.1.1)$$

where $\rho(z)$ is the mass density of air at height z, and g is the acceleration of gravity. Integrating the hydrostatic equation at constant temperature as a function of z, and under the ideal gas law we obtain

$$p(z) = p_0 \exp(-z/H) \qquad (1.1.2)$$

where H is the scale height, expressed as

$$H = \frac{RT}{g} \qquad (1.1.3)$$

with R the universal constant for ideal air, g the gravitational acceleration, and T the temperature.

1.2. ATMOSPHERIC GASES

Atmospheric gases are highly selective in their ability to absorb radiation. Each radiatively active atmospheric gas has a specific absorption spectrum, which represents its own signature. Thus the abundance of gases in the atmosphere controls the overall spectral absorption. Figure 1.2.1 presents the low-resolution IR absorption spectra of the major atmospheric gases.

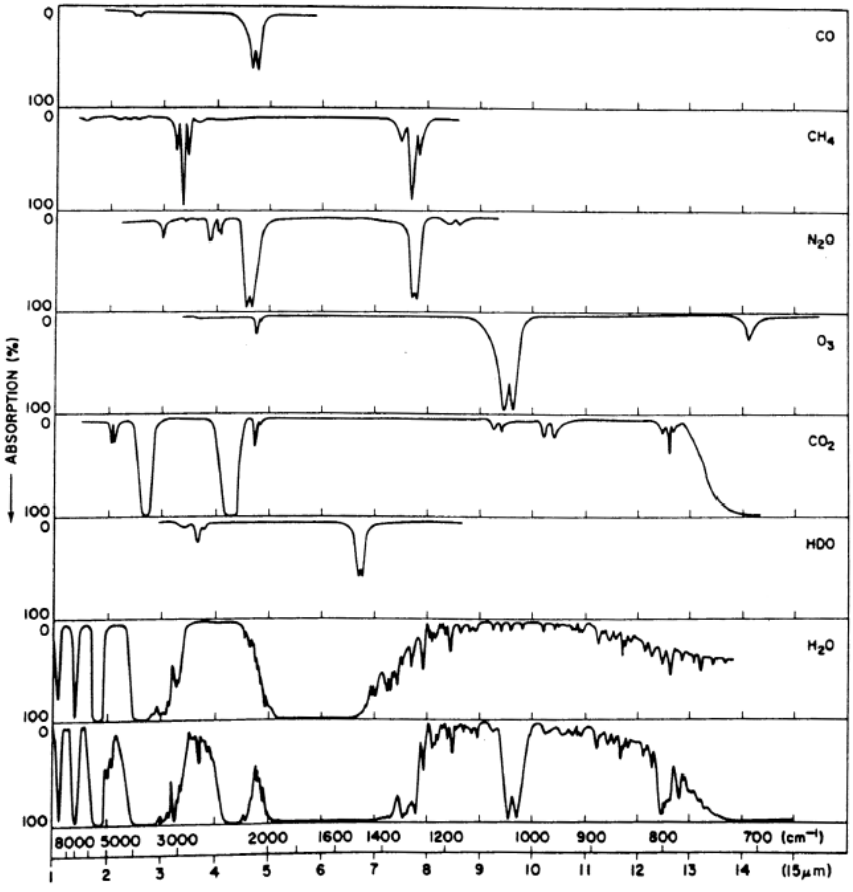

Figure 1.2.1. IR absorption spectra of major atmospheric gases.

1.2.1. ABSORPTION IN THE UV, VIS, IR

Absorption of ultraviolet, visible and near-IR radiation in the gaseous atmosphere is primarily due to H_2O, O_3, and CO_2, as shown in Figure 1.2.2.

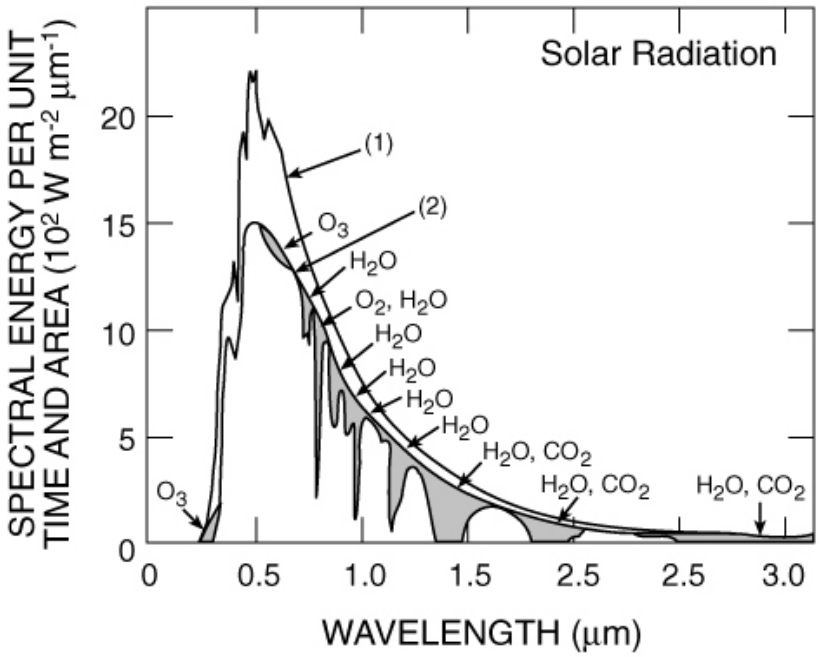

Figure 1.2.2. Spectrum of solar radiation (1) outside the Earth's atmosphere and (2) at sea level for clear sky conditions. The shaded area represents the energy absorbed by the indicated gases in a clear atmosphere.

Absorption of UV radiation in the gaseous atmosphere is primarily due molecular oxygen O_2 and ozone O_3 (see Figure 1.2.3).

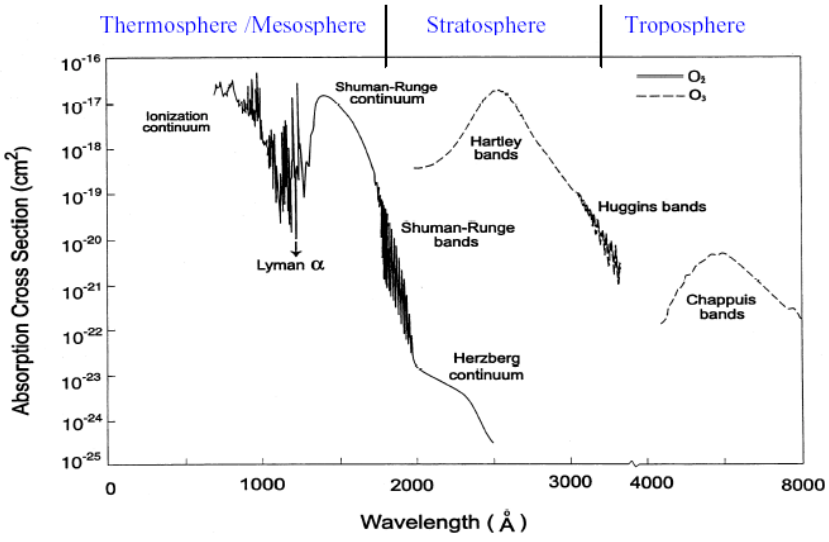

Figure 1.2.3. Spectral absorption cross-sections of O_2 (solid line) and O_3 (dashed line).

1.2.2. OZONE

The processes of ozone formation and destruction in the atmosphere are based on the following reactions, called *Chapman reactions*

$$O_2 + h\nu \rightarrow O(^3P) + O(^1D) \qquad \lambda < 175 \text{ nm} \qquad \text{(R1)}$$

$$O_2 + h\nu \rightarrow O(^3P) + O(^1P) \qquad \lambda < 242 \text{ nm} \qquad \text{(R2)}$$

$$O + O_2 + M \rightarrow O_3 + M + 24 \text{ kcal / mole} \qquad \text{(R3)}$$

$$O_3 + hn \rightarrow O(^1D) + O_2 \qquad \lambda < 310 \text{ nm} \qquad \text{(R4)}$$

$$O + O_3 \rightarrow 2O_2 + 94 \text{ kcal / mole} \qquad \text{(R5)}$$

$$O + O + M \rightarrow O_2 + M + 118 \text{ kcal / mole}. \qquad \text{(R6)}$$

Ozone is mainly produced in the stratosphere, since at higher altitudes the O_2 concentration is too low, while at lower altitudes the solar radiation with $\lambda < 242$ nm can not penetrate, due to O_2 and O_3 absorption. Figure 1.2.4 shows the vertical ozone profile for the Standard U.S. atmosphere and for the Midlatitude winter and summer atmosphere.

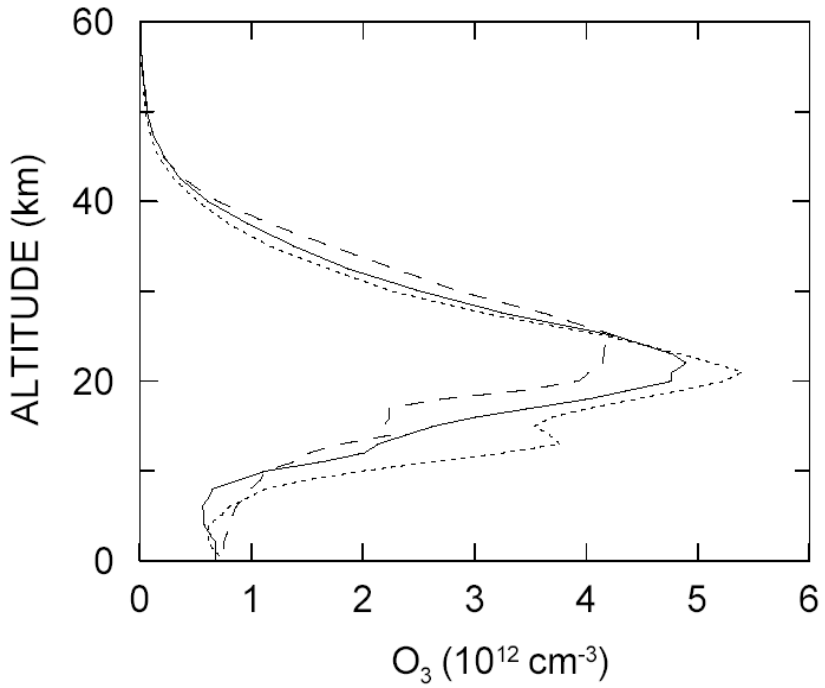

Figure 1.2.4. Vertical ozone profiles for the Standard U.S. (solid line), the Midlatitude summer (dashed line) and Midlatitude winter (dotted line) atmosphere [*Anderson et al.*, 1986].

In the reactions R3, R5 and R6 M represents a background gas, which is involved absorbing the exceeding energy; the reactions R3, R5 and R6 are exothermic and determine the strong temperature increase in the stratosphere.

The O_3 amount in the stratosphere depends on the dynamical balance between reactions R1-R6 and on a number of catalytic cycles; catalysts, generically referred to as X, act as described in the following cycle

$$\begin{array}{l} X + O_3 \rightarrow XO + O_2 \\ XO + O \rightarrow X + O_2 \\ \hline O_3 + O \rightarrow O_2 + O_2 \end{array} \qquad \text{(R7)}$$

The key feature of active catalysts, like NO_x, HO_x and Cl_x, is that, although present in atmosphere at very low concentrations, they are not destroyed during the catalytic cycles.
Other reactions convert these compounds in less efficient species, which remain as reservoir, like H_2O, HNO_3, HCl e $ClONO_2$; these species can then be transported in the troposphere, where they are removed or can be reconverted in active species through chemical reactions with gases, or reactions occurring on stratospheric clouds or aerosols.

The columnar amount of a gas can be expressed as the height of the column of unitary section occupied by the gas at standard pressure and temperature; 1 mm of height corresponds to 100 DU.
The average total ozone distribution as a function of latitude and season, derived from the Total Ozone Mapping Spectrometer (TOMS) over the years 1979-1992, is shown in Figure 1.2.5. Values are typically lower in the tropics throughout the year and highest during the spring at mid- and high latitudes but with clearly lower levels in the southern polar region. This distribution is far different from the one that is expected on the base of the Chapman model, which predicts largest concentrations in the equatorial region, where photochemistry is more intense and insolation is strongest. The discrepancy is due to the fact that the Chapman model does not take into account the effect of circulation on the ozone transport.

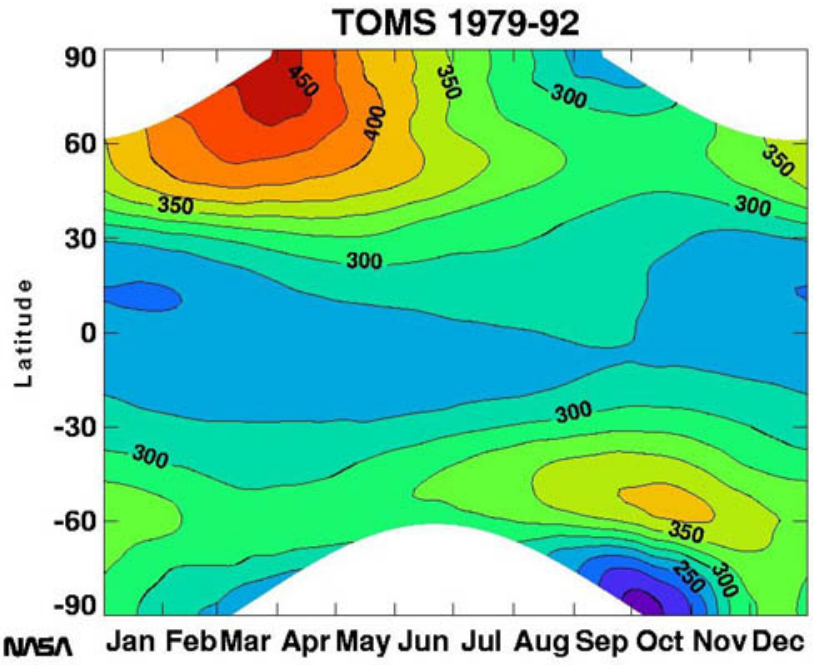

Figure 1.2.5. Latitudinal and seasonal distribution of total ozone in Dobson units. Values are averages over the TOMS measurements for the years 1979-1992.

The maxima at high latitudes are due to O_3 transport from the high equatorial stratosphere, where the ozone production is strongest, to the middle and low stratosphere in the polar regions, where O_3 is relatively inert. The polar maximum is stronger in the Northern than in the Southern hemisphere, due to the different horizontal mixing caused by the different proportion of land and ocean.

During September and October, ozone decreases quite rapidly over the Antarctic region (see Figure 1.2.6). It was recognized during the 1960s that ozone was naturally low over Antarctica as a result of the weaker poleward and downward circulation occurring in the Southern hemisphere. In 1985 *Farman et al.* [1985] showed that ozone was disappearing over Antarctica during the Southern hemisphere spring. The amounts measured were much lower than the naturally occurring low amounts over Antarctica in the Southern spring. This discover set in motion a series of intensive field campaigns, analysis works, satellite investigations, and lab studies that have nearly fully characterized the processes that control Antarctic ozone.

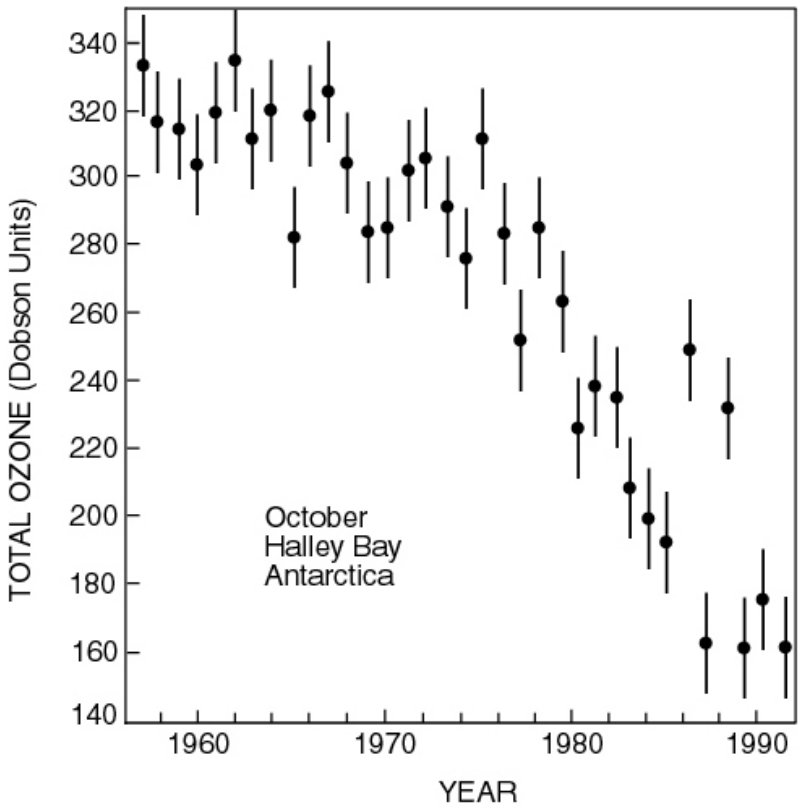

Figure 1.2.6. Evolution between 1958 and 1992 of the October mean ozone column abundance recorded at the British Antarctic Halley Bay Station.

Polar ozone losses are directly caused by chlorine and bromine catalytic reactions. The production of chlorine and bromine reactive species is accelerated by chemical reactions that take place on the surfaces of cloud particles, which could enable reactions that otherwise would not take place in the stratosphere. As the stratosphere cools to very cold temperatures over the Antarctic during the Southern winter, polar stratospheric clouds (PSCs) form. Forms of chlorine (HCl and $ClONO_2$) and bromine that do not affect ozone can react on the surfaces

of these PSCs and produce Cl_2: with sunlight Cl_2 molecules splint into active Cl, that can catalytically destroy ozone (see reactions R7). These chlorine and bromine catalytic destruction reactions are so fast that all of the ozone over Antarctica between 12 and 20 km is destroyed within a few weeks during the September-October (Antarctic spring) period.
The chlorine found in the stratosphere principally comes from chlorofluorocarbons (CFCs), extensively used in refrigerators and as propellants in aerosol cans and released into the atmosphere.
The absorption of solar radiation by ozone (see Figure 1.2.3) causes the amount of UV (200-400 nm) radiation at the Earth's surface to be very low. Nevertheless, photons of UVB (280-320 nm) and UVA (320-400 nm) radiation are energetic enough to break the bonds of DNA molecules (the molecular carriers of our genetic coding), and thereby damage cells. While most plants and animals are able to either repair or destroy damaged cells, on occasion, these damaged DNA molecules are not repaired, and can replicate, leading to dangerous forms of skin cancer (basal, squamous, and melanoma). To appreciate how important this ultraviolet radiation screening is, we can consider a characteristic of radiation damage called an action spectrum. An action spectrum gives a measure of the relative effectiveness of radiation in generating a certain biological response over a range of wavelengths. This response might be erythema (sunburn), changes in plant growth, or changes in molecular DNA. The blue line superimposed on Figure 1.2.7 shows the action spectrum for DNA: it represents the probability of DNA damage by UV radiation at various wavelengths.

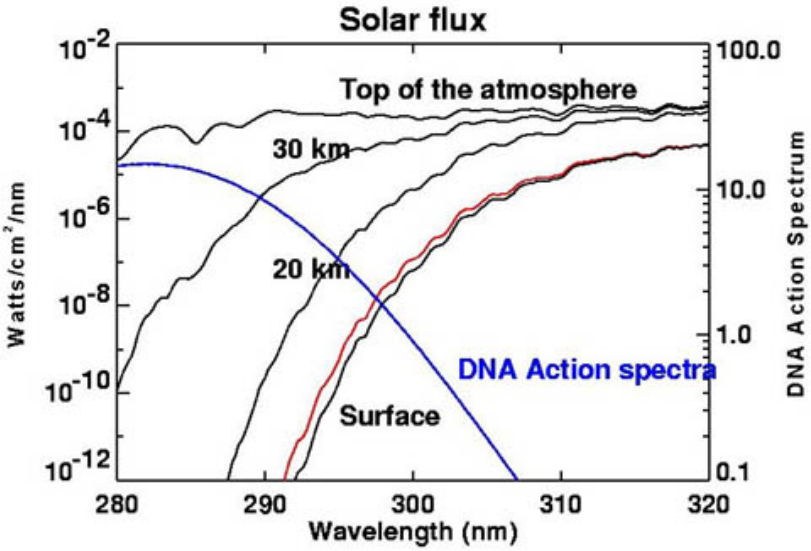

Figure 1.2.7. UV flux versus wavelength for various altitudes (top of the atmosphere, 30 km, 20 km, and the surface). The red line shows the surface flux for a 10 % reduction of ozone. The blue line shows the DNA action spectrum.

In response to a 10% decrease in protective ozone, the amount of DNA damaging UV increases (red line in Figure 1.2.7), in this case, by about 22%. Considering that DNA damage can lead to problems like skin cancer, it is clear that this absorption of the Sun's ultraviolet radiation by ozone is critical for our well being.

1.3. ATMOSPHERIC AEROSOLS

1.3.1. AEROSOL DEFINITION AND SOURCES

Atmospheric aerosols are solid or liquid particles (or both) suspended in air with diameters between about 0.002 μm to about 100 μm.
Interaction of the particulate matter (aerosols and clouds particles) with electromagnetic radiation is controlled by particle size, composition and shape. Atmospheric particles vary greatly depending on sources, production mechanisms, sizes, shapes, chemical composition, amount, distribution in space and time, and how long they survive in the atmosphere (i.e. lifetime).
Primary atmospheric aerosols are particulates that are emitted directly into the atmosphere (for instance, sea-salt, mineral aerosols, volcanic dust, smoke and soot, some organics). Secondary atmospheric aerosols are particulates that are formed in the atmosphere by gas-to-particles conversion processes (for instance, sulphates, nitrates, some organics).
Aerosols can be found in the stratosphere, where they are ejected mainly by strong volcanic eruptions, and in the troposphere. In the following, the tropospheric aerosols will be described.
The sources of tropospheric aerosols can be natural, (like sea-salt, dust storm, biomass burning, volcanic debris, gas-to-particle conversion) or anthropic (like biomass and fossil fuel burning, gas-to-particle conversion, industrial processes, agriculture's activities).
The main individual chemical species that constitute the tropospheric aerosols are sulphates, soot, sea-salt, various minerals. Generally, the aerosols are a mixture of various components with different mixing ratios.
In spite of high temporal and spatial aerosol variability, there are a rather limited number of general categories of tropospheric aerosol types with distinctly different optical properties. The following four general aerosol types are associated with different sources and emission mechanisms and are expected to exhibit significant differences in optical properties: urban–industrial aerosol from fossil fuel combustion in populated industrial regions, biomass burning aerosol produced by forest and grassland fires, desert dust blown into the atmosphere by wind, and aerosol of marine origin.

1.3.2. PHYSICAL AND OPTICAL PROPERTIES OF TROPOSPHERIC AEROSOLS

Aerosols can have diverse shapes and dimensions. In general all aqueous aerosol particles have a spherical shape, while solid particles (dust, soot) have complex shapes.
d'Almeida et al. [1991] provide a global aerosol climatology, with the main aerosol types observed worldwide. Aerosol optical properties may be calculated by means of the Mie theory, once size distribution and complex refractive index are known. The Mie theory is based on the assumption of particles of spherical shape and homogeneous composition, which is not true for the largest aerosol types; nevertheless it is far the most used, since it can be applied to the entire range of dimensions of the particles (see paragraph 1.6.3b for a detailed description).
Since atmospheric aerosols present a wide range of dimensions, the log-normal represents a suitable function which fits the observed size distributions. The distribution for particles of a single type is given by

$$\frac{dN_i(r)}{d(\log r)} = \frac{N_i}{(2\pi)^{1/2}\log(\sigma_i)} \exp\left[-\frac{(\log r - \log r_{M_i})^2}{2(\log \sigma_i)^2} \right] \quad (1.3.1)$$

where $N_i(r)$ is the number of particles with radius r, r_{M_i} is the median radius of the particle ensemble from source *i* and $\log \sigma_i$ is the standard deviation of log r.
For a mixture of particles originating from multiple sources the resulting size distribution is a combination of the individual sources

$$\frac{dN(r)}{d(\log r)} = \sum_i \frac{dN_i(r)}{d(\log r)}. \quad (1.3.2)$$

The aerosol size distributions are determined by their source, transport and removal conditions. Generally, the mode structure includes three groups of modes, which are characterized by different radii:

- an ultra-fine particle mode, or Aitken mode, or nucleation mode. Small particle formation takes place, particle number rises rapidly up by coagulation and accumulate in the range of the accumulation mode. The range of radii is 0.005 - 0.05 μm;
- an accumulation mode, or sub-micron particle mode. Most of the aerosols are in the accumulation mode, where the formation and growth processes slow down and the removal processes are still not effective; therefore this mode is for the long-living aerosol species. The range of radii is 0.05 - 0.5 μm;
- a coarse particle mode, or super-micron particle mode. Examples are soil dust, sea salt, small droplets. For these modes the removal processes are more efficient. The range of radii is 0.5 - 10 μm.

Beside the size distribution, the optical properties of the aerosol are determined also by their chemical composition. Aerosol types consist of different components, often mixed together. The aerosol components can be mixed externally and/or internally. External mixing is defined by different particles having different composition, while internal mixing is given by single particles containing more than one component. The most important mixing state for the aerosol is the mixing with water, which causes the particles' growth with humidity.
The complex refractive index reflects the aerosol chemical composition

$$n(\lambda) = n'(\lambda) - i\, n''(\lambda) \quad (1.3.3)$$

where $n'(\lambda)$ is the real part, responsible for reflection, refraction and scattering of light, and $n''(\lambda)$ is the imaginary part, responsible for absorption.
The single scattering albedo ω_0 represents the fraction of extinction due to scattering and is expressed by

$$\omega_0 = \frac{\sigma_s}{\sigma_s + \sigma_a} \quad (1.3.4)$$

where σ_s e σ_a are the scattering and absorption cross sections, respectively. The value of ω_0 equals one for purely scattering aerosol. The wavelength-dependent ω_0 values for the main aerosol types are reported by *d'Almeida et al.* [1991]; the behaviour of ω_0 as a function of wavelength is a useful tool to distinguish between different aerosol types; for example *Bergstrom et al.* [2002, 2003], *Dubovik et al.* [2002] and *Höller et al.* [2003] found that ω_0 decreases with wavelength for urban/continental aerosols, while increases for desert dust in the shortwave (0.3-5 μm) portion of the solar spectrum.

In general, the angular dependence of the scattering is described by the phase function, P. The phase function is closely related to the probability that photons incoming from an incident direction will be scattered into an outgoing direction. It is usually assumed that P depends only on the scattering angle Θ between incident and emergent directions.
When the scattered direction is within an angle Θ close to 0 it is called forward scattering. When scattered radiation has been reflected back within an angle Θ close to 180°, it is called backward scattering. Backscattering is defined when Θ=180°.
The phase function P(cos Θ) is normalized so that the total probability of scattering is unity

$$\int \mathrm{P}(\cos\Theta)\frac{\mathrm{d}\varpi'}{4\pi} = 1 \qquad (1.3.5)$$

The asymmetry factor *g* is defined as

$$g = \frac{1}{2}\int_{-1}^{+1} \mathrm{P}(\cos\Theta)\cos\Theta\,\mathrm{d}(\cos\Theta) \qquad (1.3.6)$$

and theoretically can vary between –1 and 1; *g* is 0 for isotropic scattering, positive for forward scattering and negative for backward scattering.
The phase function for the aerosol particles of spherical shape can be calculated from the Mie theory; however, spherical symmetry, upon which Mie theory is based, does not hold for the population of non-spherical particles, like dust, which constitute a large fraction of the natural and anthropogenic tropospheric aerosols. *West et al.* [1997] have measured the scattering phase function of mineral dust in a laboratory study over the scattering angle range 15°-170°, while *Mishchenko et al.* [1997] developed a method to extensively compute scattering by shape distributions of polydisperse, randomly oriented spheroids with refractive indices and size distributions representative of naturally occurring dust aerosols. Figure 1.3.1 presents the phase functions computed at two wavelengths (443 and 865 nm) for polydisperse, randomly oriented prolate and oblate spheroids of a single shape. The spheroid aspect ratio (that is the ratio of the largest to the smallest particle dimensions) varies from 1.2 (nearly spherically shaped particles) to 2.4 (highly aspherical particles), and the curves represent averages over all prolate and oblate spheroids, as well as the phase functions for the mixture of all prolate and oblate spheroids. For comparison, the phase functions for surface-equivalent polydisperse sphere is shown. The two primary effects are an increase in the side-scattering at around Θ=120° and a reduction of the backscattering. It is interesting to note that the phase function of a mixture of non-spherical particles can be fairly insensitive to which elementary shapes are used to form the mixture (prolate or oblate). Figure 1.3.2 compares the phase function denoted as “all spheroids” in Figure 1.3.1 with the phase function measured for soil particles with micron dimensions: it can be seen that the measured phase function for natural soil particles almost coincides with the theoretical one computed for a mixture of spheroids.

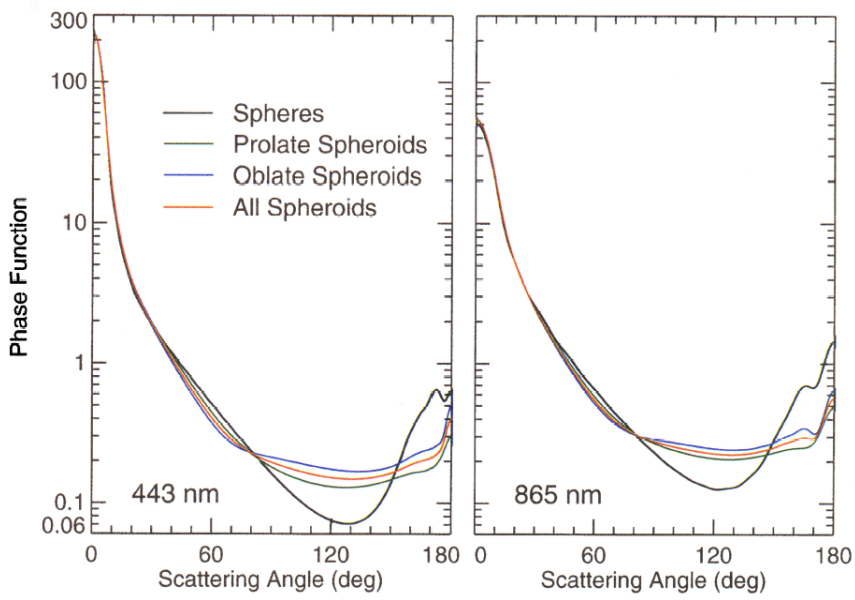

Figure 1.3.1. Phase functions for polydisperse spheres and ensemble-averaged phase functions for equiprobable shape mixtures of prolate (green curve), oblate (blue curve), and prolate and oblate spheroids (red curve) with aspect ratios ranging from 1.2 to 2.4 in steps of 0.1. The black curve represents the phase functions for projected-area-equivalent spherical particles. All curves are computed for the modified log-normal distribution of surface-equivalent sphere radii corresponding to the standard accumulation mode of dust-like aerosols at wavelengths of 443 and 865 nm. The spectral refractive indices are 1.53+0.0085*i* at 443 nm and 1.53+0.0012*i* at 865 nm [*Mishchenko et al.*, 1997].

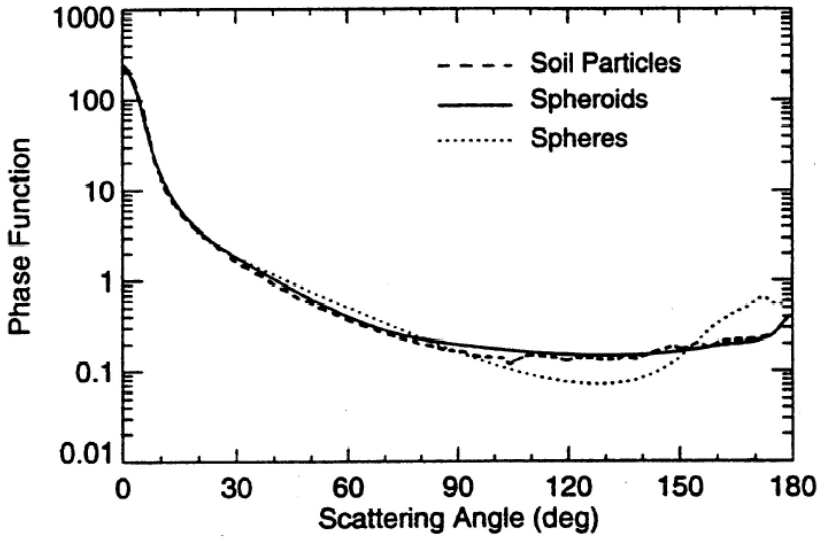

Figure 1.3.2. Scattering phase functions for natural wavelength-sized soil particles and computed for a broad shape distribution of polydisperse, randomly oriented spheroids and surface-equivalent spheres [*Mishchenko et al.*, 1997].

An analytic expression for the phase function in terms of the asymmetry factor *g* has been proposed by L. G. Henyey and J. L. Greenstein [*Henyey and Greenstein*, 1941], which is adequate for scattering patterns that are not strongly peaked in the forward direction

$$P(\cos\Theta) = \omega_0 \frac{1-g^2}{(1-g^2-2g\cos\Theta)^{3/2}}. \qquad (1.3.7)$$

A detailed comparison of the phase function for spheres, spheroids, and the Henyey-Greenstein will be given in paragraph 4.3.3c.

Atmospheric aerosols attenuate solar radiation through absorption and scattering, their effectiveness depending both on amount and dimension. The Ångstrom formula for the aerosol optical depth (AOD) includes both properties in a single expression

$$AOD(\lambda) = \beta\lambda^{-\alpha}. \qquad (1.3.8)$$

where α and β are called the Ångstrom coefficients. In (1.3.8) β expresses the amount of aerosols in the column and is also equivalent to the AOD at 1 μm, while α is related to the particles' dimensions. Large values of α indicate the major presence of small particles; the upper limit for α is 4 (Rayleigh scattering approximation), while values close to zero (positive or negative) are found for large particles.

1.3.3. RADIATIVE CHARACTERISTICS AND CLIMATIC IMPACT OF THE AEROSOLS

Aerosols scatter and absorb shortwave (solar) and longwave (thermal IR) radiation, thereby perturbing the energy budget of the Earth/atmosphere system and exerting a direct radiative forcing. Here the radiative forcing, RF, indicate a change in the radiative energy budget of the Earth's climate system due to an external perturbation or to the introduction of an agent, for example the aerosols or the greenhouse gases.
Aerosols also act as cloud condensation and ice nuclei, thereby modifying the microphysics, the radiative properties, and the lifetime of clouds. The aerosol indirect effect is usually split into two effects: the first indirect effect, whereby an increase in aerosols causes an increase in droplet concentration and a decrease in droplet size for fixed liquid water content, and the second indirect effect, whereby the reduction in cloud droplet size affects the precipitation efficiency, tending to increase the liquid water content, the cloud lifetime, and the cloud thickness.
There is also a semi-direct effect due to aerosols: the absorption of solar radiation by aerosols leads to a local heating in the atmosphere, which can suppress cloud cover. The local heating may simply lead to the evaporation of clouds, or may stabilize the atmosphere reducing cloud formation. A reduction of low clouds leads to a reduction of planetary albedo (since low clouds scatter solar radiation back to space) and a warming of climate.
The effect of a particular aerosol type in terms of the direct RF can be positive, if it causes more radiation to be absorbed, thus leading to a warming, or negative, if it induces an increase in the outgoing radiation, thus causing a cooling.
The importance of knowing the radiative impact of the aerosols is well summarized in Figure 1.3.3, from the report of International Panel on Climate Change (IPCC) [*IPCC*, 2001], which represents the global mean radiative forcing of greenhouse gases (GHG), ozone and different anthropogenic aerosols for the year 2000 relative to 1750, that is prior to the Industrial Revolution, calculated by means of model investigations.

The determination of the GHG RF is a well-posed problem, since they are uniformly distributed, are active day and night, with cloudy and cloud-free sky conditions, and their IR absorption is well quantified. On the contrary, the forcing by natural and anthropogenic aerosols is an open problem, due to the complex spatial and temporal distribution, complex chemical composition and evolution of the aerosols.
Figure 1.3.3 shows that the aerosol types which cause a negative RF (i.e. cooling) are the sulphates, the organic carbon (oc) from fossil fuel, and the biomass burning. Black carbon (bc, or soot) from fossil fuel has a warming effect, while the RF of mineral dust was found to be either positive or negative, with a very low level of scientific understanding. The well-mixed greenhouse gases are grouped together into a single rectangular bar with the individual mean contributions due to CO_2, CH_4, N_2O, and halocarbons.

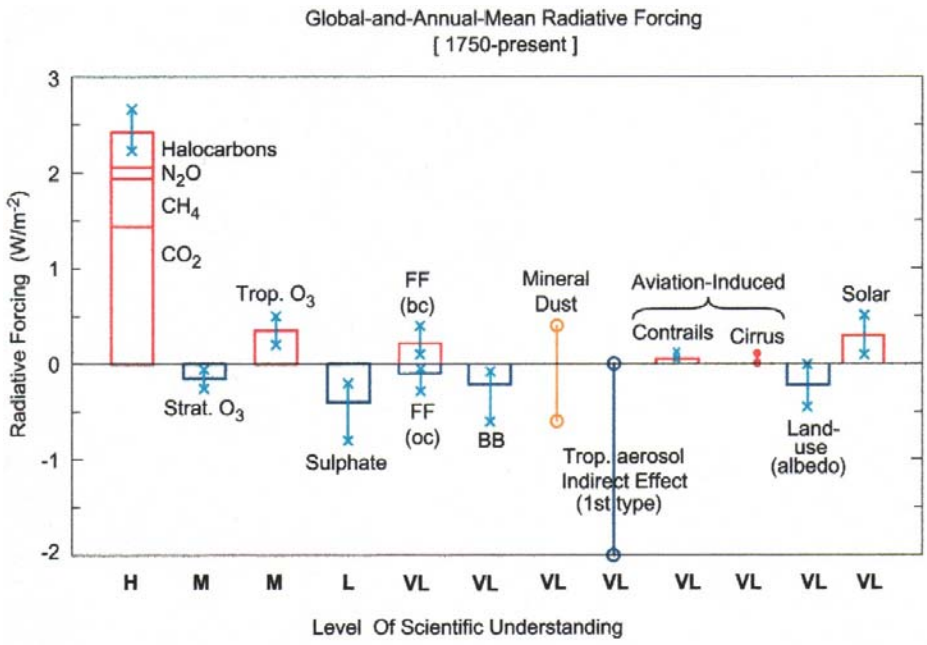

Figure 1.3.3. Global, annual mean radiative forcings (Wm^{-2}) due to a number of agents for the period from pre-industrial (1750) to present (late 1990s; about 2000). The height of the rectangular bar denotes a central or best estimate value while its absence denotes no best estimate is possible. The vertical line about the rectangular bar with "x" delimiters indicates an estimate of the uncertainty range, guided by the spread in the published values of the forcing and physical understanding. A vertical line without a rectangular bar and with "o" delimiters denotes a forcing for which no central estimate can be given owing to large uncertainties. The uncertainty range specified here has no statistical basis and therefore differs from the use of the term elsewhere in this document. A "level of scientific understanding" index is accorded to each forcing, with H, M, L and VL denoting high, medium, low and very low levels, respectively. This represents a subjective judgment about the reliability of the forcing estimate, involving factors such as the assumptions necessary to evaluate the forcing, the degree of knowledge of the physical/chemical mechanisms determining the forcing, and the uncertainties surrounding the quantitative estimate of the forcing. "FF" denotes fossil fuel burning while "BB" denotes biomass burning aerosol. Fossil fuel burning is separated into the "black carbon" (bc) and "organic carbon" (oc) components with its separate best estimate and range. The sign of the effects due to mineral dust is itself an uncertainty [*IPCC*, 2001].

The indirect forcing due to tropospheric aerosols is poorly understood. The same is true for the forcing due to aviation via their effects on contrails and cirrus clouds. Only the first type of indirect effect due to aerosols as applicable in the context of liquid clouds is considered here. The second type of effect is conceptually important but there exists very little confidence in the simulated quantitative estimates. All the shown forcings have distinct spatial and seasonal features such that the global, annual means appearing on the plot do not yield a complete picture of the radiative perturbation.

Among all the different types of atmospheric aerosols, desert dust is of primary importance first of all because potential source areas cover about one third of the terrestrial surface; a further aspect which renders the desert aerosol one of the most prominent aerosol types is the long-range atmospheric transport due to strong winds and convective processes [*d'Almeida et al.*, 1991]. Dust is a mixture of various minerals, whose optical constants depend on dust origin, mobilization properties, physical and chemical transformation during transport in the atmosphere, as well as on the aggregation status of the minerals. It is estimated that a significant fraction of the dust in the atmosphere is produced by man-induced changes [*Tegen and Fung*, 1995; *Sokolik and Toon*, 1996].
Sokolik and Toon [1996] estimated that, although the key quantities which influence the direct radiative forcing are affected by a wide range of uncertainties, the forcing due to mineral aerosol near dust source areas is comparable to the forcings observed for clouds. According to *IPCC* [2001] the global, annual mean RF for the mineral dust aerosol of anthropic origin is estimated to range between –0.6 and +0.4 W m^{-2}, with the level of scientific understanding defined "very low".
Radiative forcing of mineral dust is sensitive to size distribution and complex refractive index [*Claquin et al.*, 1998], the imaginary part being one of the critical parameters in the calculation of the forcing. The techniques currently used to determine the refractive index of dust aerosol have relatively high uncertainties (about 30-50%) that affect the modelled aerosol optical properties [*Sokolik et al.*, 1993]. *Sokolik and Toon* [1999] described a technique to model the radiative properties of mineral aerosols from UV to IR taking into account their composition. They simulated the daily mean net forcing by dust of various compositions, showing that a mixture of aggregates can cause a positive radiative forcing, while a mixture of individual minerals may produce an opposite effect.
In the Mediterranean basin transport of desert dust from the Sahara is rather common [see e.g. *Prodi and Fea*, 1979; *Chester et al.*, 1984; *Bergametti et al.*, 1989; *Moulin et al.*, 1997], with a marked seasonal behaviour of the aerosol optical depth [e.g. *Moulin et al.*, 1998]. In the Central Mediterranean the transport from Africa is modulated by the synoptic meteorological conditions [*di Sarra et al.*, 2001]: when a high-pressure system is centred over Northern Libya, dust comes from central Sahara, while when the high pressure is located over Algeria or Lybia, at latitudes below 30°, the dust-loaded airmass follow the North-western African coast. Figure 1.3.4 shows an image from the Moderate Resolution Imaging Spectrometer (MODIS) of Saharan dust streaming out over the Mediterranean Sea and north-eastward to Italy.

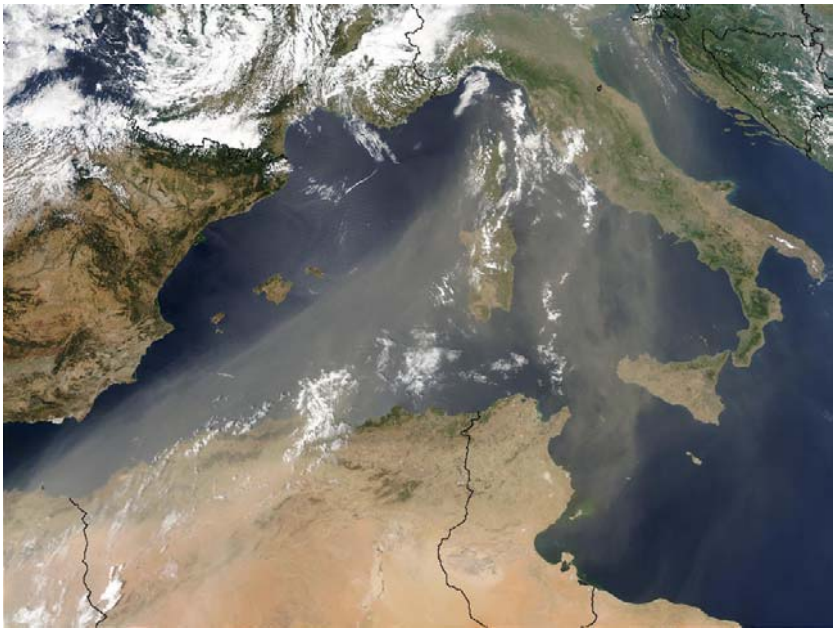

Figure 1.3.4. Image of a Saharan dust storm blowing from Northern Africa towards Italy across the Mediterranean Sea captured on July 16, 2003 by MODIS on Aqua satellite (from *http://modis-atmos.gsfc.nasa.gov*).

1.4. CLOUDS

Clouds represent one of the major factors affecting the propagation of the solar radiation in the atmosphere. In the UV and visible spectrum the reflection and scattering of the light due to clouds reduces the radiation levels at the surface: the largest irradiance variability on a short time scale is due to changes in clouds. However, enhancements of up to 25% can occur under broken cloud conditions, when the clouds do not block the sun [*Estupiñán et al.*, 1996].
Clouds' properties are highly variable in time and space: this is the principal reason of the difficulties in the parameterisation of the real clouds into models. Ground-based observations are representative of local conditions and not of the surrounding region, and are available only for a limited number of sites. Satellites offer global coverage over extended periods and area, allowing the detection of regional or global changes: however, for most satellites, the passage on a single location occurs only once a day. Moreover, surface as well as satellite observations do not provide information about the cloud base and top height and optical thickness, unless a lidar system is used.
The major characteristics of the clouds are the cloud type, coverage, droplet size, droplet concentration, and the liquid water content.
The cloud cover represents the fraction of sky that is occupied by the clouds, and is usually expressed in octas, with 0/8 for cloud-free and 8/8 for overcast sky, respectively.
The cloud types are classified according to the height of their base (Table 1.4.1): low clouds are between 0 and 2 km, middle clouds between 2 and 7 km, and high clouds between 7 and 18 km; the cumulus clouds are clouds with a vertical development and can extend until 3 km height.

Table 1.4.1. Types and height of the cloud base

Cloud type	Height of base (km)
Low level	
Statocumulus	0-2
Stratus	0-2
Nimbostratus	0-4
Mid level	
Altocumulus	2-7
Altostratus	2-7
High level	
Cirrus	7-18
Cirrostratus	7-18
Cirrocumulus	7-18
Clouds with vertical development	
Cumulus	0-3
Cumulonimbus	0-3

Cloud droplets size distribution is often approximated by a modified gamma distribution, expressed by

$$N(r) = \frac{N_0}{\Gamma(\alpha)\, r_n}\left(\frac{r}{r_n}\right)^{\alpha-1} \exp\left(-\frac{r}{r_n}\right) \qquad (1.4.1)$$

where N_0 is the total number of droplets (cm^{-3}), r_n in the radius that characterizes the distribution, α is the variance of the distribution, and Γ is the gamma function.
The cloud droplet sizes vary from a few micrometers to 100 μm with average diameter in 10 to 20 μm range. The cloud droplet concentration varies from about 10 cm^{-3} to 1000 cm^{-3} with average droplet concentration of a few hundred cm^{-3}. The liquid water content (LWC) of typical clouds varies from approximately 0.05 to 3 g(water) m^{-3}, with most of the observed values in the 0.1 to 0.3 g(water) m^{-3} region.

In contrast to atmospheric aerosols, the cloud droplets consist of a single species, i.e. water. Thus, to calculate the absorption and scattering cross sections of cloud droplets, one needs to know the size of droplets and the refractive index of water versus wavelength. For many practical applications, the optical properties of water clouds are parameterised as a function of the effective radius and LWC.
Using the effective radius r_e

$$r_e = \frac{\int_{r_1}^{r_2} \pi r^3 N(r)dr}{\int_{r_1}^{r_2} \pi r^2 N(r)dr} \qquad (1.4.2)$$

and the LWC

$$LWC = \rho_w V = \frac{4}{3}\rho_w \int_{r_1}^{r_2} \pi r^3 N(r)dr\,, \qquad (1.4.3)$$

the extinction coefficient of the cloud droplet is

$$\sigma_e = \int_{r_1}^{r_2} Q_e(r)\pi r^2 N(r)dr\,. \qquad (1.4.4)$$

As $Q_e \approx 2$ for water droplet at solar wavelengths, σ_e can be expressed as

$$\sigma_e \approx \frac{3}{2}\frac{LWC}{r_e \rho_w}\,. \qquad (1.4.5)$$

Depending on the atmospheric conditions, clouds may consist of ice crystals (e.g., cirrus clouds) or ice crystal/water droplet mixtures. Ice crystals often have the hexagonal structure with sizes on the order of several hundred micrometers. However, a large variety of shapes (called habits) and sizes of ice crystals have been reported in literature [*Hallett et al.*, 2002]. Ice crystal shapes depend on temperature and relative humidity.

1.5. SURFACE ALBEDO

The bidirectional reflectance distribution function (BRDF) is the ratio of the reflected intensity to the energy in the incident beam, and is a function of frequency, incident angle, and scattered angle. These dependencies makes it a difficult property to measure.
Fortunately many surfaces found in nature obey simpler reflectance properties first characterized by Lambert. A Lambertian surface is one whose reflectance is independent of both incident and reflected directions, but depends only on frequency (see Figure 1.5.1).

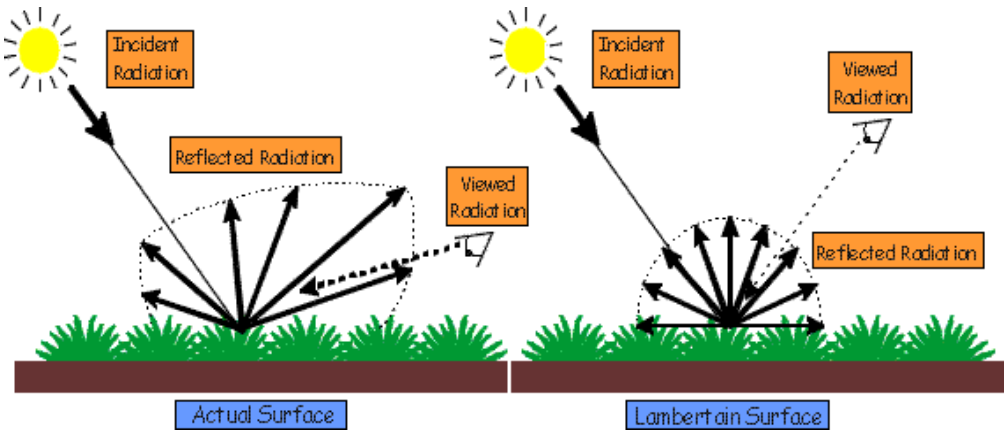

Figure 1.5.1. The directional dependence of the surface reflectance on viewing angle for an actual and a Lambertian surface.

In general the term albedo is defined as a ratio of upward and downward irradiances for any altitude. At the ground the albedo is identical with the surface albedo. At all other altitudes the albedo includes contributions due to reflections originating from the surface, as well as influences due to reflection and multiple scattering within the atmosphere above and beneath the considered height. For these reasons, sometimes the albedo is called the effective albedo.
The solar energy reflected by the surface is available for further radiative interactions (scattering/absorption on air molecules and aerosol/cloud particles) within the atmosphere.

The complementary part of the incident solar energy, which is not reflected from the ground back to the atmosphere, is absorbed by the surface. It heats the ground and is transformed into longwave radiation and then re-emitted by the Earth's surface. In this way the surface albedo is important for multiple scattering and absorption processes in the solar spectral range within the atmosphere, and for the transformation of radiation energy from the solar to the terrestrial wavelength range at the ground. Thus the surface albedo is a constraining factor for the surface and atmosphere energy budgets; it is also an important boundary condition for atmospheric solar radiative transfer models.
The surface albedo varies considerably for different ground types. Over sea the surface albedo is generally much less than 0.18, depending on surface roughness and sun position [*Payne*, 1972]; over land it is larger for most parts of the solar spectrum. In addition the surface albedo over land is more variable because it is a function of soil/vegetation type and the season of the year. Therefore several authors have studied the spectral surface albedo for different types of reflecting ground and wavelength ranges. Mostly measurements are reported which are directly obtained at the surface [e.g., *Bowker et al.*, 1985; *Blumthaler and Ambach*, 1988; *Feister and Grewe*, 1995]. Local spectral measurements of effective albedo from airborne instrument are reported by *Webb et al.* [2000; 2004] and *Wendish et al.* [2004].

1.6. THE RADIATIVE TRANSFER EQUATION FOR A PLANE-PARALLEL ATMOSPHERE

1.6.1. RADIANCE, IRRADIANCE, ACTINIC FLUX

The fundamental quantity defining the radiation field is the specific intensity, or simply intensity, of radiation.
Consider the light beam travelling in directions confined to an element of solid angle $d\omega$, across an element of area $d\sigma$ orthogonal to the beam and during a time dt, in the frequency range $[\nu,\nu+d\nu]$. The radiant energy flux dE_ν associated to the light beam is expressed in terms of the intensity I_ν by

$$dE_\nu = I_\nu \, d\nu \, d\sigma \, d\omega \, dt . \qquad (1.6.1)$$

If instead, the intensity orthogonal to an arbitrarily oriented surface element dA is considered, then the projection of $d\sigma$ onto dA has to be taken into account. If the angle between the direction considered and the normal to $d\sigma$ is θ then expression (1.6.1) becomes

$$dE_\nu = I_\nu \cos\theta \, d\nu \, d\sigma \, d\omega \, dt . \qquad (1.6.2)$$

The angular direction of the radiation is specified in terms of the polar angle θ and the azimuthal angle φ.
The intensity I_ν is a function of spatial and temporal coordinates, of the direction, and of the frequency. Under the assumption of a stratified atmosphere, which is horizontally homogeneous, the physical quantities may vary only in the vertical dimension z; this approximation is also known as a plane parallel atmosphere. In this case the intensity is denoted by $I_\nu(z,\theta,\varphi)$.

Spectral irradiance or flux measures the radiant energy flux transported through a given surface per unit time per unit wavelength; in climate studies the interest is towards the irradiance passing upward or downward through horizontal surfaces, e.g., the ground or certain layers in the atmosphere, so that it can be written as

$$F_\nu \equiv \int_0^{2\pi}\int_0^{\pi} I_\nu(z,\theta,\varphi)\cos\theta \, d\theta \, d\varphi . \qquad (1.6.3)$$

A quantity of great interest to photochemists is total convergence of radiation at a point. This quantity, called the actinic flux, F, determines the availability of photons for photochemical reactions. By definition, the intensity energy passing through a point P in a certain direction within the solid angle dω is $I_\nu d\omega$. The energy passing through P in all directions is thus

$$F_\nu^J \equiv \int_0^{2\pi}\int_0^{\pi} I_\nu(z,\theta,\varphi) \, d\theta \, d\varphi . \qquad (1.6.4)$$

F_ν^J has units of W m^{-2} which are identical to those of the irradiance F_ν.

The usefulness of actinic flux F_ν^J becomes apparent when the probability of photon absorption by a chemical species or photo-absorption is considered. Photo-absorption is the process of molecules absorbing photons, thus removing some energy from the actinic radiation field. The amount of photo-absorption per unit volume is proportional to the number concentration of the absorbing species, the actinic radiation field, and the efficiency with each molecule absorbs photons. This efficiency is called the absorption cross-section, denoted by σ and has units of m^2.

The absorption cross-section is the ratio between the number of photons (or total energy) absorbed by a molecule to the number (or total energy) convergent on the molecule.

Photochemists are interested in the probability of absorbed radiation breaking molecular bonds, and thus decomposing species AB into constituent species A and B. Notationally this process may be written in the form

$$AB + h\nu \rightarrow A + B . \qquad (1.6.5)$$

The probability that a photon absorbed by AB will result in the photodissociation of AB, and the completion of (1.6.5), is called the quantum yield or quantum efficiency and is represented by ϕ.

The specific photolysis rate coefficient for the photodissociation of a species AB, J_{AB}, is the number of photodissociations of AB occurring per unit time, per unit volume of air, per unit frequency, per molecule of AB. If $[AB]$ denotes the number concentration of AB then the rate at which $[AB]$ changes with time is

$$\frac{d[AB]}{dt} = J_{AB}[AB]. \qquad (1.6.6)$$

The photolysis rate for the photodissociation of AB at a specific frequency can be expressed as

$$J_\nu \equiv \int_{\nu_{min}}^{\nu_{max}} F_\nu^J \, \sigma_\nu \phi_\nu \, d\nu . \qquad (1.6.7)$$

1.6.2. EXTINCTION AND EMISSION OF RADIATION

Radiation and matter have the following forms of interactions: scattering, absorption, and emission. The extinction of radiation due to traversing an infinitesimal increment of path is linearly proportional to the amount of matter along the path

$$\frac{dI_\nu}{ds} = -k_\nu I_\nu \qquad (1.6.8)$$

where the extinction coefficient of the medium, k_ν, is proportional to the local density of the medium. Extinction includes all processes which reduce the radiant intensity. As will be described below, these processes include absorption and scattering which removes photons from the beam. Similarly the emission of radiation is also proportional to the amount of matter along the path

$$\frac{dI_\nu}{ds} = k_\nu S_\nu \qquad (1.6.9)$$

where S_ν is known as the source function. Emission includes all processes which increase the radiant intensity. As will be described below, these processes include thermal emission and scattering which adds photons to the beam.

Extinction and emission are linear processes, and thus additive. Since they are the only two processes which alter the intensity of radiation,

$$\frac{dI_\nu}{ds} = k_\nu(-I_\nu + S_\nu)\,. \qquad (1.6.10)$$

Equation (1.6.10) is the equation of radiative transfer in its simplest differential form.

The optical depth τ measures extinction between different layers in the vertical. The optical depth between two levels $z_2 > z_1$ is given by

$$\tau_\nu(z_1, z_2) \equiv \int_{z'=z_1}^{z'=z_2} k_\nu dz'\,. \qquad (1.6.11)$$

The radiative transfer equation for a stratified atmosphere in terms of the optical depth can be obtained by substituting (1.6.11) into (1.6.10)

$$\mu\frac{dI_\nu}{d\tau_\nu} = -I_\nu + S_\nu \qquad (1.6.12)$$

where $\mu=\cos\theta$.

Equation (1.6.12) expresses the differential form of the radiative transfer equation in a plane parallel atmosphere and is valid for all angles. The solution of (1.6.12) is difficult because S_ν depends on I_ν.

1.6.3. SCATTERING

Scattering occurs when matter reflects off a photon without absorption. The direction of the photon after the interaction is usually not the same as the incoming direction. In paragraph 1.3.2 the scattering phase function P and the asymmetry factor *g* were introduced.

The scattering regimes are:
Rayleigh scattering: $2\pi r/\lambda \ll 1$, applies to scattering by molecules and small aerosol particles;
Mie-Debye scattering: $2\pi r/\lambda \sim 1$, applies to scattering by aerosol and cloud particles;
Geometric optics: $2\pi r/\lambda \gg 1$, applies to scattering by large cloud droplets.

1.6.3A. RAYLEIGH SCATTERING

The sizes of atmospheric molecules are much smaller than the wavelengths of solar and IR radiation, and the scattering by atmospheric gases is well described by the Rayleigh

scattering. In the Rayleigh scattering approximation, a molecule (or a small particle) is considered as an individual dipole.
The intensity scattered by molecules for unpolarized incident light is given by [*Bucholtz*, 1995]

$$I = \frac{I_0}{r^2}\alpha^2\left(\frac{2\pi}{\lambda}\right)^4(1+\cos^2\Theta) \tag{1.6.13}$$

where r is the particles' radius and α is the polarizability, defined by

$$\alpha = \frac{3}{4\pi N}\left(\frac{m^2-1}{m^2+2}\right) \tag{1.6.14}$$

with N the number of molecules per unit volume and m the complex refractive index.
The Rayleigh scattering intensity is inversely proportional to the fourth power of the wavelength.
The Rayleigh scattering phase function for incident unpolarized radiation is

$$P(\cos\Theta) = \frac{3}{4}(1+\cos^2\Theta) \tag{1.6.15}$$

1.6.3B. MIE SCATTERING

The basic assumptions of the Mie theory are the spherical shape of the particles and their homogeneous composition. Mie scattering has no size limitations and converges to the limits of geometrical optics for large particles, and of Rayleigh scattering for $2\pi r/\lambda << 1$.
Mie theory calculates the scattered electromagnetic field at all points in the particle (called internal field) and at all points of the homogeneous medium in which the particle is embedded. For all practical applications in the atmosphere, light scattering observations are carried out in the far-field zone (i.e., at the large distances r from a particle). In the far-field zone the solution of the vector wave equation can be obtained as

$$\begin{bmatrix} E_l^s \\ E_r^s \end{bmatrix} = \frac{\exp(-ikr+ikz)}{ikr}\begin{bmatrix} S_2 & S_3 \\ S_4 & S_1 \end{bmatrix}\begin{bmatrix} E_l^i \\ E_r^i \end{bmatrix} \tag{1.6.16}$$

where $k = \frac{2\pi}{\lambda}$, $\exp(ikz)$ is the incident plane wave and $\frac{\exp(-ikr)}{ikr}$ is the outgoing scattered wave. E_l^i and E_r^i are the parallel and perpendicular components of incident electrical field, and E_l^s and E_r^s are the parallel and perpendicular components of scattered electrical field, and $\begin{bmatrix} S_2(\Theta) & S_3(\Theta) \\ S_4(\Theta) & S_1(\Theta) \end{bmatrix}$ is the amplitude scattering matrix.
For spheres $S_3(\Theta) = S_4(\Theta) = 0$, so that equation (1.6.16) is the fundamental equation of scattered radiation including polarization.
$S_1(\Theta)$ and $S_2(\Theta)$ are the Mie scattering amplitudes, expressed by

$$S_1(\Theta) = \sum_{n=1}^{\infty}\frac{2n+1}{n(n+1)}\left[a_n\pi_n(\cos\Theta) + b_n\tau_n(\cos\Theta)\right] \tag{1.6.17}$$

$$S_2(\Theta) = \sum_{n=1}^{\infty}\frac{2n+1}{n(n+1)}\left[b_n\pi_n(\cos\Theta) + a_n\tau_n(\cos\Theta)\right] \tag{1.6.18}$$

where π_n and τ_n are the Mie angular functions, expressed as a function of the associated Legendre polynomials.
From Mie theory it follows that the extinction cross section of a particle is

$$\sigma_e = \frac{4\pi}{k^2}\mathrm{Re}\left[S_{1,2}(\Theta = 0°)\right]. \quad (1.6.19)$$

From equations (1.6.17) and (1.6.18) for Θ=0°

$$S_1(\Theta = 0°) = S_2(\Theta = 0°) = \frac{1}{2}(2n+1)(a_n + b_n). \quad (1.6.20)$$

Thus, extinction cross section is related to the scattering in the forward direction.
The efficiency factors for extinction, scattering and absorption are defined as

$$Q_{e,s,a} = \frac{\sigma_{e,s,a}}{\pi a^2} \quad (1.6.21)$$

where πa^2 is the particle area projected into the plane perpendicular to the incident beam.
Mie efficiency factors are derived from the Mie scattering amplitude

$$Q_e = \frac{2}{(ka)^2}\sum_{n=1}^{\infty}(2n+1)\mathrm{Re}\left[a_n + b_n\right] \quad (1.6.22)$$

$$Q_s = \frac{2}{(ka)^2}\sum_{n=1}^{\infty}(2n+1)\left[|a_n|^2 + |b_n|^2\right] \quad (1.6.23)$$

$$Q_a = Q_e - Q_s. \quad (1.6.24)$$

For a given aerosol type with size distribution N(r) the extinction, scattering and absorption coefficients are determined as

$$\sigma_{e,s,a} = \int_{r_1}^{r_2} Q_{e,s,a}(r)\pi r^2 \frac{dN(r)}{r\ln 10\, d(\log r)}dr \quad (1.6.25)$$

while the phase function is

$$P(\Theta) = \frac{\int_{r_1}^{r_2} P(\Theta, r)\sigma_s N(r)dr}{\int_{r_1}^{r_2} \sigma_s N(r)dr}. \quad (1.6.26)$$

1.6.4. SOURCE FUNCTION

The source function for the thermal emission is given by

$$S_\nu^t = \frac{\alpha_\nu}{k_\nu}B_\nu(T) \quad (1.6.27)$$

where α_ν is the absorption coefficient and $B_\nu(T)$ is the Planck function. Equation (1.6.27) can be written in terms of the single scattering albedo $\omega_{0\nu}$ as

$$S_\nu^t = (1 - \omega_{0\nu})B_\nu(T). \quad (1.6.27)$$

Scattering is a source of light at a given direction because light is scattered into this beam from other directions. If the phase function P(cos Θ), as well as the scattering and absorption coefficients of the particular extinction process, are known, the contribution of scattering to the total source function S_ν can be determined. Consider the change in radiance dI_ν in a certain direction (μ,φ) due to a scattering process with phase function P(cos Θ). The scattering contribution to dI_ν from every incident direction (μ',φ') is proportional to the radiance of the incident beam, to the phase function and to the single scattering albedo, so that the source function for scattering is

$$S_\nu^s = \frac{\omega_{0\nu}}{4\pi}\int_0^{2\pi}\int_{-1}^{1} I_\nu(\mu',\phi')\,P_\nu(\mu,\varphi,\mu',\varphi')\,d\mu'd\varphi'. \qquad (1.6.28)$$

The total source function is obtained by adding the source functions for thermal emission (1.6.27) and for scattering (1.6.28)

$$S_\nu = S_\nu^t + S_\nu^s. \qquad (1.6.29)$$

Inserting (1.6.29) into (1.6.12) the radiative transfer equation is derived including absorption, thermal emission and scattering

$$\mu\frac{dI_\nu}{d\tau_\nu} = -I_\nu + (1-\omega_{0\nu})B_\nu(T) + \frac{\omega_{0\nu}}{4\pi}\int_0^{2\pi}\int_{-1}^{1} I_\nu(\mu',\phi')\,P_\nu(\mu,\varphi,\mu',\varphi')\,d\mu'd\varphi'. \qquad (1.6.30)$$

The source function for scattering is divided in two components, since diffuse radiation arises from the light that undergoes one scattering event (single scattering) or many (multiple scattering) so that it can be written as

$$S_\nu^s = \frac{\omega_{0\nu}}{4\pi}F_{0\nu}P_\nu(\mu,\varphi,\mu_0,\varphi_0)\exp(-\tau_\nu/\mu_0) + \frac{\omega_{0\nu}}{4\pi}\int_0^{2\pi}\int_{-1}^{1} I_\nu(\mu',\phi')\,P_\nu(\mu,\varphi,\mu',\varphi')\,d\mu'd\varphi' \qquad (1.6.31)$$

where μ_0 and φ_0 are the solar zenith and azimuth angles, respectively, and $F_{0\nu}$ is the spectral extraterrestrial irradiance. The first term in the right side of (1.6.31) represents the contribution to scattering due to the direct radiation from the incident direction (μ_0,φ_0) that is scattered into the direction (μ,φ).

Thus, using the source function for scattering, the radiative transfer equation for the diffuse radiation is

$$\mu\frac{dI_\nu}{d\tau_\nu} = -I_\nu + \frac{\omega_{0\nu}}{4\pi}F_{0\nu}P_\nu(\mu,\varphi,\mu_0,\varphi_0)\exp(-\tau_\nu/\mu_0) + \frac{\omega_{0\nu}}{4\pi}\int_0^{2\pi}\int_{-1}^{1} I_\nu(\mu',\phi')\,P_\nu(\mu,\varphi,\mu',\varphi')\,d\mu'd\varphi'. \qquad (1.6.32)$$

1.7. RADIATIVE TRANSFER MODELS

Radiative transfer (RT) models represent very important tools to study how different atmospheric parameters modulate the incoming solar radiation; moreover, they allow the estimation of radiation levels where measurements are not performed and to predict radiation

amounts using possible future scenarios. The retrieval of atmospheric parameters from satellite sensors also requires the RT simulation of the sensor measurements.
The most common models are one-dimensional, considering uniform horizontal distribution of absorption and scattering parameters. These models usually approximate the real atmosphere as composed by layers, where composition is homogeneous and optical properties do not vary, but are allowed to vary from layer to layer. Figure 1.7.1 shows a simple, plane parallel atmosphere model of the radiative transfer problem for Earth's atmosphere. The underlying surface is considered as a Lambertian reflector. Given an extraterrestrial solar spectrum and the sun position, the radiance, the direct and diffuse components of irradiance or actinic flux are computed in each layer, accounting for absorption of molecules, gas and aerosol, multiple scattering by molecules and aerosols, multiple reflections by contiguous layers and thermal emission.

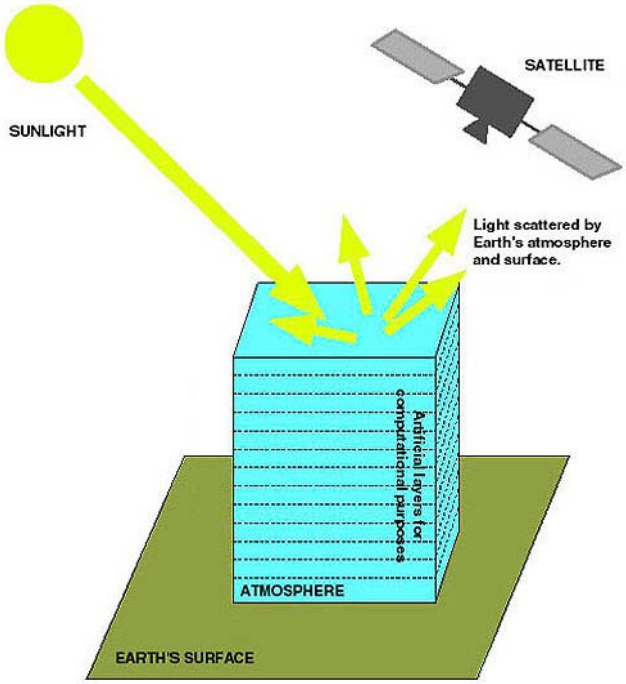

Figure 1.7.1. Simple, flat-atmosphere model of the radiative transfer problem for Earth's atmosphere.

Figure 1.7.2 shows the model used for each layer. When light enters the layer from some direction, some of that light is transmitted through (going in the same direction), some is absorbed inside the layer, and some is scattered into other directions leaving the layer, entering the layers above or below.
Earth, of course, is almost spherical, and the atmosphere forms a spherical shell around it. It turns out that creating a mathematical or computational model of the atmosphere that takes its spherical shape into account is very difficult. Treating the atmosphere as a "cake" of flat layers, rather than as a set of nested spherical shells, turns out to give computed radiances that are very close to the correct answers, except when the sun is very low in the sky. This is the most common method for treating the problem of radiative transfer in the atmosphere.

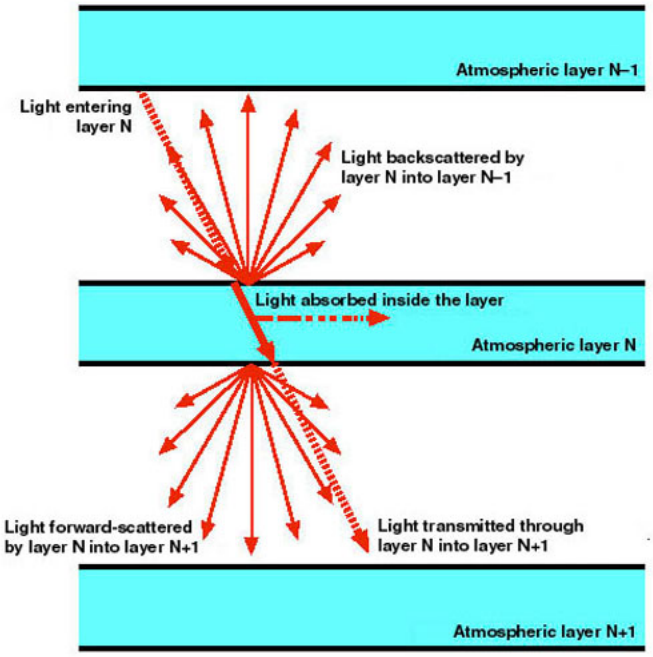

Figure 1.7.2. Scheme of transmission of solar radiation through consecutive atmospheric layers.

RT simulations of the solar radiation through the atmosphere require the solution of the RT equation (1.6.32) for the intensity I_ν at each wavelength. Equation (1.6.32) is an integro-differential equation: to solve it one needs to know the scattering and absorption coefficients and the scattering phase function as a function of wavelength in each atmospheric layer.
Equation (1.6.32) can be simplified if there is no dependency on the azimuth angle φ. For azimuthally-independent case, the phase function can be defined as

$$P_\nu(\mu,\mu') = \frac{1}{2\pi}\int_0^{2\pi} P_\nu(\mu,\varphi,\mu',\varphi')\,d\varphi'. \qquad (1.6.33)$$

Using expression (1.6.33) the azimuthally-independent RT equation for the diffuse radiation is

$$\mu\frac{dI_\nu}{d\tau_\nu} = -I_\nu + \frac{\omega_{0\nu}}{4\pi}F_{0\nu}P_\nu(\mu,\mu_0)\exp(-\tau_\nu/\mu_0) + \frac{\omega_{0\nu}}{2}\int_{-1}^{1} I_\nu(\mu')\,P_\nu(\mu,\mu')\,d\mu'. \qquad (1.6.34)$$

To find a solution of equation (1.6.32) various approximate and exact techniques have been developed. Generally the most accurate the solver is, the longer the computational time. Among the approximate methods there are the single scattering approximation, the two stream [*Meador and Weaver*, 1979], the Eddington and delta-Eddington approximations [*Joseph et al.*, 1976]. Some of the exact methods are the discrete ordinate technique [*Stamnes et al.*, 1988], the adding-doubling and the Monte Carlo techniques. The discrete ordinate method, the most used solver in RT models, will be described in detail in Appendix A.

Few studies have been conducted on the accuracy of RT models. In the UV estimates indicate that the input parameters play a major role. According to *Weihs and Webb* [1997], the main

source of uncertainty lays in the limited accuracy of the input data, which are likely to produce spectral UV values with maximum errors between ±15% and ±26% at 305 nm, and between ±4% and ±15% at 380 nm. Errors are smallest for unpolluted sites and for longer wavelengths. *Schwander et al.* [1997] found that for a polluted region as central Europe the uncertainties in the bulk input parameters (O_3 and SO_2 amounts, ground reflectivity, ground pressure, temperature, humidity and visibility) lead to uncertainties in spectral UV irradiances between 10 and 50%; limited accuracy of non-bulk parameters (vertical profiles of ozone, aerosol extinction, pressure and temperature) adds another 5% in modelled UV irradiances. Smaller uncertainties are expected when detailed characteristics of the input parameters, including the vertical distribution, are available.

CHAPTER 2

SURFACE, AIRBORNE AND SPACEBORNE MEASUREMENTS AT THE ISLAND OF LAMPEDUSA

2.1. MEASUREMENTS FROM GROUND-BASED INSTRUMENTS

The instruments described in this paragraph are deployed at the Laboratory for Climate Observation of the National Agency for New Technology, Energy, and Environment (ENEA) at the island of Lampedusa (35.5° N, 12.6° E), 45 m a.s.l. The ENEA Brewer spectrophotometer, the visible and UV MFRSR and the University of Rome lidar are set up for long term observations, while the Licor was operative only for the duration of the Photochemical Activity and Ultraviolet Radiation modulating factors II (PAUR II) campaign, held in May-June 1999. During the PAUR II campaign an articulated set of measurements of ultraviolet radiation, aerosol properties, and atmospheric chemical composition was collected in the Mediterranean [*Zerefos et al.*, 2002]: the campaign had the purpose of studying the interrelationships between changes in total ozone, tropospheric aerosols, UV radiation and photochemical activity. Measurements were performed in Greece and in Italy, at the island of Lampedusa [*di Sarra et al.*, 2001a].

2.1.1. THE BREWER SPECTROPHOTOMETER

The double monochromator Brewer MKIII (Figure 2.1.1) is designed to measure total columnar ozone and SO_2, and UV spectra from 286.5 to 363 nm. The total content of O_3 and SO_2 are derived from the measurement of UV radiation reaching the instrument at 5 prescribed wavelengths in the absorption spectrum of these gases. The Brewer contains a modified Ebert f/6 spectrometer with a 3600 lines/mm holographic diffraction grating operated in the first order for O_3/SO_2. The MKIII model differs from the previous MKII, which has a single monochromator, since it combines the filtering of two monochromators, thus ensuring a better reduction of the stray light [*Bais et al.*, 1996], the unwanted radiation measured along with desired wavelengths (caused by dirty or imperfect optics that disperse radiation in unintended directions).

Figure 2.1.1. Picture of the Brewer MKIII #123 (left) and the portable Brewer #017 (right) on the roof of the ENEA Laboratory at the island of Lampedusa.

The system is fully automated, and its functioning is driven and controlled by a computer software, which attends at the tracking of the sun across the sky, the collection and the storage of the data.
The instrument was conceived to continuously operate outdoor, thus its delicate internal components are housed in a durable shell. The range of temperatures where the system can operate normally is 0-40 °C.
The Brewer spectrophotometer consists of three major components: the foreoptics, the spectrometer and the photomultiplier.
The foreoptics can be adjusted to select the light coming from the sun or the moon, from the zenith, or from one of the two internal lamps, used for the instrument calibration: a mercury lamp, for wavelength calibration, and a standard tungsten lamp for the instrumental sensitivity check. A rotating zenith prism directs light from one of five sources towards a set of devices (iris, quartz lenses, film polarizers, neutral-density filters) which collimates, attenuates and filters the light before entering the spectrometer; these devices are mounted on two filterwheels rotated by motors controlled by the system microprocessor.
The modified Ebert spectrometer accepts light at the entrance slit and disperses it on a focal plane where six exit slits are located at the appropriate wavelengths positions: one slit is for the dark count, while the other five select the operative wavelengths for the O_3/SO_2 content retrieval: 306.3, 310.1, 313.5, 316.8 and 320.1 nm. The wavelength resolution is 0.55 nm. Each measurement consists of 5 observations, each based on 20 cycles: the 5 scans are registered on the appropriate exit file and a summary is created.
Light passing through the exit slits is focused onto the cathode of a low noise photomultiplier, which converts the photons into an electric signal, transmitted to the counter and registered in the 5 channels corresponding to the 5 wavelengths.
The microprocessor controls the position of the diffraction grating, the position of the two filterwheels, and turns the halogen and mercury calibration lamps on/off.

The retrieval of the O_3/SO_2 total content is based on the linear combination of the measured intensity at the 5 operative wavelengths, to minimize the effects of molecules and aerosols in the transmission of the incoming radiation.
The Brewer at Lampedusa (#123) was calibrated for ozone measurements in July 1998 and in March 2002, through a comparison with the travelling Brewer #17. The uncertainty on the total ozone, for cloud-free conditions, is about 1%.
Figure 2.1.2 shows the time series of daily average O_3 at Lampedusa from January 1998 to August 2003.

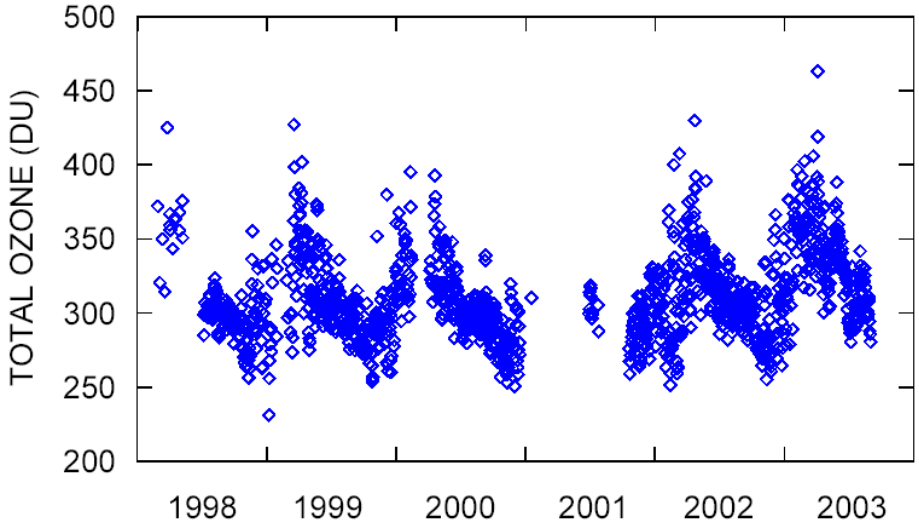

Figure 2.1.2. Time series of daily average O_3 content at Lampedusa from January 1998 to August 2003 measured by the Brewer spectrophotometer.

When performing the measurement of a UV spectrum, the light passes through a thin Teflon diffuser, mounted on the top of the instrument under a quartz dome, so that the instrument measures the downward UV irradiance. The transmitted light is collected by a fixed reflecting prism, located beneath the disc, and sent to the spectrometer.
A UV measurements is performed at steps of 0.5 nm. The raw counts are converted into counts per seconds and corrected for the dead time of the photomultiplier and for the temperature effects. The dark counts are accounted for as the average counts below 292 nm and are subtracted from all other wavelengths. The corrected raw counts are then divided for the instrumental responsivity and converted into irradiances.
The duration of a O_3/SO_2 measurement is 3-4 minutes and 9 minute for a UV scan.

Figure 2.1.3 shows an example of Brewer UV spectra; the absorption due to ozone below 310 nm causes a strong attenuation of the UV irradiance at short wavelengths.

The responsivity of the Brewer at Lampedusa is maintained by performing routine checks with 50 W lamps, and periodic calibrations with 1000 W FEL lamps, traceable to the U.S. National Institute for Standards and Technology (NIST), by means of a field calibrator [*Early et al.*, 1998]. The calibrations with the 1000 W lamp were performed once in 1999 and 2002, and are routinely carried out every approximately 50 days since May 2003. The responsivity was progressively corrected, referring the periodic checks with the 50 W lamps to the 1000 W

lamp calibrations, during the period January 1998 - May 2003; the responsivity is determined directly from the 1000 W lamp calibrations afterwards. The estimated uncertainties associated with the UV irradiance measurements are about ±5% at about 305 nm, and are better towards longer wavelengths.

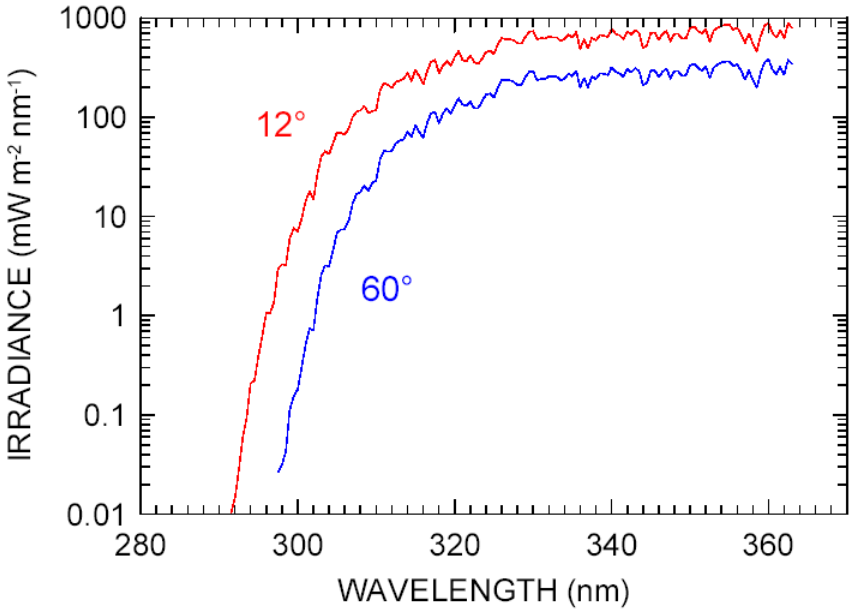

Figure 2.1.3. Brewer spectra measured on June 25, 2003 at 12° (red curve) and 60° (blue curve) solar zenith angle.

One of the most important problems with instruments that measure the irradiance, that is the radiation impingent on a horizontal surface, is the cosine response. Ideally, instrument response should be proportional to the cosine of the incident radiation and independent on the azimuth. This is not the case for most radiometers, especially at large solar zenith angles. The cosine error in the Brewer spectrometer contributes significantly to underestimate the UV irradiance: *Herman et al.* [1999] estimate a 6% on average correction, depending on both the specific Brewer instrument and particular conditions (e.g., noontime solar zenith angle).
Thus, the correction for the non ideal cosine response of the spectrometer must be considered. The angular response of the diffuser of the Brewer at Lampedusa was measured by the manufacturer in 1995. In May 2003 the diffuser was replaced; the angular response of the new diffuser was measured in May 2004 as part of the Quality Assurance of Spectral Ultraviolet Measurements in Europe (QASUME) project. The cosine correction to the global erythemal irradiance was proposed by *Bais et al.* [1998]; the cosine corrections depends essentially on the cosine response of the diffuser, and on the direct-to-global radiation ratio. In its turn, the direct-to-global ratio depends on the solar zenith angle, on total ozone (at short wavelengths), and on the aerosol optical depth.

2.1.2. THE MFRSRs

The Multifilter Rotating Shadowband Radiometer MFR-7 measures global and diffuse irradiance at six narrow bands centred at 415.6, 495.7, 614.6, 672.8, 868.7, and 939.6 nm, each with about 10 nm full width at half maximum (FWHM) bandwidths in the visible/NIR, and includes one unfiltered broad-band (350-1000 nm) silicon photodiode. The tracking shadowband (see Figure 2.1.4) allows to measure the global and diffuse irradiance with the same detector, thus the calibration coefficients are the same for the two components and smaller errors are implied with respect to the case of measurements made with different detectors [*Harrison et al.*, 1994a].

Figure 2.1.4. The Multifilter Rotating Shadowband Radiometer MFR-7 (right side) and UVMFR-4 (left side) at Lampedusa

The detector consists of a Spectralon plane diffuser and an integrating cavity where an array of seven photodiodes with interference filters are mounted. The interior of the detector assembly is thermally insulated to improve the accuracy of the measurements, since both photodiodes and interference filters are sensitive to temperature. The rotating shadowband is a metallic strip mounted along a celestial meridian, blocking a strip of sky (including the sun) with a 3.3° umbral angle: the band is moved by a stepping motor driven by a microprocessor. At each measurement interval, the microprocessor calculates the sun position using an approximation for the solar ephemeris. Four measurements are performed in sequence: the first one is with the band at the nadir, so that the global component is measured, then a second one is performed with the shadowband blocking the sun disk completely; since in this case not only the direct component, but also a part of the diffuse irradiance is blocked, two more measurements are made, with the band rotated to 9° on either side of the sun. These two side measurements permit a correction for the "excess sky" that is blocked by the shadowband when the sun-blocking measurement is made. The microprocessor then subtracts the corrected diffuse component from the global irradiance to obtain the direct-horizontal component. Finally, division of the direct- horizontal component value by the cosine of the

solar zenith angle results in the value of the direct-normal component. The entire sequence is completed in less than 15 seconds, so that the measurements can be considered simultaneous. The MFR-7 absolute response of each channel is measured using a 1000 W FEL NIST-traceable spectral irradiance standard lamp by the manufacturer. Period calibrations by means of the Langley technique [*Harrison et al.*, 1994b] permit to evidence any temporal degradations of the instrument's response [*Schmid and Wehrli*, 1995]. The Langley method is applied selecting for the calibration cloud-free half days characterized by small and stable aerosol amount. It also allows to derive the aerosol optical depth in each band, after correcting the signals for changes of the Sun-Earth distance and subtracting the molecular extinction, O_3 (for the bands at 495.7, 614.6, and 672.8 nm), NO_2 (for the band centred at 415.6 nm) and H_2O (for the 939.6 nm band) contributions. The 939.6 nm channel has not been calibrated yet, so it will not be used in the studies described in the following chapters. NO_2 correction is done using the column amount based on the Global Ozone Monitoring Experiment (GOME) data [*Burrows et al.*, 1999b]. Figure 2.1.5 presents an example of MFRSR irradiance and AOD at 415.6 nm: both cloud-free (188, 189 and 191) and cloudy (186, 187 and 190) days are showed.

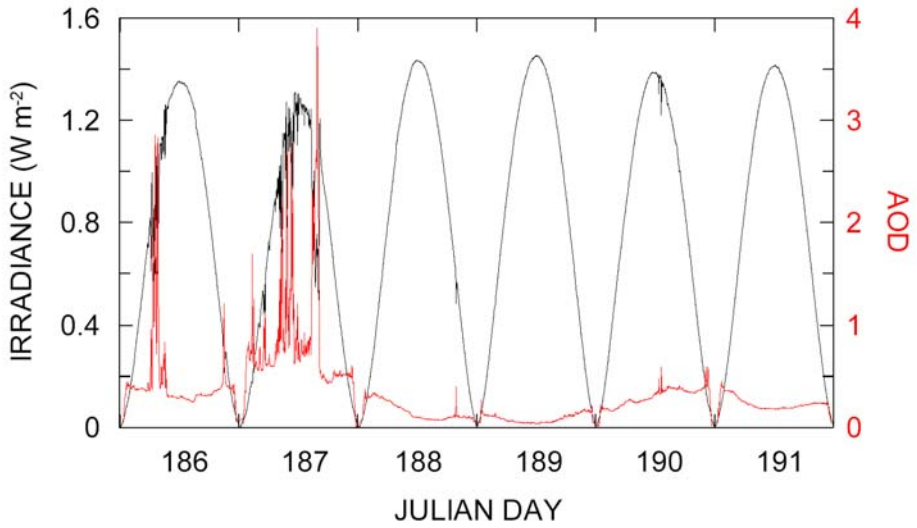

Figure 2.1.5. Example of MFR-7 irradiance (black curve) and AOD (red curve) at the band centred at 415.6 nm from July 5 (julian day 186) to 10 (julian day 191) 2003.

The UV Multifilter Rotating Shadowband Radiometer UVMFR-4 measures global and diffuse irradiance at 4 narrow bands in the UV centred at 299.8, 305.4, 311.3, and 317.6 nm, with bandwidths of about 2 nm FWHM. The basic functioning is the same as that for the MFR-7. In the UV the calibration by means of the Langley method is unpractical due to the large role played by ozone and its variations. The correction of the daily ozone variability, although in principle possible, would produce relatively large errors on the estimated extraterrestrial constant. Alternatively, UV-MFR4 can be calibrated by comparing the measured global irradiances with those determined by the Brewer spectrophotometer, as will be described in paragraph 4.3.1a.

2.1.3. THE LICOR

The Licor LI-1800 spectroradiometer measures global irradiance in the range 300-1100 nm with a 6 nm bandwidth at a wavelength interval selectable at 1, 2, 5 or 10 nm. A description of the instrument is given by *Cachorro et al.* [1998]. The optical receiver of the LI-1800 is a Teflon diffuser. The system contains a 800 line/mm holographic grating monochromator and a silicon detector; a filter wheel with seven filters serves to proper attenuation and stray light rejection, with one filter for the measurement of dark counts. The detection apparatus is not temperature stabilized. The estimated accuracy is ±10-15% depending on wavelength.
The LI-1800 was operating at Lampedusa only during the Photochemical Activity and Ultraviolet Radiation modulating factors II (PAUR II) campaign, from May to July 1999. An example of Licor spectra acquired at 20° and 60° solar zenith angle during the campaign is given in Figure 2.1.6: the absorption due to water vapour centred at 690, 726and 936 nm and to O_2 at 764 nm are discernable.

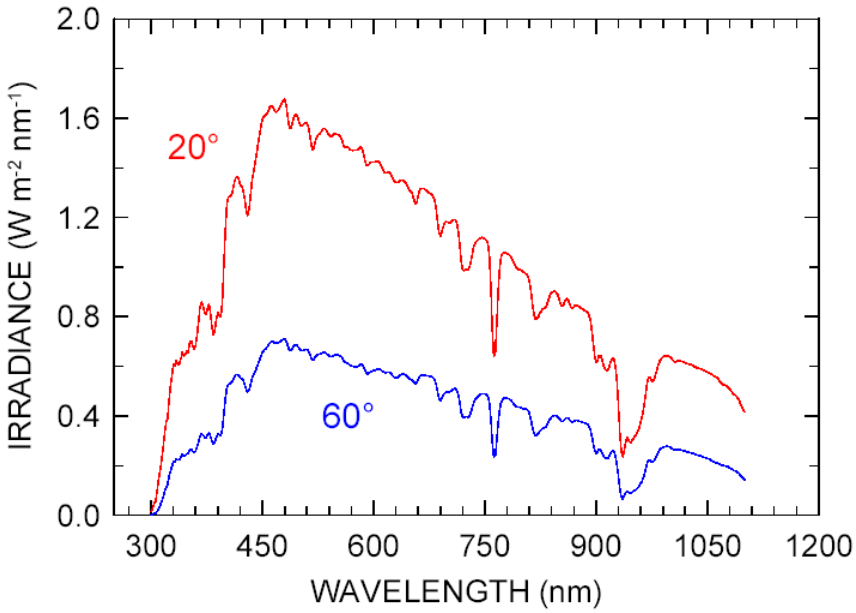

Figure 2.1.6. Licor spectra measured at Lampedusa on 25 May 1999 at 20° (red curve) and at 60° (blue curve) solar zenith angle.

2.1.4. THE LIDAR

The LIDAR (LIght Detection And Ranging) system allows to derive information about the atmospheric structure and composition through the analysis of the signal from a laser source which is backscattered by molecules, aerosols and clouds. The retrieval of the observable physical parameters is based on the measurement of the power received by the detector, which can be expressed as a function of the distance *r* by the so called "lidar equation"

$$P(r) = P_0 \frac{A}{r^2} \eta \frac{c\tau}{2} \beta(r) T_r(r)^2 \qquad (2.1.1)$$

where P_0 is the emitted power, A is the detector area, η is the optical efficiency of the system, τ is the duration of the pulse, c is the light speed, β is the backscattering coefficient and T_r is the atmospheric transmissivity.

The information on the atmospheric composition is enclosed in the terms T_r and β. The transmission can be written as

$$T_r(r) = \exp\left[- \int_0^r \alpha(x)dx \right] \qquad (2.1.2)$$

where α is the atmospheric extinction coefficient, which is sum of the contributions of molecules, aerosols and gases. Similarly, the backscattering coefficient β is the sum of the contributions of molecules and aerosols.

The lidar developed by the University of Rome "La Sapienza" and deployed at the ENEA laboratory at Lampedusa since 1999 is designed to observe tropospheric aerosols from 0.4 to 10 km in daylight conditions. The system was upgraded in 2002 to expand the sounding interval toward lower altitudes by adding a refractive 50 mm aperture telescope that allows the retrieval of useful signals from above approximately 60–100 m.

The radiation source is a solid-state neodymium: yttrium/aluminum/garnet (Nd:YAG) laser emitting linearly polarized pulses at 532 nm with a repetition rate of 10 Hz. The backscattered radiation, collected by two 100 mm diameter Cassegrain telescopes, is collimated and filtered through 1-nm bandwidth interference filters. A high quality polarizing filter in each receiving system selects the signal with polarization parallel or perpendicular to that of the laser beam. The polarisers ensure that the cross-talk between the two depolarisation channels is negligible. The radiation is then detected by photomultipliers, whose output signals are digitised by fast analog-to-digital converters. The acquisition system is programmed to perform an integration of the backscattered signals over 300 laser shots, corresponding to 5 minutes. The vertical resolution of the measurements is 30 m. The analyses have been carried out on 30 minute signal averages, corresponding to 1800 laser shots. The retrieval of the backscatter ratio *R*, defined as the ratio between the total (aerosol + molecules) parallel polarized backscattered signal, and the portion due to atmospheric molecules, and of the aerosol backscattering coefficient β_s also for the parallel polarization, is obtained as follows: the lidar signal, after subtraction of the background contribution, is normalized to a theoretical profile for the molecular atmosphere, calculated on the basis of the 12:00 GMT meteorological analyses performed by the National Centers for Environmental Prediction (NCEP); the normalization is carried out in the aerosol-free region above the aerosol layer.

The theoretical profile contains a correction for the molecular extinction; correction for the extinction due to the aerosols is calculated assuming a constant extinction-to-backscattering ratio, *e*, throughout the aerosol layer. The choice of the extinction-to-backscattering ratio is critical, since this constant strongly affects the derived aerosol profiles. A few measurements of *e* for tropospheric aerosols in arid regions have been published. *Spinhirne et al.* [1980] obtained estimates of *e* from multi-angle lidar measurements carried out in Arizona with a ruby laser; from their data set they obtained $e = 19.5 \pm 8.3$ sr. *Sasano and Browell* [1989] derived estimates of *e* from multiple wavelength lidar observations, for different aerosol conditions: for Saharan dust aerosol, values between 15 and 62 sr were obtained. *Rosen et al.* [1997] measured the extinction-to-backscattering ratio, using a nephelometer and a backscattersonde, in New Mexico, for desert aerosols and found values of *e* around 41.6 and 32.2 sr, respectively at 490 and 700 nm, with a 20% standard deviation in the range of measured values. Model analyses on the optical properties of irregularly shaped dust particles suggest that a larger extinction-to-backscattering ratio applies to this kind of aerosols [*Mishchenko at al.*, 1997].

For the profiles acquired during the PAUR II campaign, a methodology, described in *Di Iorio et al.* [2003] was adopted, which derived estimates of *e* by combining optical depth and backscatter measurements.
Profiles of R_c, the perpendicular polarization backscatter ratio, are derived from the cross-polarized signals with the same procedure applied for the determination of *R*. The aerosol depolarisation ratio δ, defined as the ratio between the cross-polarized and the parallel-polarized signals from the aerosol, is obtained through the expression

$$\delta = \frac{R_c - 1}{R - 1}\delta_m \qquad (2.1.3)$$

where δ_m=0.014 [*Weber at al.*, 1967], is the depolarisation ratio for the molecular atmosphere. The value of δ is an indication of the particles' shape. A large value of δ is expected when the scatterers have irregular shape (or inhomogeneous refractive index). The accurate determination of the depolarisation ratio in daytime is generally difficult, due to the large contribution to the signal due to the background radiation. The large background makes particularly difficult the detection of the cross-polarized signal from the molecules (approximately 1/100 of the parallel polarization signal from the molecules), in the height regions devoid of aerosol. The detection of a significant signal from these regions is required for a correct calibration of the lidar profile. Thus, although the aerosol particles evidently show a large depolarisation, it is sometimes difficult to derive an accurate estimate of δ from the 30 minute averages ordinarily performed. To reduce the indetermination on the measure of δ, longer integration periods have to be selected. The estimated measurement uncertainties on *R* and δ are smaller than 10 and 30% respectively.
The total aerosol backscatter ratio R_t, i.e. the ratio between the sum of the parallel and cross polarization signal from aerosol and molecules divided by the sum of the parallel and cross polarization signal from the molecules, may be expressed as

$$R_t = 1 + \frac{(R - 1) + (R_c - 1)}{\delta_m + 1}\delta_m . \qquad (2.1.4)$$

For non-spherical scatterers producing a depolarisation ratio value of 0.2, R_t is larger than *R* by 10% for *R*=2, and by less than 15% for values of *R*<5. When δ=0.1, R_t is larger than *R* by less than 8% for *R*<10.

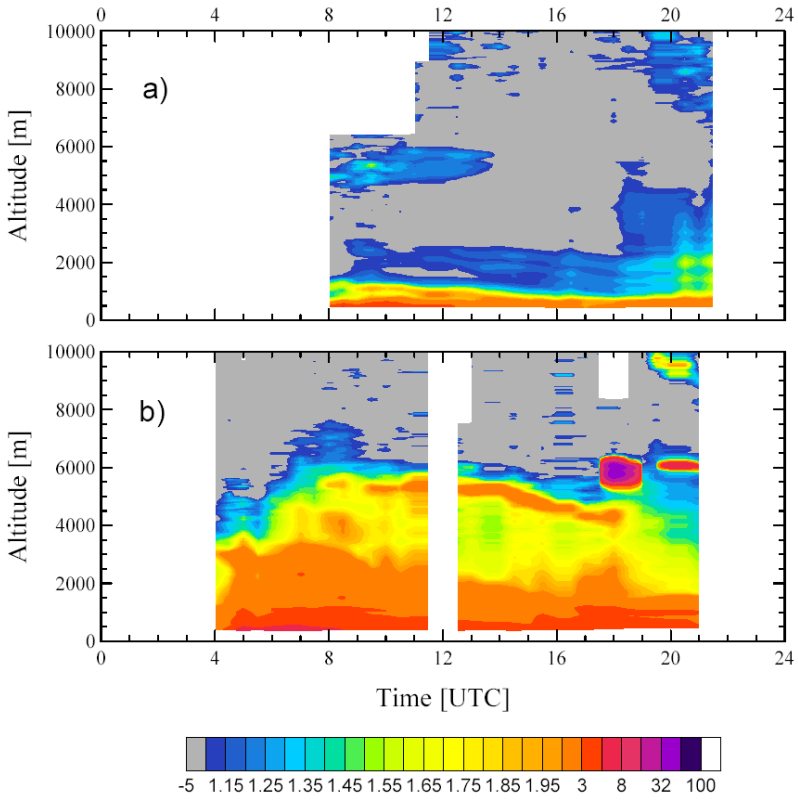

Figure 2.1.7. Time evolution of the lidar backscatter ratio *R* measured at Lampedusa on two days with very different aerosol characteristics: a) 25 May 1999, a day with low aerosol amount, and b) 2 June 1999, a day with a large amount of desert dust.

Figure 2.1.7 shows two examples of lidar measurements of backscatter ratio *R*. The white area represents the lack of measurements, while purple colour identify the presence of thick clouds (like in graph b) from 18 to 19 UTC). The aerosol clouds are identified by green to red colours.

2.2. MEASUREMENTS FROM AIRBORNE INSTRUMENTS

During the PAUR II campaign the ultralight aircraft of the *Fraunhofer Institüt für atmosphärische Umweltforschung*, (IFU, Germany), performed sixteen flights from Lampedusa airport measuring solar radiation, ozone and aerosol parameters from the surface up to 3-4.5 km.

The following instruments were installed aboard the aircraft: an UV photometer for determination of ozone concentration, a Forward Scattering Spectrometer Probe (FSSP-100) optical particle counter for particles of diameter between 0.4 and 8 μm, a laser particle counter for particles of diameter larger than 0.3 μm, a TSI-3010 condensation nuclei counter, for particles of diameter between 0.01 and 3 μm, an AVM III aerosol scatterometer, two solar pyranometers (upward and downward looking), an UV-B radiometer, four $J(O^1D)$ and $J(NO_2)$ filter radiometers (upward and downward), a dew point mirror, a pressure transducer, and a GPS receiver.

2.2.1. THE FILTER ACTINOMETERS

Aboard the aircraft, two pairs of 2π sr photoelectric detectors for upwelling and downwelling components of the actinic fluxes were deployed. The first pair of upward+downward looking sensors is aimed at the measurement of NO_2 photolysis rate, $J(NO_2)$, while the second pair is matched for the O_3 photolysis rate, $J(O^1D)$. The radiometer characteristics and calibration procedures are described in detail by *Junkermann et al.* [1994]. The photoelectric detectors consist of three main components: a photosensitive device, an optical filter, and an optical input system designed to receive light from all directions of a hemisphere. The input system consists of a set of coaxial quartz tubes inside a quartz dome; the volume between the tubes is filled with quartz grains, which serve as a scattering medium. The scattered light is conducted by the quartz tubes through the optical fiber onto the photoelectric sensor. The spectral response of the detectors is adapted to the $\sigma_x(\lambda,T)\cdot\phi_x(\lambda,T)$ product by a combination of optical filters with appropriate photoelectric sensors. In the case of $J(O^1D)$ detector, an interference filter and a photomultiplier constitute the photoelectric sensor. In the case of $J(NO_2)$ detector the filter system is a coloured glass filter and the light sensitive device is a UV-photodiode.
The spectral sensitivity of the $J(NO_2)$ detector reasonably matches the product of the NO_2 absorption cross section by the quantum yield for the formation of $O(^3P)$: the transmission band is centred at 370 nm and has a 70 nm FWHM bandwidth. The $J(O^1D)$ detector has an interference filter with centre wavelength at 301 nm and 6 nm FWHM bandwidth [*Junkermann*, 2001], whose spectral behaviour approximates the product of the O_3 absorption cross section by the $O(^1D)$ quantum yield. The filter characteristics of the $J(NO_2)$ and $J(O^1D)$ sensors however do not perfectly match the $\sigma_x(\lambda,T)\cdot\phi_x(\lambda,T)$ product, thus conversion of the measured actinic flux into photolysis rates requires corrections for total ozone, solar zenith angle and temperature. The radiometers were calibrated against chemical actinometers.
The accuracy of the absolute calibrations for the $J(NO_2)$ and the $J(O^1D)$ detectors against chemical actinometers, are ±8% and ±15%, respectively [*Junkermann*, 2001]; reproducibility and angular response of the sensors are better than ±5%. Example of profiles measured during PAUR II at Lampedusa will be given in paragraph 5.2.3.

2.2.2. UV PHOTOMETER

The UV photometer measures ozone concentrations in ambient air. The photometer's primary components are a mercury lamp, two identical sample chambers, two detectors, and a scrubber. The lamp provides 254 nm radiation that is transmitted through the length of the chambers to the detectors, one chamber containing the air sample with ozone and other containing air with the ozone removed. Ozone strongly absorbs radiation at this wavelength, allowing virtually continuous measurements of ozone by comparing the detected signals in the two chambers, and periodically alternating the roles of the two chambers. Measurement of the chamber temperature and pressure allows for the calculation of the ozone mixing ratio which is invariant between the chamber and the atmosphere. Example of profiles measured during PAUR II at Lampedusa will be given in paragraph 3.3.1.

2.3. MEASUREMENTS FROM SPACE-BORNE SENSORS

2.3.1. THE MULTI-ANGLE IMAGING SPECTRO-RADIOMETER (MISR)

The MISR instrument [*Diner et al.*, 1998] was launched aboard the Terra spacecraft on December 1999. It has been designed at the Jet Propulsion Laboratory (JPL) to view the Earth's atmosphere in nine different directions in order to detect the angular variation of the sunlight reflected by clouds, aerosols and the surface. MISR nine cameras (CCDs) are arranged in the following configuration (see Figure 2.3.1): a nadir viewing camera (identified as AN), a group of four cameras pointing in the forward direction (AF, BF, CF and DF with increasing off-nadir angle), and a group of four cameras pointing in the afterward direction (AA, BA, CA, DA). The fore and aft cameras are displaced in a symmetrical arrangement with respect to the nadir camera, with nominal viewing angles of 26.1, 45.6, 60.0 and 70.5°. Each camera images the underlying scene in four spectral bands centred at 446.4, 557.5, 671.7, and 866.4 nm with bandwidths of 41.9, 28.6, 21.9, and 39.7 nm, respectively. The time interval between the observation of a point on the surface by the DF and DA cameras is 7 minutes.

On-board calibration is performed monthly by multiple in-flight methodologies, using solar-reflecting diffuse panels, detector standards, and a goniometer to verify that there is no degradation in the reflectance shape of the panels. In addition, semi-annual overflight field campaigns are conducted. A 3% absolute radiometric uncertainty at the maximum signal is estimated [*Diner et al.*, 1998].

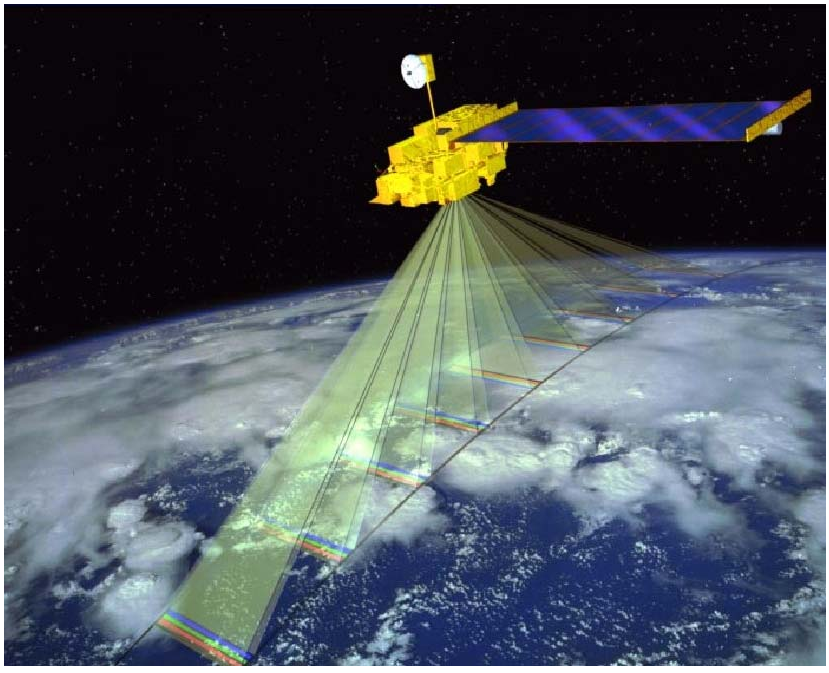

Figure 2.3.1. Computer-generated image shows the Terra spacecraft, with the MISR instrument on board, orbiting Earth. Direction of flight is toward the lower left. The actual locations imaged by the 9 cameras, each with 4 colour bands, along Earth's surface are illustrated here with translucent surfaces *(*JPL image P-49081 from *www-misr.jpl.nasa.gov*).

The 705 km orbit of the Terra satellite is near-polar and sun-synchronous, with a 10:45 am equator crossing time on the descending node, and a global coverage repeat cycle of 16 days, corresponding to 233 orbits. The swath width has been designed to be 360 km, so that the coverage of a latitude circle is achieved every 9 days at the equator and every 2 days at the poles.
The cross-track dimension of a pixel is 275 m for the off-nadir cameras and 250 m for the nadir camera, while the sample spacing in the along-track direction is 275 m in all cameras. Typically, MISR observes the Earth at a lower resolution, obtained averaging the adjacent samples, so that only the nadir camera acquires images with all four bands at 275 m resolution (1×1 pixels), while the other eight cameras produce data at 275 m resolution in the red band, with the remaining channels averaged at 1.1 km resolution (4×4 pixels).
The estimate of the TOA fluxes is based, for most satellite instruments, on the observations of the radiance in a single direction. The measurements at several viewing angles provided by MISR give the opportunity to attempt a more detailed reconstruction of the outgoing radiation scattered by the Earth atmosphere and surface. In general, large viewing angles provide enhanced sensitivity to atmospheric aerosol and to cloud reflectance effects, whereas more smaller angles are required for land surface viewing. Moreover, having the off-nadir cameras in pairs either side of nadir enhances the number of scattering angles (see Figure 2.3.2), thus the possibility to determine the aerosol and/or cloud phase function.
After the 36 channels of imaging data are radiometrically calibrated, georectified, and averaged to a uniform resolution of 1.1 km, they then are analysed to determine aerosol properties over both land and ocean at a resolution of 17.6×17.6 km^2.

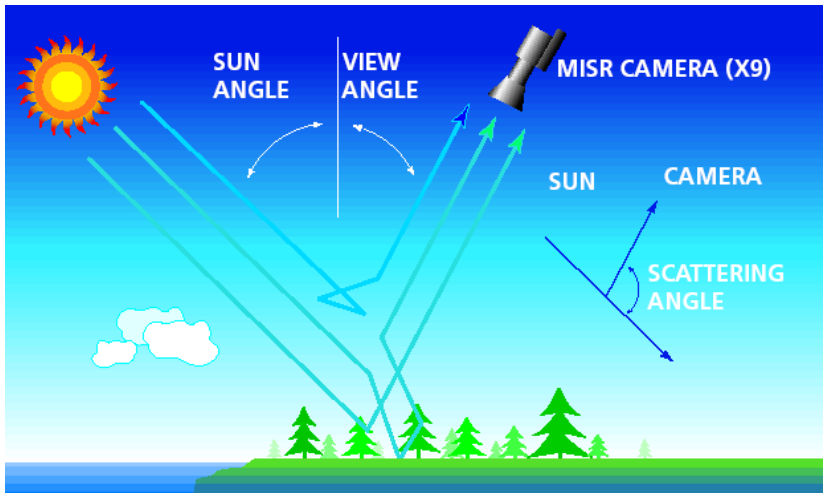

Figure 2.3.2. Scheme of the MISR viewing geometry.

An aerosol retrieval algorithm has been implemented to derive the AOD and optical properties over both land and ocean [*Martonchik et al.*, 1998]. The algorithm requires a predetermined set of aerosol models and their associated radiative atmospheric parameters, established from a review of published aerosol climatologies [*World Climate Programme*, 1984; *Shettle*, 1989; *d'Almeida et al.*,1991; *Krekov*, 1993]: in general, tropospheric aerosols fall into a small number of categories, which include sea spray, sulphates, nitrate, mineral dust, biomass burning particles and soot. The retrievals are performed by comparing observed TOA radiances with model radiances calculated for a suite of aerosol compositions

that covers a range of expected natural conditions and for varying surface reflectance properties: a set of pre-computed look-up tables is used. A chi-squared statistical formalism to assess the magnitude of the residuals in the comparisons is adopted to accept a candidate aerosol type.
Figure 2.3.3 presents an example of MISR view of a dust plume in the Easter Mediterranean Sea on October 18, 2002 from the nadir and the DF cameras; the retrieved heights of the clouds and some parts of the dust plume are also shown.

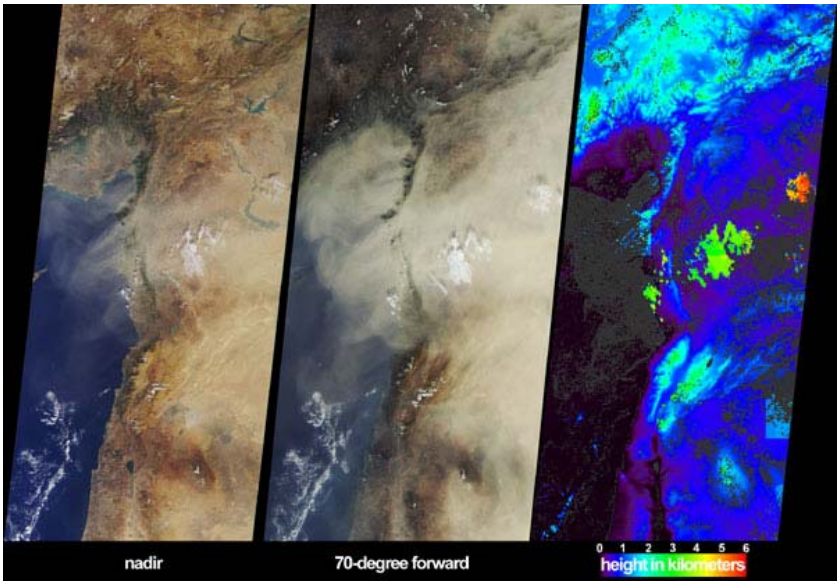

Figure 2.3.3. MISR images of a large dust plume extended across countries bordering the eastern Mediterranean Sea on October 18, 2002. Information on the horizontal and vertical extent of the dust are provided by these views. The left-hand panel portrays the scene as viewed by the instrument's vertical-viewing (nadir) camera. Here only some of the dust over eastern Syria and South-eastern Turkey can be discerned. The dust is much more obvious in the central panel, which is a view from MISR's most steeply forward-looking camera. In addition, this perspective makes shadows cast by clouds onto the dust layer more apparent, providing a visual clue that the dust is at a lower altitude than these clouds. The right-hand panel is an elevation field derived from automated MISR stereoscopic processing, in which the heights of clouds and certain parts of the dust plume are retrieved. The MISR image is from *www-misr.jpl.nasa.gov*.

2.3.2. THE TOTAL OZONE MAPPING SPECTROMETER (TOMS)

The NASA Total Ozone Mapping Spectrometer (TOMS) instrument started its measurements in October 1978 on board the Nimbus 7 satellite until May 1993 and continued with Meteor 3 (from August 1991 to December 1994), ADEOS (from August 1996 to December 1997) and with the actual Earth-Probe TOMS (from July 1996). The EP/TOMS provides measurements of total column ozone by measuring the backscattered Earth radiance in the six triangular bands of 1 nm FWHM bandwidth centred at 308.6, 313.5, 317.5, 322.3, 331.2, 360.4 nm. The experimental apparatus uses a single monochromator and scanning mirror to sample the backscattered solar ultraviolet radiation at 35 sample points at 3° intervals along a line perpendicular to the orbital plane. It then quickly returns to the first position, not making

measurements on the retrace. The time interval for a complete scan is eight seconds. The present sun-synchronous orbit is 750 km, but was 500 km before December 1997. The orbit inclination of 98.4° was unchanged, with a local equator crossing time varying from 11:03 am to 11:30 am, that is around local noon. The instrument instantaneous field-of-view (IFOV) varies approximately from 26×26 km^2 at nadir to 60×33 km^2 at the maximum side-viewing scan angle.
Periodic calibration of the instruments are performed by rotating the scanner to view one of three ground aluminum diffuser plates which reflect the solar irradiance.

The total ozone is derived from the measured backscattered radiance I_{TOA} normalized to the incident solar irradiance F. The quantity N

$$N = -100 \log\left(\frac{I_{TOA}}{F}\right) \qquad (2.3.1)$$

is defined.
The retrieval is based on the comparison of the N values measured and those derived from a radiative transfer model. The model is implemented to calculate look-up tables of N for various total ozone amounts, surface pressure, surface and clouds reflectivities and latitude; other information required are the temperature dependent ozone cross sections at the TOMS wavelengths, Rayleigh scattering coefficients, climatological temperature and ozone profiles for the location, the sun position, the satellite viewing angle and IFOV.

Algorithms have been developed to estimate other parameters from the retrieved ozone.
For a cloud-free scene the aerosol absorption is accounted for by the aerosol index (AI) expressed in the EP/TOMS data as

$$AI = -100\left[\log\left(I_{331}/I_{360}\right)_{meas} - \log\left(I_{331}/I_{360}\right)_{calc}\right] \qquad (2.3.2)$$

where I_{meas} is the measured backscattered radiance and I_{calc} is the calculated radiance for a purely Rayleigh atmosphere. The AI definition implies that UV absorbing aerosols (desert dust and soot) produce positive values, while non-absorbing aerosols (for example sulphates) correspond to negative values; however, moderately absorbing aerosols that are near the Earth's surface cannot be differentiated from non-absorbing aerosols [*Hsu et al.*, 1999].
The erythemal irradiance at the surface (at local noon or daily integrated) can be calculated in two steps [*Herman et al.*, 1999]. In a first step, the clear sky (cloud and aerosol free) irradiance is calculated by means of the radiative transfer model, and then a cloud correction factor is applied. This factor, which represents the ratio between cloudy sky and clear sky irradiance transmittance, is evaluated using the TOMS 360 nm reflectivity and the model assuming a homogeneous cloud layer between 700 and 500 hPa. Because the reflectivity of a cloud can be as high as that of snow (depending on age, depth and purity), snow cover can be misinterpreted as a cloud, thus causing an underestimation of the UV irradiance at the surface. The cloud correction factor is presumed to be valid throughout the day, thus large daily discrepancies between ground-based measurements and TOMS-derived erythemal doses can arise for cases with cloud-cover variability during the day.
Reflecting aerosols are taken into account in the cloud correction factor, while absorbing aerosols are included in the estimated UV irradiance using the TOMS aerosol index to obtain a correction factor based on an aerosol plume assumed as a thin layer at about 3 km height.
Global TOMS products are presented on a 1° latitude ×1.25° longitude grid, covering a latitudinal range from 85° S to 85° N.
Figure 2.3.4 shows an example of TOMS global map of ozone, corresponding to March 21 2003.

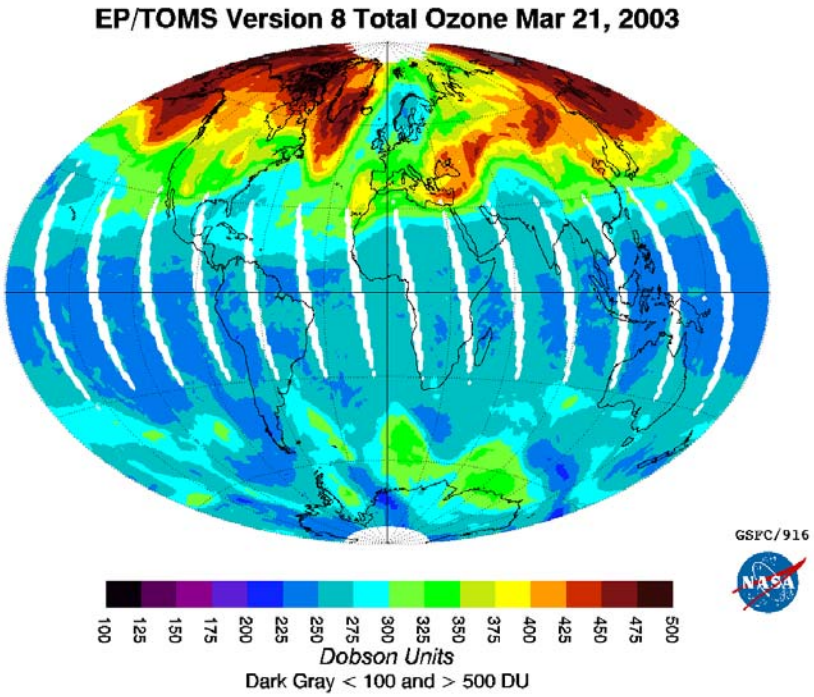

Figure 2.3.4. Global map of ozone measured form TOMS sensor on March 21, 2003 (from TOMS web site, *http://toms.gsfc.nasa.gov/index.html*).

CHAPTER 3

THE RADIATIVE TRANSFER MODEL UVSPEC

3.1. BASIC CHARACTERISTICS

The UVSPEC was originally designed to calculate spectral irradiance in the ultraviolet and visible spectral ranges, hence the name. It is the central program of a package of RT routines and programs called libRadtran, useful for RT calculations in the Earth's atmosphere. It is described by *Mayer et al.* [1997], *Kylling et al.* [1998], and *Kylling and Mayer* [2001].
The model allows the choice of one among three methods for the solution of the radiative transfer equation: the two stream [*Meador and Weaver*, 1979], the discrete ordinate method (DISORT algorithm) for plane-parallel atmosphere [*Stamnes et al.*, 1988] (see Appendix A for details) and the pseudo-spherical approximation of DISORT (SDISORTalgorithm) which accounts for the sphericity of the atmosphere [*Dahlback and Stamnes*, 1991], useful for high (>70°) solar zenith angles, when a correction to the photon path length is needed with respect to the plane-parallel scheme. DISORT and SDISORT apply to the inhomogeneous non-isothermal plane-parallel atmosphere.
The model can simulate radiation quantities such as spectral radiance, direct and diffuse irradiances and actinic fluxes at each level between the ground and the TOA with arbitrary wavelength steps between 200 and 800 nm, assuming an extraterrestrial solar spectrum and taking into account the atmospheric structure and composition, and the surface characteristics. When the model is employed to simulate a measurement performed by an instrument, for example a spectroradiometer, the calculated spectrum can be convolved with the instrumental slit function.
Spectrally resolved (or line-by-line) calculations are straightforward in the UV and visible spectral ranges, where gas absorption generally occurs in broad bands with only slow spectral variation, the most important the these being the Hartley, Huggins and Chappuis bands of ozone (see paragraph 1.2.1).
The solar irradiance at the Earth's surface can be written (in absence of thermal emission) as the product of the atmospheric transmittance T and the extraterrestrial irradiance E_0

$$E(\lambda) = T(\lambda) \cdot E_0(\lambda) \qquad (3.1.1)$$

To simulate $E(\lambda)$ the atmospheric transmittance $T(\lambda)$ must be calculated, at the desired wavelength resolution. Since the computational time depends on the number of calls to the RT solver, the wavelength resolution for the transmittance calculation must be optimised. In the UV and visible the solar extraterrestrial spectrum is highly variable due to the Fraunhofer structure originating in the solar atmosphere. On the other hand, the atmospheric

transmittance due to ozone absorption, Rayleigh scattering and atmospheric extinction is a smooth function of wavelength. Thus, UVSPEC calculates $T(\lambda)$ at low resolution and uses an efficient scheme to interpolate it at a high resolution grid before multiplying it for a high resolution $E_0(\lambda)$ to obtain a highly resolved model spectrum.
The number of streams, *n*, can be selected. It is set to 2 for the two stream solver, while it is set to larger values for the discrete ordinate method (keeping in mind that the computation time varies approximately as n^3): default values are 6 for the irradiance and 16 for the radiance calculation.
The atmosphere is divided into layers with constant gas concentration and aerosol optical properties. These properties may vary from layer to layer. UVSPEC is a 1-D RT model, meaning that the properties of each layer and of the surface are horizontally homogeneous. Ozone is assumed to be the only absorbing gas in the UV, visible and near infrared; absorption bands of other atmospheric constituents, like SO_2, NO_2, H_2O or O_2, exist in this spectral range, and differences between model simulations and observations are expected in correspondence.
The model inputs are the Sun position (zenith and azimuth angles), the zenith and azimuth viewing angles (in the radiance simulation), total ozone, spectral ground albedo, vertical profiles of pressure, temperature, air density, and ozone. The wavelength dependence of the ozone cross sections with temperature is taken into account. The day of the year can be specified if the Earth-Sun distance has to be considered. The default properties for the aerosols are a rural type aerosol in the boundary layer, background aerosol above 2 km, spring-summer conditions and a visibility of 50 km from the aerosol model by *Shettle* [1989]. Other aerosol properties can be specified at each layer by spectral single scattering albedo, ω_0, asymmetry factor, *g*, and extinction coefficient. If the aerosol phase function is known at each layer, then it can be included in the RT calculation in terms of Legendre polynomials, in the form

$$P(\cos\Theta) = \sum_{l=0}^{N} \varpi_l P_l(\cos\Theta) \qquad (3.1.2)$$

where ϖ_l is the *l*-th moment and $P_l(\cos\Theta)$ is the *l*-th Legendre polynomial.
If not specified, the Henyey-Greenstein phase function (see equation 1.3.4) is assumed, for which the *l*-order moment of the expansion in Legendre polynomials is g^l.
The model use was limited to clear sky conditions, due to the difficulties in modelling the clouds' optical properties for their high variability in space and time.

Recently, the model was updated to perform also RT calculation in the solar and thermal infrared, where the absorption spectra are characterized by thousands of narrow absorption lines and spectral calculations are far too slow. Thus a band parametrization has to be used, and the most accurate is the k-correlation approximation. UVSPEC contains several correlated-k parametrizations, in particular those described by *Kato et al.* [1999], *Fu and Liou* [1992, 1993] and *Kratz* [1995]. Correlated-k is a powerful way to calculate spectrally integrated quantities, however it takes away some flexibility; for example the wavelength grid is no longer chosen by the user but by the parametrization, and the model output is integrated over the spectral bands.

3.2. IMPROVEMENTS

Two main modifications to the original model by *Mayer et al.* [1997] have been implemented, to provide a more detailed description of the aerosol properties and atmospheric vertical structure.
The improvements are an increase of the atmospheric vertical resolution, to allow a more detailed description of the tropospheric structure, and a new parameterization of the aerosol to include in the model the aerosol properties observed at Lampedusa.
In the basic model the atmospheric layers are 1 km thick from 0 to 25 km, 2.5 km from 25 to 50 km, 5 km from 50 to 120 km. As above discussed, high vertical resolution lidar observations show that during the PAUR II campaign large differences in the aerosol vertical distribution occurred, with maximum altitudes variable from 1 to 8 km [*di Sarra et al.*, 2001b]. The lidar profile in conjunction with the ground-based AOD measurements was used to define the vertical profile of the aerosol extinction coefficients. The atmosphere was divided in 64 homogeneous layers from 0 to 120 km with a vertical resolution of 150 m in the lowest 2.1 km, 300 m between 2.1 and 8.4 km, 1 km up to 25 km, and growing thickness up to the altitude of 120 km.
The original version of UVSPEC includes 4 prescribed aerosol types (urban, rural, maritime and tropospheric) for the lowest 2 km of the atmosphere. During PAUR II campaign the aerosol size distribution has been derived for the days of May 18, 25 and 27, 1999 from ground to about 3-4 km by means of a combination of aircraft and ground-based measurements [*Di Iorio et al.*, 2003]: the size distributions have been used to calculate the wavelength dependent aerosol extinction and absorption coefficients, and the asymmetry factor applying the Mie theory for fixed complex refractive indices. Thus, for each day, the corresponding aerosol type was added to the prescribed types.

3.3. MODEL CONFIGURATION

The UVSPEC model inputs have been selected to represent the atmospheric and surface conditions at Lampedusa during the measurements. Most of the model input parameters (total ozone, aerosol optical depth and vertical distributions) have been directly measured or, in the case of the ozone profile for the PAUR II campaign, derived from a combination of climatological distribution and measurements, as described below. When measurements are not available, the default model value or values from literature are taken.
In all the simulations the SDISORT algorithm for solution of the RT equation will be used.
The choice of the model input set-up common to all the examined cases are described.

3.3.1. TOTAL OZONE AND VERTICAL PROFILE

Total ozone is continuously measured by the Brewer spectrometer during the day. For the model calculation, the observed values are linearly interpolated at the solar zenith angles where the simulations are performed. No stratospheric ozone profiles are available at Lampedusa, while the lower tropospheric ozone concentration was measured during the PAUR II campaign by the UV photometer aboard the IFU ultralight aircraft. *Bhartia et al.* [1985] have derived climatological mid latitude ozone profiles from solar backscatter ultraviolet (SBUV) and balloon observations, for total ozone values from 225 to 525 Dobson units (DU). The ozone profile at Lampedusa is assumed to correspond to the climatology matching the measured total ozone. However, since the climatological profiles by *Bhartia et*

al. are not differentiated at altitudes below 4 km, measurements of the ozone UV-photometer are used in the lower atmospheric layers; the measured and the climatological profiles are assumed to join at 10 km altitude. Keeping fixed the ozone concentration at the measured values at low altitudes, the climatological part was scaled to fit the measured total ozone. The used ozone profiles, and the climatological profiles by *Bhartia et al.* [1985] for May 18, 25 and 27 are shown in Figure 3.3.1.

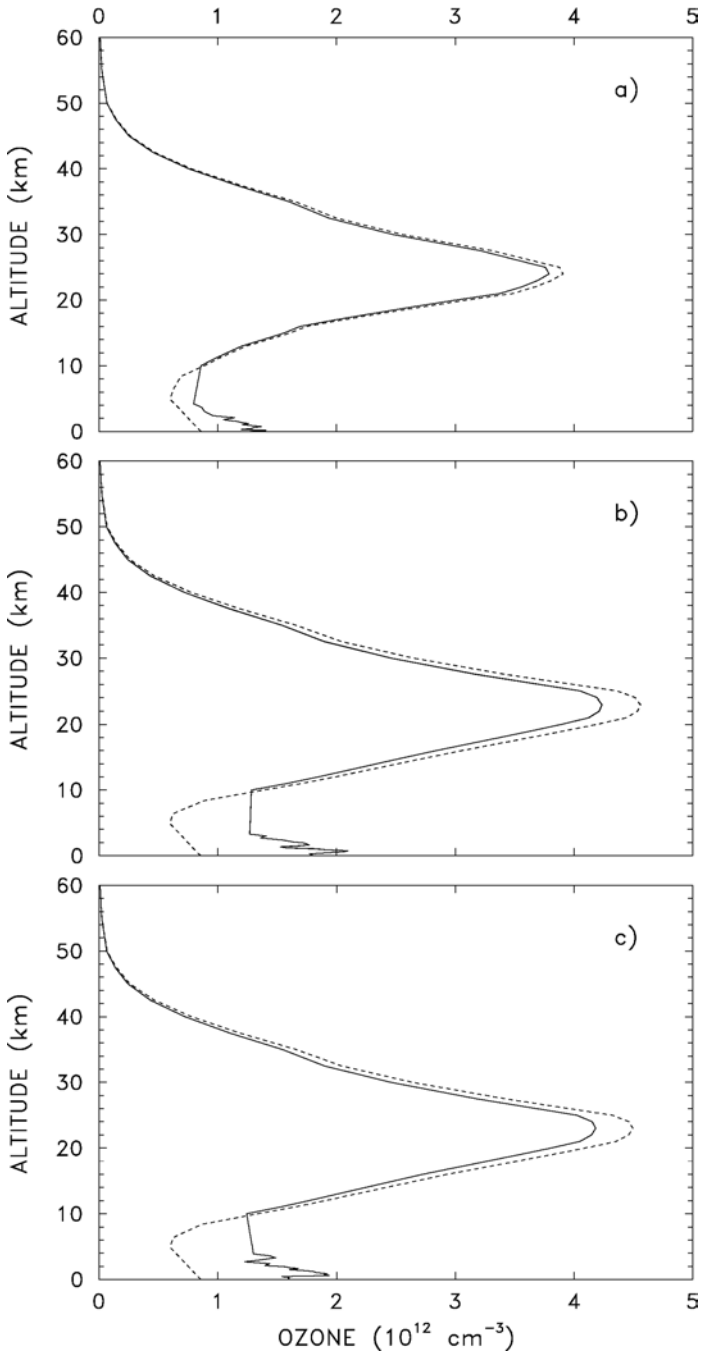

Figure 3.3.1. Climatological ozone profile (dashed curve) and climatological profile corrected in the troposphere with the airborne profile (solid curve) for a) May 18, b) May 25 and c) May 27. For each day, both profiles are normalized to the total ozone amount measured by the Brewer spectrophotometer.

The tropospheric ozone concentrations measured by the aircraft are larger than the climatological profile by 31%, 80% and 78%, respectively on May 18, 25, and 27. *Kourtidis et al.* [2002] have shown that higher tropospheric ozone concentrations are associated in the Mediterranean to airmasses originating in Europe; the increased ozone is accompanied by an enhanced concentration of NO_x, indicating that photochemical production may play a significant role. It is noticeable that largest deviations from the climatology occur on May 25 and 27, when the trajectories originate from Europe. As discussed by *Brühl and Crutzen* [1989], tropospheric ozone may play a significant role in the absorption of UV radiation due to the strong scattering and consequent enhanced photon path lengths in the troposphere. This role may be amplified when large tropospheric aerosol amounts, leading to a further increase of the scattering, are present.

The temperature-dependent ozone absorption cross sections from the Global Ozone Monitoring Expriments (GOME) [*Burrows et al.*, 1999a] are used.

3.3.2. AEROSOL OPTICAL DEPTH AND VERTICAL PROFILE

The aerosol optical depth in the visible is measured by the MFR-7. One hour averages around the solar zenith angle of the simulation are calculated. The spectral behaviour for the AOD is derived from the Ångström parameters α and β, calculated from the AOD at 415.6 and 868.7 nm, according to the expression 1.3.8.
The lidar provides the aerosol vertical distribution between 0.4 and 10 km. The aerosol extinction coefficient profile at 532 nm is derived by multiplying the lidar-derived backscattering coefficient by the extinction-to-backscattering ratio *e*. The value of *e* is estimated by the combination of lidar and photometer observations, and is used in the lidar retrieval algorithm, as described by *Di Iorio et al.* [2003]. The optical depth of the aerosol layer sounded by the lidar is estimated by subtracting the upper troposphere and stratospheric aerosol optical depth. These contributions are derived from *Russell et al.* [1993], who reported values of 0.01 and 0.003 respectively.
The estimate of the extinction profile in the lowest atmospheric layers, where lidar measurements are not available, is based on the similarity between the lidar and the particle counters' measurements for the days of the PAUR II campaign [*Di Iorio et al.*, 2003].
Above the aerosol layer, up to 10 km, the background tropospheric aerosol type for mid-latitude summer conditions and the background stratospheric type from 10 to 30 km [*Shettle*, 1989] are assumed. The resulting extinction profile is then scaled to give the measured AOD value. To study the sensitivity of the radiation quantities on the different aerosol vertical distributions, the extinction profile by *Shettle* [1989] (hereafter referred to as "standard profile") scaled to the observed AOD, was also used as a reference in the model calculations for the selected cases. The aerosol extinction profile by *Shettle* has a maximum at the surface, and shows a fast decrease with height. The measured and the standard profiles are depicted in Figure 3.3.2 for May 18, 25 and 27 1999 and Figure 3.3.3 for June 14 and 16 2002.

3.3.3. ATMOSPHERIC PROFILE

Vertical profiles of pressure and temperature at 12:00 UT are obtained from the National Centers for Environmental Prediction (NCEP) analyses, and the molecular density profile is calculated assuming a perfect gas behaviour. The atmospheric vertical structure is assumed not to vary appreciably during the day.

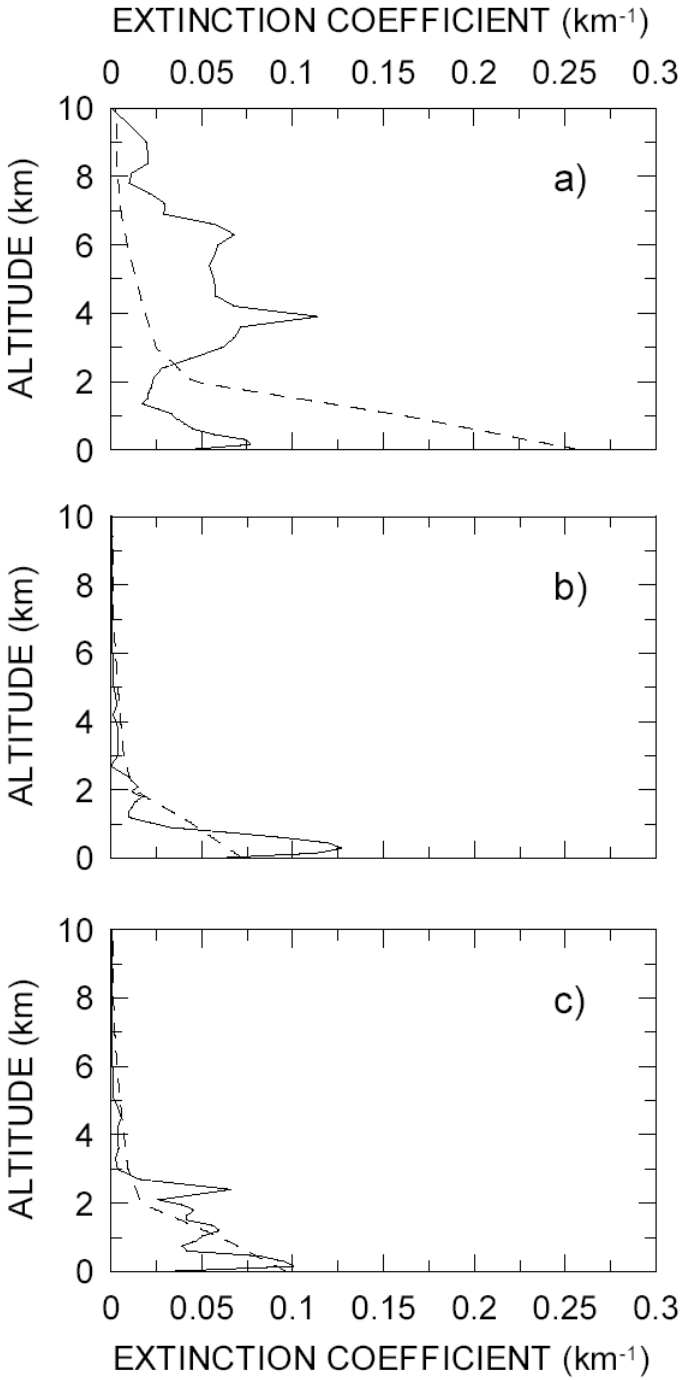

Figure 3.3.2. Aerosol extinction profile at 532 nm for a) May 18, b) May 25 and c) May 27, 1999: the solid lines are the measured profiles, and the dashed lines show the standard profile by *Shettle* [1989] for mid-latitude summer conditions. Both are scaled to match the measured aerosol optical depth.

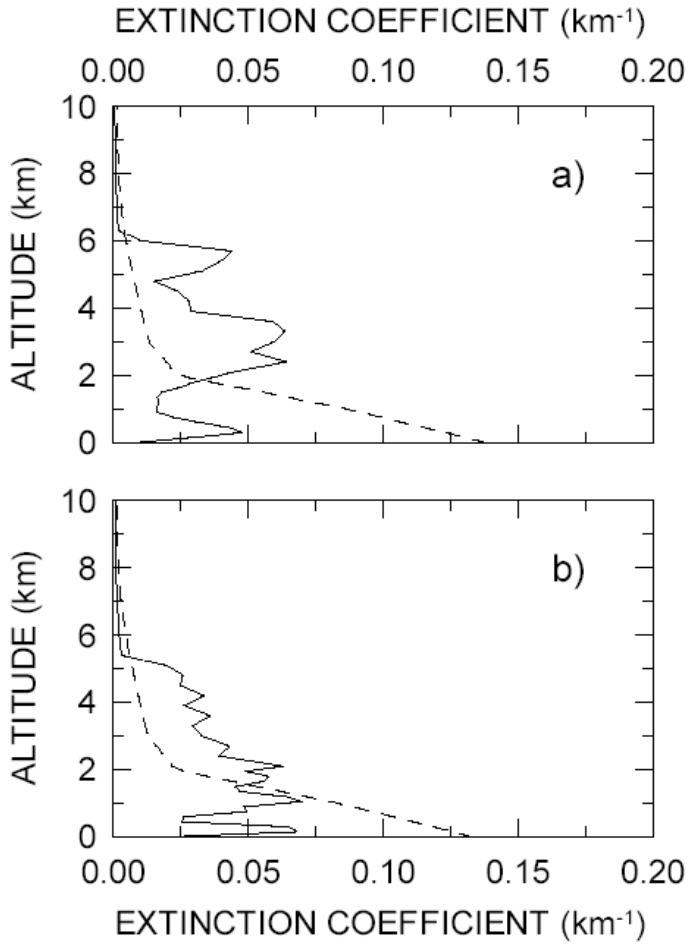

Figure 3.3.3. Aerosol extinction profile at 532 nm for a) July 14, and b) July 16, 2002: the solid lines are the measured profiles, and the dashed lines show the standard profile by *Shettle* [1989] for mid-latitude summer conditions. Both are scaled to match the measured aerosol optical depth. Note the different scale with respect to the graphs in Figure 3.3.2.

3.3.4. SURFACE ALBEDO

The UV irradiance at a specific point is influenced by the albedo of the surface within a region of radius of about 20 km [*Ruggaber et al.*, 1998], and the determination of the albedo to be used in the model should take into account all the different types of surface in the surroundings [*Weihs and Webb*, 1997]. Thus, the surface albedo at Lampedusa is calculated as the average of land and water albedo [*Doda and Green*, 1980] weighted for the respective surface area, corresponding to values between 0.05 and 0.08 in the UV. Values are reported in Table 3.3.1. *Payne* [1972] indicates that the shortwave reflectivity of the sea surface depends on the sun altitude, on the surface roughness, which is related to the wind speed, and on the atmospheric transmittance. While the effect of the surface roughness is negligible for solar zenith angles smaller than 65°, and for low wind speed, as is the case of the selected days, the dependence on the atmospheric transmittance and sun altitude can be significant. It must be considered that small changes of the albedo, when its value is small, produce minor effects on the surface irradiance. Test calculations have been performed by using the solar zenith angle dependence of the ultraviolet albedo reported by *Doda and Green* [1980], showing that the effect on the surface UV irradiance is small. In the visible, the ocean surface

albedo from *Payne* [1972] has been used, with a value of 0.06. The surface is assumed to be Lambertian and the albedo is not varied with solar zenith angle.

Table 3.3.1. Surface albedo in UV and visible used for RT simulations at Lampedusa

Wavelength (nm)	Surface albedo
280	0.081
300	0.081
306	0.051
310	0.064
320	0.068
330	0.081
340	0.076
350	0.081
360	0.092
370	0.086
380	0.082
390	0.087
400	0.060
800	0.060

The previous considerations evidence that for a detailed analysis of radiation data from the specific site of Lampedusa, a characterization of the spectral reflection properties of the underlying surface should be performed.

3.3.5. EXTRATERRESTRIAL SOLAR IRRADIANCE

The high resolution (0.05 nm steps) extraterrestrial spectrum is derived from ATmospheric Laboratory for Applications and Science (ATLAS) 3 measurements shifted to air wavelength between 280 and 407.8 nm, from ATLAS 2 measurements from 407.8 and 419.9 nm, and from the Modtran 3.5 model above 419.9 nm [*Kylling et al.*, 1998]. Figure 3.3.4 depicts the spectrum from 200 to 800 nm.

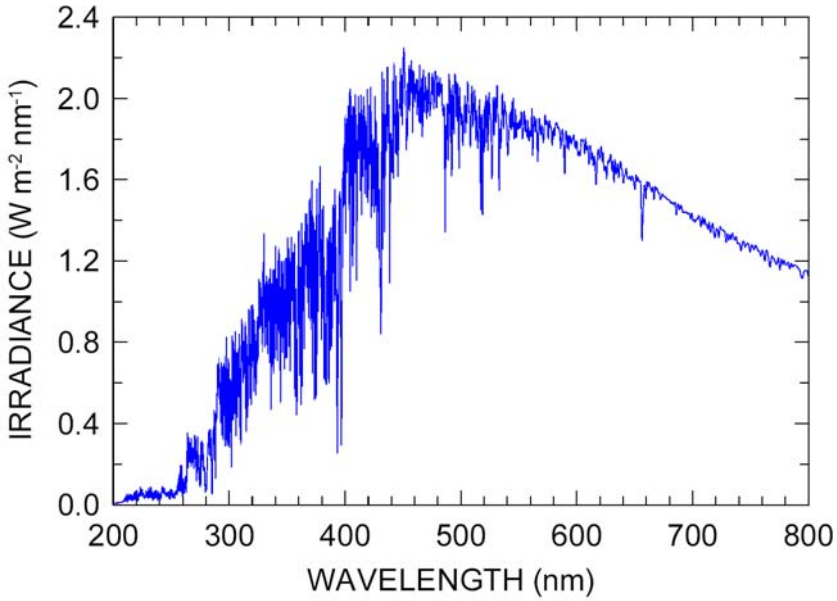

Figure 3.3.4. High resolution extraterrestrial spectrum used in the UVSPEC model.

CHAPTER 4

RETRIEVAL OF AEROSOL OPTICAL PROPERTIES AND ESTIMATE OF THEIR RADIATIVE FORCING

4.1. INTRODUCTION

The main scope of my research was to estimate the radiative properties and effects of the different aerosol types occurring at the island of Lampedusa. This can be achieved inferring the optical characteristics (i.e. absorption and scattering properties) of the aerosols from a combination of accurate measurements of solar radiation in the UV, visible and near IR with the simulations by means of a radiative transfer model in the same spectral regions. The used measurements were performed by:

a) ground-based instruments sited at the ENEA Station for Climate Observation;
b) instruments deployed on an ultralight aircraft, which performed several flights during the PAUR II field campaign;
c) satellite-borne sensor (MISR).

Most of the analysis developed during my research is based on the "closure" approach, that is applied when the aerosol properties are to be determined using a redundant set of radiometric quantities obtained by independent instruments or methods; in this type of studies the application of radiative transfer models is fundamental.

In order to assess the radiative impact of an aerosol layer it is necessary to know the portions of incident radiation that is absorbed and scattered, i.e. the single scattering albedo, ω_0, and how the radiation is scattered in the atmosphere, i.e. the asymmetry factor, g. It is worth reminding that obtaining information about the particles' absorption and scattering properties directly from measurements requires the contemporary use of various chemical and optical instruments, deployed in situ, which allow to derive the aerosol size distribution and the complex refractive index: due to the difficulty of having such an extended set of observational quantities, growing effort is devoted to the application of alternative methods, like the ones described in this thesis.

These goals have been achieved in three studies.

1. In the first study cloud-free days during the PAUR II campaign with dust from the Saharan desert (May 18, 1999) and continental/maritime aerosols from Europe (May 25 and 27, 1999) have been selected, when a set of ground-based measurements were available. The RT model was initialised with all the measured parameters, allowing for a detailed comparison of the observed and the simulated irradiances in the UV and

visible. The objectives of the analysis of the PAUR II data are: a) to study the dependence of UV and visible radiation at the surface on different aerosol loadings and optical properties, b) to identify the role played by tropospheric ozone, also in the presence of large aerosol amounts, c) to derive estimates of some important aerosol properties, such as the single scattering albedo, that are of fundamental importance for the determination of the aerosol radiative effects, and d) to estimate the local direct aerosol radiative forcing in the UV and visible.

2. The second study describes a closure experiment, when ground-based measurements were combined with space-borne observations from the Multi-angle Imaging Spectro-Radiometer (MISR), to derive column-integrated aerosol optical properties, ω_0 and g, by means of RT calculations. Two days of July 2002, 14 and 16, when airmasses originating from Africa and loaded by a moderate amount of desert dust reached Lampedusa, were selected.
3. In the third study the column-integrated ω_0 is estimated from measurements performed at Lampedusa by the visible MFRSR at 415.6 nm and 868.7 nm from July 2001 to September 2003. The RT model is used to reproduce the measured diffuse-to-direct ratio, using the measured AOD as input. The determination of ω_0 as a function of wavelength is a useful tool to distinguish between different aerosol types; it will be shown that the wavelength dependence of the retrieved ω_0 is consistent with the aerosol classification based on AOD, Ångström parameter and airmass trajectory analysis presented in the paper by *Pace et al.* [2004]. ω_0 values at the two wavelengths are determined for the biomass burning and urban/industrial aerosols from the European continent, and for desert dust from the Saharan region.

In the first two studies the measured aerosol parameters are used as model input to calculate the direct radiative forcing at the surface and at the TOA, and the different effects of various aerosol characteristics and amounts are explained.
It is worth noting that the contemporary use of measurements from ground-based, airborne and spaceborne instruments was not possible in the three analyses. In fact, data from the aircraft instrumentation are available only for the days of the PAUR II campaign, while MISR observations are performed since December 1999.

4.2. DERIVATION OF THE AEROSOL PROPERTIES AND OF THEIR DIRECT RADIATIVE FORCING AT THE SURFACE AND AT THE TOP OF THE ATMOSPHERE DURING THE PAUR II CAMPAIGN

4.2.1. MEASUREMENTS

The dataset of ground-based measurements used includes lidar profiles, total ozone content, UV, visible, and near-IR spectra. A detailed description of the instruments was given in paragraph 2.1. The ground-based measurements were completed by the aircraft observations in the period May 10-28. A description of the instrumented aircraft is given in paragraph 2.2 and, with more details, in *Junkermann* [2001].

Measured UV and visible spectra are reduced to the mean Sun-Earth distance and, together with O_3 total columns, interpolated at fixed solar zenith angles. The interpolation of the spectra is made with a second order polynomial, using the three closest in time acquired

spectra. Linear interpolation is used to derive the total ozone amounts at fixed solar zenith angles.

Previous studies have shown that very large changes of the aerosol distribution occurred during the campaign, the aerosol vertical distribution and amount depending on the origin of the airmasses. When the airmass trajectory comes from Europe and/or North Atlantic, the aerosol optical depth is relatively low, and the particles are generally confined to the region below 3 km. When the airmass originates from Africa, much larger values of the optical depth are found, and the aerosol cloud may reach altitudes of 7-8 km. Also the aerosol properties appear significantly different, since the two cases are characterized by low (for the Saharan case) and large (for the European case) values of the Ångström exponent [*di Sarra et al.*, 2001b, 2002]. The spectral UV observations at the ground have shown that these different aerosol conditions largely affect the atmospheric transmittance [*di Sarra et al.*, 2001a].

To emphasize the role of the aerosol, cloud-free periods with different aerosol loading, when ground-based and air-borne observations were available, were selected for the model computations. Three cases were identified: May 18, 25, and 27, for different values of the solar zenith angle, SZA (60° on May 18, 40° on May 25 and 27). In Figure 4.2.1 5-day isentropic trajectories from the NASA Goddard Space Flight Center [*Schoeberl et al.*, 1992] ending at Lampedusa at approximately 2.5 km on May 18, 25, and 27, are depicted.

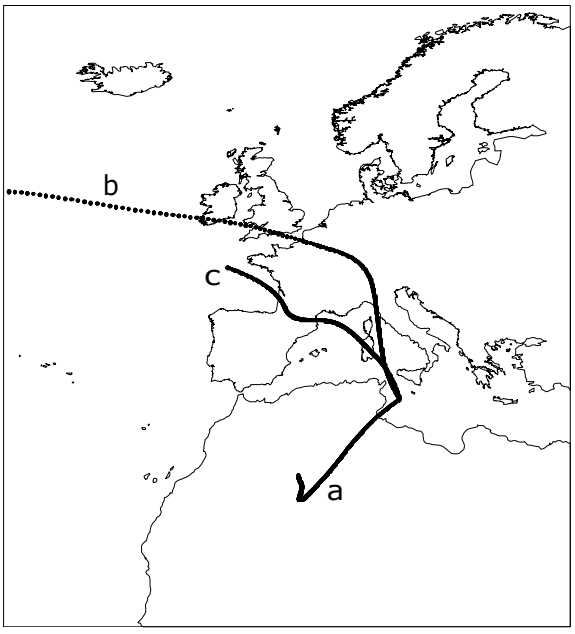

Figure 4.2.1. Five-days backward trajectories ending at Lampedusa between 2 and 3 km on a) May 18, b) May 25, and c) May 27, 1999 (from *Di Iorio et al.*, 2003).

To compare spectra measured in different aerosol conditions at 60° SZA, also June 1, when only ground-based measurements were carried out, has been considered. However, on June 1 no detailed information on the aerosol microphysical properties was available, and the data for this day have not been used in the model analysis.

As reported by *Di Iorio et al.* [2003] on May 25 and 27 the airmasses pass over Europe before reaching Lampedusa: its composition is expected to be prevalently of anthropogenic particles and crustal aerosol from continental airmasses, and marine aerosols. On May 18 and June 1 the airmasses spent the last several days over central Africa, and the particles are expected to be mainly composed of desert dust.
The irradiances were calculated at fixed SZAs, within or close to those of the aircraft flights. On May 25 the aircraft performed one flight from 13:45 to 14:32 GMT and the model was run for a SZA of 40° in the afternoon (13:57 GMT). On May 27 the aircraft flew between 13:24 and 14:46 GMT and the calculation was made at 40° in the afternoon (13:58 GMT). On May 18 clouds were present before 15:00; the aircraft flight was performed between 13:25 and 15.15 GMT, and the calculations were made for 60° in the afternoon (15:31 GMT).
In Figure 4.2.2 the lidar-derived aerosol backscatter ratio (see paragraph 2.1.4) profiles for the component of the signal with the same polarization of the linearly polarized laser beam, for May 18, 25, and 27, and June 1, are shown.

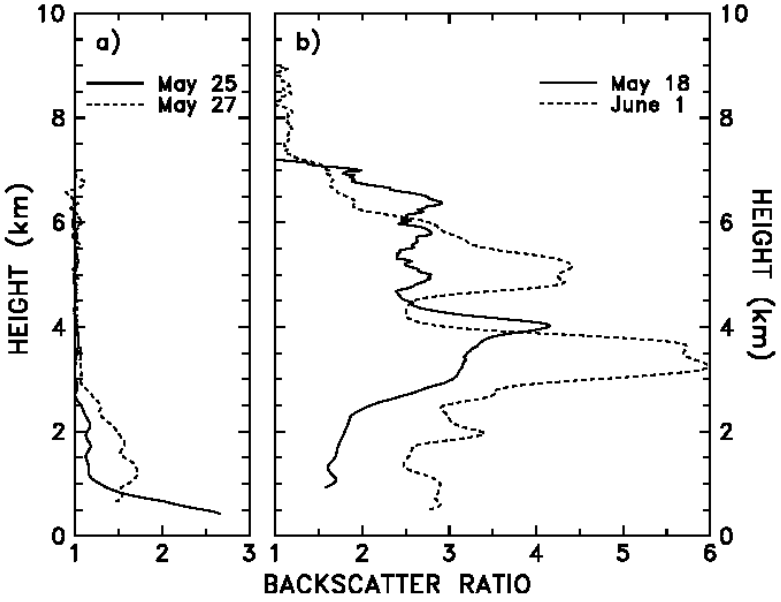

Figure 4.2.2. Backscatter ratio profiles obtained by lidar on May 18, 25, 27, and June 1 (see text).

Significant differences in the aerosol amount and vertical extension appear, as expected, due to the different origin of the airmasses. On May 18 and June 1, for example, the strong convection over the Sahara desert lifted the aerosol particles to 7-8 km. Over North Atlantic and Europe such a strong convection is unlikely, and particles are mostly confined below 3 km.
In Table 4.2.1 the average values of the aerosol optical depths at 415.6 and 868.7 nm, measured by the MFRSR, and of total ozone, measured by the Brewer, are reported for the 4 days. Data for May 25 at 60° SZA and for June 1 at 40° SZA are also reported. The averages are calculated over a 1 hour interval centred at the indicated SZA. Average values of the diffuse-to-direct radiation ratio (DDR) at 415.6 nm, measured by the MFRSR, are also reported. The standard deviation of the average for the aerosol optical depth and the diffuse-to-direct ratio is indicated. It may be noted that on May 18 and June 1, when low total ozone

values are measured, the aerosol optical depth is large, while the opposite occurs on May 25 and 27. A negatively correlated behaviour between total ozone and aerosol optical depth has been found at Lampedusa during PAUR II and is attributed to the influence of tropospheric anticyclones, that induce the transport of desert aerosols over Lampedusa, on the stratospheric vertical structure and advection [*di Sarra et al.*, 2002]. The amount of diffuse radiation is significantly larger on May 18 and June 1 than on May 27 and 25 respectively, indicating that the aerosol largely affects the transfer of visible radiation.

Table 4.2.1. Solar zenith angle (SZA), aerosol optical depth (AOD) at 415.6 and 868.7 nm, ozone amount (DU) and diffuse-to-direct ratio (DDR) at 415.6 nm for the cases selected in this study.

Day	SZA	AOD (415.6 nm)	AOD (868.7 nm)	Ozone (DU)	DDR (415.6 nm)
May 18	60°	0.511±0.014	0.434±0.003	293.5	2.00±0.17
May 25	40°	0.165±0.003	0.0704±0.0008	355.2	0.385±0.008
May 27	40°	0.224±0.007	0.0842±0.0003	349.9	0.49±0.01
May 25	60°	0.164±0.008	0.0586±0.0007	352.9	0.73±0.03
June 01	40°	0.712±0.015	0.668±0.018	301.6	1.25±0.05

In Figure 4.2.3 the ultraviolet spectra measured at 40° SZA in the afternoon of May 27 and June 1, and at 60° SZA on May 18 and 25, are depicted. Significant differences in the measured irradiances appear. At short wavelengths, the effect of ozone absorption is dominating, and higher irradiances are observed on the days when the total ozone is low. At longer wavelengths the effect of the aerosol overcomes the effect of the ozone, and significantly higher irradiances are found on the days characterized by low aerosol optical depth. At 40° SZA the irradiance at 340 nm, where the absorption by ozone may be neglected, is by 14% larger on May 27 than on June 1. Similarly, at 60° SZA the irradiance at 340 nm is 15% larger on May 25 than on May 18.

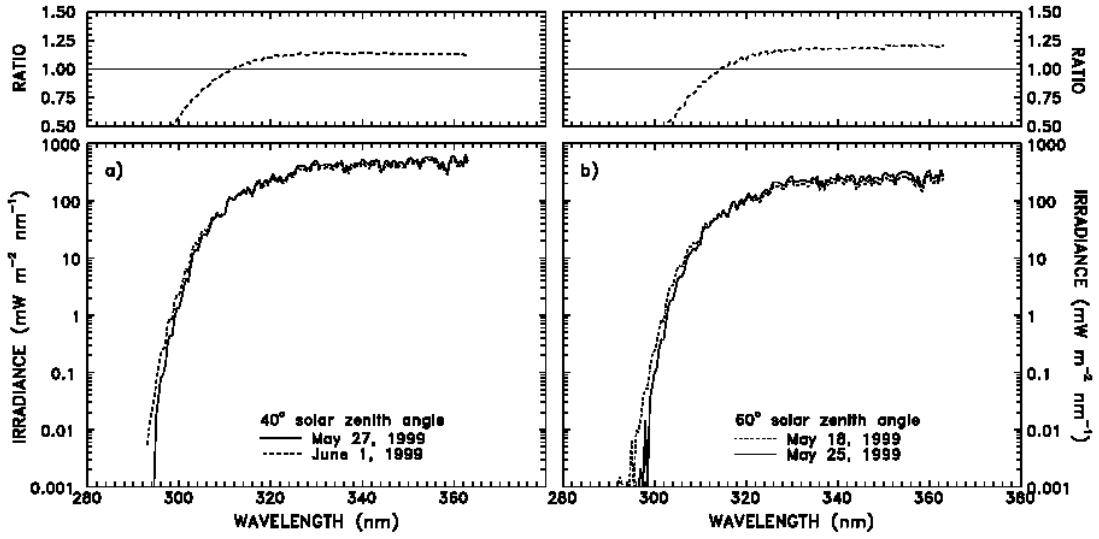

Figure 4.2.3. UV spectra at a) 40° SZA for May 27 and June 1, and b) 60° SZA for May 18 and 25. The ratio of the solid and dashed curves is shown in the upper graphs.

Figure 4.2.4 shows the spectra measured on the same days and SZAs by the Licor spectrometer. The large aerosol effect is evident throughout the visible and near-IR spectral range. Differences also appear in correspondence with the water vapour absorption bands around 690, 726 and 936 nm; at 60° SZA the difference in the water vapour content of May 18 and 25 seems to compensate for the irradiance difference produced by the aerosol in the 920-980 nm region. The peak at 764 nm is due to an O_2 absorption band.
The influence of the aerosol on the ultraviolet radiation transfer is also evident from the values of the diffuse-to-direct radiation ratio at 415.6 nm observed on the different days, respectively at 40 and 60° SZA.

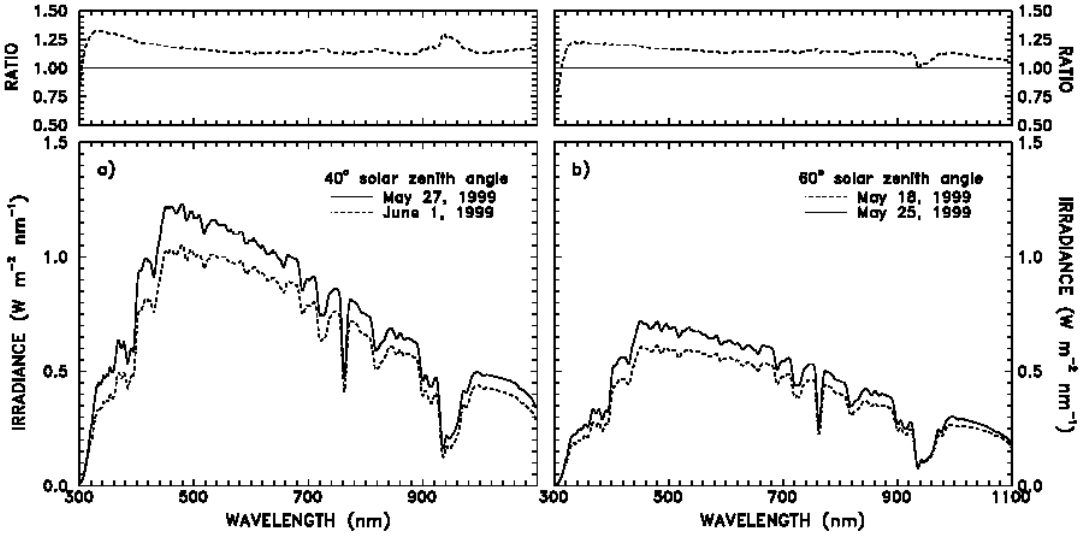

Figure 4.2.4. Spectra measured with the Licor spectrometer at a) 40° SZA for May 27 and June 1, and b) 60° SZA for May 18 and 25. The ratio of the solid and dashed curves is shown in the upper graphs.

4.2.2. MODEL

In this study the UVSPEC RT model is used to reproduce the measured spectra shown in Figures 4.2.3 and 4.2.4. The model was operated in six-stream mode for the calculation of the irradiance, and used the SDISORT solver. The spectral irradiance is calculated at 0.05 nm intervals. The high resolution spectral irradiances are then convoluted with the Brewer and the Licor slit functions, assumed to be wavelength-independent and approximated by triangles with 0.55 nm and 6 nm FWHM bandwidth, respectively. The instrumental slit functions were not accurately determined, and may somewhat differ from the modelled curves.
The model set-up for the other inputs are described in paragraph 3.3, with an additional analysis for the aerosol properties described below.
The aerosol size distribution has been derived from the particle counters observations and from the optical depth measurements made during the campaign [*Di Iorio et al.*, 2003]. The aerosol optical depth supplied to the model is derived from observations as well. Being the aerosol size distribution derived from the measurements, no dependence on ground visibility and humidity was taken into account; no prescribed aerosol type and size distribution are assumed. The aerosol layer was divided into a number of sub-layers, where the size distribution is allowed to change, but the refractive index is kept constant; the refractive index

is also assumed to be wavelength independent. In Tables 4.2.2a, b, and c the retrieved parameters of the three modal size distributions of May 18, 25 and 27, respectively, for the various sub-layers are reported.

Table 4.2.2a. Parameters of three modal size distributions retrieved by *Di Iorio et al.* [2003] on May 18 at different layers.

Mode	Mixing ratio by volume	Radius (μm)	σ
	0-2.4 km		
1	0.9989098	0.07	1.45
2	8.4321E-04	0.94	1.32
3	2.4699E-04	4.50	1.14
	2.4-3.6 km		
1	0.9989098	0.07	1.45
2	7.8945E-04	1.06	1.34
3	3.0074E-04	4.60	1.14
	3.6-4.2 km		
1	0.9989098	0.07	1.45
2	7.9664E-04	1.12	1.38
3	2.9356E-04	4.55	1.16

Table 4.2.2b. Parameters of three modal size distributions retrieved by *Di Iorio et al.* [2003] on May 25 at different layers.

Mode	Mixing ratio by volume	Radius (μm)	σ
	0-0.6 km		
1	0.9975754	0.07	1.45
2	2.3724E-03	0.23	3.12
3	5.2174E-05	4.66	1.12
	0.6-1.05 km		
1	0.9997205	0.07	1.45
2	2.7480E-04	0.44	2.82
3	4.6901E-06	5.05	1.05
	1.05-2.7 km		
1	0.9997438	0.07	1.45
2	2.4916E-04	0.64	2.46
3	7.0535E-06	5.33	1.04

Table 4.2.2c. Parameters of three modal size distributions retrieved by *Di Iorio et al.* [2003] on May 27 at different layers.

Mode	Mixing ratio by volume	Radius (μm)	σ
	0-1.5 km		
1	0.9993621	0.07	1.45
2	6.1801d-04	0.32	3.16
3	1.9895d-05	5.17	1.14
	1.5-2.1 km		
1	0.9997219	0.07	1.45
2	2.7204d-04	0.24	4.00
3	6.0591d-06	5.05	1.08
	2.1-2.7 km		
1	0.9992981	0.07	1.45
2	6.8729d-04	0.46	2.64
3	1.4642d-05	5.50	1.09

The wavelength dependent aerosol extinction and absorption coefficient, and asymmetry factor have been calculated applying the Mie theory to the retrieved size distribution for different values of the refractive index.
A sensitivity study was performed to infer a variability range for the real and imaginary parts. The method and the results of the comparison between measured and modelled UV irradiances are described in detail in the next section. To study the influence of the aerosol size distribution on the surface irradiance, Mie calculations were also performed using the size distributions for maritime polluted aerosol, desert background (or wintertime) and wind carrying dust (or summertime) particles reported by *d'Almeida et al.* [1991]: the first aerosol type was used when airmasses originated from Europe, while the two desert types were chosen for the case when the airmass originated from Africa. The parameters of these three modal log-normal size distributions are reported in Table 4.2.3. Different values of the aerosol refractive index were assumed, depending on the prevailing component expected to be present in the particles, i.e. water-soluble for the continental aerosol, and mineral for the dust case. Refractive indices as a function of wavelength are also derived from *d'Almeida et al.* [1991] and reported in Table 4.2.4.
To illustrate the differences among the measured size distributions and those reported by *d'Almeida et al.* [1991], the measured ones were integrated over the height interval for the three selected flights and normalized to 1 particle per unit volume; Figure 4.2.5 presents the different size distributions.
The main error source in the calculation of the aerosol optical properties from Mie theory is the non sphericity of the particles. When the AOD is known, however, the particle shape has a negligible influence on the estimates of the aerosol radiative forcing [*Díaz et al.*, 2000].

Table 4.2.3. Parameters of three modal size distributions by *d'Almeida et al.* [1991], used in this study in the indicated cases.

Component	Mixing ratio by volume	Radius (μm)	σ
	Maritime polluted (May 25 and 27)		
Water-soluble	0.5939	0.0285	2.239
Soot	0.4051	0.0118	2.00
Sea-salt	9.6E-4	0.30	2.51
	Desert background (wintertime) (May 18)		
Mineral	0.9274	0.07	1.95
Mineral	0.07246	0.39	2.00
Mineral	9.661E-5	1.90	2.15
	Wind carrying dust (summertime) (May 18)		
Mineral	0.8542	0.05	1.65
Mineral	0.14568	0.27	2.67
Mineral	7.2842E-5	4.00	2.40

Table 4.2.4. Complex refractive index of the aerosol components used in this study by *d'Almeida et al.* [1991].

Wavelength (nm)	Water soluble		Mineral	
	n'	*n"*	*n'*	*n"*
280	1.53	1.68e-2	1.53	2.70e-2
300	1.53	8.00e-3	1.53	2.50e-2
350	1.53	5.00e-3	1.53	1.70e-2
400	1.53	5.00e-3	1.53	1.30e-2
450	1.53	5.00e-3	1.53	8.50e-3
500	1.53	5.00e-3	1.53	7.80e-3
550	1.53	6.00e-3	1.53	5.50e-3
600	1.53	6.00e-3	1.53	4.50e-3
650	1.53	7.00e-3	1.53	4.50e-3
700	1.53	7.00e-3	1.53	4.00e-3
750	1.53	8.50e-3	1.53	4.00e-3
800	1.52	1.00e-2	1.53	1.20e-3

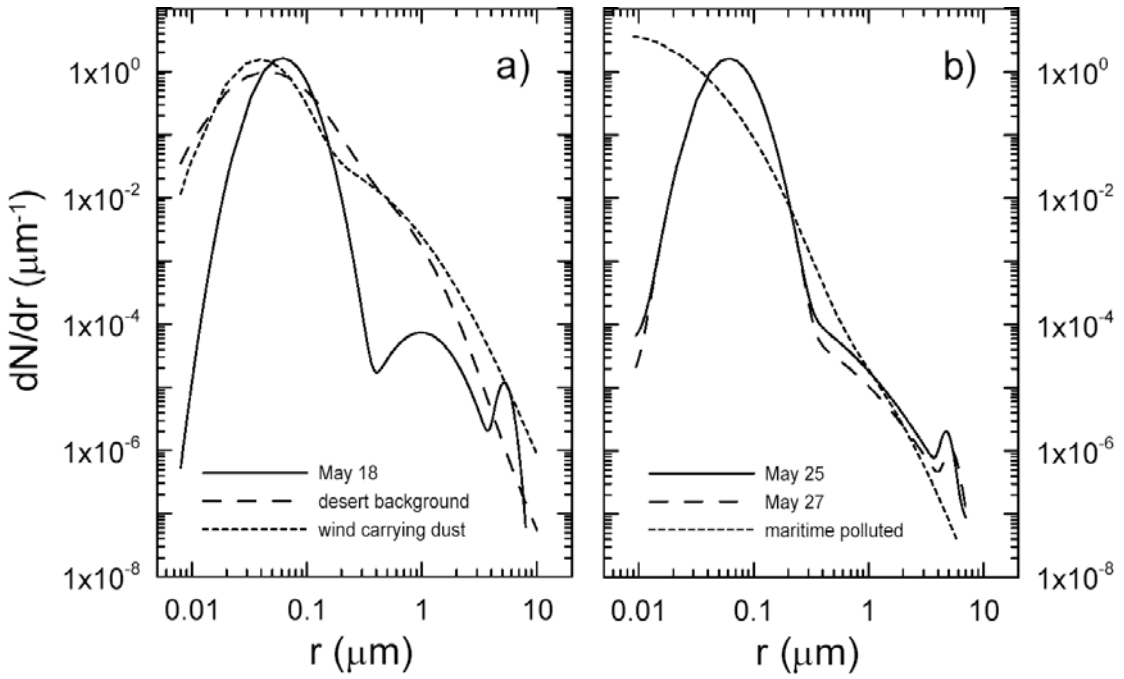

Figure 4.2.5. Column-integrated size distributions normalized to 1 particle per unit volume for a) desert background and wind carrying dust [*d'Almeida et al.*, 1991] and May 18, and b) maritime-polluted aerosol [*d'Almeida et al.*, 1991] and May 25 and May 27 (from *Di Iorio et al.*, 2003).

4.2.3. RESULTS AND DISCUSSION

As discussed above, the RT model was initialised with all the available measured parameters, allowing for a detailed comparison of the observed irradiances with the measured spectra. In what follows two types of analyses will be performed. The first one is aimed at deriving an estimate of the imaginary part of the aerosol refractive index (integrated over the column), by searching the values that produce the best agreement between model and measurements. The second analysis is a sensitivity study aimed at understanding the influence of some key parameters, namely aerosol size distribution and refractive index, and ozone vertical profile, on the model results. The effect of tropospheric aerosols on UV absorption by ozone will be also investigated. The role of these parameters in the observed different aerosol conditions (low and high load, continental/marine and desert aerosol) will be emphasized.

4.2.3A. BREWER SPECTRA: LOW AEROSOL AMOUNT (MAY 25 AND 27, 1999)

The conditions of May 25 and 27 are very similar, thus providing the opportunity to compare model and measurements under relatively well-defined conditions, without the complexity introduced by large aerosol loadings.

Figure 4.2.6a shows the ratio between the model results and the spectrum measured by the Brewer on May 25 at 40° SZA. The figure displays the model results for 3 different values of the imaginary part n'' of the aerosol refractive index; the real part n' was fixed at 1.366, that is the column average of the estimates of n' obtained by *Di Iorio et al.* [2003]. Curves showing 10 nm running averages of the ratio are also depicted. The fluctuations in the model-measurement ratio are mainly attributed to possible differences between the assumed and the true instrumental slit function, and to possible small wavelength shifts of the spectrometer.

The comparison is limited to wavelengths larger than 300 nm, due to the increase of the experimental uncertainties below this wavelength. We assume that the 5% deviation from unity in the ratio limits the values of the refractive index that may be considered plausible, ±5% being the estimated error of the Brewer irradiances.
The upper curve is thus obtained using the smallest value of n'' for which the running mean of the model-measurement ratio remains below 1.05. In the same way, the lower curve is calculated with the largest value of n'' for which the running mean remains above 0.95. The central curve is obtained with a refractive index of 1.366 - 0.052 i, value that gives the best agreement. This procedure produces a wide range of uncertainty for the imaginary part n'' (-0.012 ÷ -0.16), indicating that the simulated irradiance is not strongly dependent on the aerosol absorption properties.

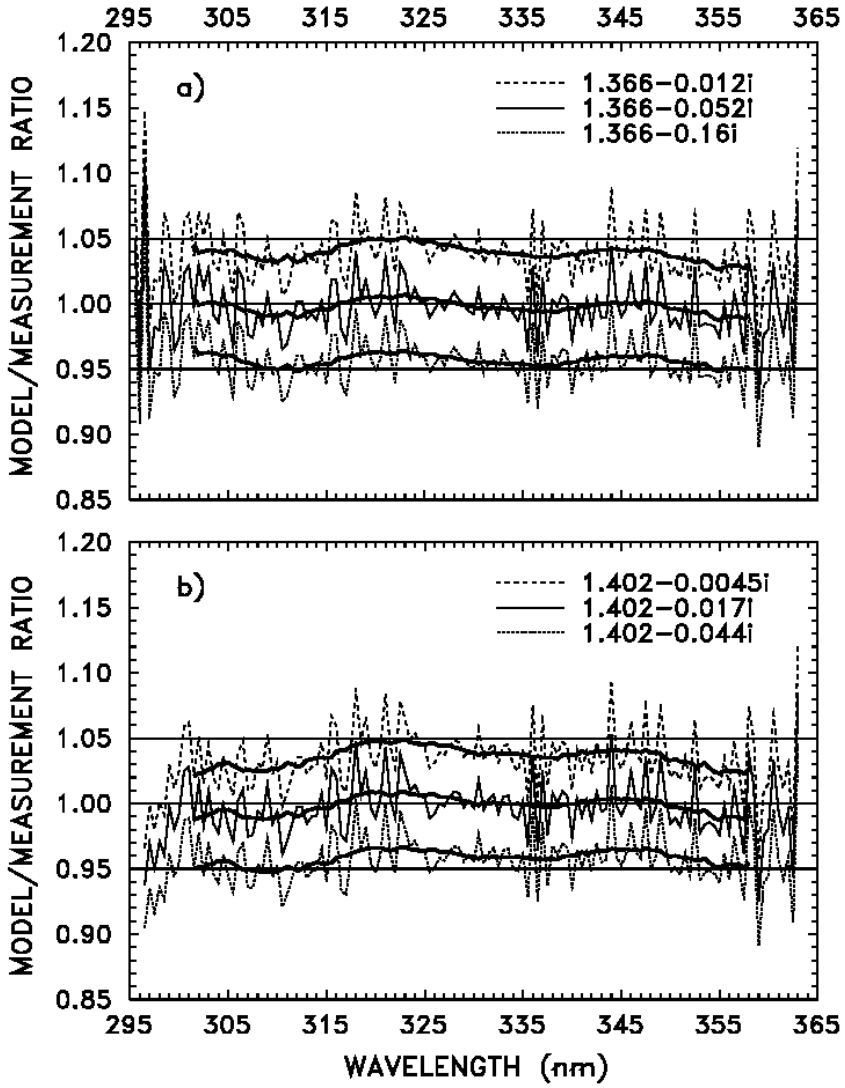

Figure 4.2.6. Ratio of the modelled and measured UV spectra for a) May 25, and b) May 27, at 40° SZA. The curves refer to three different values of the imaginary part of the aerosol refractive index. The thick solid curves are 10 nm running averages of the ratio.

Following the same criteria adopted for May 25, for $n' = 1.402$, the results for May 27 are for n'' the range of values (-0.0045 ÷ -0.044), and the refractive index which yields the best agreement is 1.402 - 0.017 i (see Figure 4.2.6b). These values correspond to aerosol of very different compositions: values of n'' of the order of $10^{-2} \div 10^{-3}$ are typical for dust-like, water-soluble and mineral aerosol components, while for soot particles n'' is between 0.1 and 1, depending on wavelength.
The retrieved ranges of values for n'' on May 25 and 27 correspond to moderately to highly absorbing particles.
In the radiative transfer model the AOD at 415.6 nm was fixed to the measured value. The profile of the aerosol extinction coefficient (whose integral matches at 415.6 nm the measured optical depth) is also derived from the observations, as previously discussed. Changes of the refractive index imply variations of the extinction coefficient, and the number of particles is varied by means of an altitude independent scaling factor to obtain the measured optical depth at 415.6 nm. Because of these constraints, the model has intrinsically a poor sensitivity on the real part of the aerosol refractive index. Some dependence on the real part of the refractive index is induced by the wavelength changes of the optical properties, that are not fixed in the UV. For instance, the aerosol optical depth in the UV may somewhat change, depending on both the real and imaginary parts of the refractive index (the size distribution is fixed); these changes are however small, since the aerosol optical depth at 415.6 nm is not allowed to vary. To investigate the role played by the real part of the refractive index, n'' was fixed at the value giving the best agreement between model and measurements, and n' was varied for both days in the range 1.3 - 1.7. These values correspond to large changes in the aerosol composition, 1.3 applying to water, and 1.7 to soot particles. The resulting change of the model-to-measurement ratio is within –2/+4% for May 25, and within –4/+5% at all wavelengths for May 27 (10 nm running average). The sensitivity test was repeated also for the upper and lower values of the imaginary part n'', and similar results were found. Thus, as expected, little can be said on the real part of the refractive index with this method.
A larger sensitivity on the imaginary part should emerge, since its variations imply changes of the amount of absorption by the particles. A limited sensitivity of this method in the case of small optical depth is somewhat expected, since the effects of the aerosol on the radiative transfer, and on the surface irradiance, are small when the optical depth is small.
The sensitivity of the simulated spectra on the aerosol size distribution was examined comparing the UV irradiance calculated using the aerosol extinction and absorption coefficients and the phase function from the 3-modal size distribution from *d'Almeida et al.* [1991] for the maritime polluted aerosol type (see previous paragraph), and the results obtained with the measured size distribution. The changes of the size distribution have been implemented without modifications to the extinction profile and aerosol optical depth at 415.6 nm. In both cases the refractive index is assumed to correspond to the best estimated values.
Figure 4.2.7 illustrates the comparison for May 25 and May 27. Using the size distribution by *d'Almeida et al.* [1991] the model-to-measurement ratio remains within ±5%. If the water-soluble aerosol refractive index and the size distribution by *d'Almeida et al.* [1991] are used together, a differences of 7-9% (May 25) and 3-8% (May 27) on the 10 nm running average curve appear. The change of size distribution and refractive index implies a modification of the aerosol optical depth in the UV spectral range: the AOD at 350 nm is 2.7% higher on May 25, and 7.3% lower on May 27 for the *d'Almeida et al.* distribution than for the *Di Iorio et al.* [2003] distribution.

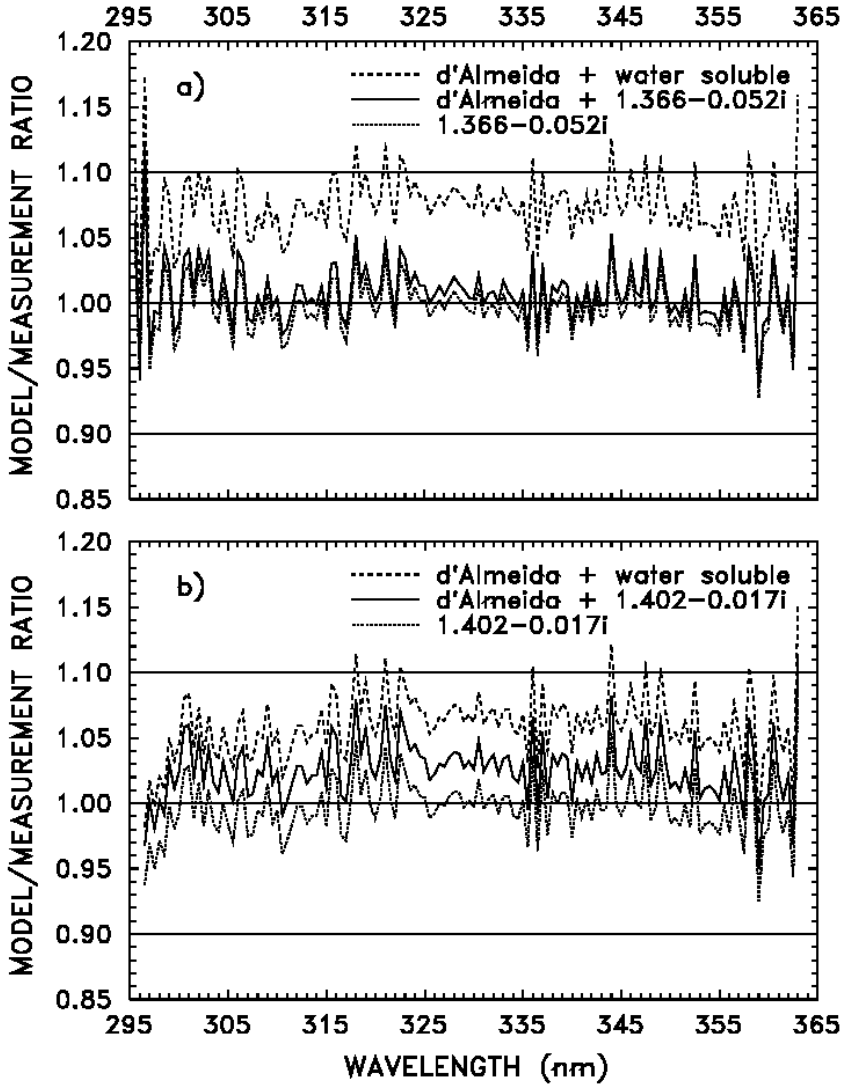

Figure 4.2.7. Comparison of the model-measurement ratio obtained with the measured aerosol size distribution, and with that by *d'Almeida et al.* [1991] for a) May 25 and b) May 27. The model simulations with the *d'Almeida et al.* distribution have been performed using refractive index estimated in this study, and the refractive index for the water-soluble component by *d'Almeida et al.* [1991].

The sensitivity on the ozone profile has been studied by calculating the surface irradiance for two different vertical distributions, both corresponding to the observed total ozone amount. The first profile, P1, is given by the climatology by *Bhartia et al.* [1985], and the second one, P2, is the combination of the tropospheric ozone measurements and the climatology (see Figure 3.3.1): both profiles correspond to the same total ozone values. Figure 4.2.8 shows the ratio R_{mc}, between the calculated irradiance spectra obtained with profile P2 and P1 respectively.

The increase of tropospheric ozone associated with the change of the ozone vertical profile produces a reduction of R_{mc}, i.e. a reduction of the surface irradiance, by approximately 1% at 320 nm, 6% at 305 nm, and up to 10% at 295 nm, both on May 25 and 27. The decrease of the irradiance is due to the efficient absorption by tropospheric ozone. This phenomenon is particularly important at small SZAs, since for low sun condition UV radiation is mostly

scattered in the stratosphere, subtracting influence to the enhanced tropospheric ozone [*Brühl and Crutzen*, 1989].

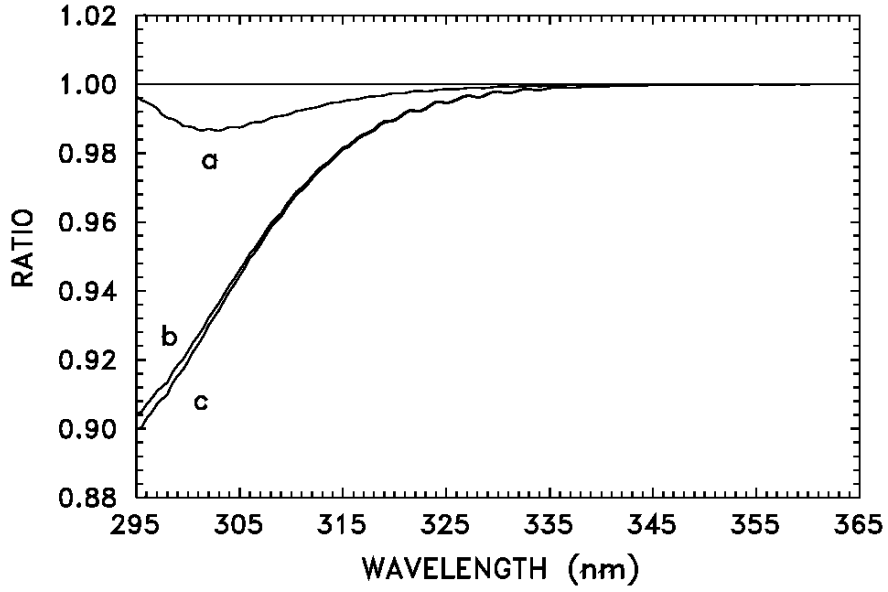

Figure 4.2.8. Ratio of the UV irradiance calculated with the climatological ozone profile to that calculated with the climatological profile corrected to the measured tropospheric ozone for a) May 18, b) May 25, and c) May 27.

4.2.3B. BREWER SPECTRA: HIGH AEROSOL AMOUNT (MAY 18, 1999)

The dependence of the model results on the aerosol properties has been studied also for the UV spectrum of May 18, obtained at 60° SZA. Existing estimates of the imaginary part n'' of the atmospheric dust refractive index show a wide spread, which produces large uncertainties in the determination of the aerosol optical characteristics [*Sokolik et al.*, 1993]. Figure 4.2.9 shows the model-measurement ratio for n'' equal to -0.0031, -0.0044, and -0.0068, with the real part n' fixed at 1.536. The three selected values of n'' produce respectively the +5% deviation, the best agreement, and the -5% deviation between model and measurements. These values identify a relatively narrow interval, which is indicative of the strong dependence of the surface UV irradiance on the aerosol absorption in the case of May 18. Similarly to the previous cases, the real part n' does not seem to significantly affect the modelled spectra. The refractive index which gives the best agreement is 1.536 - 0.0044*i*.
The imaginary part of the refractive index retrieved by *Di Iorio et al.* [2003] above 3600 m, that is in the region of largest aerosol concentration, falls within the obtained interval of values.

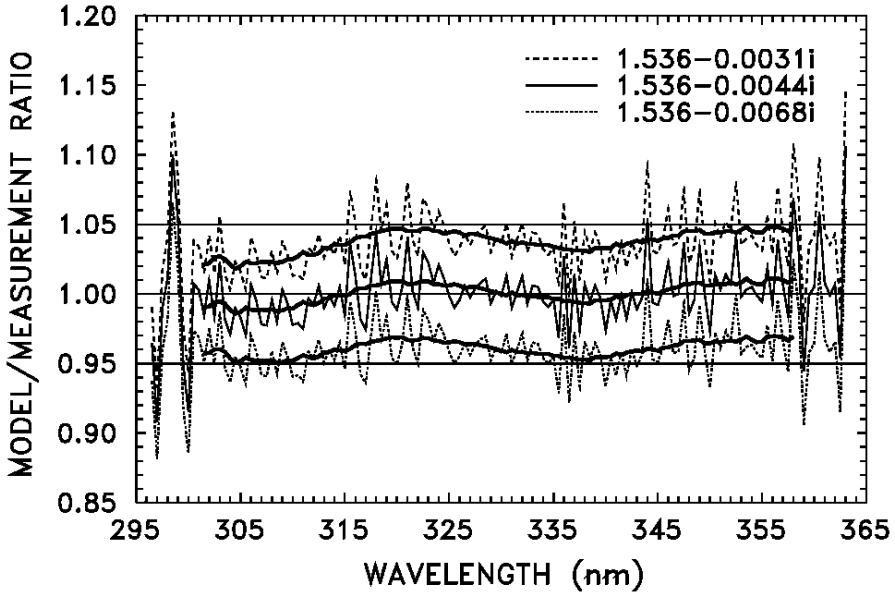

Figure 4.2.9. Ratio of the modelled to the measured UV spectra for May 18 at 60° SZA. The curves refer to three different values of the imaginary part of the aerosol index of refraction. The thick solid curves are 10 nm running averages of the ratio.

The refractive index inferred by the comparison between modelled and measured irradiances constitutes an essential information for the determination of the aerosol optical properties, like the single scattering albedo ω_0 and the asymmetry factor g. Table 4.2.5 shows values of ω_0 and g calculated at 500 nm with the Mie theory for three separate aerosol layers, whose altitude limits are identified from the characteristics of the lidar profile: from the ground to 2400 m, from 2400 m to 3600 m, and from 3600 to 4200 m.

Table 4.2.5. Aerosol single scattering albedo ω_0 and asymmetry factor g at 500 nm obtained with the size distribution of May 18 for different imaginary and real parts of the refractive index. Calculations were performed for the three indicated layers.

	ω_0			g		
	0-2.4km	2.4-3.6km	3.6-4.2km	0-2.4km	2.4-3.6km	3.6-4.2km
1.536-0.0031i	0.84	0.83	0.83	0.75	0.77	0.76
1.536-0.0068i	0.74	0.73	0.73	0.77	0.79	0.78
1.536-0.0044i	0.80	0.78	0.79	0.76	0.77	0.77
1.3-0.0044i	0.77	0.76	0.76	0.85	0.87	0.86
1.7-0.0044i	0.82	0.81	0.81	0.70	0.72	0.72

It is worth noting that 4200 m is not the top of the aerosol layer (which reached 7 km), but the maximum altitude reached by the ultralight aircraft. The values reported in Table 4.2.5 are consistent with those computed for mineral dust by other authors. *d'Almeida et al.* [1991] give a variability range of ω_0 between 0.725 and 0.777 and of g between 0.778 and 0.822 at 500 nm for the desert aerosol in July. *Sokolik and Toon* [1996] found $\omega_0 = 0.85$ and $g = 0.75$, while *Díaz et al.* [2001] obtained $\omega_0 = 0.87$ and $g = 0.83$.

To emphasize the role played by a detailed knowledge of the size distribution in conditions of high aerosol load, the surface irradiance spectrum was calculated assuming the measured vertical distribution and optical depth at 415.6 nm, and the two size distributions given by *d'Almeida et al.* [1991] for desert dust: the desert background (wintertime) and wind carrying dust (summertime), that differ in the content of large particles (radius > 1 μm), which is larger for the second distribution (see Table 4.2.3). Figure 4.2.10 shows the model-to-measurement ratio for the two distributions by *d'Almeida et al.* [1991], using a) the retrieved refractive index of 1.5 - 0.0042 *i*, and b) the mineral aerosol refractive index tabulated by *d'Almeida et al.* [1991]. In case a) the model-to-measurement ratio is about 10-13% (wintertime) and 2-4% (summertime) higher than in the reference case (retrieved size distribution and refractive index), and is about 1-7% (wintertime) and 9-12% (summertime) lower in case b). Thus, the description of the aerosol optical properties through standard parameters can lead to an inadequate determination of atmospheric absorption and scattering.

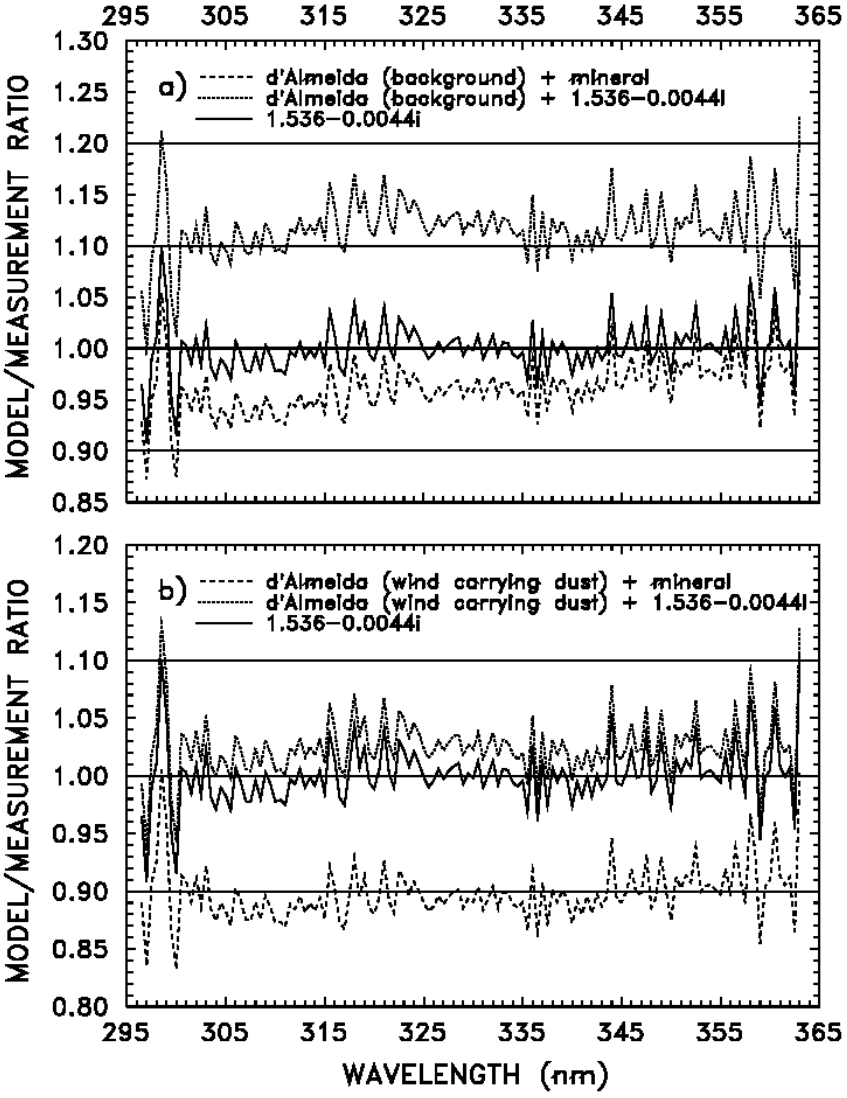

Figure 4.2.10. Comparison of the model-measurement ratio obtained with the retrieved aerosol size distribution and with those by *d'Almeida et al.* [1991] for a) the desert background, and b) wind carrying dust.

The diffuse-to-direct ratio, DDR, which is measured by the MFRSR, is correlated with the AOD [see e.g. *Yu et al.*, 2000]. The value of DDR is independent of the instrumental calibration (in the MFRSR measurements) and of the extraterrestrial solar spectrum (in the model results), and is a useful parameter for a comparison. The DDR was computed at 415.6 nm, in correspondence to the MFRSR measurements, for the 3 selected cases; the results are reported in Table 4.2.6. The model somewhat overestimates the measured DDR in the low aerosol cases, while a good agreement exists on May 18. The reader is reminded that these results are relative to different values of the SZA, and should not be directly compared.

Table 4.2.6. Measured and modelled diffuse-to-direct radiation ratio (DDR). Measured values are averages over one hour intervals centred at the time of the simulation. The indicated uncertainty is the standard deviation of the average.

Day	DDR (measurement)	DDR (model)
May 18	2.00±0.17	2.05
May 25	0.385±0.008	0.413
May 27	0.49±0.01	0.55

Also for May 18, the model was run with different ozone vertical distributions, with, in particular, different amounts in the troposphere. The enhancement of the amount of tropospheric ozone in the P2 with respect to the P1 profile is much smaller on May 18 than on May 25 and 27. Thus, tropospheric ozone seems to play a minor role on May 18, when a 31% increase of the ozone content below 10 km leads to a maximum reduction of the surface irradiance by 1.3% at 303 nm (see Figure 4.2.8). This small variation, much smaller than the one derived on May 25 and 27, is also due to the decreasing role of tropospheric ozone absorption for increasing SZAs.

To clarify the role of tropospheric aerosol, model calculation were then performed using the aerosol vertical profile of May 25, and different values of the optical depth (the profile is scaled accordingly). The aerosol size distributions of May 25 and the refractive indices of May 18 and 25 were used in the calculations; moreover, highly absorbing (refractive index of 1.5 - 0.1 i) and non-absorbing (refractive index of 1.5 - 10^{-8} i) particles were also assumed as limiting cases. Calculations were made at 40° and 60° SZA. In all these cases, the aerosol vertical profile was not varied, while the aerosol optical depth was increased up to a factor of 8.

In the case of aerosols characterized by relatively high absorption (i.e. index of refraction of May 25), a reduction of R_{mc}, i.e. a decrease of the surface irradiance, takes place as a consequence of the tropospheric ozone increase. The reduction of surface irradiance is however smaller than the one obtained with the measured value of the aerosol optical depth, indicating that the large amount of absorbing aerosol produces a decrease of the diffuse radiation in the troposphere, thus somewhat reducing the role of the UV absorption by tropospheric ozone. This effect appears for values of the AOD around 0.5, and is amplified when highly absorbing particles (refractive index of 1.5 - 0.1 i) are simulated.

Increased aerosol amounts showing low absorption are expected to produce an enhanced scattering in the troposphere, and an increased disproportionate role of tropospheric ozone. An increase of R_{mc} with respect to the case with the measured value of the AOD is obtained when the refractive index of May 18, or the value of 1.5 - 10^{-8} i is used. The effect is negligible if the AOD remains below 0.6, and becomes appreciable for larger values.

In summary, this analysis leads to the following conclusions: a) the effect of the aerosol on R_{mc} is negligible or small for low to moderate aerosol optical depths; b) for large optical depths (AOD>0.6), the importance of the absorption by tropospheric ozone depends on the aerosol properties: non absorbing particles produce an increase of the scattering in the troposphere, and a reduction of the surface irradiance due to the disproportionate role of tropospheric ozone; absorbing particles, although may compete with ozone in the absorption of UV radiation, produce a reduction of the diffuse radiation in the troposphere, and a reduction of the role of tropospheric ozone.

4.2.3C. LICOR SPECTRA

The irradiance from 300 to 800 nm (the upper limit for the UVSPEC model is 800 nm) at 2 nm steps was compared with the Licor measurements to test the model reliability also in the visible range of the spectrum. Modelled spectral irradiances were convoluted with a triangular slit function (6 nm FWHM) before the comparison. The retrieved size distribution and the aerosol refractive index estimated in the UV region were used as input for the simulation in the visible.
Figure 4.2.11 shows the measured and modelled spectra for the three days. The ±10% estimated range of uncertainty of the Licor spectral irradiances is also displayed. The large difference between model and measurements in the wavelength bands centred approximately at 692, 726 and 764 nm are due to the absorption by water vapour and molecular oxygen, not considered in the model.

The comparison shows that a good agreement between model and measurement exists in the three cases. A model overestimate is present at longer wavelengths, as a possible consequence of a wavelength dependence of the aerosol refractive indices.
The range of variability for the imaginary part of the aerosol refractive index in the visible was found for May 18 following the same procedure used in the UV spectral range, taking in this case as limits the assumed ±10% uncertainty. The comparison was carried out in a spectral band where ozone, O_2 and H_2O absorption is negligible, i.e. between 668 and 682 nm. Values of n'' ranging from -0.002 to -0.05 were found.

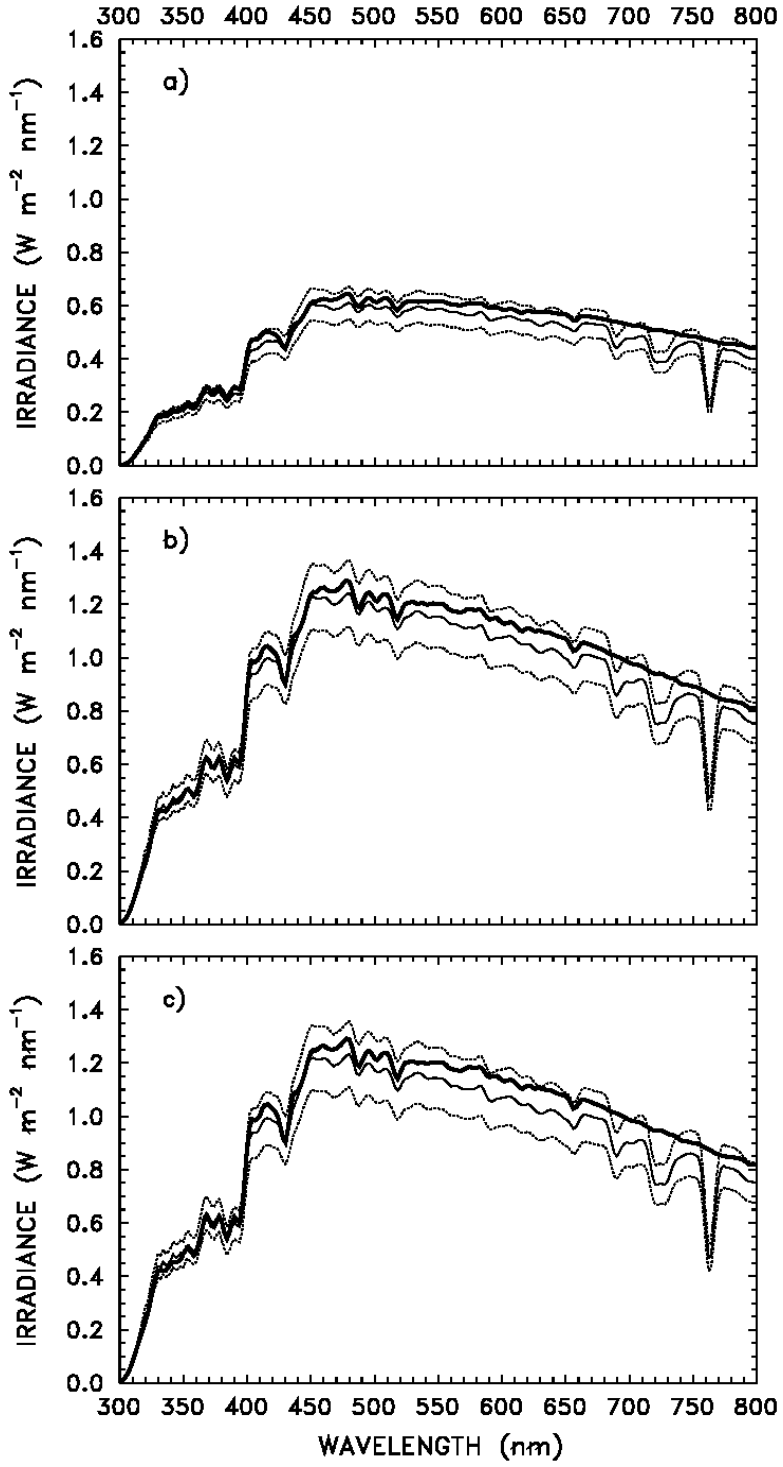

Figure 4.2.11. Measured and modelled spectra in the range 300-800 nm for a) May 18, b) May 25, and c) May 27. Dotted curves correspond to the measured irradiance respectively ±10%.

4.2.3D. RADIATIVE FORCING

At the ground level the aerosol direct radiative forcing RF is defined as the downward global irradiance with aerosol minus that without aerosol. At the top of the atmosphere (TOA) RF is the upward diffuse irradiance without aerosol minus that with aerosol: positive values indicate

a larger upward irradiance for the aerosol free case. An estimate of the RF can be derived by integrating the calculated spectra shown in Figure 4.2.11 over the wavelength range 300-800 nm, for the three selected cases. The reader is reminded that these results are obtained at different SZAs and are instantaneous values. The daily average RF is also estimated for each of the three days, assuming that the AOD does not change during the day; the daily averages are smaller than the instantaneous forcing, due to changes of SZA, and the temporal integration that includes the night period. The results are reported in Table 4.2.7. As expected, on all three days the surface RF is negative, indicating that the aerosol reduces the amount of solar radiation reaching the ground. On May 25 and 27 the surface RF is similar, while is almost two times larger on May 18. It must be recalled that the AOD of May 18 is much larger (more than two times) than on May 25 and 27. Thus, as it will be discussed below, the RF per unit optical depth is larger on May 25 and 27 than on May 18, and the largest forcing obtained on May 18 is mostly due to the much larger aerosol amount. The AOD observed in correspondence to Saharan dust events is however usually much larger than in normal conditions in the Mediterranean [see e.g. *di Sarra et al.*, 2002], and larger forcings are expected.

Table 4.2.7. Instantaneous and daily average aerosol radiative forcing, in W m^{-2}, at the surface and at the top of the atmosphere (TOA), calculated by integrating the simulated spectra over the spectral range 300-800 nm.

	May 18	May 25	May 27	Notes
surface	-70.8	-37.2	-39.1	*instantaneous*
TOA	-7.5	+3.3	+0.2	*instantaneous*
surface	-36.7	-18.8	-20.0	*daily average*
TOA	-1.6	+1.1	-0.6	*daily average*

At the TOA different effects can be observed for the various cases. On May 25 the aerosol layer produces a reduction of the planetary albedo: the imaginary part of the aerosol refractive index is high and the overall effect is a reduction of the upward irradiance with respect to the aerosol-free case. On May 18 the aerosol absorption is lower than on May 25 and a fraction of the incoming radiation larger than in the aerosol-free case is reflected. A result similar to that of May 18 is found on May 27: the aerosol of May 27 is, however, more absorbing than the desert type of May 18, and the increase of outgoing radiation at the TOA is small. The difference between the daily average RF of May 18 and that of May 25 (or 27) is of the order of 17 W m^{-2} at the surface, and between 1 and 2.7 W m^{-2} at the top of the atmosphere. These values may be taken as representative of the additional forcing induced in the Mediterranean by the desert dust with respect to conditions when the aerosol distribution is dominated by transport from North.

The net amount of energy that is absorbed in the atmosphere as a consequence of the aerosol presence is defined also as the atmospheric radiative forcing and is given by the TOA forcing minus the surface forcing. In the examined case, relatively to the spectral interval 300-800 nm, the daily average values are between 19 and 36 W m^{-2}, where the lowest value is for the cases of low aerosol amount, and the highest for the dust event.

It should be stressed that the strong cooling effect due to aerosol can not be directly compared to the warming produced by greenhouse gases, which is an order of magnitude smaller [*IPCC*, 2001]. Aerosols act on a regional scale, and their forcing on a global scale must take into

account their distribution and variability. Highest forcings in Table 4.2.7 are instantaneous values; seasonal and large scale forcings are much smaller.
In order to compare these results with those of previous studies, the instantaneous and daily mean values of the surface and TOA radiative forcing efficiency (RFE) was calculated: RFE is defined as the aerosol forcing per unit of AOD at 500 nm, integrated over the wavelength range 400-700 nm. A summary of the main results of some intensive field campaigns for different types of aerosols and the results of this study can be found in paragraph 4.2.

4.3. DIRECT RADIATIVE FORCING OF SAHARAN DUST IN THE MEDITERRANEAN FROM MEASUREMENTS AT LAMPEDUSA ISLAND AND MISR SPACE-BORNE OBSERVATIONS

4.3.1. OBSERVATIONS AND METHODOLOGY

In this analysis ground-based measurements performed at Lampedusa from the Brewer spectrophotometer, the aerosol lidar, and two sun-photometers/radiometers (MFRSR), and space-borne observations from the Multi-angle Imaging Spectro-Radiometer (MISR), are combined to derive column-integrated aerosol optical properties needed in radiative transfer calculations. In particular, this analysis is aimed at deriving the column-integrated values of the single scattering albedo, ω_0, and of the asymmetry factor, g, which best describe the aerosol properties on two days of July 2002, when airmasses originating from Africa and loaded by a moderate amount of desert dust (AOD at 500 nm of about 0.23) reach Lampedusa. On both days the dust layer extends up to 5.5-6 km altitude. As a first step, the column-integrated values of ω_0 and g which give the best agreement between measurements and model simulations are determined: the best match search is made over the MFRSR global irradiances and MISR equivalent reflectances. The bands of the ground-based and the space-borne instruments differ both in the central wavelength and in bandwidth, thus wavelength-independent values for ω_0 and g are used as input in the radiative transfer model to reproduce the MFRSR irradiances and the MISR equivalent reflectances in their respective visible bands. Model simulations of the spectral ultraviolet irradiance are also performed. Finally, the model is applied to estimate the aerosol radiative forcing at the surface and at the top of the atmosphere. Such an estimate is constrained by the measured MISR radiances and takes advantage from the multi-angle geometry of the instrument. The effects of different aerosol phase functions, describing in a qualitative manner the behaviour of spherical and non spherical particles, on the simulated equivalent reflectances are also investigated. Phase functions for spherical and non-spherical particles have different side and back-scattering, thus influencing the estimate of the aerosol radiative forcing.

4.3.1A. GROUND-BASED MEASUREMENTS

The dataset of ground-based measurements used includes lidar profiles, total ozone content, UV spectra, UV and visible MFRSR irradiances (for a description of the instruments see paragraph 2.1).
As in the previous case (see paragraph 4.2.1), AODs are derived from MFRSR observations; the MFRSR is calibrated with the Langley plot technique. In this analysis, also the measurements of global and diffuse irradiance obtained by the MFRSR are used.
The accuracy on the global irradiances can be estimated, taking into account the uncertainty on the extraterrestrial solar irradiance and on the instrumental extraterrestrial flux derived

with the Langley method. *Thuillier et al.* [1998] show that different extraterrestrial solar spectra agree within 3%. Taking into account the uncertainties associated with the instrumental extraterrestrial flux, with the analog-to-digital conversion of the signal, and on the extraterrestrial irradiance, an overall accuracy of 3.2% on the global irradiance measured by the MFRSR is estimated, which corresponds to 0.04-0.05 W m^{-2} nm^{-1}, depending on the band.

The extraterrestrial solar irradiance, weighted for the transmission curve of each MFRSR band, was derived by comparing the measured and modelled direct component of the downward flux. The differences of the extraterrestrial irradiances derived on the two days are smaller than 2%.

The use of the Langley method is unpractical for the UV-MFR, due to the large role played by ozone and its variations. The correction of the daily ozone variability, although in principle possible, would produce relatively large errors on the estimated extraterrestrial constant. Thus, the UV-MFRSR was calibrated by comparing the measured global irradiances with those determined by the Brewer spectrophotometer. Initially, the Brewer spectra are convoluted with the UV-MFRSR filter functions, assumed of Gaussian shape; then the UV-MFR measurements, performed every 3 minutes, are interpolated at the time of the Brewer UV scan. The ratio of the Brewer global irradiance and the UV-MFR signal for each channel, averaged over the central hours of the day, gives the UV-MFR calibration factor. This factor can be multiplied to the UV-MFR direct radiation signals (obtained as the global minus the diffuse) to derive calibrated irradiances. Finally, from the Beer-Lambert law the AOD is derived, knowing the extraterrestrial flux and after subtracting the Rayleigh and the absorbing gas contributions. The Rayleigh optical depth is calculated after *Bucholtz* [1995].

On the basis of the broadband channel of the MFRSR, on the lidar data and on visual observations at Lampedusa, two cloud-free days, July 14 and 16, 2002, when ground-based observations where simultaneous to the MISR passage above Lampedusa, were identified. Figure 4.3.1 shows the lidar backscatter ratio, R, profiles derived from signals integrated over 10 minutes intervals, for the two days. R exceeds one when aerosols are present. The local time of the MISR overpass is 12:08 on July 14 and 11:55 on July 16.

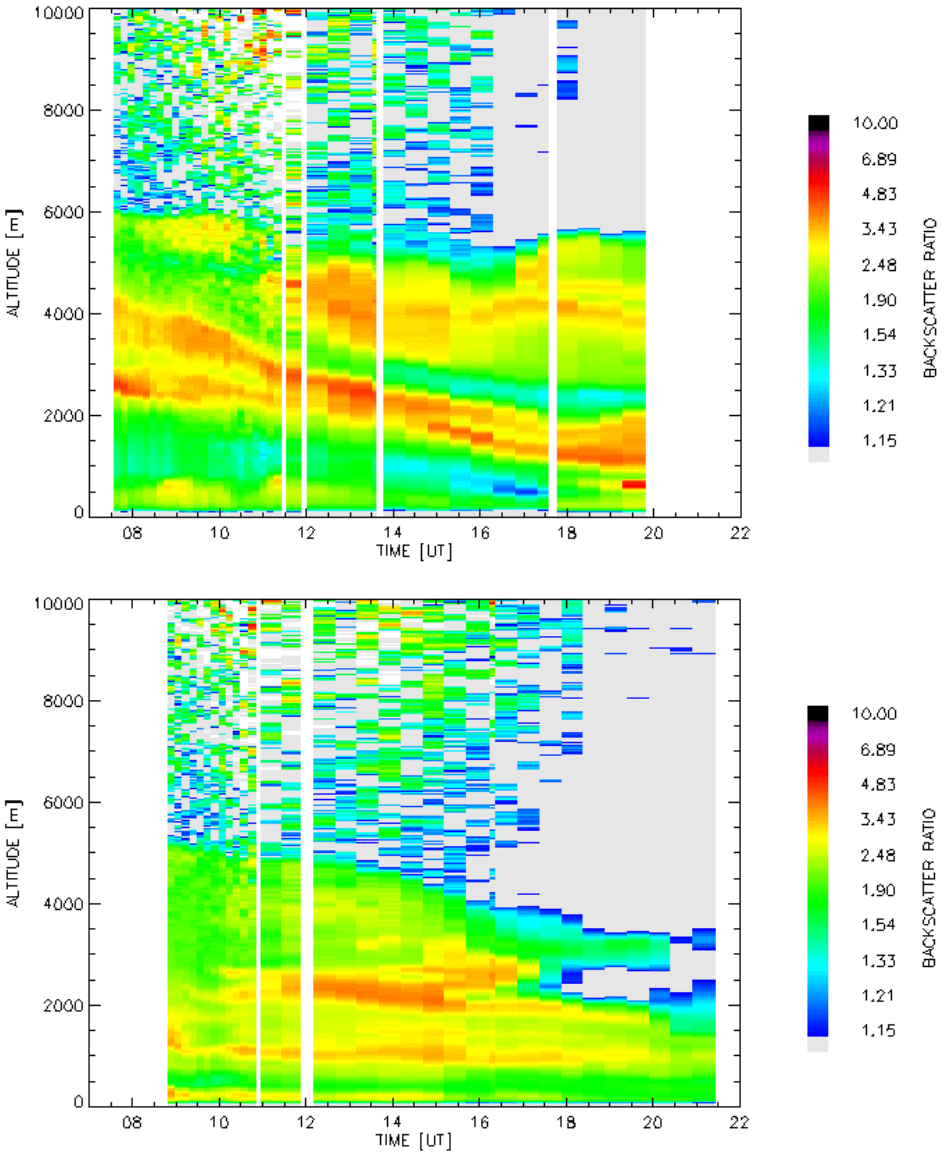

Figure 4.3.1. Evolution of the lidar backscatter ratio profiles for July 14 (upper panel) and July 16 (lower panel).

On July 14 (Figure 4.3.1a) aerosols are detected up to 6 km, with largest values of the backscatter ratio in the 2-4 km and 5-6 km layers. On July 16 (Figure 4.3.1b) most of the aerosols are confined below 5 km. In Figure 4.3.2 the profile of the aerosol backscattering coefficient, β_a, closest in time to the satellite overpass is depicted, showing a maximum aerosol amount between 3 and 4 km on July 14 and below 3 km on July 16. The reader is reminded that R is scaled to the backscattering produced by the molecules, while β_a, i.e. the backscattering cross section per unit volume, is, although in a complex way, more directly related to the aerosol concentration and mass.

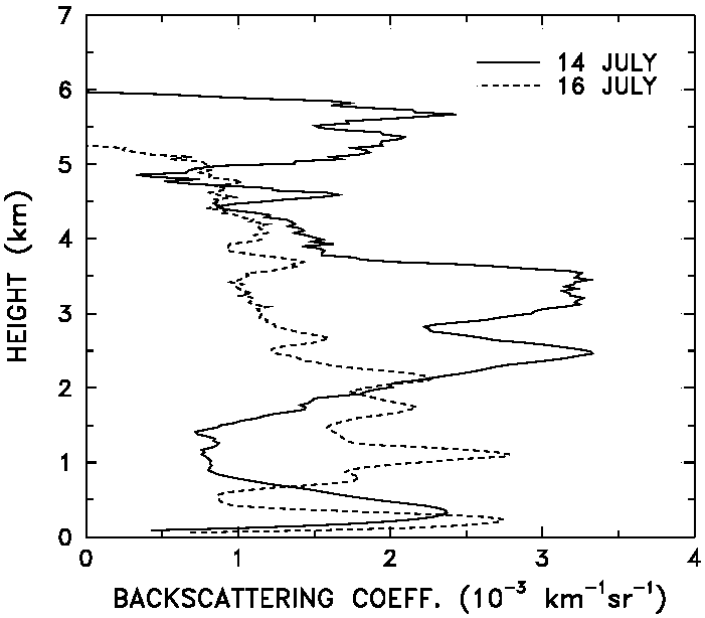

Figure 4.3.2. Lidar backscattering coefficient profiles for July 14 (solid line) and 16 (dashed line) at the time of the MISR overpass.

From the daytime lidar observations, taking into account the instrumental sensitivity, it is possible to exclude that cirri with an optical depth > 0.003 were present on the two days at the time of the satellite overpass. The influence of thinner cirri, that might have been present on the two days, was neglected in the analysis.
To identify the origin of the airmasses arriving at Lampedusa on July 14 and 16, backward trajectories were calculated by means of the HYSPLIT transport model [*Draxler and Rolph*, 2003], which uses meteorological model vertical velocity fields. Trajectories ending over the island at different altitudes at the time of the satellite overpass were calculated.

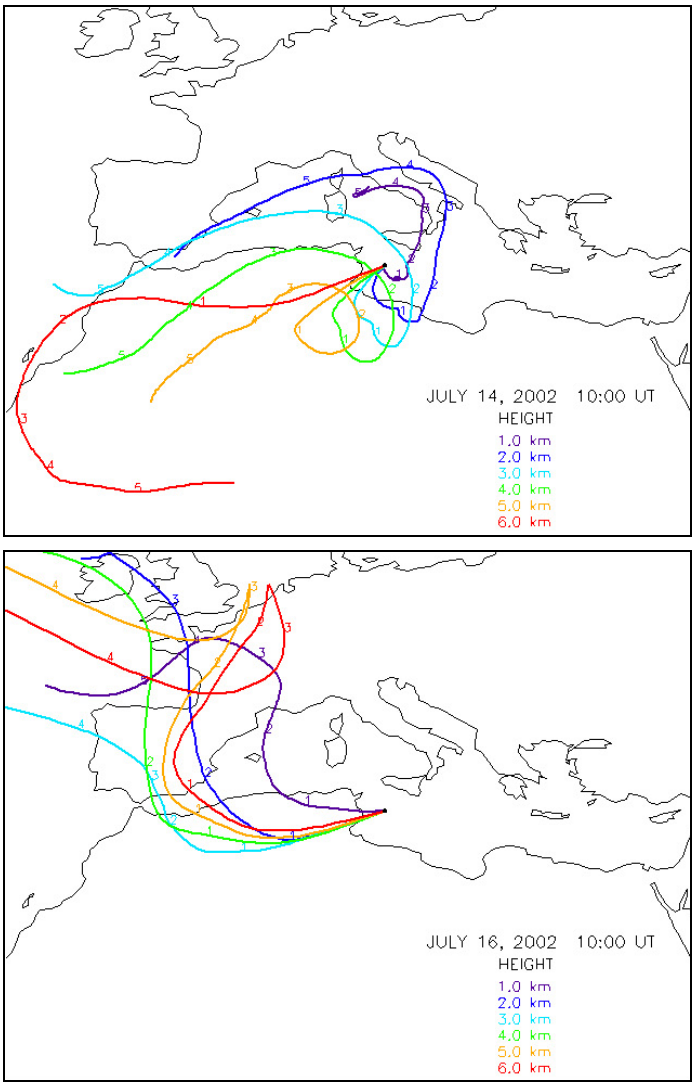

Figure 4.3.3. Isentropic backward trajectories at various heights ending at Lampedusa on July 14 (upper map) and July 16 (lower map) at various altitudes.

Figure 4.3.3a shows that on July 14 the airmass arriving at Lampedusa at 1 km originates from North, while the airmasses at 2 and 3 km were over Morocco 5-7 days earlier, flowed afterwards toward southern Spain and Italy, spent the last 2 days over North-Western Libya and over the Mediterranean, and reached Lampedusa from South. The airmasses arriving at Lampedusa at 4-6 km spent most of the last 6-7 days over Africa, running South of the Atlas Mountains, then over North-Western Libya, Tunisia, and reaching Lampedusa from South West. This pattern finds a striking correspondence in the backscattering profile (Figure 4.3.2), that has a minimum in the region 0.8-1.5 km altitude range, corresponding to the trajectory that does not pass over Africa, and higher values in the above layers, up to 5-6 km. On July 16 the airmasses arriving at Lampedusa at altitudes between 1 and 6 km follow a similar path (Figure 4.3.3b), reaching the island roughly from West, after spending only the last 1-2 days over Africa (North Algeria and Tunisia). The values of R and β_a are lower on July 16 than on 14 throughout the region 2-6 km. The opposite occurs in the region 0.7-2 km. It must be noted that in this altitude range the airmass did not pass over Africa on July 14, while on July 16 also the trajectory ending at 1 km passed over North Africa. As shown by *di*

Sarra et al. [2001b] the aerosol backscatter ratio is generally larger for trajectories that spend a long time over Africa.
Table 4.3.1 shows the AOD at 415.6 and 868.7 nm averaged in one hour interval around the time of the satellite overpass, derived from the visible MFRSR measurements and the retrieved Ångström parameters, α and β.

Table 4.3.1. Aerosol optical depth (AOD) measured by the MFRSR at 415.6 and 868.7 nm, and the derived Ångström parameters.

Day	AOD (415.6 nm)	AOD (868.7 nm)	α	β
14/07/2002	0.230±0.002	0.217±0.001	0.080	0.215
16/07/2002	0.259±0.001	0.155±0.002	0.698	0.140

The values of AODs on the two days are similar. It is worth noticing that these values are in the lower limit of the range previously observed during Saharan dust events at Lampedusa [see e.g. *di Sarra et al.*, 2002; *Di Iorio et al.*, 2003]. The Ångström exponent provides information about the particles' size: in both cases α is relatively small, meaning that there is a component of large size aerosols which has dominant optical properties. The different trajectories, the characteristics of the source regions, and the longer time of residence over Africa probably produced airmasses containing larger particles on July 14 than on 16. The presumably stronger convective activity associated with the part of the trajectory spent over Africa may also have played a role.
Figure 4.3.4 shows the images from the Moderate Resolution Imaging Spectrometer (MODIS) captured on July 14 and 16 at the same time of MISR observation (it should be reminded that MODIS and MISR are aboard the same satellite, Terra): it is clear how the desert dust dominates the aerosol load on 14, while on 16 the dust has moved away eastward from Lampedusa.
The aerosol depolarisation (see paragraph 2.1.4) provides an indication of the particle shape: values close to zero are expected for spherical particles, and higher values are produced by non-spherical particles [*Reagan et al.*, 1989]. The average aerosol depolarisation over three different layers of the cloud has been calculated from the lidar measurements averaged over one hour interval around the time of the satellite overpass. The lidar configuration does not allow to retrieve the aerosol depolarisation below about 1.5 km. On July 14 the average depolarisation (and its standard deviation) was 0.46±0.14 for the 1.35-4.8 km layer, and 0.56±0.09 between 4.8 and 6 km. These rather high values confirm that large asymmetrical particles from the Sahara were present on July 14. On July 16 the average depolarisation values were 0.47±0.09 in the layer 0.45-2.4 km, and 0.25±0.07 between 2.4 and 5.1 km, indicating somewhat distinct properties in the two layers.

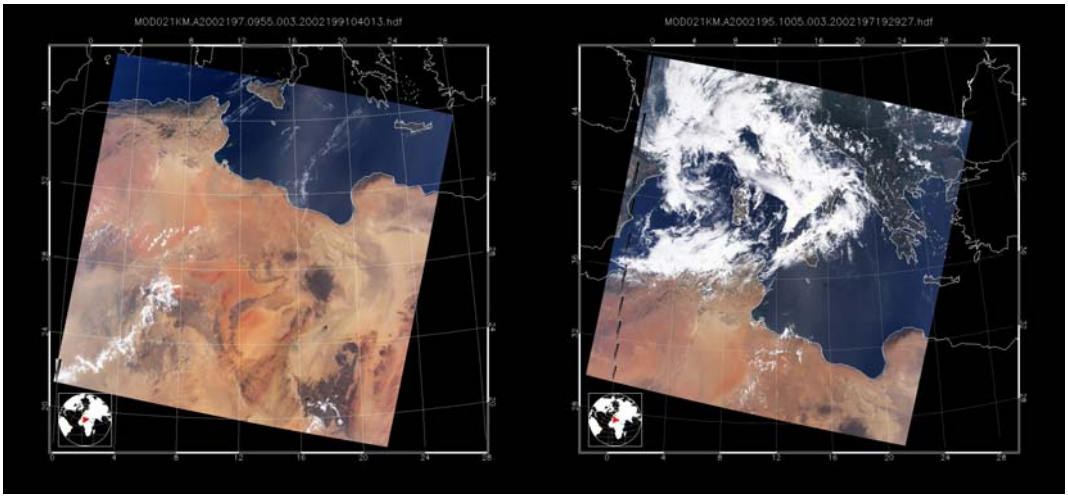

Figure 4.3.4. MODIS images of the Central Mediterranean on July 14 (left) and 16 (right). The dust cloud is visible in both pictures as a yellow shadow.

4.3.1B. SATELLITE DATA

This analysis tries to take advantage of the good radiometric accuracy, and the multi-angle viewing geometry of MISR. The measurements at several viewing angles provided by MISR give the opportunity to attempt a more detailed reconstruction of the outgoing radiation scattered by the Earth atmosphere and surface. Moreover, the multi-angle geometry may be used to derive some atmospheric properties (in particular, it may provide information on the aerosol phase function), at the same time reducing the number of assumptions on the atmospheric structure needed to estimate the TOA fluxes for example through a radiative transfer model.

The calibrated, co-registered and geolocated MISR radiances for the 36 channels (9 viewing angles for 4 wavelengths) at 1.1 km sampling have been used. The geometric parameters, that is the solar zenith and azimuth angles, and the viewing zenith and azimuth angles for each of the nine cameras at the time of the satellite passage over Lampedusa are reported in Table 4.3.2.

Table 4.3.2. Geometric parameters corresponding to the MISR observations on July 14 and 16.

	July 14, 2002				July 16, 2002			
	Solar zenith angle = 20.09° Solar azimuth angle = 308.42°				Solar zenith angle = 22.38° Solar azimuth angle = 303.77°			
Camera	Viewing zenith angle	Viewing azimuth angle	Scattering angle	Glitter angle	Viewing zenith angle	Viewing azimuth angle	Scattering angle	Glitter angle
DF	70.06	11.93	100.15	62.34	70.90	21.13	102.93	67.59
CF	59.95	10.75	109.41	52.53	61.00	24.42	113.22	59.84
BF	45.63	8.05	122.19	38.66	47.46	30.37	127.49	50.08
AF	26.55	0.18	138.17	20.75	30.31	44.32	146.46	40.27
AN	7.87	282.58	152.62	13.43	15.99	102.21	170.54	37.69
AA	27.49	212.33	148.20	35.28	29.29	164.03	161.56	48.37
BA	46.34	204.89	134.95	53.83	46.63	178.85	142.51	61.55
CA	60.55	202.20	123.04	67.78	60.51	185.01	127.94	72.80
DA	70.81	200.93	113.97	77.80	70.62	188.29	117.48	81.24

For this purpose, the MISR radiances have been averaged over all the pixels occupied by the sea included in the area between 35.4° and 35.6° latitude N and between 12.4° and 12.75° longitude E, excluding the pixels that correspond to the island surface: a total of 538 and 539 pixels have been used in the averages for July 14 and 16, respectively. The MISR radiances are converted into equivalent reflectances with the formula

$$\rho(i,k) = \frac{\mathrm{L}(i,k) \cdot \pi \cdot \mathrm{d}^2}{\mathrm{E}_0(i)} \qquad (4.3.1)$$

where $\mathrm{L}(i,k)$ is the radiance measured in the *i* band by the *k* camera, d is the Earth-Sun distance in AU, and $\mathrm{E}_0(i)$ is the extraterrestrial solar irradiance in the *i* band. The uncertainty associated to the reflectances can be estimated taking into account the standard deviation of the radiance averaged over the integrating area, and the uncertainties associated to the absolute radiometric, relative pixel-to-pixel, band-to-band, and camera-to-camera responses [*Bruegge et al.*, 1999], which have been evaluated from the in-flight calibration performed in June 2002. The radiance values for July 14 vary over the MISR pixels within 0.3 and 1% (depending on the camera viewing angle) in the blue band, in the range 0.9-3% in the green, and 1.8-4.3% in the red. For July 16 the ranges are 0.3-0.9% in the blue, 1.2-2.8% in the green, and 2.3-2.8 % in the red band. The resulting total relative uncertainty varies between 3 and 5%, the highest values being for the red band and the cameras at the smallest viewing angles; the band-weighted exo-atmospheric irradiance measured by the MISR has uncertainties that can be neglected with respect to the other terms.
A preliminary check, aimed at removing radiance measurements contaminated by Sun glint was carried out. In the MISR retrieval algorithm a region is potentially glitter-contaminated when the glitter angle is lower than 30° [*Diner et al.*, 1999]. On July 14 the AF and AN cameras measurements where contaminated by sun glint (see Table 4.3.2), and only the remaining seven cameras are used in the analysis. No influence of Sun glint was detected on July 16.

4.3.1C. MODEL

The UVSPEC model is used in this study to reproduce the MFRSR global irradiances and MISR equivalent reflectances in the visible. The radiance simulations are performed with 16 streams to give an accurate description of the photon paths through the atmosphere; 6 streams are used to calculate the irradiance.
Given the asymmetry factor *g*, the model uses the Henyey-Greenstein (HG) aerosol phase function (see paragraph 1.3.2), which may be taken only as an approximation of the real aerosol phase function, particularly because it misses information for non-spherical particles. However, there is an important advantage in using the HG phase function: relevant parameters, such as ω_0 and *g*, may be derived without knowing (or assuming) aerosol size distribution and composition, as is our case. It is assumed that the derivation of these parameters by matching measured and modelled irradiances and radiances constitutes a reasonable constraint also on the HG phase function, that depends on these parameters.
Data, as well as air trajectories, suggest that different aerosol components may be present on the two days (i.e. a mixture of dust particles and background aerosols, which plausibly may contain sea-salt particles and/or sulphates). In particular, different types of particles (marine aerosols in the lowest layer, desert dust above) were probably present on July 14. On both days, dust largely constitutes the dominant aerosol fraction. It must be emphasized that also the distribution and composition of desert dust may significantly vary, depending on the characteristics of the source regions, intensity of the mobilization process and of the

convection, time of travel, etc. The values of ω_0 and g that are retrieved from the analysis should thus be considered as "optically equivalent" parameters, that include the influence of a non homogeneous vertical aerosol distribution, and different aerosol properties on the two days.
In paragraph 4.3.2c the effect of different aerosol phase functions, for both spherical and non-spherical particles, on the reflectance pattern as a function of the scattering angle are examined.

4.3.2. RESULTS AND DISCUSSION

4.3.2A. SIMULATIONS OF GROUND-BASED IRRADIANCE AND SATELLITE RADIANCES

To derive information on the aerosol properties on July 14 and 16, model simulations are performed varying ω_0 and g between 0.4 and 1.0 at 0.01 steps. For each day the root mean square difference (RMSD) is defined as

$$\mathrm{RMSD} = \sqrt{\frac{1}{4}\sum_{i=1}^{4}\Delta^2(i)} \qquad (4.3.2)$$

with

$$\Delta(i) = 100 \cdot \frac{\mathrm{I^s}(i) - \mathrm{I^m}(i)}{\mathrm{I^m}(i)} \qquad (4.3.3)$$

where $\mathrm{I^m}(i)$ and $\mathrm{I^s}(i)$ are the measured and simulated irradiances, respectively, in the i band. The two MFRSR measurements closest to the time of the satellite overpass are chosen and temporally interpolated.

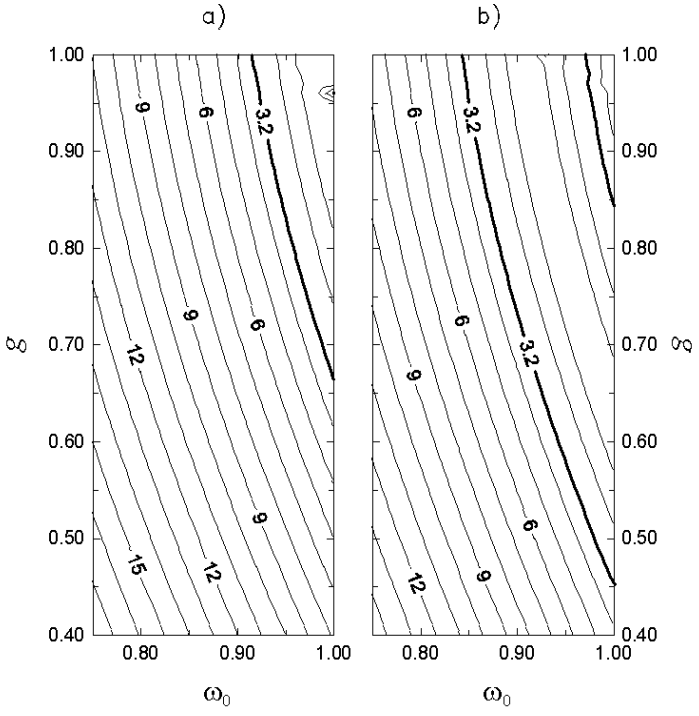

Figure 4.3.5. Plots of the RMSD between measured and modelled MFRSR irradiances for a) July 14 and b) July 16. The thick curve indicates the 3.2% measurement uncertainty.

Figure 4.3.5 shows the plots of the RMSDs: the 3.2% threshold value is highlighted. This threshold delimits a region of values of ω_0 and g that produce simulated global irradiances within the measurement uncertainties. On July 14 ω_0 varies between 0.90 and 1.00 and g between 0.66 and 1.00, while on July 16 ω_0 is in the range 0.84-1.00, and g in the range 0.45-1.00.
The same analysis is then applied to the MISR reflectivity. For MISR observations the RMSD is defined as

$$\mathrm{RMSD} = \sqrt{\frac{1}{3}\frac{1}{\mathrm{K}}\sum_{i=1}^{3}\sum_{k=1}^{\mathrm{K}}\Gamma^2(i,k)} \qquad (4.3.4)$$

with

$$\Gamma(i,k) = 100 \cdot \frac{\rho^{\mathrm{s}}(i,k) - \rho^{\mathrm{m}}(i,k)}{\rho^{\mathrm{m}}(i,k)} \qquad (4.3.5)$$

where $\rho^{\mathrm{m}}(i,k)$ and $\rho^{\mathrm{s}}(i,k)$ are the measured and simulated equivalent reflectances defined in Equation 4.3.1, respectively, in the i band for the k camera. The sum in expression (4.3.4) is performed on all the MISR cameras, excluding those affected by sun glint. Figure 4.3.6 presents the plots of the RMSD on the two days. Minima of RMSD are higher than 10%; this difference is primarily due to discrepancies between model and observations in the green and red bands.

Overlapping the regions of minimum RMSD derived for the MFRSR irradiances and the MISR reflectances (i.e. where the RMSD of the global irradiances at the surface is <3.2%, and the RMSD of the MISR reflectances is <11% on July 14 and <13% on July 16) identifies the best values of ω_0 and g. The retrieved pairs of (ω_0, g) responding to these criteria are: (0.96,0.80), (0.97,0.79), (0.97,0.80) on July 14, and (0.88,0.81), (0.88,0.82), (0.89,0.81), (0.89,0.82) on July 16. The absolute minima of the RMSDs occur for $\omega_0 = 0.96$ and $g = 0.80$ on July 14, and for $\omega_0 = 0.88$ and $g = 0.81$ on July 16.

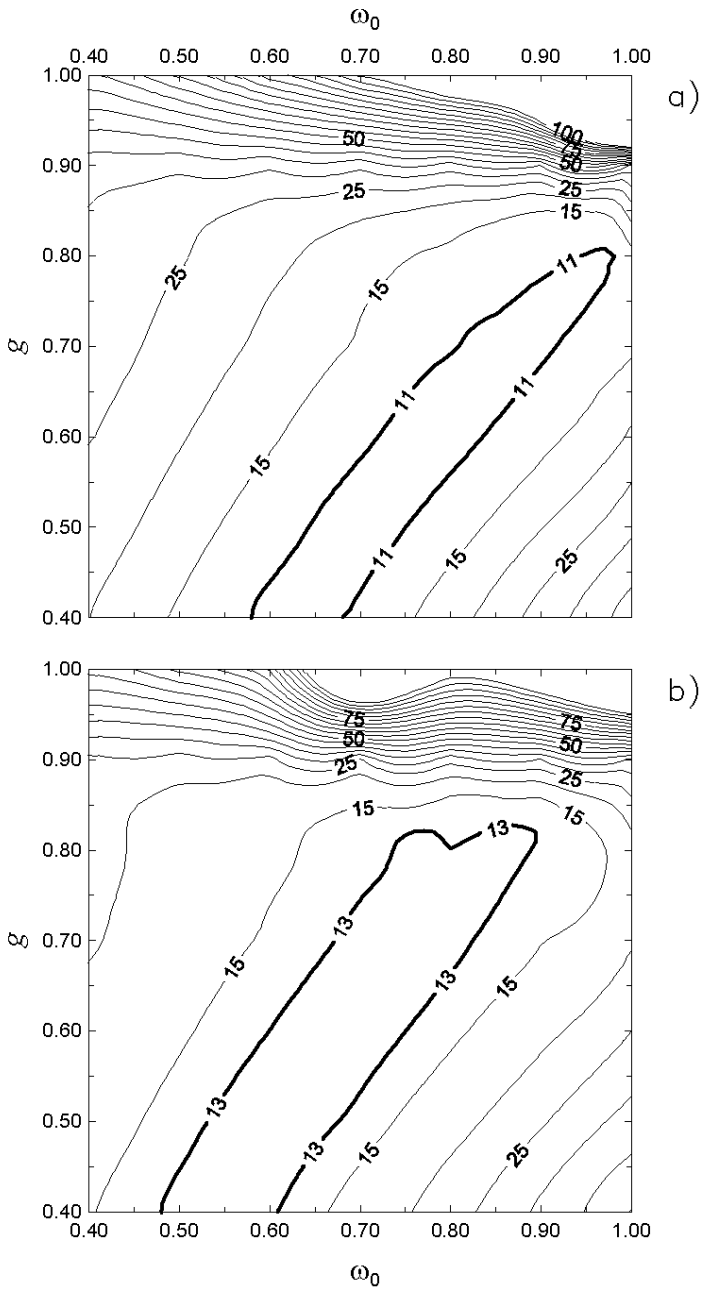

Figure 4.3.6. Plots of the RMSD between measured and modelled MISR equivalent reflectances for a) July 14 and b) July 16. The thick curves show the regions with lowest RMSDs.

Few studies deal with the optical properties of desert dust in the Mediterranean. *Kouvarakis et al.* [2002] report a value of $\omega_0 = 0.87$ at 532 nm for the dust episodes collected at Crete in May 1999 during the PAUR II campaign. *Di Iorio et al.* [2003] retrieved the column averaged ω_0 and g of the desert dust from data collected at Lampedusa island during PAUR II, comparing the measured aerosol size distribution with the lidar-derived backscattering profile and found $\omega_0 = 0.75$ and $g = 0.79$ at 532 nm. In Table 4.2.4 of paragraph 4.2.3b the wavelength-dependent ω_0 and g at 500 nm for the desert dust that best reproduce the measured UV spectral irradiance are in the range 0.73-0.84 and in the range 0.75-0.79,

respectively. The main findings of the studies conducted worldwide on the dust optical characteristics have been summarized by *d'Almeida et al.* [1991] and, more recently, by *Dubovik et al.* [2002].

Figure 4.3.7a shows the comparison between satellite and calculated equivalent reflectances as a function of the camera viewing angle for July 14, when the glitter-contaminated AF and AN cameras have been excluded. The shape of both measurement and model curves is characterized by a higher signal at the further off-nadir cameras (DF and DA) due to the larger atmospheric airmasses. A good agreement is achieved in the blue band (2.1% RMSD) at all camera angles, while a model overestimate (up to 15%) is present in the green and red channels. Model underestimates measurements at the DF and DA cameras in the green band by 7 and 8%, respectively, and at the DF, CF, CA and DA cameras in the red band, with differences of –23, -8, -6 and –22%.

On July 16 (Figure 4.3.7b) the MISR blue radiance is underestimated by the model, with differences as large as 11% for the AN camera. Similarly to July 14, on July 16 the model overestimates the space-borne measurements in the green band, except for the DF and DA cameras, and in the red band, except for the DF, CF, CA and DA cameras.

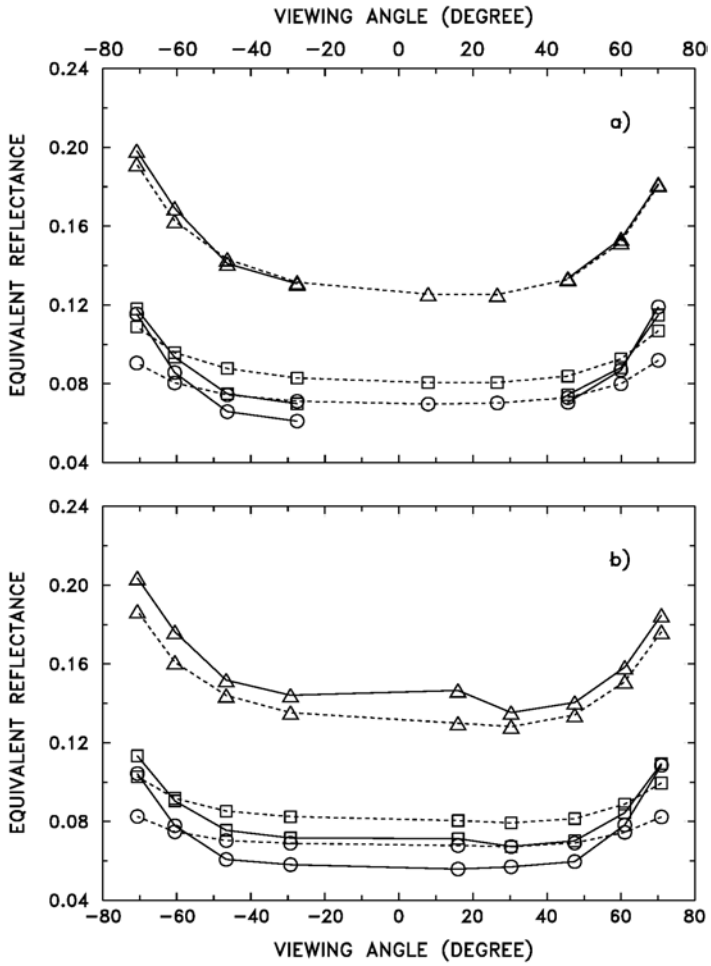

Figure 4.3.7. Modelled (dashed lines) and measured (solid lines) MISR equivalent reflectances as a function of the viewing zenith angle for a) July 14 (ω_0 = 0.96 and g = 0.80) and b) July 16 (ω_0 = 0.88 and g = 0.81). Triangles, squares, and circles identify measured reflectances in the blue, the green, and the red bands, respectively.

The RT model has been initialised with a wavelength-dependent surface albedo, and assumed a Lambertian surface. A different treatment of the surface albedo may possibly produce smaller differences between modelled and measured reflectivities. The use of a more complex surface albedo would however require further assumptions, and would add a degree of arbitrariness.

The wavelength-independent best values of ω_0 and g were used to reproduce with the model the Brewer spectral irradiances measured at the SZA s of the MISR observations. The spectral model-to-measurement ratio for July 14 and 16 is shown in Figure 4.3.8; the thick lines are 10-nm running averages of the ratio. As a first case, the AOD in the UV is derived from the Ångström formula, using the coefficients α and β derived from AOD measurements in the visible (Table 4.3.1). In this case, model results exceed measurements (i.e. the modelled irradiances are larger than observations), with differences between 11 and 21% for July 14 (Figure 4.3.8a), and between 5 and 18% for July 16 (Figure 4.3.8b).

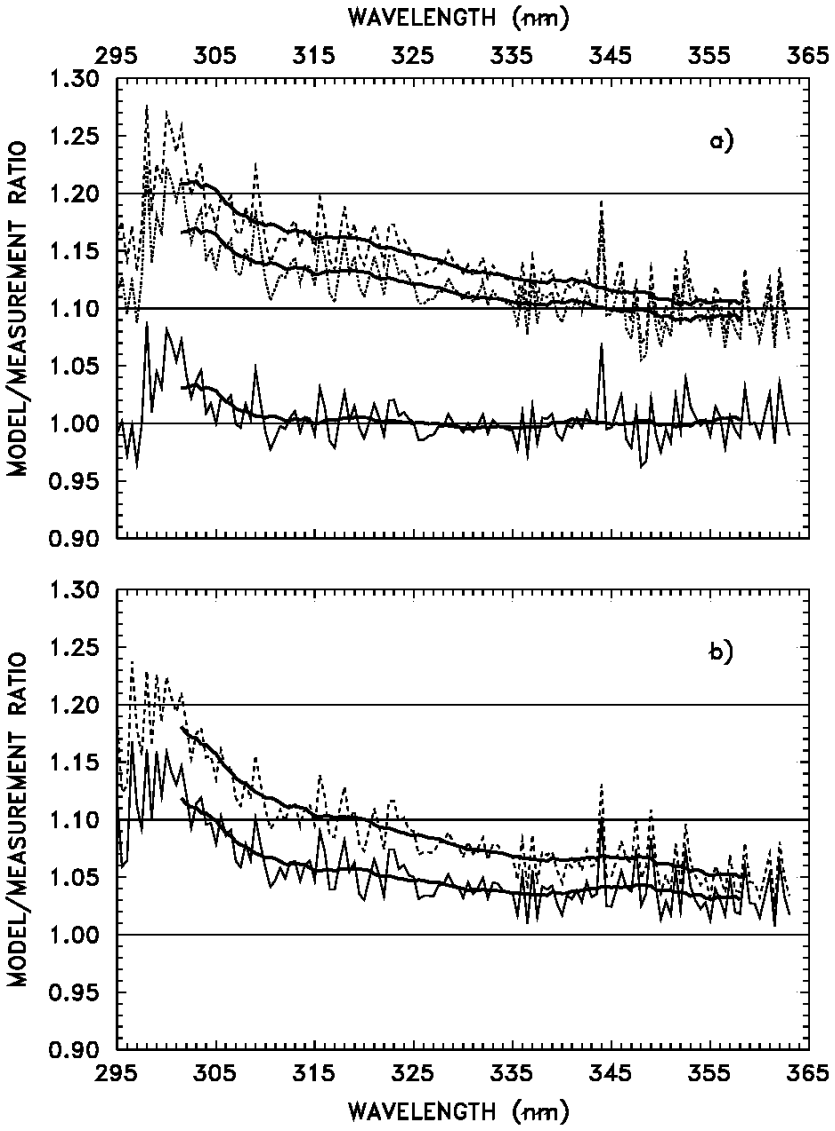

Figure 4.3.8. Ratio of the modelled and measured UV spectra for a) July 14 and b) July 16, at the time of the satellite overpass. For graph a) the two dashed curves, from top to bottom, represent the ratios obtained with aerosol optical depth estimated from coefficients α and β of Table 4.3.1 and Table 4.3.3, respectively, and $\omega_0 = 0.96$ and $g = 0.80$; the solid curve is obtained with $\omega_0 = 0.78$ and $g = 0.80$ and optical depth derived from coefficients α and β of Table 4.3.3 (see text). For graph b) the two curves, from top to bottom, represent the ratios obtained with aerosol optical depth estimated with coefficients α and β of Table 4.3.1 and in Table 4.3.3, respectively. The thick solid curves are 10-nm running averages of the ratio.

As a second case, the Ångström formula is applied using the coefficients α and β derived from the AOD measurements at 317.6 nm and 415.6 nm (Table 4.3.3). In this case the coefficients α and β are quite similar for the two days. It is worth noting that the values of α in Table 4.3.3 are much larger than those in Table 4.3.1, indicating a change in the aerosol optical properties with wavelength.

Table 4.3.3. Aerosol optical depth (AOD) measured by the UV-MFR-4 at 317.6 nm and by the MFRSR at 415.6 nm and the derived Ångström parameters.

Day	AOD (317.6 nm)	AOD (415.6 nm)	α	β
14/07/2002	0.432±0.005	0.230±0.002	2.336	0.030
16/07/2002	0.474±0.004	0.259±0.001	2.250	0.036

A steep increase of the AOD of Saharan dust in the UV was also observed by *Cattrall et al.* [2003], who performed Sun-photometric measurements from Dry Tortugas island (24.6° N, 82.9° W) in July and August 1998. The dust refractive index, mostly its imaginary part, strongly increases in the UV [see e.g. *d'Almeida et al.*, 1991], possibly producing a significant increase of the optical depth. Part of this increase may also be due to a different composition of the smaller particles, to which UV wavelengths are more sensitive than visible wavelengths.

Consequently, the radiative effects of the desert dust aerosol in the UV [*di Sarra et al.*, 2002] may be larger than what may be expected from measurements of the AOD in the visible spectral range. Using the relatively large values of the optical depth in the UV estimated with the parameters of Table 4.3.3, the model simulation for July 14 still gives an overestimate of 9-16%, while for July 16 the 10-nm average of the model-to-measurement ratio oscillates around 1.03-1.05 (the model overestimates measurements by 3-5%) for wavelengths larger than 320 nm, and is up to 1.12 below 310 nm. It is worth noting that the differences larger on July 14 than on 16 indicate that on the first date aerosols were characterized by a stronger wavelength dependence of ω_0 and g.

As a third case, model simulations for July 14 are performed fixing g at 0.80, and varying ω_0 in order to determine the value for which the model-to-measurement ratio is closest to 1; a value of $\omega_0 = 0.78$ produces differences between 0 and +3%. Thus, a decrease of ω_0 in the UV is needed to reproduce the measured irradiance. This result confirms that the optical properties of desert dust change significantly in the UV. The change is more evident on July 14 than on 16. As noted by *d'Almeida et al.* [1991], ω_0 of desert dust is expected to increase with wavelength.

In the radiative forcing calculations, reported in the next section, the values of ω_0 and g retrieved in the visible are used, since the Brewer spectral range (290-360 nm) contributes by 6-8% and 3-9% to the radiative forcing at ground and the TOA, respectively, depending on the examined days. Thus, the influence of the behaviour of ω_0 in the UV on the radiative forcing is neglected.

4.3.2B. RADIATIVE FORCING

The aerosol direct radiative forcing (RF) is calculated between 290 and 800 nm integrating the modelled spectral irradiances and using the pairs of ω_0 and g previously derived. Table 4.3.4 reports the results for the two days.

Table 4.3.4. Instantaneous aerosol radiative forcing, RF, at the surface and at the top of the atmosphere (TOA), calculated by integrating the simulated spectra over the spectral range 290-800 nm.

			instantaneous RF (W m^{-2})	
Day	ω_0	g	surface	TOA
14/07/2002	0.96-0.97	0.79-0.80	-(12.3-13.9)	-(5.3-6.2)
16/07/2002	0.88-0.89	0.81-0.82	-(23.1-25.0)	-(1.2-1.9)

As expected, at the ground aerosols produce a reduction of the radiation with respect to the aerosol-free case; conversely, at the TOA the presence of aerosol particles induces an increase of the portion of incident radiation that is scattered back to space. The difference between the two days is remarkable although the SZAs and the AODs are very close: on July 16 the RF at the surface is significantly higher and at the TOA is lower than that on July 14. This difference is attributed to the higher absorption and the lower backscattering for the aerosol of July 16, in accordance with the retrieved values of ω_0 and g. The reader is reminded that desert dust on both days was the dominant aerosol component. Dust originating from different source regions may show different optical properties, and largely different radiative effects.

The variations of the aerosol optical properties with altitude may affect the obtained results. It is however not possible to derive information on the vertical distribution of the aerosol optical properties from the available measurements. An analysis of the influence of different aerosol properties at different altitudes would require a large number of assumptions on their size distribution and composition. Thus, it was chosen to use the available constraints provided by the observations to derive column-integrated optical parameters, whose effects are similar to those produced by the more complex real situation. On the considered days desert dust (although originating from different regions of North Africa) is the dominant component of the aerosol over the column.

On July 14 the back-trajectories and the stratification in the lidar profile indicate a neat distinction between the aerosols respectively below and above 1.5 km, and this case was selected to investigate the influence of the presence of two layers with distinct properties. On the basis of the available measurements, the aerosol concentration profile can be derived, under the assumption of the composition and dimension of the aerosol in the lowest layer, which can be reasonably constituted by sea-salt and water-soluble particles. Aerosol particles of maritime-polluted type are assumed between 0 and 1.5 km, with $\omega_0 = 0.96$ and $g = 0.69$ at 500 nm [*d'Almeida et al.*, 1991], and a layer of dust-like particles between 1.5 and 6 km. For the layer 1.5-6 km (i.e. for the desert dust only) the values of ω_0 and g that minimize the difference between modelled and measured global irradiances and equivalent reflectances were searched and the results gave $\omega_0 = 0.96$ and $g = 0.82$. The differences in the RT considering two different aerosol layers instead of one are negligible at the surface between 290 and 800 nm (+1.3%) and correspond to a +3% at the TOA.

The SZA at the time of the satellite overpass is very close on the two days, and a direct comparison of the MISR radiances for each band is possible. The radiances of July 14 in the green and red bands are higher than those of July 16, while the opposite occurs for the blue band. This behaviour is consistent with the derived AOD spectral behaviour: the AOD in the blue band, as well as the upwelling radiance, is higher on July 16, while in the green and red bands (those which mainly control the visible RF) the AOD and the upwelling radiance are higher on July 14.

In order to compare these results with previous works, the radiative forcing efficiency (RFE) in the visible was calculated, that is the radiative forcing between 400 and 700 nm per unit of AOD at 500 nm. A comparison of the RFE estimation during some intensive field campaigns for different types of aerosols and the results of this study can be found in paragraph 4.5.

4.3.2C. SENSITIVITY ON THE AEROSOL PHASE FUNCTION

Since no information about the aerosol phase function are available, the modelled radiances are obtained using the Henyey-Greenstein (HG) phase function (see paragraph 1.3.2). With the aim of studying the sensitivity of the simulated radiances to different phase functions, also spherical and non-spherical particles were considered. It is worth stressing that the following analysis is qualitative, and is meant to examine how the various phase functions reproduce the MISR radiance pattern as a function of the scattering angles. The effects of non-spherical particle shape on the aerosol retrieval and on the satellite radiances have been widely studied [e.g. *Mishchenko et al.*, 1995; *Kahn et al.*, 1997; *Tanré et al.*, 2001; *Müller et al.*, 2003]. In the following analyses the same ω_0 derived in the previous sections will be assumed; this assumption is somehow crude, since the phase functions depends on the refractive index, and on the single scattering albedos. Nevertheless, it is beyond the purpose of this study a complete investigation of the effect of combined changes of phase function and optical attenuation of desert dust, and we will not vary the value of ω_0.

For spherical particles (SP), the three-modal size distribution of May 18, 1999 was considered. Since the Ångström parameter α on May 18, 1999 was different from the values found in July 2002, a balancing of the three modes of the size distribution of May 18, 1999 was operated to reproduce the AOD measured on July 14 and 16, 2002 at 418.6 and 868.7 nm, and thus the Ångström parameter α. To do so, the contribution to the AOD at 415.6 nm and 868.7 nm from the first two modes of the size distribution (median radii of 0.07 and 1.24 μm) and the contribution of the third mode (median radius 5.3 μm) were considered separately, and the mixing ratios which allowed to obtain the measured AODs was searched. The calculation was made applying the Mie theory and using the refractive index of 1.536-0.0044*i* found on May 18, 1999. Finally, the aerosol phase function was calculated at 532 nm, and assumed not to vary with wavelength. The results are reported as solid curves in Figure 4.3.9d and h. Substantial differences were found on the two days, with a larger fraction of big particles on July 14 than on 16: the effective radii of these new size distributions are 4.35 μm for July 14 and 0.99 μm for July 16. The resulting asymmetry factor g is 0.85 on July 14 and 0.69 on July 16, far from that found in the reflectance simulations with HG phase function for July 14 (g = 0.80) and for July 16 (g = 0.81).

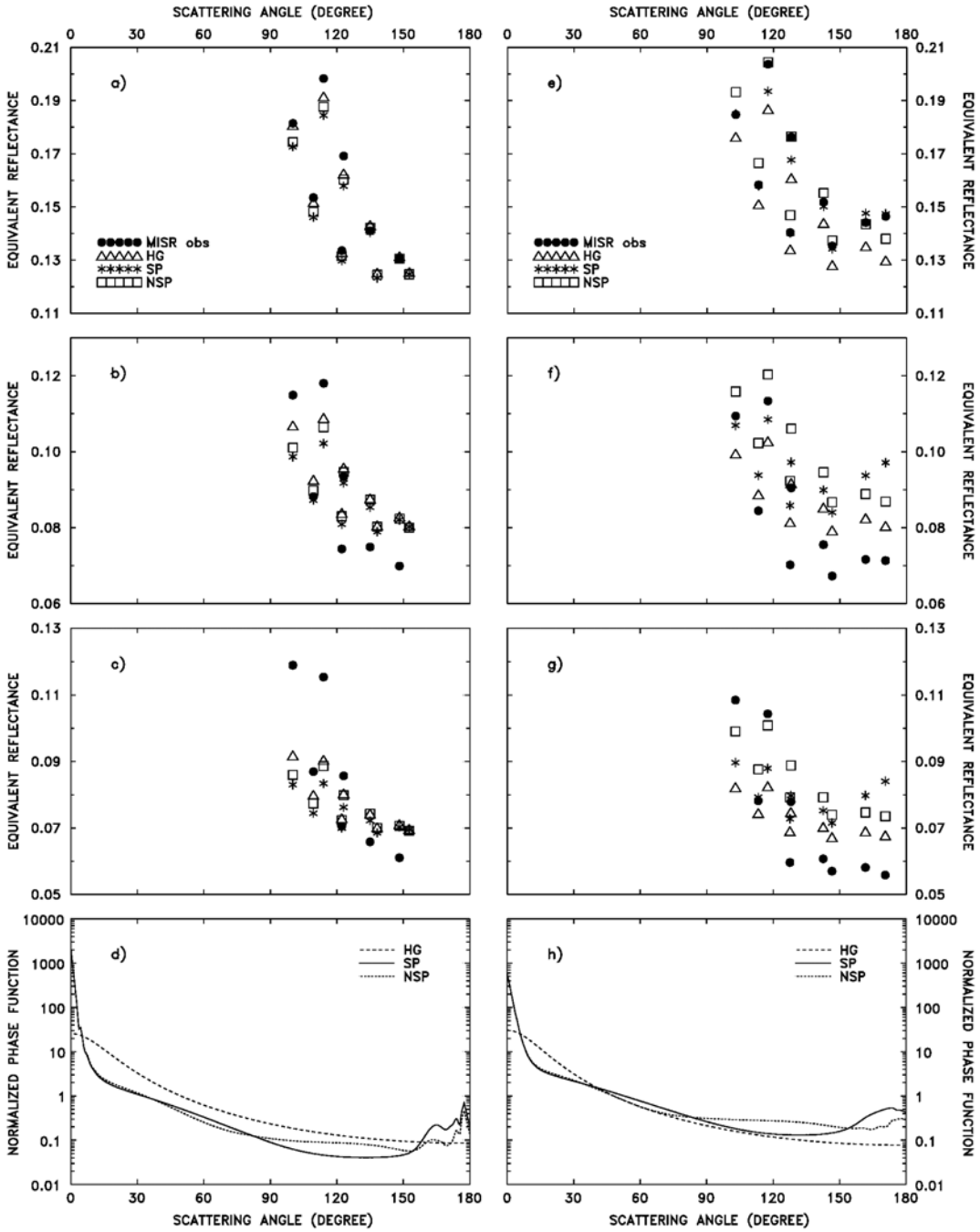

Figure 4.3.9. Equivalent reflectances in the blue, green and red (from top to bottom) MISR bands simulated using different phase functions (d-h) (see text) vs. scattering angle for July 14 (left panels) and July 16 (right panels). Measurements are also shown (full circles).

In order to obtain a phase function which reproduces the features of non-spherical particles (NSP), i.e. a higher side scattering (at scattering angles, θ, between approximately 90° and 150°) and a lower backscattering (θ>150°), the ratio of the non-spherical to spherical phase functions reported by *Mishchenko et al.* [1997] was adopted for dust-like type particles at wavelength 443 nm; the authors consider a size distribution of polydisperse and randomly oriented prolate and oblate spheroids, with the maximum radius for the equivalent sphere (the sphere with the same projected area as that of the spheroid) of 2 μm. It must be emphasized

that the dust size distribution often, and also in our case, contains a significant amount of particles larger than 2 μm. Calculations made for spheroids with a size distribution that includes particles up to 15 μm of radius produce similar results with respect to the same distribution of spheres [*Müller et al.*, 2003]. An accurate description of the phase function of non-spherical particles would require the detailed knowledge of their shape (and composition), and a complex treatment of their interaction with the radiation. Given the large number of assumptions that have to be made, the determination of the optical behaviour of non-spherical dust particles is inherently qualitative. In the following analyses it is assumed that the behaviour described by *Mishchenko et al.* [1997] provides a sufficient description of the effect of the non-sphericity.
The value of the asymmetry factor *g* for the NSP phase function is 0.86 for July 14 and 0.65 for July 16; these values are not far from those obtained on the two days with the SP phase function. The impact of the HG, SP and NSP phase functions on the equivalent reflectances is reported in the left (July 14) and right (July 16) panels of Figure 4.3.9 as a function of the scattering angle. The SP phase function has a minimum between 100° and 150°; the HG curve is above the SP and NSP phase functions for $\theta<160°$ on July 14, while it is below the SP and NSP for $\theta>80°$ on July 16.
On both days the three phase functions HG, SP and NSP reproduce the reflectance patterns for $\theta<150°$. On July 14 the best reflectance pattern is given by the HG phase function in the blue band. On July 16 the simulated reflectances in the blue obtained using the SP phase function reproduce the patterns of the measured quantities at all scattering angles, included the highest one. In the other two bands the reflectance patterns are not reproduced neither by the spherical or the non-spherical particles' phase function for both days: this would indicate that, first of all, the changes of the phase function with the wavelength should be taken into account. Moreover, in the green and red bands the differences between the reflectances at the lowest and highest scattering angles are larger for the measurements than for the simulations.
It should be noted that on July 16 the MISR AN camera (viewing zenith angle of 16° and scattering angle of 170.5°) measures equivalent reflectances in the blue band higher that those of the near AF and AA cameras (see Figure 4.3.7b). This behaviour may be due to a possible influence of sun glints, or the dependence on the scattering angle may be attributed to the differences of the phase function around the backward direction: the HG and the NSP phase functions are rather flat between 150 and 170°, and can not reproduce the AN peak; the SP function, with a more pronounced backscattering, gives conversely highest reflectances in the AN and AA directions.

4.4. DETERMINATION OF THE SINGLE SCATTERING ALBEDO OF DIFFERENT AEROSOL TYPES IN THE CENTRAL MEDITERRANEAN

In this paragraph, information about the column-integrated single scattering albedo of different aerosol types are retrieved using only measurements from a single ground-based instrument, the MFRSR, performed in a time period of two and half years. Differently form the previous analyses, when measurements from various instruments in a short time period allowed to retrieve detailed information about the aerosol properties, the combination of MFRSR measurements on a longer time period and of the RT model allows to derive the average ω_0 for different families of particles, without focusing on single episodes.

4.4.1. MEASUREMENTS

The MFRSR measurements of global and diffuse irradiance performed from July 2001 to September 2003 have been used to derive the AOD in five of the six narrowband channels, centred respectively at 415.6, 495.7, 614.6, 672.6 and 868.7 nm, and the Ångström parameter. Measurements are performed every 15 s and averaged over longer intervals, and finally stored for the analysis. The averaging interval was changed during the measurement period, starting from 10 minutes in July 2001, to 1 minute in 2003. In order to derive the AOD, the Lambert-Beer law is applied using values of the instrumental extraterrestrial constant determined by means of Langley plots (see paragraph 2.1.2). In the period considered between 65 and 169 calibrations (depending on the channel) were possible. To verify the instrumental stability, averages were calculated over the whole measurement period, and over shorter time intervals. The constants calculated over 6-month periods differ by less than ±4% at 415.6 nm, and by less ±2% at the other channels. The instrumental characteristics remained thus reasonably constant throughout the observation period; these variations were however taken into account by using yearly averages of the extraterrestrial constants. The standard deviations of the average extraterrestrial constant is always <2.8% at 415.6 nm, and <2% at the other channels, implying an absolute error on AOD due to the uncertainty on the constant [*di Sarra et al.*, 2002] smaller than approximately 0.02. Systematic errors on AOD due to erroneous values of the extraterrestrial constant are believed to remain within the estimated uncertainties. The measurements are interpolated at SZAs of 20, 30, 40, 50 and 60°.

The Ångström exponent, α, has been calculated from the values of the aerosol optical depth at 415.6 and 868.7 nm; the uncertainty on α is derived from the error propagation law.

Figure 4.4.1 from *Pace et al.* [2004] shows the behaviour of α versus AOD at 495.7 nm (hereafter indicated as τ) for cloud-free conditions at all the SZAs in the period July 2001 - September 2003. Gaps in the measurements derive from the presence of clouds and, in minor part, from problems in the instrument operation.

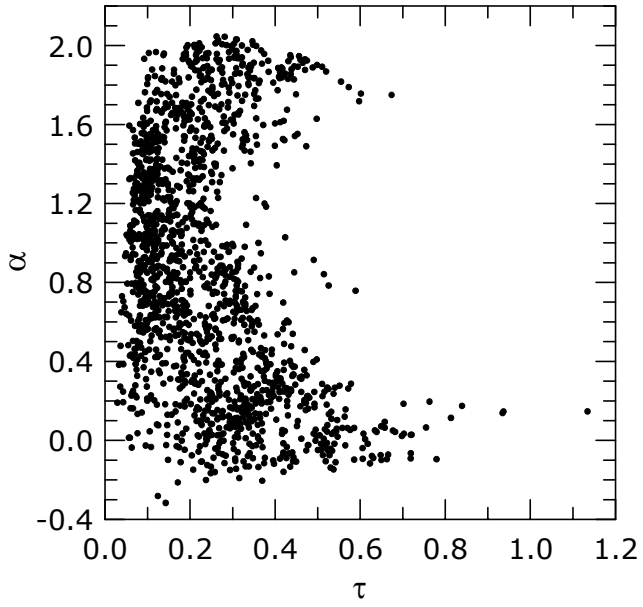

Figure 4.4.1. The Ångström exponent, α, as a function of the aerosol optical depth at 495.7 nm, τ, for cloud-free conditions in the period July 2001-September 2003 [from *Pace et al.*, 2004].

The τ-α plot is a qualitative tool for identifying different types of aerosol. This method has been used in a large number of studies, and basically takes advantage of the properties of α, which depends mainly on size distribution (see paragraph 1.3.2), and τ, which depends mainly on the aerosol columnar density.
Therefore the τ-α plot qualitatively indicates amount and dimension of the observed aerosol.

The dependency of α on the size distribution have been largely used to distinguish between aerosol types characterised by large particles, i.e. desert dust [e.g. *Eck et al.*, 1999; *Dubovik et al.*, 2002], or small particles, i.e. anthropogenic aerosols like urban-industrial [*Eck et al.*, 1999; *Smirnov et al.*, 2000; *Dubovik et al*., 2002; *Kubilay et al.*, 2003] or biomass burning aerosol [*Kaufman et al.*, 1998; *Eck et al.*, 1999, 2001; *Reid et al.*, 1999; *Dubovik et al.*, 2002; *Balis et al.*, 2003].
The measurements in Figure 4.4.1 evidence the presence of different aerosol types. Two main groups can be identified: the first one, corresponding to large values of τ and low values of α, is attributable to Saharan dust; the second one, characterized by large values of both τ and α, is due to advection of airmasses loaded of urban-industrial or biomass burning aerosol from the European continent. The distribution of data points in the figure is however continuous, suggesting that other families of particles are present (for example marine aerosols), as well as cases of mixing of different aerosol types in the air column.
The data shown in Figure 4.4.1 have been classified on the basis of the trajectory analysis in order to identify the average properties of the aerosol originating from different geographical sectors. 5-day backtrajectories ending at Lampedusa at 2000 m were calculated by means of the HYSPLIT Dispersion Model, operated with the inclusion of vertical wind [*Draxler and Rolph*, 2003].
The selected sectors are:
A) Southern, coinciding with the African continent, that comprises airmasses that are expected to be dominated by desert dust cases;
B) Western, including the Atlantic Ocean, the Western Mediterranean Basin, the Iberian Peninsula and Western France, that takes into account the airmasses coming more directly from the Atlantic Ocean and probably dominated by marine and/or low continental aerosol loading;
C) Northern, North-Eastern sector, including the Central and Eastern Europe, probably strongly influenced by anthropogenic aerosols.
Figure 4.4.2 presents the backtrajectories calculated for SZA=60° on 2002 and 2003.
By the combination of the τ-α and the trajectory analysis, two main aerosol types have been identified: the biomass burning-urban/industrial aerosol (BU), characterized by $\alpha \geq 1.5$ and $\tau \geq 0.15$, and the desert dust (DD) cases, described by $\alpha \leq 0.5$ and $\tau \geq 0.1$.

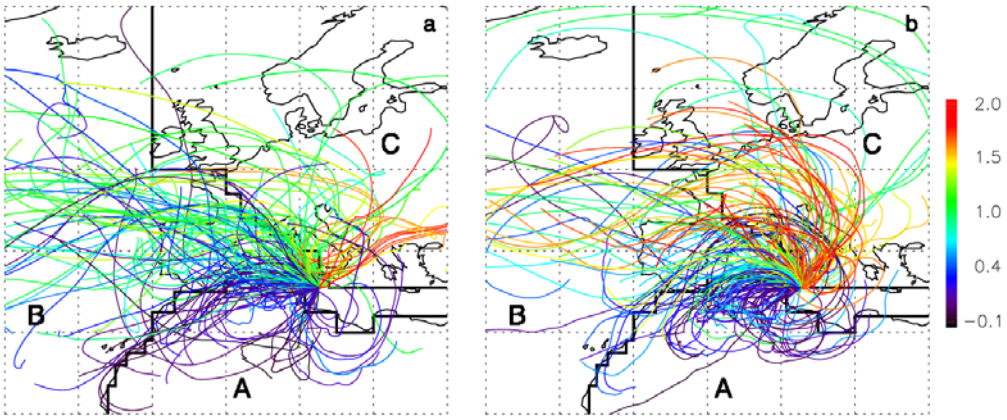

Figure 4.4.2. Five-day trajectories ending at Lampedusa at 2000 m, in a) 2002, and b) 2003. The colour of the trajectories refers to the corresponding value of α measured at Lampedusa. Two trajectories per day, corresponding to a SZA of 60°, are displayed. Three sectors, A, B, and C, that correspond to different source regions, are identified [*Pace et al.*, 2004].

4.4.2. METHODOLOGY

The ratio of the diffuse to the direct component (DDR) of the irradiance is reasonably accurate [*Halthore et al.*, 2004] and is the most appropriate quantity to be compared with RT simulations, because it is independent on calibration constants and in particular on the extraterrestrial solar spectrum, which has to be assumed in the model. Although the extraterrestrial solar spectrum in the UV-visible-near IR have been accurately measured, some discrepancies exist [e.g. *Drummond and Thekaekara*, 1973; *Kurucz*, 1992].

Herman et al. [1975] first introduced the DDR method to determine the imaginary part of the refractive index for desert dust, comparing the measured and the calculated DDR. This method is based on the sensitivity of the diffuse radiation to absorption by dust (and on the weak dependence on the real part of the refractive index), and allows a unique solution once the ground albedo is known. When the albedo is not known, a solution is still possible, but the uncertainties due to potential errors increase. A similar approach has been adopted by *Petters et al.* [2003] to derive the ω_0 in the UV wavelengths for cloud-free summer days in the South-Eastern United States; they simulated the DDR measured at the seven operational wavelengths of the ultraviolet MFRSR (UVMFR-SR) by means of a radiative transfer model, varying the ω_0 values until the model output matched the measurements.

In this study the method by *Herman et al.* [1975] is applied to derive ω_0 at the two MFRSR channels centred at 415.6 nm and 868.7 nm. The diffuse and direct irradiance are calculated using the RT model UVSPEC, assuming a plane-parallel atmosphere with standard vertical profiles of temperature, pressure and ozone for mid-latitudes.

The DDR is a function of the SZA, thus one SZA was chosen for the analysis. The smallest SZA reached at Lampedusa during a year varies between 12° in June and 59° in December, so irradiances are simulated at 60° SZA to span the entire year of measurements. The comparison of the measurements with the model calculations are performed for both morning and afternoon SZA.

The model inputs are those described in paragraph 3.3, with standard vertical profiles of ozone and aerosol [*Shettle*, 1989]. Aerosols in the model are specified giving the wavelength-dependent optical depth, asymmetry factor and single scattering albedo at each layer. It is

also assumed that the single scattering albedo and the asymmetry factor do not vary with altitude.
The asymmetry factor *g* at 415.6 nm and 868.7 nm has been assumed from *d'Almeida et al.* [1991]. For the BU aerosol *g* values are 0.65 at 415.6 nm and 0.60 at 868.7 nm, obtained from the size distribution of urban/industrial aerosol type, composed by water-soluble, soot and dust-like particles. For the DD the background desert aerosol by *d'Almeida et al.* [1991] has been adopted: through Mie calculations we estimated *g* to be 0.84 at 415.6 nm and 0.73 at 868.7 nm.
The radiative transfer model is run to compute look-up tables for the two aerosol types, expressing DDR as a function of the AOD and ω_0 at 415.6 and 868.7 nm: variations of the AOD from 0 to 1.2 at 0.2 steps and ω_0 values from 0.7 to 1.0 at 0.06 steps are assumed. The DDRs are calculated at the central wavelengths of the MFRSR bands, so that no assumptions have to be made either on the aerosol optical properties in other spectral intervals, nor on the instrumental filtering function. The comparison of the measurements with the model results at 60° SZA is performed averaging the instantaneous MFRSR measurements in cloud-free conditions in a SZA interval centred at 60°. The total number of cases is 168. Since the acquisition rate has changed with time, from 10 minutes to 1 minute, and in order to have a sufficient number of values to average, we have chosen SZA intervals of (60±2.5)°. Due to the different acquisition rates and to the SZA values within the chosen interval, it was necessary to apply a correction factor to those measurements performed at SZAs other than 60°. The correction factor was calculated as the ratio DDR(SZA)/DDR(60°) by means of the radiative transfer model, with the aim of accounting for the changes of DDR with SZA. Model simulations showed that the correction factor does not significantly depends on the aerosol type, but on the AOD; for example, for AOD values of 0.2 the ratio DDR(62°)/DDR(60°) is 1.09 at 415.6 nm and 1.06 at 868.7 nm, while for AOD values of 1 the ratio DDR(62°)/DDR(60°) is 1.17 at 415.6 nm and 1.13 at 868.7 nm.

A graphical representation of the look-up table for the DD at 415.6 nm is shown in Figure 4.4.3. It can be noticed that for low AODs the DDR does not show a dependence on ω_0: on the contrary, medium to high AOD changes of ω_0 produce larger DDR variations. For example, for AOD at 415.6 nm equal to 0.6 a change of ω_0 from 0.76 to 0.94 determines a 37% increase in DDR.

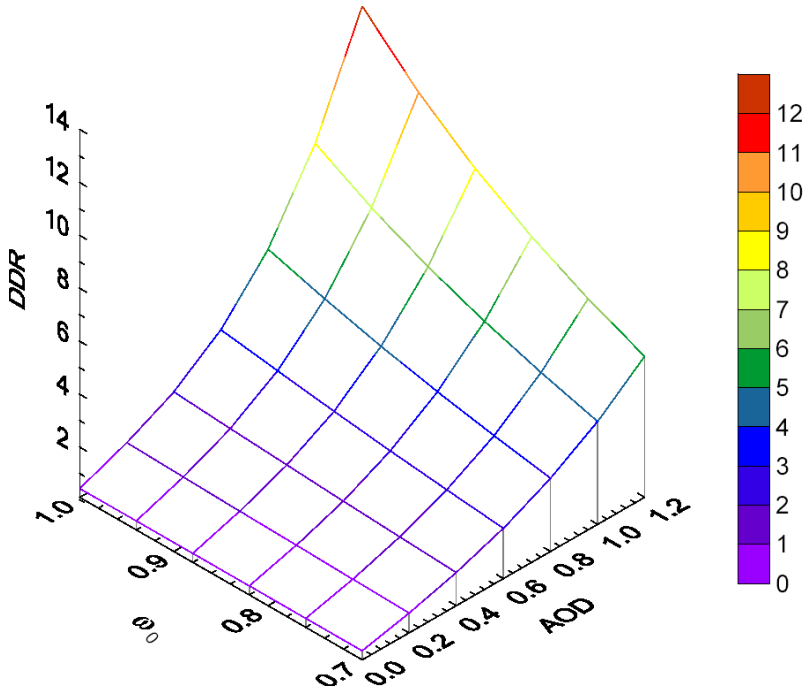

Figure 4.4.3. Surface plot of the DDR at 415.6 nm as a function of AOD and ω_0 at 60° SZA. This case refer to the desert dust.

For each measurement of DDR and AOD an inversion procedure allows the retrieval of ω_0. This procedure consists in the fitting of the DDR surface with a third order polynomial in the AOD and ω_0 variables (the maximum order in AOD and ω_0 is three, while the maximum total order is six due to mixed terms in AOD and ω_0); once the coefficients are determined, fixing the AOD reduces the problem to the solution of a third order polynomial in ω_0, a monotone function in the interval (0.70, 1.00), for which the number of real zeros in the interval is one or null.
The sensitivity of the retrieved ω_0 to the AOD, DDR, *g* and surface albedo will be examined at the end of paragraph 4.4.3.

4.4.3. RESULTS AND DISCUSSION

Table 4.4.1 illustrates the average ω_0 retrieved for the two aerosol types over the entire period of MFRSR data. The spectral behaviour of ω_0 is clear for the desert dust, with a decrease at the shorter wavelengths while, due to the large standard deviations of the results for the biomass burning-urban/industrial aerosol cases, no significant spectral behaviour is discernable.

Table 4.4.1. Average and standard deviation of the single scattering albedo, ω_0, at 415.6 nm and 868.7 nm for the two aerosol types: BU refers to the biomass burning-urban/industrial aerosol and DD to the desert dust. The averages are calculated over all the cases at 60° SZA found in the period July 2001-September 2003.

Aerosol type	ω_0 (415.6 nm)	ω_0 (868.7 nm)
BU	0.87±0.08	0.82±0.07
DD	0.81±0.05	0.94±0.05

Situations of Saharan dust outbreaks at Lampedusa are frequent in spring and summer [*di Sarra et al.*, 2001b] and characterized by high values of the AOD: among the 94 analysed cases, the average AOD at 415.6 nm is 0.404, with a maximum value of 1.159. These episodes are clearly detectable also by the backtrajectory analysis [*Pace et al.*, 2004], and it can be assumed that dust is the prevalent aerosol component carried by the air masses from the Saharan desert, thus determining the optical properties of the aerosol: this reasons may explain the lowest standard deviations in Table 4.4.1 with respect to the other cases. Nevertheless, episodes of continental air mass (74 cases) are almost as common at Lampedusa as those of Saharan dust, with an average AOD at 415.6 nm of 0.339. Moreover, air masses from Europe may carry different aerosol types, for example polluted and continental aerosols with varying mixing ratios, mixed with particles from biomass burning, particularly in summer; thus assuming pure continental aerosol properties could result in a wide range of values for the retrieved ω_0.

The large uncertainties associated with the ω_0 for the biomass burning-urban/industrial aerosols suggest that the absorption properties of the aerosol particles for these cases may significantly vary. The DDR at 415.6 nm for the all the biomass burning-urban/industrial aerosol cases have been examined as a function of the AOD (see Figure 4.4.4). Two classes of data can be clearly identified: for class *b* the DDR values are lower than those for class *a* for the same AOD (23% reduction of DDR for AOD of 0.4), meaning that the aerosol particles in class *b* absorb more radiation than those in class *a*. Another relevant point that can be highlighted is that the AOD values for class *a* do not exceed 0.4, while for class *b* the AOD reaches values of about 0.8.

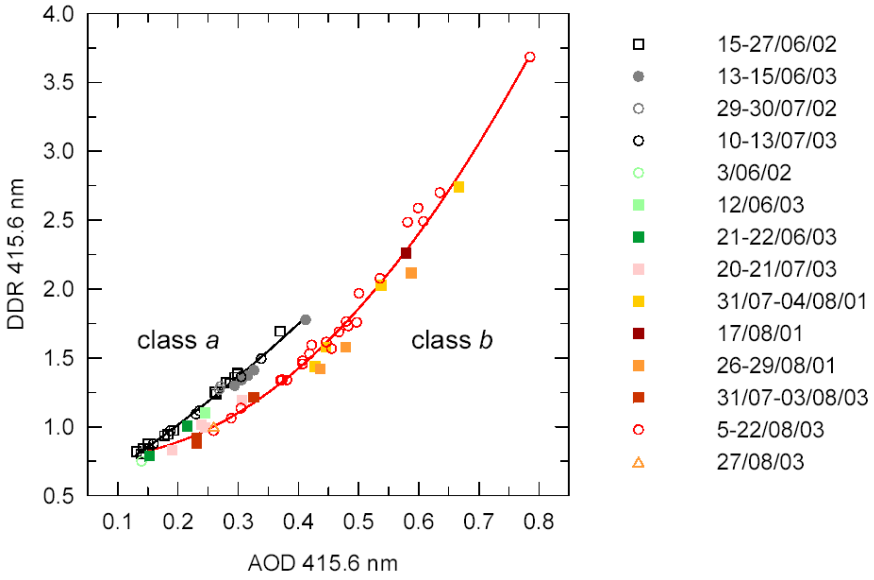

Figure 4.4.4. DDR as a function of the AOD measured by the MFRSR at 415.6 nm, 60° SZA, for the episodes of biomass burning-urban/industrial aerosols divided in two classes. The second order polynomial fit is also shown.

In order to explain the differences in the optical properties of the aerosols characterizing classes *a* and *b*, the airmass trajectories ending at Lampedusa in a time period of five consecutive days belonging to each class were examined. The model used to calculate the airmass backtrajectories is the HYSPLIT Dispersion Model [*Draxler and Rolph*, 2003], which uses vertical velocity fields. Days with AOD at 415.6 nm lower than 0.25 where disregarded, since for these cases the two classes are not clearly distinguishable. The trajectory analysis is carried on in conjunction with the detection of fires from the ESA World Fire Atlas (http://dup.esrin.esa.int/ionia/wfa/index.asp), which locates fires worldwide based on the retrieval from the Along Track Scanning Radiometer (ATSR-2 until 2002 and AATSR from 2003). The aim of this analysis is to verify if biomass burning aerosols may have affected the aerosol load of airmasses arriving at Lampedusa and coming from North.
Two periods representative for class *a* are from 24 to 27 June 2002 (hereafter referred to as case a1) and from 13 to 16 June 2003 (case a2). Fig. 4.4.5 presents the 5-days trajectories at 750 and 2000 m for the two periods and the corresponding maps of the active fires detected from ATSR; the fires present 5 days before the airmass arrives at Lampedusa on all the days of each period are considered, thus from 19 to 26 June 2002 for case a1 and from 8 to 15 June 2003 for case a2. In period a1 the airmasses pass over Sardinia or arrive from the Balkan region passing over Southern Italy and Sicily in days when fires are not detected. In period a2 trajectories at 750 and 2000 m travel from the Balkan region through Southern Italy and Sicily, where a small number of fires is active. The continental airmasses during the days under consideration, and for the entire class *a*, may have been only slightly affected by biomass burning aerosols, thus we can conclude that their optical characteristics are prevailing of urban/industrial type.

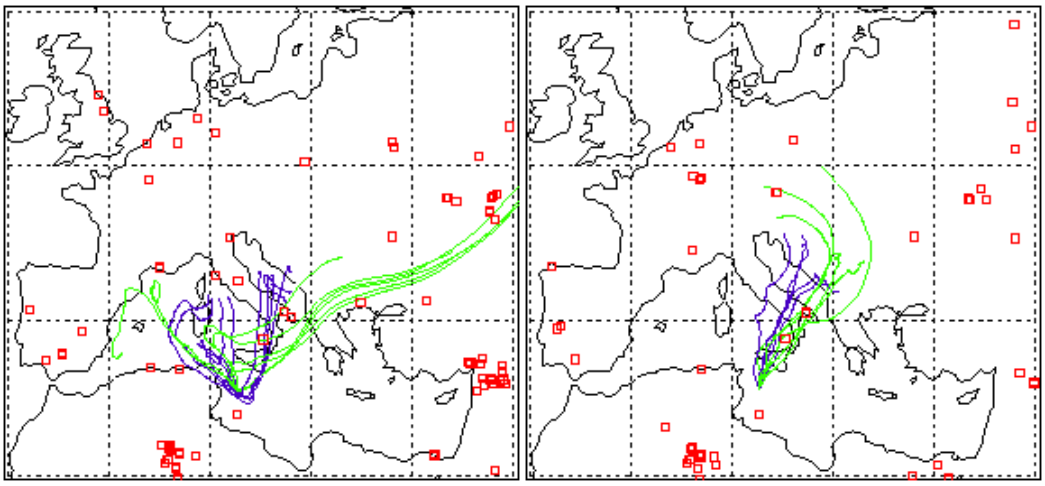

Figure 4.4.5. Backtrajectories at 750 m (blue curve) and 2000 m (green curve) for the cases a1 (24 to 27 June 2002, left panel) and a2 (13 to 16 June 2003, right panel). The fires location from the ESA World Fire Atlas for the two periods are shown: the fires are represented by the red open squares.

A quite different situation was observed for the periods belonging to class *b*. The map of fires in Figure 4.4.6 evidences a large number of active fires in the Balkans, Southern Italy, Sicily and the costs of Northern Africa from 31 July to 4 August 2001 (case b1): the difference with respect to the maps for cases a1 and a2 is striking. During the days of case b1 the airmasses from Eastern Europe pass over Southern Italy and Sicily and are presumably loaded with biomass burning aerosols produced by fires.

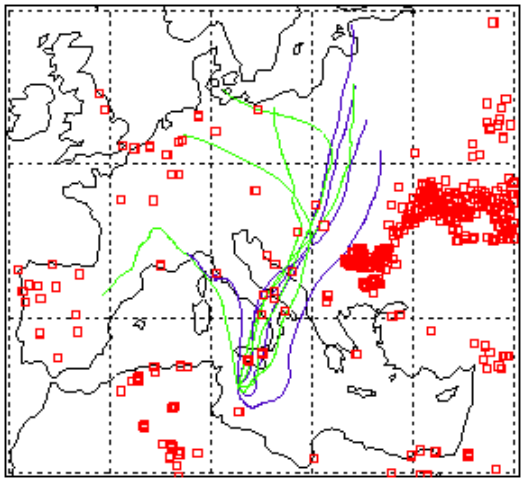

Figure 4.4.6. Backtrajectories at 750 m (blue curve) and 2000 m (green curve) and 2000 m for the cases b1 (31 July to 4 August 2001). The fires location from the ESA World Fire Atlas for the two periods are shown: the fires are represented by the red open squares.

The case of August 2003, discussed by *Pace et al.* [2004], is particularly interesting: this period is characterized by intense fires that loaded the airmasses with high AOD values, also due to the persistently stable meteorological conditions over the Mediterranean. The larger

content of absorbing aerosols (black carbon) during the days belonging to class *b* may explain the lower values of the DDR with respect to the days of class *a* for the same AOD.
ω_0 has been calculated for class *a* and *b* separately, employing the optical properties of urban/industrial (UN) and biomass burning (BB) aerosols, respectively. For biomass burning aerosol the asymmetry factor is obtained averaging the results (at the wavelengths of 440 and 870 nm) of different studies on the optical properties of smoke aerosols from Amazonia and Africa [*Procopio et al.*, 2003]: *g* values are 0.63 at 415.6 nm and 0.53 at 868.7 nm. The results in Table 4.4.2 show that the mean ω_0 are larger for class *a* than for class *b*, and that the uncertainties are reduced compared to those in Table 4.4.1, especially for class *b*.

Table 4.4.2. Average and standard deviation of ω_0 for the urban/industrial (class *a*) and biomass burning cases (class *b*). The number of corresponding data is also shown.

Class	N	ω_0 (415.6 nm)	ω_0 (868.7 nm)
a	30	0.96±0.02	0.87±0.07
b	44	0.82±0.04	0.80±0.05

Figure 4.4.4 depicts all the cases with $\alpha \geq 1.5$, which are characterized by the same colour when occurring on consecutive days. It is worth noting that these cases were detected in summer, when stable atmospheric conditions and transport of airmasses from Europe to Africa led to episodes of polluted aerosols and biomass burning at Lampedusa [*Duncan and Bey*, 2004]. As can be seen, the cases belonging to class *a* (black and grey symbols) occur in June and July; the episode of UN aerosols from 15 to 27 June 2002 is remarkable for its duration and because AOD at 415.6 nm spanned values from about 0.15 to 0.4. Episodes of BB aerosols are found in July and August: however, the largest AOD and duration are observed in August, generally the driest month of the year, when the development of fires is favoured. The long time period of BB observed at Lampedusa from 5 to 22 August 2003 is notable for the values of the AOD at 415.6 nm, which ranged from about 0.25 to 0.8.

Figure 4.4.7 shows the frequency of occurrence of the retrieved ω_0 at 415.6 and 868.7 nm for the three aerosol types. The most important feature emerging from the analysis of the graphs is the different wavelength dependence of ω_0 for the DD, UN, and BB aerosols, as expected from the results reported in Tables 4.4.1 and 4.4.2. The increase of ω_0 with the wavelength for the DD and the opposite behaviour for the UN aerosol is evident, while no net wavelength-dependence of ω_0 for the BB aerosol can be detected.

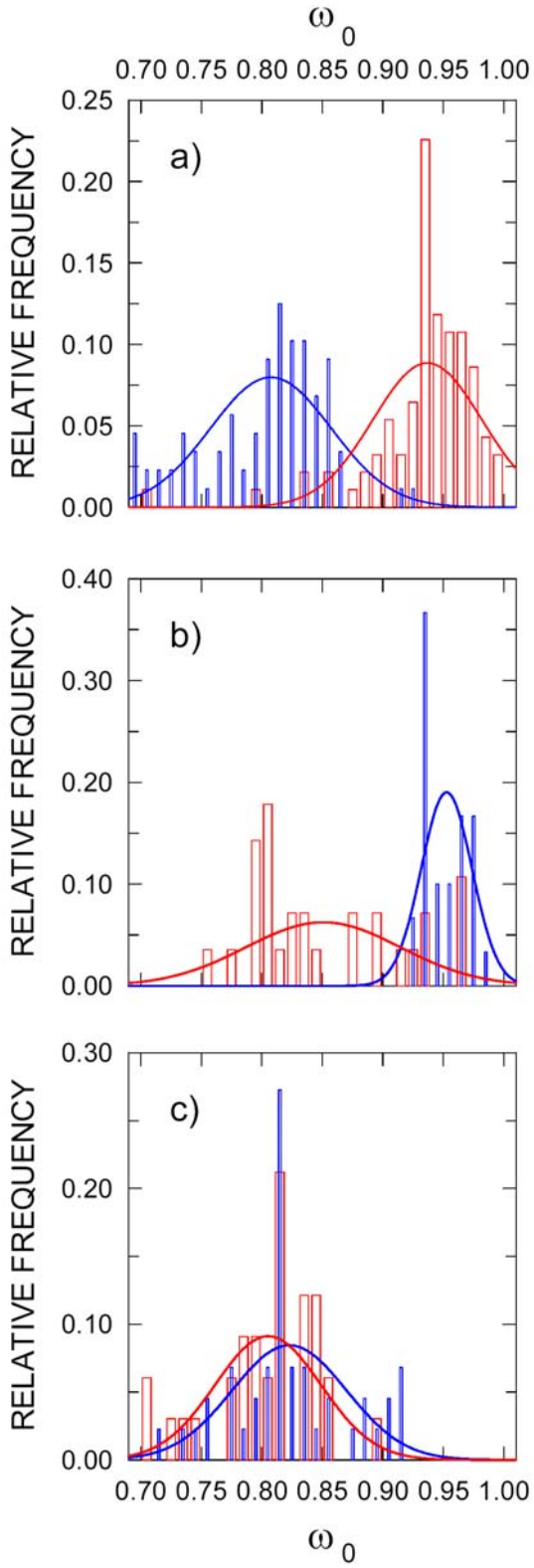

Figure 4.4.7. Relative frequency of occurrence of the retrieved ω_0 at 415.6 nm (blue bars) and 868.7 nm (red bars) for a) desert dust, b) urban/industrial, and c) biomass burning. The Gaussian fits for the two wavelengths are also shown with a solid and a dashed line, respectively.

The ω_0 values obtained through the look-up tables have been compared to the values published in literature. The Mie calculations based on the size distribution and refractive index for the desert background aerosol from *d'Almeida et al.* [1991] give the ω_0 at 415.6 nm of 0.80 and at 868.7 nm 0.98, values within our results. *Sokolik and Toon* [1996] present the spectral dependence of ω_0 from various dust models: a wide range of values reflects the discrepancies in adopted size distributions and refractive indices. ω_0 around 400 nm and 900 nm are in the ranges 0.62-0.95 and 0.70-0.95, respectively. *Moulin et al.* [2001] determined the dust absorption in the visible-NIR from SeaWiFS images and estimated ω_0 for different aerosol size distributions, refractive index and dust vertical distributions; the 18 possible combinations gave ω_0 values in the blue in the range 0.82-0.90 and 0.92-0.99 around 870 nm. *Tanré et al.* [2001] derived ω_0 from the AERONET measurements performed at Sal Island and the Banizoumbou sites, finding values of 0.94±0.05 and 0.95±0.03 at 441 nm and 0.96±0.04 and 0.97±0.02 at 870 nm, respectively; their results show a lower absorption than that found by *Kaufman et al.* [2001] in the coast of Senegal from Landsat TM observations, which gave 0.88 in the blue and 0.98 at wavelengths larger than 670 nm. *Dubovik et al.* [2002] present optical properties of desert dust obtained from measurements at AERONET sites worldwide: ω_0 at 440 nm and 870 nm are 0.92 and 0.96 (±0.03) in the Persian Gulf, 0.92 and 0.97 (±0.02) in the Saudi Arabia, 0.93 and 0.99 (±0.01) at Cape Verde, and 0.98 and 0.97 (±0.03) at Lanai. *Cattrall et al.* [2003] show that the absorption by desert dust obtained by means of remote sensing techniques results in larger ω_0 values with respect to the estimations of dust models constructed on the base of laboratory measurements, which range from 0.6 to 0.74 around 400 nm and from 0.92 to 0.98 around 870 nm: at the Dry Tortugas site ω_0 at 412 nm and 865 nm is 0.89 and 1.00 (±0.02), respectively. Our results are in agreement, within the estimated uncertainty, with most of the above cited studies at 868.7 nm, while the absorption at 415.6 nm is generally larger.

The optical parameters for urban/industrial and mixed aerosol reported in *Dubovik et al.* [2002] show values at 440 nm and 870 nm of 0.94 and 0.96 (±0.02) at Greenbelt (MD), of 0.94 and 0.92 (±0.03) in Paris, 0.90 and 0.85 (±0.02) at Mexico City, and 0.91 and 0.86 (±0.03) at the Maldives. The ω_0 values derived with Mie calculation from the size distribution and the refractive index in *d'Almeida et al.* [1991] are 0.97 at 415.6 nm and 0.93 at 868.7 nm.
The ω_0 for two sites, Almería (Spain) and Vienna (Austria), influenced by continental/polluted aerosols, have been evaluated by *Horvath et al.* [2002]: both sites experience different aerosol loadings. The ω_0 at 440 nm changes between 0.86 and 0.92 at Almería and between 0.84 and 0.92 at Vienna, depending on the aerosol amount and absorption characteristics. *Horvath et al.* [2002] also report ω_0 at 440 nm for central and southern Europe to vary between 0.8 and 0.9.
During the Indian Ocean Experiment (INDOEX) the columnar ω_0 at 440 nm was derived at a coastal site of India by means of active and passive remote sensing ground-based, airborne and spaceborne instruments [*Léon et al.*, 2002]: values for polluted aerosols were found in the range 0.88-0.93, with an uncertainty of 0.04.

The ω_0 for biomass burning have been evaluated by *Eck et al.* [2003a] in various sites in Southern Africa during SAFARI 2000: they found values at 440 nm between 0.86 and 0.90 and at 870 nm between 0.80 and 0.85. The ω_0 regional variability is due to the aging of the aerosol cloud, which leads to modification and contamination of the plume by different aerosol sources. *Eck et al.* [2003b] present ω_0 derived in 4 locations interested by high AOD

biomass burning episodes (AOD at 440 nm from 2.2 to 2.5): ω_0 at 440 nm ranges between 0.85 and 1.0 and at 870 between 0.78 and 1.0. *Dubovik et al.* [1998] determined ω_0 from AERONET measurements of radiance and irradiance at Cuiabá (Brazil) in the period 1993-1995: the spectral ω_0 values present both an increase and a decrease with wavelength. The optical parameters for biomass burning aerosol reported in *Dubovik et al.* [2002] show values at 440 nm and 870 nm of 0.94 and 0.91 (±0.02) in the Amazonian Forest of Brazil and Bolivia, of 0.91 and 0.87 (±0.03) in the Brazilian cerrado, 0.88 and 0.80 (±0.015) in the African savanna of Zambia, and 0.94 and 0.92 (±0.02) in the Boreal forest of United States and Canada. The average ω_0 values retrieved by *Procopio et al.* [2003] at two AERONET sites in Amazonia are 0.93±0.01 at 440 nm and 0.87±0.02 at 870 nm. *Bergstrom et al.* [2003] found large uncertainties associated to the retrieved ω_0, higher for the case of low AOD: around 450 nm ω_0 was between 0.79 and 0.92 for the day with low AOD and between 0.86 and 0.89 for the high AOD day, while ω_0 around 850 nm was in the range 0.36-0.85 for the low AOD day and in the range 0.80-0.88 for the high AOD day.
The previous studies reveal a wide range of variability for ω_0 of urban/industrial as well as of the biomass burning aerosol; our results are within these ranges at both wavelengths.
In order to assign an uncertainty to the retrieved ω_0, a sensitivity analysis is necessary. The sensitivity of the retrieved ω_0 to the AOD have been tested for the three aerosol types, by adding to the average AOD its standard deviation, without changing the DDR. The results are summarized in Table 4.4.3, where relatively small variations of the averages ω_0 values are shown.

Table 4.4.3. Average and standard deviation of ω_0 at 415.6 nm and 868.7 nm, assuming an increase in the AOD equal to its standard deviation.

Aerosol type	ω_0 (415.6 nm)	ω_0 (868.7 nm)
UN	0.95±0.03	0.85±0.08
BB	0.81±0.04	0.79±0.04
DD	0.80±0.04	0.92±0.05

If the change in ω_0 is expressed as a function of the percent AOD standard deviation (see Figure 4.4.8), more interesting aspects can be highlighted. There is a linear behaviour of the change in ω_0 for all the aerosol types, with a change of about -0.02 at 415.6 and 868.7 nm for a 3% variation in the AOD, and of -0.03/-0.04 for a 5% variation.

The sensitivity of ω_0 to the DDR was tested using the same approach: we estimated the change in ω_0 due to a decrease of the average DDR equal to its standard deviation keeping fixed the AOD at its mean value. As shown in Table 4, the average ω_0 values do not remarkably change; Figure 4.4.9 illustrates how the ω_0 retrieval depends on percent DDR variations: for a 3% increase of DDR, the change in ω_0 is about 0.02 for the DD and UN aerosols at 415.6 nm and 868.7 nm, while is about 0.03-0.04 for a 5% increase of DDR. Data regarding the BB cases are more scattered, but their behaviour on average does not sensibly differ from those of the other aerosol types.

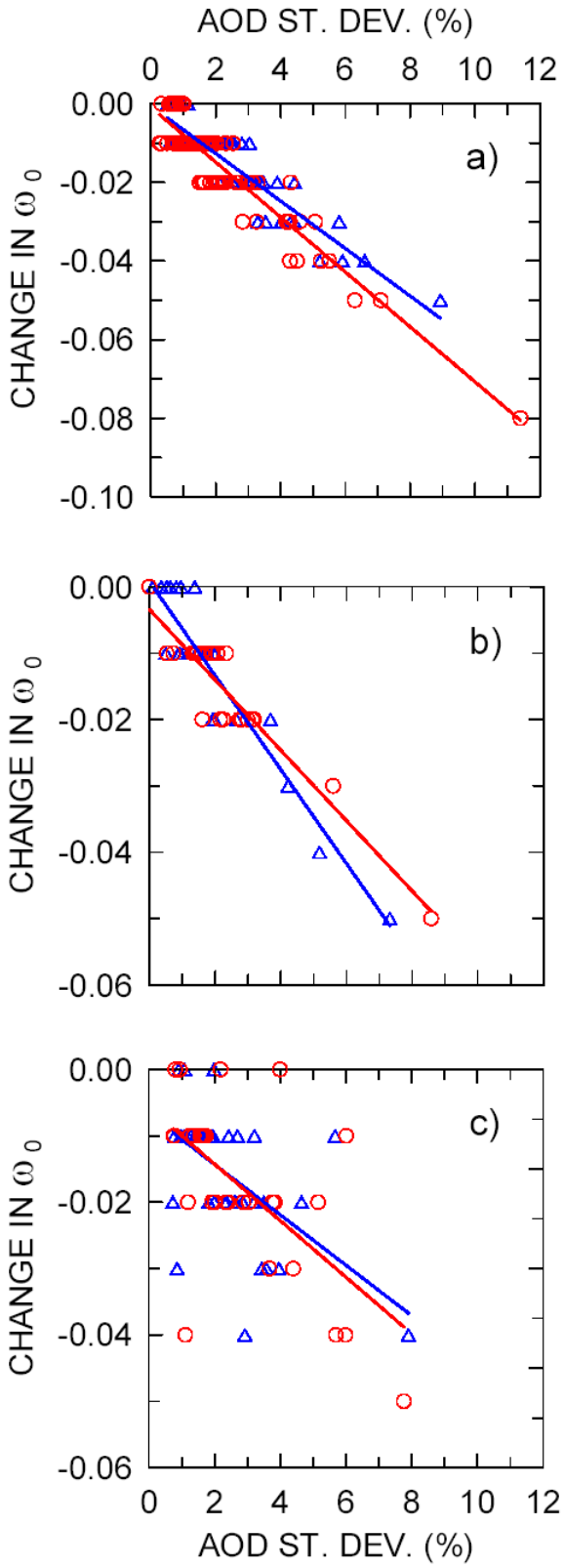

Figure 4.4.8. Change in ω_0 due to a percent increase of AOD for a) desert dust, b) urban/industrial, and c) biomass burning aerosol. Open triangles refer to the 415.6 nm, while open circles to the 868.7 nm wavelength; the regression lines, solid and dashed, respectively, are also shown.

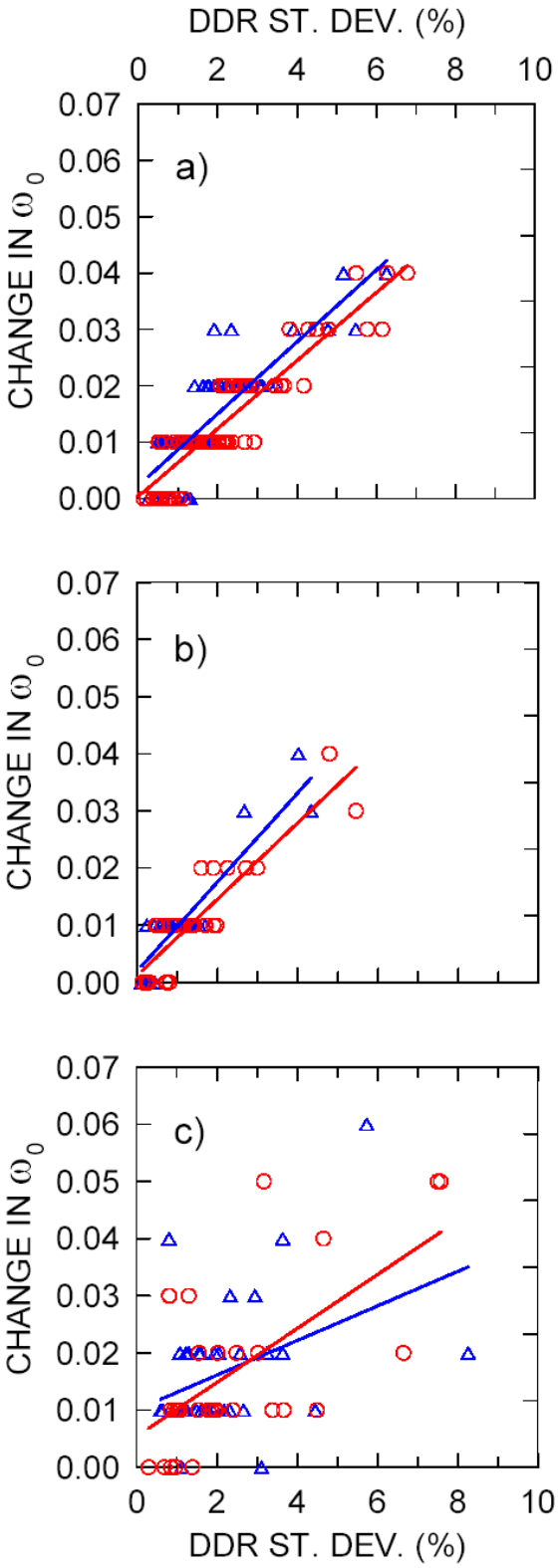

Figure 4.4.9. Change in ω_0 due to a percent increase of DDR for a) desert dust, b) urban/industrial, and c) biomass burning aerosol. Open triangles refer to the 415.6 nm, while open circles to the 868.7 nm wavelength; the regression lines, solid and dashed, respectively, are also shown.

The asymmetry factor *g* assumed as model input was taken from the literature, as previously explained. A variation of ±0.06 in the value of *g* was chosen to test the change in ω_0 due to a change in *g* for the three aerosol types; differences of ±0.06, in fact, can be reasonably considered as the uncertainty in the values of *g* for a particular aerosol type. The average ω_0 values at both wavelengths do not sensibly vary for values of *g* within the interval ±0.06 (see Figure 4.4.10): at 415.6 nm ω_0 changes of 0.03 for the DD (*g* between 0.78 and 0.90), and 0.04 for the UN aerosols (*g* between 0.59 and 0.71) and for the BB (from 0.57 to 0.69), while at 868.7 nm the variations of ω_0 are 0.05 for the DD (*g* between 0.67 and 0.79), 0.06 for the UN aerosols (*g* between 0.54 and 0.66), and 0.04 for the BB (from 0.47 to 0.59).

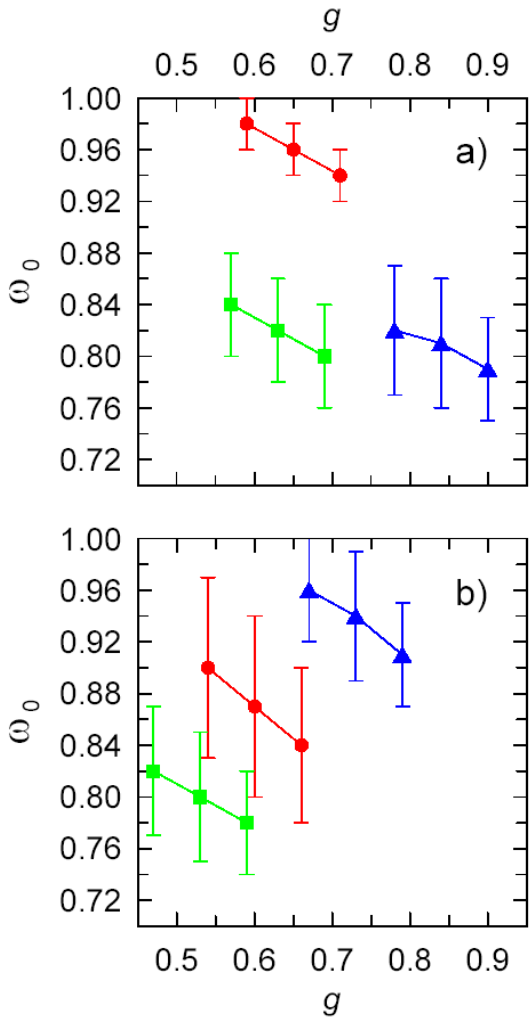

Figure 4.4.10. Average ω_0 obtained for the assumed asymmetry factor *g* and for *g*±0.06 for a) 415.6 nm and b) 868.7 nm. Error bars refer to the standard deviation. Blue triangles represent the desert dust, red circles the urban/industrial and green squares the biomass burning aerosol.

Finally, the sensitivity of the derived ω_0 to the assumed surface albedo was studied, increasing by 0.05 to the values of 0.10 at 415.6 nm and 0.07 at 868.7 nm, corresponding to an increase of 50% and 71%, respectively. Table 4.4.4 shows that ω_0 at 415.6 changes by 0.01 for the

DD and by 0.02 for the UN and BB, while at 868.7 nm ω_0 variations correspond to 0.01 for all the aerosol types.

Table 4.4.4. Average and standard deviation of ω_0 at 415.6 nm and 868.7 nm, assuming an increase in the surface albedo of 0.05.

Aerosol type	ω_0 (415.6 nm)	ω_0 (868.7 nm)
UN	0.94±0.02	0.86±0.07
BB	0.84±0.05	0.79±0.05
DD	0.80±0.04	0.93±0.04

This analysis evidences that the uncertainty on the albedo does not produce a large variation on the ω_0 values.

4.5. CONCLUSIONS

The aim of the studies presented in this chapter is to determine the optical properties of the aerosol reaching the island of Lampedusa from different origin.
In the first study (paragraph 4.2) the influence of tropospheric aerosols and ozone on the UV radiation through the application of the RT model initialised with a large set of observations was investigated, allowing for a detailed characterization of the atmospheric properties. The model was applied to three clear sky days during the PAUR II campaign with different aerosol loadings and ozone amounts, when as much and as accurate as possible information on the atmospheric structure was available at the island of Lampedusa. In one of the three days, May 18, 1999, desert dust was transported to Lampedusa, and particles up to 7 km were detected by lidar. In the two other cases, May 25 and 27, airmasses originated from Europe and the North Atlantic, and a much lower aerosol optical depth was measured; aerosol particles were mostly confined to the lowest tropospheric region.
The comparison of measured and calculated UV spectra allows to identify a range of values for the imaginary part of the aerosol refractive index. For May 25 and 27 a wide range of values for n'' was derived: in these cases, mostly because of the relatively low values of the aerosol optical depth (and, consequently, of the small radiative effects), the simulated irradiance did not strongly depend on the imaginary part of the aerosol index of refraction. On May 25 the values of n'' range from -0.012 to -0.16, and are centred around -0.052 (real part $n' = 1.366$); on May 27 the derived values were in the range -0.0045 ÷ -0.044, centred at -0.017 ($n' = 1.402$). Simulated spectra show a strong dependence on n'' on May 18: values between -0.0031 and -0.0068 were found, the best agreement with the Brewer spectral irradiance occurring for $n'' = -0.0044$ (with $n' = 1.536$). Single scattering albedo and asymmetry factor were calculated by means of the Mie theory. For the interesting case of dust outbreak on May 18 the obtained values of ω_0, between 0.73 and 0.84, and g, in the range 0.75-0.79, are in good agreement with previously published results, and with those obtained by *Di Iorio et al.* [2003] from the combination of lidar, particle counters, and sun-photometer measurements on the same day.
The optical properties of aerosol derived from standard size distribution and refractive indices do not adequately describe the atmospheric transmission, especially in the day characterized by the strong dust outbreak (May 18). As an example, if the size distribution for the desert dust in summertime and the mineral refractive index from *d'Almeida et al.* [1991] were used

to derive the aerosol absorption and scattering properties, the UV surface irradiance varies by ~10%.
The use of actual, rather than climatological ozone profiles, is required to obtain accurate results, especially for high tropospheric ozone content and small solar zenith angles. When the climatological profile was used, the measured and modelled spectra differed by more than 9% at wavelengths shorter than 296 nm on May 25 and 27. The effect was smaller in the case of May 18, characterized by a lower tropospheric ozone amount than on May 25 and 27 (with a smaller difference with respect to the climatology), and by a larger solar zenith angle. The role of tropospheric ozone was studied for different aerosol optical depths and absorption properties. For aerosol optical depths from low to moderate the effect of the aerosol is negligible or small, while for high optical depths a dependence on the aerosol characteristics was found: non-absorbing aerosols produce an increased scattering in the troposphere, and an enhanced absorption by ozone; absorbing aerosols reduce the diffuse irradiance in the troposphere, thus decreasing the effectiveness of UV absorption by tropospheric ozone.

In the second study (paragraph 4.3) visible and ultraviolet irradiances measured at ground, and reflectances measured from space during transport of desert dust over the Mediterranean are reconstructed and analysed with a radiative transfer model. Ground-based measurements, that include aerosol backscattering and depolarisation profiles by lidar, were performed at the island of Lampedusa in two days of July 2002, simultaneously to the observations by the MISR instrument aboard the Terra spacecraft. The backward trajectories of July 14 indicate that the airmass spent a few days over the central Sahara before arriving at Lampedusa, while on July 16 the airmass originated from North Atlantic and ended at Lampedusa after passing over the northern margin of Algeria and Tunisia. The Ångström parameter and the aerosol depolarisation reveal the presence of large particles of irregular shape on both days; the Ångström parameter is lower, and the depolarisation higher on July 14, suggesting a strong impact of the passage over central Sahara. Differences in the aerosol vertical distribution are also observed, with most of the dust located between 2 and 6 km on July 14, and between 1 and 5 km on July 16.
The RT model was applied to reproduce the spectral radiation measurements both at ground and from space, with the aim of deriving information about the aerosol properties.
The wavelength-independent ω_0 and g in the visible which reproduce the irradiance measurements at ground and the reflectance observations from the satellite have been estimated: ω_0 ranges between 0.96 and 0.97 on July 14 and between 0.88 and 0.89 on July 16; g varies in the range 0.79-0.82 for both days. On July 16 ω_0 is smaller than on July 14: this may reflect a different chemical composition of the particles in the two days, with the aerosol on July 16 containing a larger amount of absorbing substances. This result show that dust optical properties may be significantly different, possibly depending on the characteristics of the source region.
The MISR equivalent reflectances measured at nine viewing angles on the two days have been simulated by the model, using the aerosol optical parameters, α and β and the best match ω_0 and g (ω_0 = 0.96 and g = 0.80 for July 14 and ω_0 = 0.88 and g = 0.81 for July 16), previously obtained. Since no information about the aerosol phase functions is available, the Henyey-Greenstein function is used in the model. The equivalent reflectances in the blue band are well reproduced on both days, while in the green and red bands the model overestimates the reflectance at the viewing angles closest to the nadir, and underestimates the measurements at the steeper viewing angles, where the signal is more effectively affected by the presence of aerosols.

The observed optical depth shows a sudden increase in the ultraviolet spectral range. The Ångström exponent calculated using the optical depth at 317.6 nm is significantly larger (around 2.3) than the one obtained in the visible. Values of ω_0 lower than in the visible, down to 0.78, are needed to reproduce with the model the observed UV spectral irradiances measured by the Brewer spectrometer on July 14.
Two different phase functions were used to study their influence on the equivalent reflectances pattern. The phase functions were derived from an assumed size distribution matching the observed optical depths at different wavelengths, for spherical and non-spherical particles. The influence of non-spherical particles is largest when scattering angles in the 150-180° range are sounded by MISR (July 16). Our results show that the shape of the phase function play a significant role when trying to retrieve the aerosol radiative impact from a single radiance measurement.

In the third study (paragraph 4.4) the single scattering albedo (ω_0) for three major aerosol types observed to occur at Lampedusa has been estimated using the measurements of direct and diffuse irradiance performed at 60° SZA by a multi-filter rotating shadowband radiometer (MFRSR) at 415.6 nm and 868.7 nm from July 2001 to September 2003: these aerosol types are urban/industrial (UN) and biomass burning (BB) aerosols from the European continent, and desert dust (DD) from the Saharan region. The aerosol classification is based on AOD, Ångström parameter and airmass trajectory analysis presented in the paper by *Pace et al.* [2004].
A detailed radiative transfer model has been applied to reproduce the MFRSR diffuse-to-direct ratio (DDR), using the measured AOD as model input. The DDR is the most appropriate quantity to be compared with radiative transfer simulations, because it is independent of calibration constants and in particular of the extraterrestrial solar spectrum, which has to be assumed in the model, introducing additional uncertainties. ω_0 has been retrieved as the value giving the best match between measurements and model results. The results show that the average ω_0 of the desert dust increases with λ, as expected, from 0.81±0.05 at 415.6 nm to 0.94±0.05 at 868.7 nm; on the contrary, ω_0 of the biomass burning-urban/industrial aerosol (BU) presents a large standard deviation and a weak wavelength-dependence.
The cases of BU aerosols present two distinct absorption capacities for a fixed AOD: the analysis performed by means of airmass backtrajectories ending at Lampedusa permitted to discriminate the cases with prevailing optical characteristics of urban/industrial type (higher ω_0 at both wavelengths) and cases of biomass burning (lower ω_0).
The average ω_0 of the urban/industrial aerosols reproduces the spectral behaviour reported in the literature, decreasing from 0.96±0.02 at 415.6 nm to 0.87±0.07 at 868.7 nm; for the biomass burning ω_0 does not present a wavelength-dependence, being 0.82±0.04 at 415.6 nm and 0.80±0.05 at 868.7 nm.
The aerosols originating from Europe, UN and BB, are mainly detected at Lampedusa during the cloud-free days of summer, when stable atmospheric conditions and transport of airmasses from Europe to Africa occur. The episodes of UN aerosols are found in June and July, while those of BB with the largest AOD and duration are observed in August, generally the driest month of the year, when the development of fires is favoured.
Sensitivity studies were performed in order to check how the uncertainties of the measured AOD and DDR, and of the assumed asymmetry factor *g* and surface albedo could influence the retrieved ω_0. The results show that a 3% variation in the AOD or DDR gave a change in ω_0 of about 0.02 at 415.6 and 868.7 nm. The average ω_0 values at both wavelengths do not sensibly vary for values of *g* within the interval *g*±0.06: the variations at 415.6 nm are 0.03-

0.04 and 0.04-0.06 at 868.7 nm. The influence of the surface albedo has been tested increasing the assumed values of 0.10 and 0.07 at 415.6 nm and at 868.7 nm by 0.05: the result is that ω_0 changes are between 0.01 and 0.02.
The principal feature emerging from the previous analyses evidence how the knowledge of the aerosol optical properties is a complex problem, not only for the variability of the aerosol types, but also because cases of occurrence of the same aerosol type present a high variability in particles amount, dimensions and composition, reflected in their properties.
Estimates of the local direct aerosol radiative forcing were obtained both at ground level and at the TOA. On the days considered in paragraphs 4.2 and 4.3 (on May 1999 and July 2002), aerosols produce a reduction of the downward radiative flux at the surface. The forcing efficiency at the surface is largest for aerosol of continental/marine origin, transported from North. However, largest values of the aerosol optical depth are usually found in Saharan dust events, and the resulting surface forcing is largest.
The forcing at the top of the atmosphere is negative, thus producing a cooling, in the desert dust case, and close to zero or positive for aerosol originating from North.
In most of the previous studies on the aerosol RF worldwide, the RF is estimated over the shortwave, SW, spectral region, and a direct comparison with these results is not possible. In a few cases, estimates over the 400-700 nm are available. The estimate of RF requires the knowledge of a large series of parameters. These estimates are generally carried out during intensive measurement campaigns, often also using satellite observations and radiative transfer calculations.
Fouquart et al. [1987] during the Etude de la Couche Limite Atmospherique Tropicale Seche (ECLATS) experiment carried out in the 1980 dry season near Niamey (Niger), calculated the SW downward flux at the surface for clear sky by means of radiative transfer modelling. They estimated a dust RF larger than 135 W m^{-2} for an aerosol optical depth of 0.93 at 0.55 μm, corresponding to a surface RFE of about 145 W m^{-2}.
Several studies have been performed to estimate the SW RF at the TOA due to Saharan dust. *Ackerman and Chung* [1992] used Earth Radiation Budget Experiment (ERBE) satellite data to study the effects of dust on the radiative SW fluxes at the TOA. They found that in a case of dust outbreak in the Saudi Arabian peninsula during July 1985 the RF ranged between 40 and 90 W m^{-2}. *Hsu et al.* [2000] determined the shortwave monthly average TOA RF due to Saharan dust in the eastern Atlantic; using a combination of TOMS and ERBE data they found that in July 1985 the averaged dust forcing was 40-50 W m^{-2}.
Observations of aerosol radiative forcing were carried out during various phases of the Indian Ocean Experiment (INDOEX) campaign in the Arabian Sea and Indian Ocean (*Jayaraman et al.* [1998]; *Conant* [2000]; *Satheesh and Ramanathan* [2000]; *Rajeev and Ramanathan* [2001]). *Jayaraman et al.* [1998] report estimates of the RF for coastal aerosol of the western India and for the interior Arabian Sea and Indian Ocean, obtained during the pre-INDOEX cruise in January-February 1996. They found that the instantaneous surface RFE in the range 400-700 nm is -209 and -117 W m^{-2} for coastal and ocean data, respectively, at solar zenith angles lower than 60°. *Podgorny et al.* [2000] used a radiative transfer model to calculate the RFE at the surface and at the TOA. *Conant* [2000] has examined the effect of anthropogenic aerosols on SW radiative forcing calculations taking into account aerosol and radiation measurements carried out at the island of Kaashidoo in the first phase of the INDOEX campaign in February-March 1998. *Satheesh and Ramanathan* [2000] and *Rajeev and Ramanathan* [2001] used data from the Kaashidoo Climate Observatory and from the Clouds and Earth's Radiant Energy System (CERES) data of February-March 1998 and January-March 1999 to derive the RFE at the surface and at the TOA.

The Tropospheric Aerosol Radiative Forcing Observational Experiment (TARFOX) took place in 1996 with the aim of reducing the uncertainties in the calculation of the aerosol SW radiative forcing by collecting a great number of observations in the summer haze plume off the eastern coast of the United States. *Hignett et al.* [1999] used TARFOX measurements as input to a radiative transfer model; the aerosol forcings are calculated at the surface level and compared with values deduced from airborne measurements. *Redemann et al.* [2000] used a broadband radiative transfer model to reproduce the vertical pattern of the SW aerosol forcing, retrieving the effective aerosol refractive index from a combination of lidar and sunphotometer observations, and from *in situ* measurements of the particle size distribution.
Recent estimates of the surface and TOA RF based on the TARFOX and INDOEX measurements are reported, together with the results of this chapter, in Table 4.5.1. At the surface, the instantaneous RFE for the PAUR II campaign (note that in Table 4.5.1 the highest value is relative to May 25, and the lowest to May 18) are comparable to those by *Jayaraman et al.* [1998]; the daily averages are however significantly larger than those found by *Podgorny et al.* [2000], and *Conant* [2000]. Assuming that about 40% of the solar energy in the SW can be associated to the 400-700 nm spectral range, these results are also compatible with those obtained by *Hignett et al.* [1999]. The instantaneous RFEs on July 2002 are lower than the other values, due to the low solar zenith angles considered in the calculations.

Table 4.5.1. Instantaneous and daily average aerosol forcing efficiency in W m^{-2} (per unit AOD at 500 nm) at the surface and at the top of the atmosphere (TOA).

Reference	Spectral range	Daily average forcing efficiency	Instantaneous forcing efficiency
	Surface		
Present study: May 1999	400-700 nm	-54.1 ÷ -102.3	-105.5 ÷ -201.5
Present study: July 2002	400-700 nm		-39.3 ÷ -79.0
Jayaraman et al. [1998]	400-700 nm		-117 ÷ -209
Podgorny et al. [2000]	400-700 nm	-44	
Conant [2000]	400-700 nm	-40	
Podgorny et al. [2000]	SW	-82	
Satheesh and Ramanathan [2000]	SW	-70 ÷ -75	
Hignett et al. [1999]	SW	-90 ÷ -160	
Redemann et al. [2000]	SW		-160
	TOA		
Present study: May 1999	400-700 nm	-3.2 ÷ +5.6	-12.0 ÷ +16.5
Present study: July 2002	400-700 nm		-20.1 ÷ -5.1
Podgorny et al. [2000]	400-700 nm	-11	
Podgorny et al. [2000]	SW	-20	
Satheesh and Ramanathan [2000]	SW	-25	
Rajeev and Ramanathan [2001]	SW	-24	
Redemann et al. [2000]	SW		-103

The value of the TOA forcing efficiency derived for the desert dust case is smaller than those found in the other experiments whose results are reported in the table. There are two main reasons for this difference. The first reason is that the single scattering albedo of desert dust at Lampedusa is lower than in TARFOX and INDOEX, and the larger absorption by the aerosol allows a smaller amount of radiation to exit from the atmosphere. The second reason is that the vertical distribution of the desert dust is very different from what generally

expected for tropospheric aerosols (see Figures 3.3.2 and 3.3.3). For example dust particles on May 18 occupied the lower and middle troposphere, extending up to an altitude of 7 km. Moreover, the size distribution of the desert dust includes a significant number of relatively large particles, that produce a strong forward scattering of the radiation. The combination of the peculiar aerosol vertical distribution, and of the presence of large particles, may distinctly affect the distribution of the radiation in the atmosphere. If the particles, as is the case, are in the mid troposphere, where most of the radiation is in the direct beam, the largest fraction of the scattering occurs downwards. Contrarily, when the particles are located in the lower troposphere, where the amount of diffuse radiation is larger, the contribution to the upward scattering may be also large. This effect should be more relevant for low albedo conditions. To verify this effect, the radiative transfer model was run with the dust microphysical and optical properties (i.e. size distribution, refractive index, and optical depth of May 18), but with the vertical distribution of May 25, scaled to the optical depth of May 18. In this case the TOA forcing is about 20% larger than on May 18, indicating that the different vertical distribution plays a role.

CHAPTER 5

INFLUENCE OF AEROSOL AND OZONE VERTICAL DISTRIBUTIONS ON RADIATION LEVELS AND RADIATIVE FORCING

5.1. INTRODUCTION

The influence of the vertical ozone and aerosol distributions on the radiation levels and on the aerosol radiative forcing has been studied by means of RT simulations at the surface and at various altitudes in the atmosphere. Two analyses were devoted to this goal.

1. In the context of PAUR II, UV and visible actinic fluxes and ozone have been measured in the troposphere during aircraft flights performed at Lampedusa on May 18, 25 and 27, 1999. The profiles of actinic fluxes in cloud-free days with desert dust and continental/maritime aerosols were reproduced with the model using both measured and model default ozone and aerosol vertical distributions: the differences with respect to observations have been explained.
2. The RT model has been used to estimate the visible direct radiative forcing due to desert dust at the surface and at the top of the atmosphere using different vertical aerosol profiles measured at Lampedusa (on May 18, 1999 and July 14 and 16, 2002) and model default as input. The discrepancies have been pointed out and discussed, and the impact of the aerosol optical depth and of ω_0 on the computed RF is also examined.

5.2. INFLUENCE OF THE AEROSOL AND OZONE VERTICAL DISTRIBUTIONS ON THE ACTINIC FLUX PROFILES DURING THE PAUR II CAMPAIGN

In this study measurements of vertical profiles of actinic fluxes in the troposphere in the photodissociation bands of O_3 and NO_2 (R1 and R3 in paragraph 1.2.2) are presented. The airborne measurements were carried out in the Mediterranean during the PAUR II campaign in May 1999, with different aerosol conditions and characteristics. The measurements are then compared with results from the UVSPEC RT model, initialised with a large set of observational parameters. In particular, the description of the aerosol properties in the model

is derived from simultaneous measurements. The effect of the aerosol, and of different ozone distributions, on the actinic fluxes is studied on the basis of the measurements and of the model results.

5.2.1. MEASUREMENTS

The experimental set-up of the aircraft was presented in paragraph 2.2. Data were stored during the flight on a data logger every two seconds, producing high resolution vertical profiles of the measured quantities. Altitude is derived from pressure measurements; temperature and relative humidity were simultaneously measured.
The three cases of May 18, 25 and 27 (examined in paragraph 4.2), with different aerosol loading and types, have been considered. May 18 represents a case of dust outbreak: the airmass had spent, according to isentropic trajectories, several days over Sahara before reaching Lampedusa, and the aerosol cloud extends up to 8 km. May 25 and 27 are characterized by airmasses coming from Europe and/or North Atlantic: in these cases the aerosol amount is relatively low, with much of the particles confined below 3 km. The main aerosol components are expected to be anthropogenic, crustal, and marine. The measured aerosol vertical profiles are shown in Figure 3.3.2, together with the extinction profile by *Shettle* [1989] (hereafter indicated as standard profile), both scaled to the observed AOD.
Figure 5.2.1 depicts the climatological ozone profile by *Bhartia et al.* [1985] and the measured profile connected to the climatological one at 10 km altitude.
On May 18 the aircraft flight was performed between 13:25 and 15.15 GMT; the descending part of the flight, started at 14:29 GMT, is used in the analysis. On May 25 the aircraft performed one flight from 13:45 to 14:32 GMT, and data from the ascent, which ended at 14:15 GMT, are used. On May 27 the aircraft flew between 13:24 and 14:46 GMT, and data till 14:11 GMT, corresponding to the ascent, are used.
Table 5.2.1 shows the range of variability for the solar zenith angle (SZA) and the total ozone during the three portions of the flights, and the average (with its standard deviation) AOD at 415.6 nm.

Table 5.2.1. Solar zenith angle (SZA), total ozone, aerosol optical depth (AOD) at 415.6 nm and wavelength-independent aerosol refractive index used in the model simulations for May 18, 25 and 27.

Day	SZA	Ozone (DU)	AOD (415.6 nm)	Refractive index
May 18	47.2-55.1°	291.2-296.6	0.507±0.042	1.536-0.0044*i*
May 25	39.5-43.7°	354.5-356.3	0.162±0.012	1.366-0.052*i*
May 27	35.4-42.7°	348.6-349.1	0.230±0.024	1.402-0.017*i*

The ozone concentration in the 0-4.5 km altitude range was between 48 and 59 ppbv on May 18, and between 64 and 90 ppbv on May 25 and 27.

5.2.2. MODEL

The UVSPEC model set up is the same as that in paragraph 4.2.3. As previously described, the aerosol size distribution has been retrieved from the data collected during the aircraft flights by the FSSP and the condensation nuclei counter [*Di Iorio et al.*, 2003], while the

values for the aerosol refractive index are those giving the best agreement between measured and modelled UV irradiances at the ground level, for values of the solar zenith angles close to those of the aircraft flights. The values of the refractive indices retrieved on the three days, assumed not to depend on wavelength, are reported in Table 5.2.1.
Actinic flux calculations are performed in the wavelength region between 285 and 490 nm, at steps of 0.5 nm. The number of streams is set equal to 16 to accurately represent the geometry of the radiation field. Spectral actinic fluxes are convoluted with the wavelength dependent sensitivity response of the $J(NO_2)$ and $J(O^1D)$ detectors, and integral fluxes $F(NO_2)$ and $F(O^1D)$ are derived. For the comparison with the measured profiles, actinic fluxes are computed every 300 m; solar zenith angle and ozone are varied with altitude, to match the measurement conditions.

5.2.3. RESULTS AND DISCUSSION

The signals from the actinometers show few spikes, i.e. a sudden increase or decrease of the signal, lasting for one or two measurement points, and, as a function of height, smooth oscillations. The oscillations, whose amplitude is generally smaller than ±10% of the signals, are attributed to changes of the aircraft attitude, and to different conditions of illumination of the radiometers and the wing, along the spiralling trajectory. They are present mostly in the ascent section of the flight. The narrow spikes of vertical extension smaller than 30 m were removed from the data as these can be attributed to shading by the support rod above the wing where the radiometers are attached. The signals were then averaged over a 300 m interval, and transformed into actinic fluxes $F(NO_2)$ and $F(O^1D)$.
The normalization coefficients $f(NO_2)$ and $f(O^1D)$ to be multiplied by the signals to obtain actinic fluxes are estimated minimizing the squared differences between normalized measurements and model results. For the derivation of $f(NO_2)$ and $f(O^1D)$ the model was initialised with the measured aerosol and ozone profiles. The values of $f(NO_2)$ and $f(O^1D)$ for the three cases are shown in Table 5.2.2.
It is interesting to note that the estimated normalization coefficients on the three cases fall within a relatively narrow interval of values, that is ±7.8% of the average for $f(NO_2)$, and ±2.8% of the average for $f(O^1D)$. This may be taken as a first indication that the model provides a reasonable overall description of the radiation field, despite some simplifying assumptions on the structure of the atmosphere. The differences can be attributed mainly to the lack of detailed information on the aerosol and the ozone distribution above the aircraft maximum altitude. It is worth noting that if the average $f(NO_2)$ and $f(O^1D)$ values are applied to the profiles of the three days, the model results remain within the experimental uncertainties of the measurements.

Table 5.2.2. Estimated calibration factors, in W m^{-2} V^{-1}, for the $F(NO_2)$ and $F(O^1D)$ actinic flux radiometers, for the three selected flights.

Day	$f(NO_2)$	$f(O^1D)$
May 18	72.5	0.585
May 25	80.0	0.578
May 27	83.3	0.606

5.2.3A. LOW AEROSOL CASES: MAY 25 AND 27, 1999

On May 25 and 27 the ultralight aircraft reached a maximum altitude of 2985 and 3865 m, respectively. The measured $F(NO_2)$ and $F(O^1D)$ are shown in Figure 5.2.1, for May 25, and in Figure 5.2.2 for May 27. An increase of the actinic radiation with altitude is observed, as expected by the progressively decreasing overhead total ozone and aerosol optical thicknesses.

The surface actinic fluxes are similar on both days, for both wavelength bands. This similarity is an effect of the relatively low values of the AOD on the two days, and of the similar total ozone amounts. The $F(NO_2)$ values are expected to strongly depend on the aerosol extinction, while $F(O^1D)$ is largely affected by the ozone amount and distribution, and by aerosol as well.

A good agreement between measurements and model results is found on both days at all altitudes for $F(NO_2)$. The reader is reminded that the signal was scaled to overlap the modelled actinic fluxes, and absolute differences are not meaningful. A good agreement is found when the calculations are carried out with the measured extinction profile, as well as with the standard profile. The relative difference between two model results, one obtained with the measured, and one obtained with the standard aerosol profile, is shown in the right graphs of Figures 5.2.1 and 5.2.2. When the standard profile is used, differences in the weighted actinic fluxes vary between -2.7 and 0.9% for May 25, and between 0.3 and 2.3% for May 27. It is interesting to note that, although at some altitudes there are significant differences between the measured and the standard aerosol extinction profiles, the distance between the modelled actinic fluxes obtained with the two aerosol distributions is small. This effect is a consequence of the relatively small values of the AOD, and of the limited influence that a small amount of particles plays on the actinic fluxes.

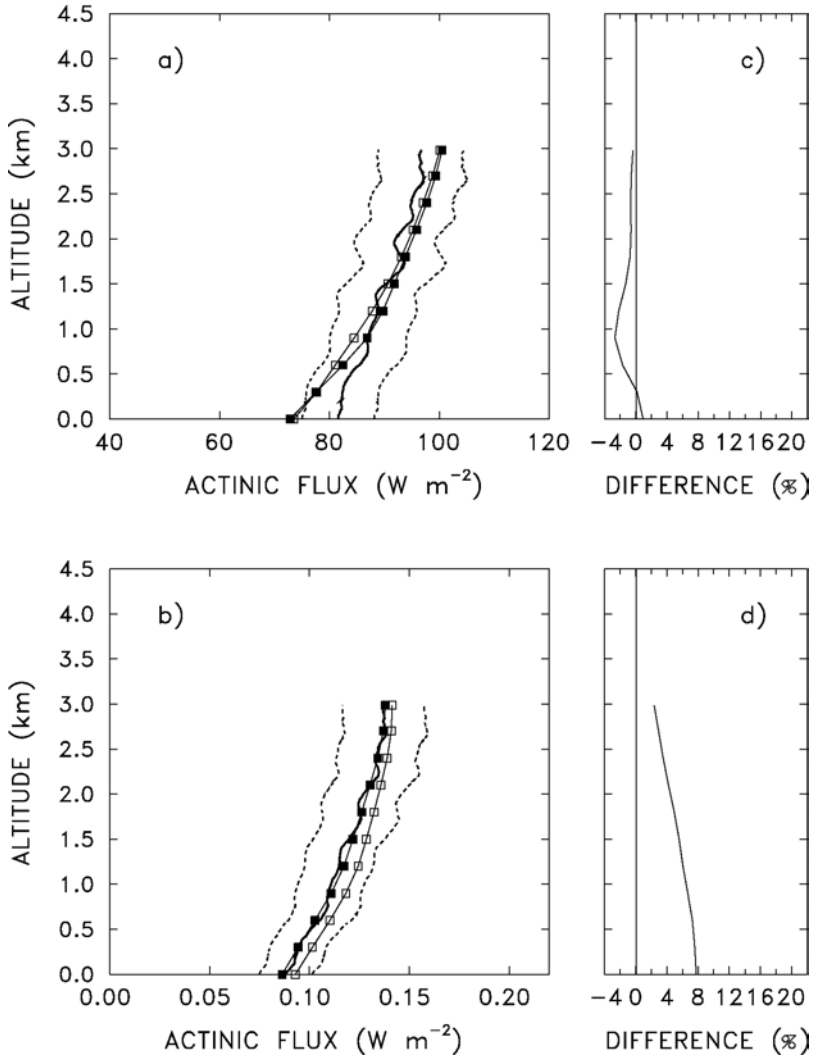

Figure 5.2.1. Measured (solid line) and model-derived a) $F(NO_2)$ and b) $F(O^1D)$ actinic flux profiles for May 25. The dashed lines indicate the estimated uncertainties on the measured profile. Solid squares identify model results obtained with the measured ozone and aerosol profiles; open squares identify model results obtained with the standard aerosol and the measured ozone profiles in graph a), and with the climatological ozone and measured aerosol profiles in graph b). Graph c) displays the percent difference between modelled $F(NO_2)$ obtained with the measured ozone and aerosol profiles, and modelled $F(NO_2)$ obtained with measured ozone and standard aerosol profile. Graph d) shows the percent difference between the modelled $F(O^1D)$ obtained with the measured aerosol and ozone profiles, and the modelled $F(O^1D)$ estimated with the measured aerosol and the climatological ozone profile.

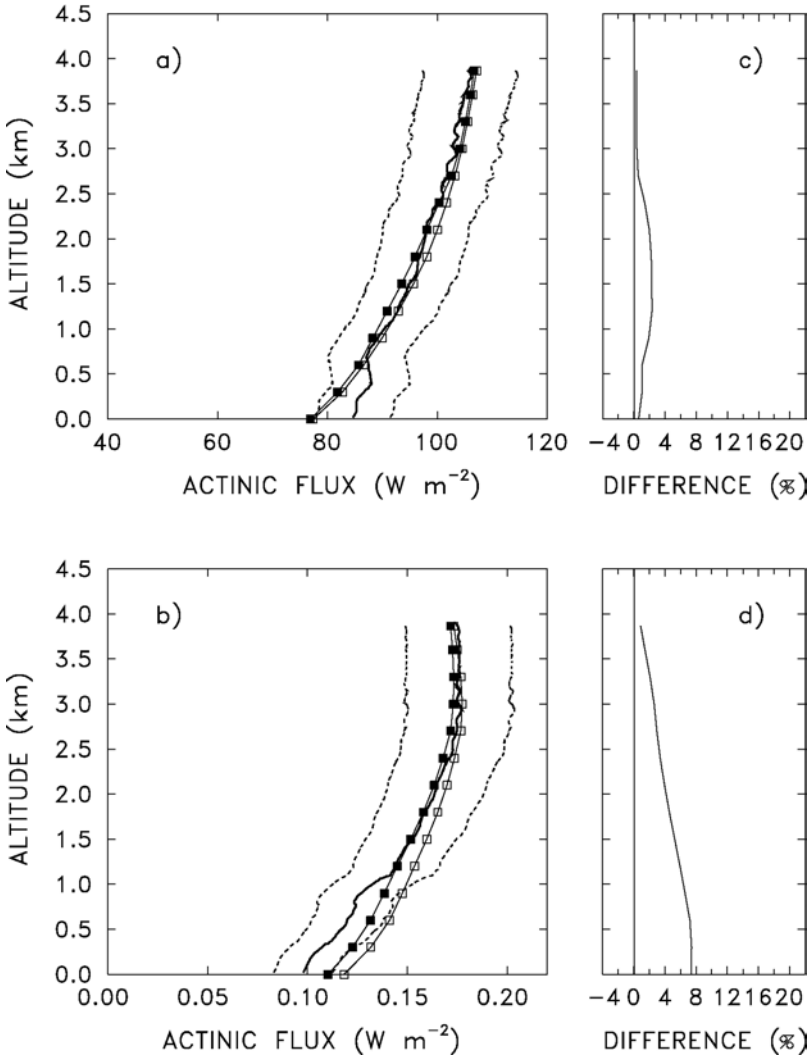

Figure 5.2.2. As in Figure 3, but for May 27.

On both days the maximum absolute difference between the two modelled profiles occurs at the altitude where the measured and the standard aerosol extinction profiles intersect. For example, on May 25 the two profiles cross at about 900 m (see Figure 5.2.2b), height where the largest absolute difference (negative, -2.7%) is found; the transmission through the layer from 900 to 2000 m is lower for the standard profile, while below the crossing height the extinction associated to the measured profile is larger. Near the surface the effect due to the strong aerosol peak at about 300 m prevails, leading to a positive difference between the profiles. A similar, but opposite in sign, feature can be found on May 27, when the crossing of the aerosol extinction profiles at about 1200 m leads to a maximum difference of 2.3% in the actinic fluxes.

As expected, the ozone vertical distribution does not sensibly affect the simulated $F(NO_2)$, since the transmission band of the $J(NO_2)$ detector is in a region where there is no significant absorption by ozone.

The $F(O^1D)$ measured profiles are compared with model calculations performed with either the measured or the reference (climatological) ozone profiles. $F(O^1D)$ calculated with the climatological profile, with lower content in the troposphere, is larger than $F(O^1D)$ estimated with the measured ozone profile. Differences are between 2.4 and 7.7%, from the top to the

surface for May 25, and between 0.9 and 7.4% for May 27. The largest difference is found at the surface. A similar behaviour has been observed for the UV irradiance at the surface (see paragraph 4.2.3). The observed differences are attributable to the increase in the scattering due to tropospheric aerosols, which determine a longer photon path length and a more effective absorption by tropospheric ozone, particularly at small solar zenith angles [*Brühl and Crutzen*, 1989].
Discrepancies between model and measurements in certain altitude ranges can be attributed to changes of the surface albedo, as the aircraft passed over different ground covers. An interesting feature can be observed on May 27, when the measured $F(NO_2)$ values are larger than the simulations by 10% at surface level; the opposite occurs for $F(O^1D)$ (-11% difference). The difference disappears at higher altitudes, where the effect of the ocean albedo becomes dominant. The same behaviour, although less evidently, appears on May 25.
In the lowest altitude range the measured fluxes are strongly influenced by the land albedo, since the aircraft takes off and lands on the airport. Land and ocean surfaces show a different spectral behaviour: the land albedo in the UV is smaller than the ocean albedo, while the opposite occurs in the visible [*Doda and Green*, 1980; *Feister and Grewe*, 1995]. $F(O^1D)$ is influenced by the behaviour of the albedo in the UV, while $F(NO_2)$ depends on the albedo at approximately 400 nm.
Hofzumahaus et al. [2002] report a discrepancy of about 12% in the lowest altitudes between modelled and measured profiles of actinic fluxes in the range 280-420 nm, that may be due to an underestimate of the UV surface albedo.
Further differences can be due to changes in the aerosol optical depth or to the assumption of an altitude independent aerosol refractive index.

5.2.4B. HIGH AEROSOL CASE: MAY 18, 1999

On May 18 the measured $F(NO_2)$ and $F(O^1D)$ profiles are reasonably well reproduced by the model calculations performed with the measured aerosol and ozone profiles, indicating that the model input parameters are representative of the real atmospheric conditions (Figure 5.2.3).
$F(NO_2)$ calculated with the standard aerosol profile differs significantly from the measured profile above 1000 m (Figure 5.2.3a), due to the large differences between the two aerosol distributions, and in particular to the presence of a thick aerosol layer from 2400 m to 7200 m (see Figure 3.3.2a); this layer causes a strong attenuation of the downwelling radiation. The differences between model calculations obtained with the lidar-derived and the standard aerosol profiles are 12% at 4200 m, and 17% at 2400 m, where the two aerosol extinction curves intersect. The difference decreases to nearly zero at ground level, where the amount of downward actinic flux is mainly affected by the total aerosol optical depth: nevertheless, a negative difference is found at the surface as a consequence of the strong aerosol concentration in the lowest levels of the standard profile.

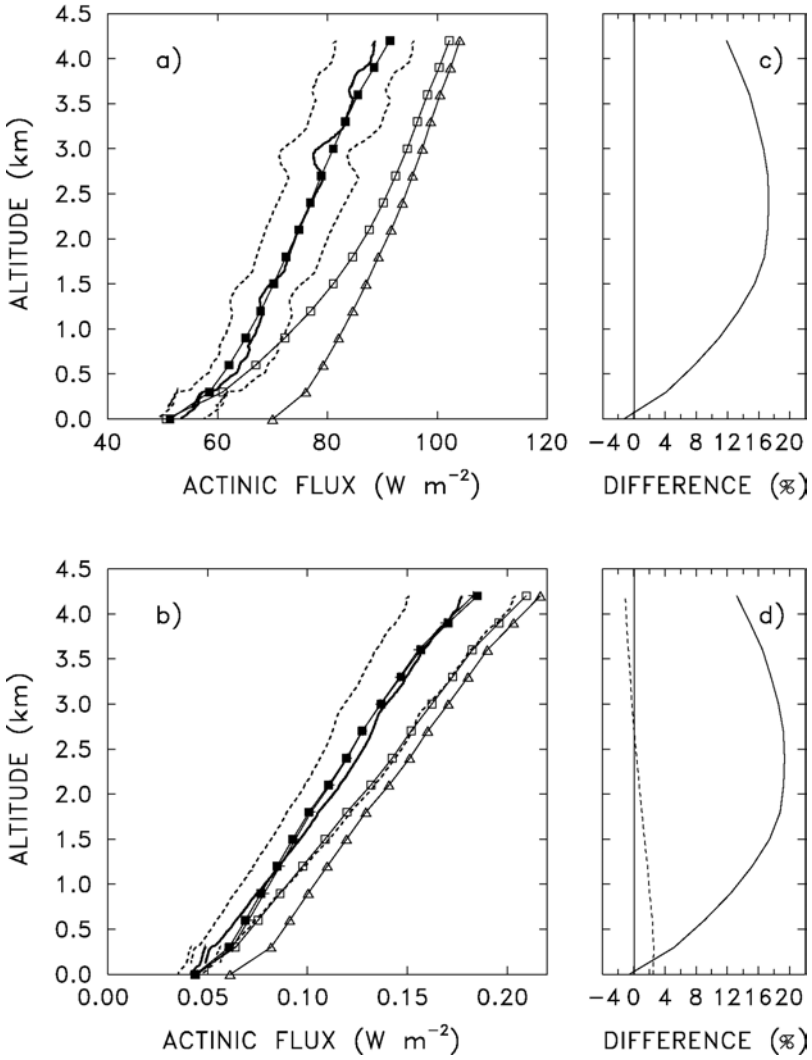

Figure 5.2.3. Measured (solid line) and model-derived a) $F(NO_2)$, and b) $F(O^1D)$ actinic flux profiles for May 18. Dashed lines indicate the estimated uncertainties on the measured profile. Solid squares identify model results obtained with the measured ozone and aerosol profiles; open squares correspond to model results derived with the measured ozone and the standard aerosol profile; and triangles are relative to model results for an aerosol-free atmosphere. Crosses in b) (the data points are very close the solid square symbols) identify results obtained with the climatological ozone profile. Graph c) displays the percent difference between modelled $F(NO_2)$ obtained with the measured ozone and aerosol profiles, and modelled $F(NO_2)$ obtained with measured ozone and standard aerosol profile. Graph d) shows the percent difference between the modelled $F(O^1D)$ obtained with the measured aerosol and ozone profiles, and the modelled $F(O^1D)$ estimated with the measured aerosol and the climatological ozone profile (dashed line), and the difference between the modelled $F(O^1D)$ obtained with the measured aerosol and ozone profiles, and the modelled $F(O^1D)$ estimated with the standard aerosol and the measured ozone profile (solid line).

$F(O^1D)$ has been simulated also using the climatological mid-latitude ozone profile (Figure 5.2.3b). The results show that tropospheric ozone does not sensibly affect the UV distribution in this case of low total ozone amount, and high solar zenith angle; the difference between the two calculated actinic fluxes is less than 2.5% at the surface, decreases with altitude, and

becomes negative above 3000 m. In the middle troposphere the effect of the larger stratospheric ozone amount of the climatology thus prevails on the larger tropospheric amounts of the measured profile. The enhanced efficiency of tropospheric ozone as UV absorber, due to the strong scattering in the troposphere, is expected to decrease for increasing solar zenith angle [*Brühl and Crutzen*, 1989]. Moreover, the tropospheric ozone concentration is much larger on May 25 and 27 than on May 18 (see Figure 3.3.1). On May 18 the tropospheric ozone concentration is relatively close to the climatological values, and the effect on $F(O^1D)$ is smaller than on May 25 and 27.

The aerosol vertical distribution sensibly affects the $F(O^1D)$ profile calculated with the measured ozone profile: when using the standard aerosol extinction profile, the calculated $F(O^1D)$ values are larger that those obtained with the measured profile by about 19% at 2400 m, while discrepancies decrease to a negative value at the surface.

This result indicates that: a) the photolysis rates at the surface are largely controlled by the column aerosol amount, and the detailed knowledge of the aerosol vertical distribution is not essential; b) the knowledge of the aerosol vertical distribution is required to accurately characterize the photochemistry of the middle troposphere. This is particularly important in the regions where the transport of desert dust takes place. The dust may travel long distances, and affect wide portions of the globe. The dust vertical profile often shows peaks above 2 km altitude [see e.g. *Karyampudi et al.*, 1999; *di Sarra et al.*, 2001b], and is inherently different from the generally used climatological aerosol profiles.

To study the impact of the desert dust on the actinic flux profiles, model simulations were performed also for an aerosol-free atmosphere. The overall aerosol effect is a reduction of both $F(NO_2)$ and $F(O^1D)$, as a consequence of the extinction by the dust layer, while an increase in the backscattered radiation with respect to the aerosol-free case is expected above the aerosol layer; these results are in agreement with those reported by *Liao et al.* [1999] for a layer of mineral dust located at 3-6 km and for 60° solar zenith angle. The reduction of $F(NO_2)$ due to Saharan aerosol varies between 27% and 12% from ground to the top level, corresponding to 18.7 and 12.7 W m^{-2} respectively, while the differences between $F(O^1D)$ calculated with and without aerosols are in the range 28-15% (from the ground to the top level), corresponding to 0.017 and 0.032 W m^{-2}, respectively.

A direct comparison of the observed actinic fluxes on the three selected days is not possible, since measurements are obtained at different solar zenith angles. To better identify the role played by the different aerosol properties and distributions, and in particular of the desert dust, model calculations of $F(NO_2)$ and $F(O^1D)$ at fixed solar zenith angles, assuming that all the other parameters remain unchanged, were carried out. Simulations were performed at 40° and 60° solar zenith angles. As previously shown, the model is capable to accurately reproduce the observed actinic fluxes, and it is assumed that the model results at 40° and 60° solar zenith angles provide a meaningful representation of the real fluxes in the atmosphere. The obtained profiles are shown in Figure 5.2.4.

On May 18 the strong attenuation of $F(NO_2)$ due to the high aerosol amount is evident. The largest relative decrease of $F(NO_2)$ on May 18 with respect to May 25 and 27, about 24%, occurs at the peak of the aerosol extinction, at ~3 km, for 60° SZA. For SZA = 40°, the decrease at 3 km altitude is 14%. A smaller decrease of the fluxes of May 18 occurs at the ground (7% at 40°, and 15% at 60° SZA). The aerosol effect on $F(NO_2)$ evidently increases with SZA, as a consequence of the progressive increase of the atmospheric airmass, and AOD along the Earth-Sun direction.

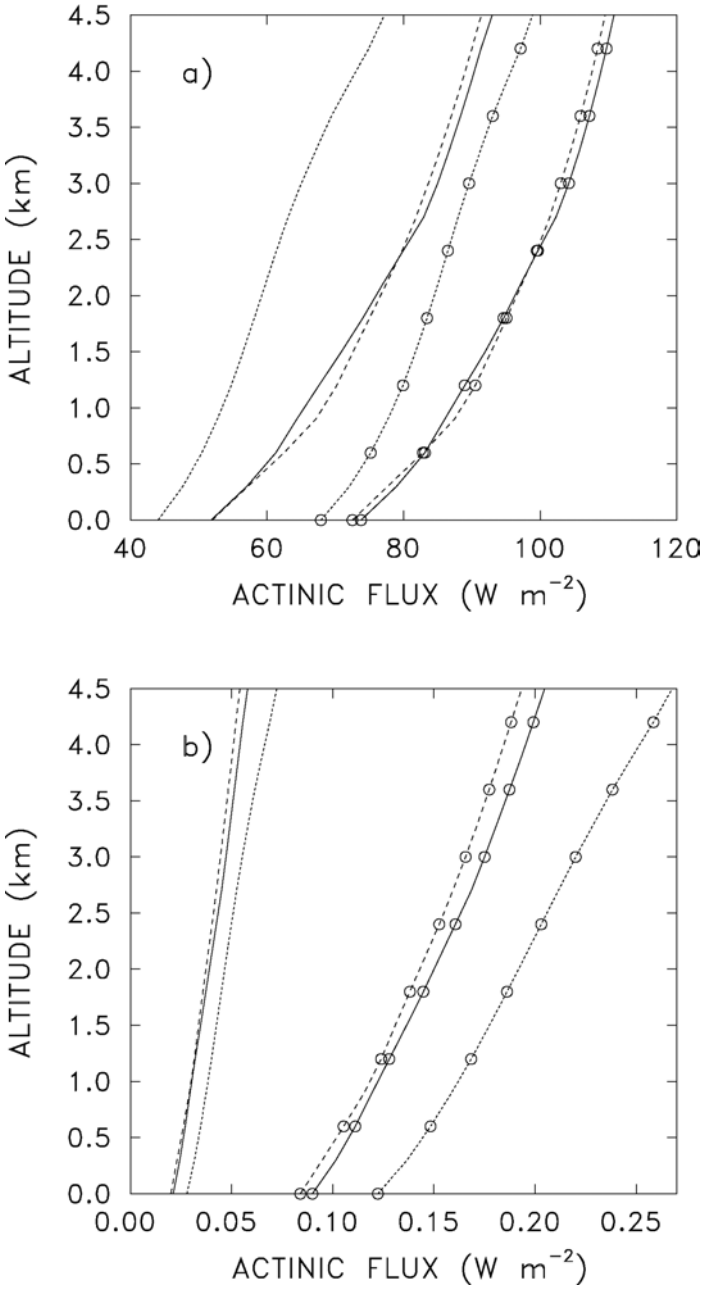

Figure 5.2.4. Simulated a) F(NO_2), and b) F(O^1D) actinic flux profiles for May 18 (dotted lines), May 25 (dashed lines), and May 27 (solid lines), at 40° (lines with open circles) and 60°solar zenith angles (lines without symbols).

On May 25 and 27 the values of F(NO_2) are close, and the differences between the two profiles change with altitude. These differences may be attributed to the combined effect of the AOD values, the aerosol extinction profiles, and the optical properties of the particles, much more absorbing on May 25. The difference between F(NO_2) above 3 km is essentially due to the upward radiation scattered by the aerosols, since the atmospheric structure above 3 km is essentially the same on May 25 and 27, and the same surface albedo applies. Below 2.5 km, the stronger attenuation due to the larger aerosol optical depth produces lower actinic fluxes on May 27 than on May 25. At 40° SZA the strong absorption by the dense aerosol

layer below 1 km of May 25 produces a smaller $F(NO_2)$ than on May 27 in the lowest 500 m, despite the difference in the AOD. This effect is reduced at 60° SZA.
The differences among the profiles of $F(O^1D)$ of May 18, 25, and 27, are due to the combined effect of ozone and aerosol. In the $F(O^1D)$ spectral band ozone has a dominant effect, and the profiles are largely determined by total ozone, and its vertical distribution.

5.3. INFLUENCE OF THE VERTICAL PROFILE OF SAHARAN DUST ON THE VISIBLE DIRECT RADIATIVE FORCING AT THE SURFACE AND AT THE TOP OF THE ATMOSPHERE

In this study the effect of different vertical profiles of desert dust on the estimated instantaneous and daily average aerosol radiative forcing RF at the surface and at the top of the atmosphere in the visible spectral range is investigated. The impact of the AOD and of the single scattering albedo ω_0 on the computed RF is also examined. Direct and diffuse irradiances with and without aerosols are computed using the UVSPEC model, initialised with measurements performed at Lampedusa during three different days (May 18, 1999 and July 14 and 16, 2002) when desert dust was present.

5.3.1. DATA

The days under consideration were previously presented. Data of July 14 and 16, 2002 were used to derive the wavelength-independent ω_0 and g by comparing the radiometric quantities measured from the ground (the MFRSR global irradiances in four visible bands) and from space (the MISR equivalent reflectances at three visible bands) with the corresponding model simulations. The values which give the best model-measurement agreement are $\omega_0 = 0.96$ and $g = 0.80$ for July 14 and $\omega_0 = 0.88$ and $g = 0.81$ for July 16. The differences in ω_0 and g between the two days reflect the different trajectories of the air masses that arrived at Lampedusa. The aerosol vertical distribution from the lidar measurements adds credit to what derived from the backward trajectory analysis: the strong convection typical of the central Sahara lifted the aerosol particles up to 6 km on July 14, while on July 16 the largest aerosol load was found in the 0-2.5 km layer.
The AOD at 500 nm was the same, 0.227, on the two days. The values of the Ångström exponent α calculated from the 415.6 nm and 868.7 nm MFRSR bands indicate on both days the presence of large particles. The value of α is smallest on July 14 ($\alpha = 0.080$) than on July 16 ($\alpha = 0.698$); the lidar depolarisation shows that the particles have irregular shapes.
The model simulations were performed assuming a Henyey-Greenstein aerosol phase function, since detailed information on the particles' shape, size distribution and refractive index was not available.
The retrieved values of ω_0 and g are a sort of equivalent column-average optical properties, and include the effect of a non homogeneous vertical distribution; although different types of particles may be present over the column, mineral dust was on both days the largely dominant component.
An additional interesting case of desert dust selected for this study is 18 May, 1999. On this day the airmasses arriving at Lampedusa had spent the last 10 days over the central Sahara, and the lidar detected enhanced aerosol amounts from the surface up to 8 km; measurements of the aerosol size distribution were obtained from an ultralight aircraft, simultaneously to

MFRSR and spectral ultraviolet and visible irradiance observations at the ground. The AOD at 500 nm was 0.49, and the Ångström exponent was 0.22. In this study 18 May, 1999 represents a case of high dust loading: the dust cloud was relatively highly absorbing, being the retrieved ω_0 at 532 nm between 0.78 and 0.80, depending on altitude.

5.3.2. METHODOLOGY AND RESULTS

The direct aerosol RF has been calculated by means of the RT model in the visible (400-700 nm), with the main inputs specified in the previous paragraph.
The daily change of the AOD and of the aerosol optical properties was not taken into account in the model calculations, since the purpose of this study is to assess how estimates of the RF are affected by different aerosol vertical distributions. The dependence of the sea surface albedo on the solar zenith angle (SZA) has been accounted for, according to the results by *Payne* [1972]: assuming a wind speed of 7 m/s, the average value measured by the meteorological station on July 14 and 16, the surface albedo varies between 0.02 at 20° and 0.37 at 90° SZA. As reported in *Payne* [1972], the surface albedo is almost constant for solar zenith angles smaller than 40°, and shows a steep increase for larger SZA.

5.3.2A. DEPENDENCY ON THE SOLAR ZENITH ANGLE

Table 5.3.1 shows the RF at the surface and at the TOA as a function of SZA, and the daily average RF for July 14 and 16. The daily average is lower than the instantaneous RFs since the integration over the whole day also takes into account also the nighttime period. The negative values at the TOA indicate that aerosols produce an increase of the upwelling radiation, this effect corresponding to a larger atmospheric albedo.

Table 5.3.1. Instantaneous and daily average aerosol RF (W m^{-2}) at the surface and at the TOA for July 14 and 16.

SZA	July 14		July 16	
	surface	TOA	surface	TOA
20°	-11.0	-5.1	-18.9	-3.1
30°	-11.4	-5.6	-19.1	-3.5
40°	-11.9	-6.1	-19.3	-3.8
50°	-13.0	-7.1	-19.8	-4.5
60°	-14.0	-8.0	-19.8	-4.8
70°	-14.2	-8.7	-18.6	-5.2
80°	-9.7	-6.0	-11.9	-3.1
daily average	-6.7	-3.6	-10.2	-2.2

The dependence of the aerosol radiative forcing on the SZA is shown in Figure 5.3.1. At TOA the radiative forcing has a minimum at 70° on both days. At the surface RF is minimum at 50° on July 14, and at 70° on July 16. This behaviour is determined by the combination of distinct phenomena.
At the TOA the upwelling radiation strongly depends on the aerosol phase function, that in its turn depends on the particles' dimension; for particles of large radii, as is the case of July 14 and 16, a strong scattering peak occurs in the forward direction. As the SZA increases, a larger portion of the forward hemisphere includes the region of the upwelling scattered irradiance, and the RF increases with SZA up to 70°.

The RF is also dependent on the surface albedo; for non-absorbing aerosol (ω_0 close to 1), like that of July 14 and 16, the highest RF occurs for low surface albedo, i.e. on the ocean for small values of SZA [*Haywood and Shine*, 1997].

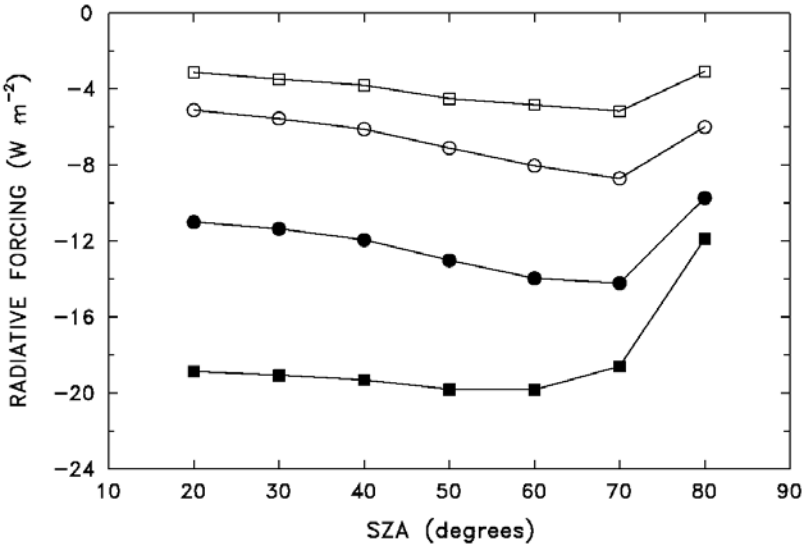

Figure 5.3.1. Radiative forcing (W m^{-2}) at the surface (full symbols) and at the TOA (open symbols) as a function on the solar zenith angle (SZA) for July 14 (circles) and 16 (squares).

At the surface the increase in the photon path length with SZA leads to an increase of the attenuation by aerosols, and thus to an increase in the RF up to a SZA of 50° (July 14) and 70° (July 16). At high SZA the atmosphere is optically thick and the RF tends to decrease both at the TOA and at the surface.

Similar results were found in other studies. *Haywood and Shine* [1997] used a radiative transfer code to calculate the direct radiative forcing of sulphates and soot aerosol at the TOA for different surface albedos, solar zenith angles and aerosol vertical profiles. For sulphate aerosols the (negative) forcing shows a decrease for increasing SZA with a minimum at 70° for values of surface albedo between 0 and 0.20. For soot particles the forcing is positive and slowly decreases for increasing SZA to a minimum at 90°.

Boucher et al. [1998] compared the performance of different radiative transfer models and studied the sensitivity of the shortwave TOA RF of sulphate aerosols to various optical parameters, among which the AOD, the surface albedo, the SZA, the aerosol particle radii. Although the conditions fixed for the model simulations (AOD at 550 nm of 0.20, surface albedo of 0.15, particle radii of 0.170 and 0.679 μm) are different from those encountered in July 2002, their results show a negative RF with a minimum at 70-75° SZA.

Downward shortwave RF obtained from measurements of aerosol optical properties during TARFOX have been reported by *Hignett et al.* [1999], who observed a decrease from 18° to 48° SZA.

During the STAAARTE-MED project [*Formenti et al.*, 1998], aerosol scattering and absorption coefficients were measured in Greece and used as input to a radiative transfer model to estimate the diurnal cycle of the shortwave RF at the surface and at the TOA; the aerosol is constituted by a mixture of sea salt, soil dust, sulphates and black carbon from biomass-burning. A minimum (absolute value) RF at the TOA was found around local noon.

Over the sea, an increase of the aerosol absorption is associated with a decrease of the RF at the TOA, and with an enhancement of RF at the surface.
Horvath et al. [2002], using aerosol optical properties measured at Almería (Spain) and Vienna (Austria), calculated the spectral and the integrated shortwave RF at the surface and at the TOA. They analyzed the dependence on wavelength and solar zenith angle, for values of the surface albedo of 0.15 and 0.20. Their results show that the RF at the surface is maximum (absolute value) at 50° SZA for Almería and at 60° SZA for Vienna.

In the present calculations the absolute values of the RF at the TOA are higher on July 14 than on 16, due to a higher single scattering albedo (ω_0 = 0.96 for July 14 and 0.88 for July 16), being the asymmetry factor similar on both days (g = 0.80 for July 14 and 0.81 for July 16). Accordingly, the RF values at the surface are lower on July 14 than on 16. The atmospheric RF (see paragraph 4.2.3d) is positive on both days. The daily average atmospheric RF is 3 W m^{-2} for July 14 and 8 W m^{-2} for July 16, as a consequence of the different absorption properties of the particles.

The RF at the surface for the diffuse radiation only, RFD, can be defined as the change of the net (downward minus upward) diffuse irradiance with and without aerosols. RFD is positive for all SZA, since the presence of aerosols increases the amount of diffuse radiation reaching the ground, and is maximum at 20°, since the largest part of the scattering takes place in forward direction. The daily average values of RFD are 34.9 W m^{-2} for July 14 and 29.5 W m^{-2} for July 16, due to the larger ω_0 on July 14.

5.3.2B. Dependency on the aerosol vertical distribution

The impact of the aerosol vertical profile on the RF has been studied repeating the model calculations with the vertical distribution for mid-latitude atmosphere given by *Shettle* [1989] (hereafter indicated as standard profile), and comparing the results with those obtained with the measured profiles. The standard profile was scaled to match the measured AOD. The other aerosol properties (ω_0 and g) were unchanged. Figure 3.3.3 shows the lidar-derived and the standard aerosol extinction profiles for the two days of July 2002. The corresponding profiles of 18 May, 1999 can be found in Figure 3.3.2. The standard profile has the maximum extinction at the ground; the 0-1.5 km layer contributes by 65% to the total AOD, while the 1.5-10 km layer contributes by 33%. The lidar-derived extinction profiles are significantly different from the standard distribution: on July 14, 2002 as well as on 18 May, 1999 the layers 0-1.5 km and 1.5-10 km contribute by 17% and 82%, respectively, to the total AOD. On July 16, 2002 the same layers contribute by 34% and 65%, respectively. Differences in the observed aerosol vertical distributions can be attributed to the origin of the air masses arriving at Lampedusa. It is worth emphasizing that profiles showing largest aerosol extinction in the mid troposphere, and/or relatively thick layers at altitudes between 2 and 8 km, are somewhat typical for desert dust, and are related to the dust mobilization process and to the strong convective activity occurring over desert areas, mainly at low latitudes.

The percent differences between RFs obtained with the standard and with the observed profiles are reported in Table 5.3.2.

Table 5.3.2. Percent differences between the RF calculated with the standard profile with respect to the values obtained with the measured profile (in Table 5.3.1).

SZA	July 14		July 16	
	surface	TOA	surface	TOA
20°	+1.1	+5.3	+0.6	+9.1
30°	+1.5	+4.8	+0.5	+8.2
40°	+1.0	+3.8	+0.4	+7.2
50°	+0.2	+2.6	+0.1	+5.6
60°	-0.3	+1.4	-0.1	+4.8
70°	-0.7	+0.9	-0.4	+4.1
80°	-1.0	+1.4	-0.7	+6.0
daily average	+0.3	+2.9	+0.2	+6.5

The instantaneous and daily average RFs at the surface are not substantially affected by the aerosol vertical distribution. A small dependency on SZA occurs: a positive difference is found at small SZA, indicating that when the sun is high aerosols at low altitude are more effective in reducing the visible radiation, while the opposite occurs at large SZA. Absolute values of the differences are larger on July 14 than on 16, since the differences between standard and measured profiles are higher on the first day.

At the TOA the differences are positive and larger at the smallest SZA, that is +5.3 % on July 14 and +9.1 % on July 16 at 20°; the standard profile is thus more efficient in increasing the radiation scattered back to space. The difference between the two calculated RF decreases as the SZA increases, as a consequence of the stronger scattering by aerosols in the lowest atmospheric layers when the sun is closer to the zenith; conversely, for large SZA most of the downward radiation originates from scattering occurring in the mid- and high troposphere, where the aerosol content is low (for non-volcanic conditions, as in this case) and the vertical distribution of the aerosol particles in the low troposphere has minor effects. The RF increase for the standard profile is different on the two days, since the sensitivity on the aerosol height is stronger for absorbing aerosols. *Torres et al.* [1998] have shown that in the case of low surface reflectivity and non-absorbing aerosols the aerosol layer height has a small effect on the backscattered radiance at 380 nm at the TOA, while for moderately absorbing particles an aerosol layer near the surface is more effective than a layer in the mid troposphere in increasing the backscattered radiance. When the surface albedo is low, most of the upward radiation in the UV is due to scattering from atmospheric molecules, which occurs primarily in the low troposphere, where the molecular density is high. Thus, aerosols absorb mainly the upward radiation originating from the lowest altitudes, and the highest the aerosol layer, the greatest the portion of scattered radiation that is involved in the absorption. This mechanism is expected to play an important role also in the visible over the ocean (mainly for small SZA), where the surface albedo is low. When the surface albedo is high a larger fraction of the upward radiation originates from the surface, and the aerosol vertical distribution should produce a smaller effect on the outgoing flux.

The results obtained by *Haywood and Shine* [1997] are in agreement with the previous observations; they estimated the shortwave TOA RF of sulphate aerosols (ω_0 = 1.00 and g = 0.62 at 500 nm) and of soot (ω_0 = 0.24 and g = 0.36 at 500 nm) for different altitudes of the aerosol layer. The conclusions they achieved are that for cloud-free sky the sensitivity of the sulphate aerosols is small, while the RF is positive and strongest for a layer of soot at the highest altitude, this effect increasing with the AOD.

5.3.2c. Dependency on the aerosol vertical distribution for different optical depths

To study the sensitivity on the aerosol optical depth, the same calculations were repeated for a doubled (AOD_d) and a halved AOD (AOD_h) at all wavelengths. All the other parameters were not changed (except for the measured extinction vertical profile, that was scaled to match the AOD). In the first case (0.454 AOD at 500 nm), the instantaneous and the daily average RF at the TOA and at the surface are nearly two times larger than the values obtained with the measured AOD: we found a daily average RF of –12.9 W m^{-2} (surface) and –6.8 W m^{-2} (TOA) on July 14, and of –19.5 W m^{-2} (surface) and –3.9 W m^{-2} (TOA) on July 16. Calculations were also performed with the scaled standard aerosol profile. The differences between the RF obtained with the standard and with the measured profile are lower at the TOA and at the surface than those previously obtained with the measured AOD: at the TOA the difference is 3.9% on July 14 and 7.0% on July 16 at 20°, and 2.4% and 5.4% for the daily average. In the second case (0.11 AOD at 500 nm) the forcings are nearly halved, and the differences are larger than those estimated using the measured AOD: at the TOA the difference is 6.7% on July 14 and 12.0% on July 16 at 20°, and 3.4% and 8.1% for the daily average.

In Figure 5.3.2 the RFs at the surface for the three considered AODs are plotted as a function of the SZA. For the measured AOD and for AOD_h the maximum (absolute value) RF occurs at the same SZA (70° for July 14 and 60° for July 16). When the AOD_d is assumed in the calculations, the SZA at which the largest RF occurs decreases to 60° on July 14 and 50° on July 16: the reason is that, fixing the SZA, the photon path length is longer and attenuation is stronger in the case of AOD_d than in the case of AOD.

It is worth noting that the RF efficiency (RFE) is nearly constant in the three cases, meaning that the RF is nearly linear in the AOD: the daily average RFEs at the surface are in the range –(28.4-30.1) W m^{-2} for July 14 and –(42.9-45.6) W m^{-2} for July 16, while the RFEs at the TOA are in the range –(15.0-16.4) W m^{-2} for July 14 and –(8.6-10.0) W m^{-2} for July 16.

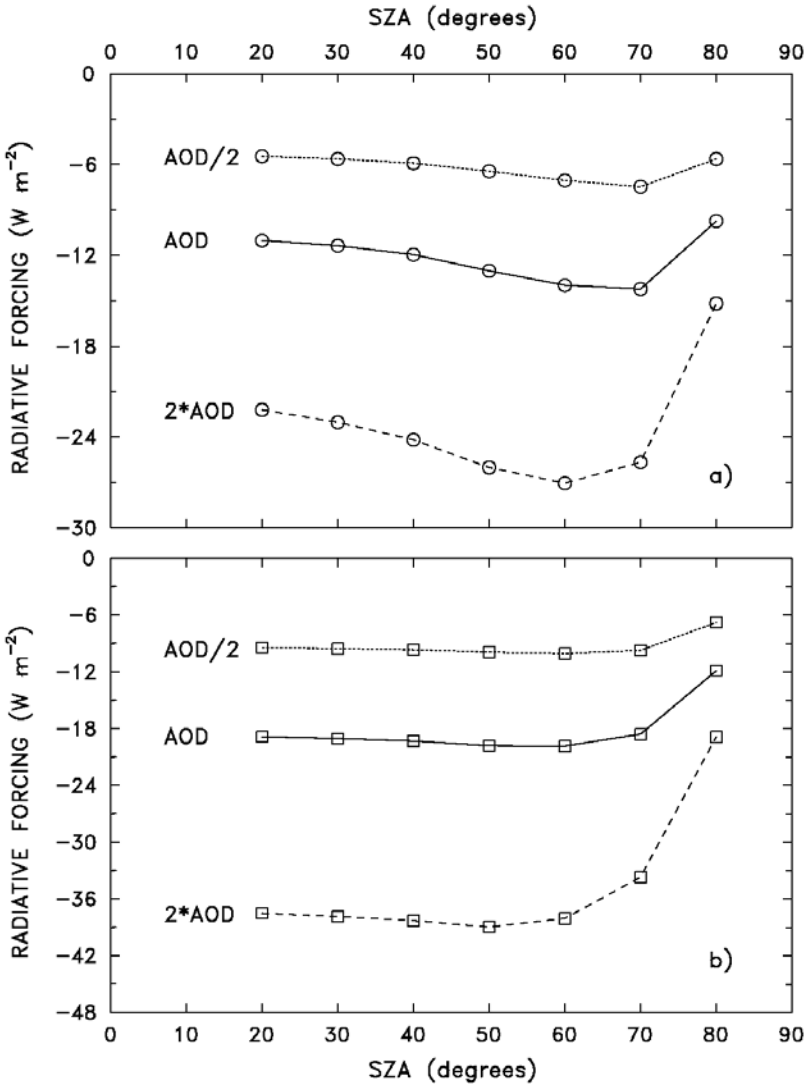

Figure 5.3.2. Radiative forcing (W m^{-2}) at the surface as a function on the solar zenith angle (SZA) for different AOD: the measured AOD (solid curve), the halved AOD (dotted curve), and the doubled AOD (dashed curve). Graph a) is for July 14 and b) for July 16.

5.3.2D. DEPENDENCY ON THE SINGLE SCATTERING ALBEDO

In order to examine the effect of absorbing particles (as is often the case for desert dust) on the RF, the instantaneous and daily average RF for both days were calculated using the measured parameters, except for ω_0, that was assumed to be 0.75. The results are reported in Table 5.3.3.

Table 5.3.3. Instantaneous and daily average aerosol RF (W m^{-2}) at the surface and at the TOA for July 14 and 16, fixing $\omega_0 = 0.75$.

SZA	July 14		July 16	
	surface	TOA	surface	TOA
20°	-33.6	-0.7	-32.2	-0.8
30°	-33.6	-1.1	-32.2	-1.1
40°	-33.4	-1.2	-32.0	-1.2
50°	-33.3	-1.7	-31.7	-1.7
60°	-32.0	-1.4	-30.4	-1.3
70°	-28.4	-1.3	-26.8	-1.2
80°	-17.1	+0.5	-16.1	+0.4
daily average	-17.0	-0.5	-16.2	-0.5

Figure 5.3.3 shows the instantaneous RF at the surface and at the TOA as a function of SZA for July 14; the same conclusions can be drawn for July 16. At the surface the largest aerosol RF (absolute value) occurs at low values of the SZA; RF rapidly decreases for SZA>50°. At the TOA RF is still negative but very small, and reaches the minimum value at 50° SZA, then increases up to positive values at 80° SZA. This behaviour for very low sun is due to the long photon path length within the absorbing aerosol layer, that prevents the radiation from being reflected to space.

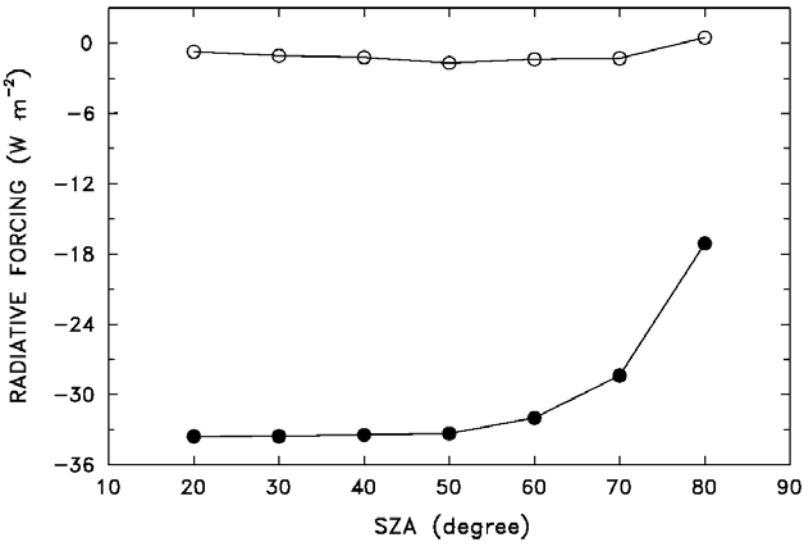

Figure 5.3.3. Radiative forcing (W m^{-2}) at the surface (full symbols) and at the TOA (open symbols) as a function on the solar zenith angle (SZA) for July 14, after fixing $\omega_0 = 0.75$.

The daily average RFE is between –71.3 and –75.0 W m^{-2} at the surface, and –2.3 W m^{-2} at the TOA, while the atmospheric RF is between 15.7 and 16.5 W m^{-2}, depending on the day. The daily average RFD is between 23.5 and 24.6 W m^{-2}. These values are smaller than those obtained with larger ω_0, due to the effect of the stronger absorption and reduction of scattered fluxes.

The sensitivity to the aerosol profile has been tested also performing the model simulations with the standard profile. When the standard aerosol profile is used, no significant effect on

the RF at the surface is discernible. At the TOA the daily average RF is still small, although slightly higher (absolute value) than the one obtained with the measured aerosol profile. The increase is about 0.5 W m^{-2} on July 14, and 0.3 W m^{-2} on July 16. According to *Torres et al.* [1998], a layer of absorbing aerosols near the ground level (as for the standard profile) produces a much higher backscattered radiance at 380 nm than an aerosol layer at high altitudes. At 80° SZA the standard profile does not produce a positive RF: this can be explained with the fact that for high SZA the molecular scattering and the absorption by the aerosols occur mainly at higher altitudes where the aerosol content of the standard profile is low.

Figure 5.3.4 shows the instantaneous TOA RFs on July 14 and 16 calculated with $\omega_0 = 0.75$ using the measured and the standard profiles. The RFs calculated with the measured profiles on July 14 and 16 do not sensibly differ at any SZA, despite the different aerosol vertical distributions. The absolute values of the RF obtained with the standard profile is instead significantly higher on July 14 than on 16.

In order to explain this behaviour, the spectral RFs at 50° SZA have been reported in Figure 5.3.5 at 20 nm intervals. The curves of the RF obtained with the measured profiles on July 14 and 16 intersect at approximately 530 nm, where the values of the AOD on the two days nearly match. The different spectral behaviour of the AOD produces a compensation of the forcings respectively below (where the AOD on July 14 is higher than on July 16) and above 530 nm (where the AOD on July 16 is higher than on July 14), and the spectrally integrated RFs are consequently very close. It is interesting to note that on both days the RF at wavelengths shorter than 430 nm is positive for the measured profile, while is always negative for the standard profile; the differences between the RFs obtained with measured and standard profiles are largest at shorter wavelengths, and progressively decrease with wavelength.

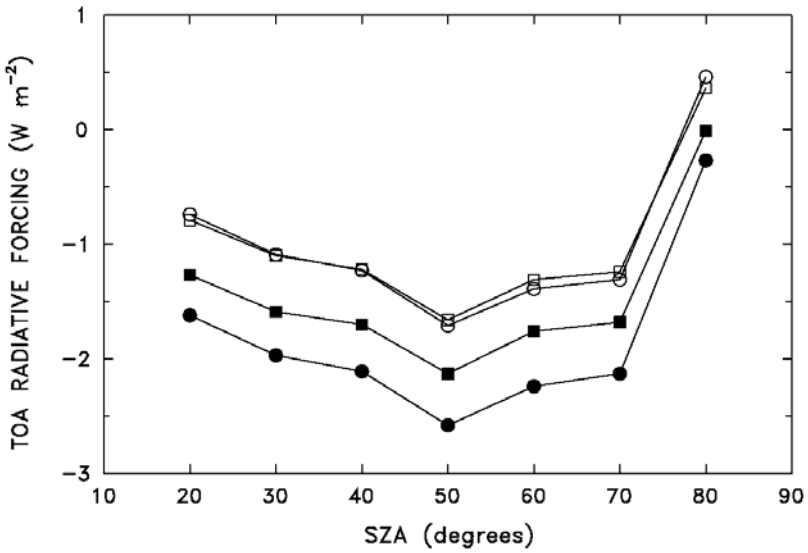

Figure 5.3.4. Radiative forcing (W m^{-2}) at the TOA as a function on the solar zenith angle (SZA) with $\omega_0 = 0.75$ for July 14 (circles) and July 16 (squares). Open and full symbols indicate the forcings obtained with the measured and with the standard aerosol profiles, respectively.

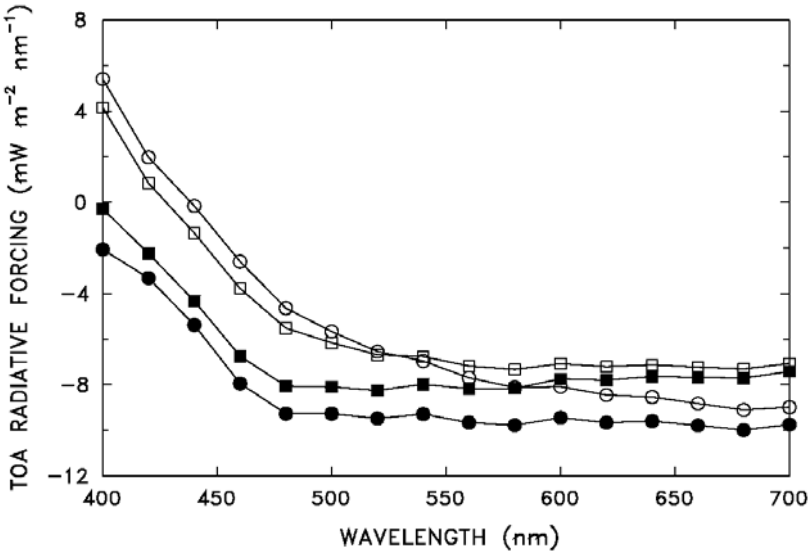

Figure 5.3.5. Spectral radiative forcing (mW m^{-2} nm^{-1}) at the TOA at 50° SZA with ω_0 = 0.75 for July 14 (circles) and 16 (squares). Open and full symbols indicate the forcings obtained with the measured and with the standard aerosol profiles, respectively.

This peculiar behaviour permits to identify clearly the role played by the aerosol vertical distribution. At short wavelengths, as the altitude of the aerosol layer increases, the fraction of the upwelling radiation interested in aerosol absorption (originated from the strong molecular scattering in the lowest atmospheric layers) becomes larger. At longer wavelengths, aerosol scattering contributes in a more significant way to the upwelling radiation, and the dependence on the aerosol height decreases. This is the reason for the decrease with wavelength of the differences between forcings obtained with the measured and standard profiles.
In the measured profile the main part of the aerosol layer is located in the mid troposphere, thus absorbing a large fraction of the upward radiation scattered by molecules. This effect is in fact greater on July 14, where the maximum aerosol concentration is between 2 and 6 km, and produces a positive forcing at short wavelengths.
As previously noted, the spectral RF computed using the standard profiles is negative in the entire wavelength range; the RFs on July 14 is higher (absolute values) than on July 16, and the two curves do not intersect between 500 and 550 nm. Being the aerosols localized mainly at lowest altitude, they absorb only a fraction of the upwelling radiation scattered by molecules, and the RF remains negative. For wavelengths > 500 nm the differences are attributable principally to the spectral behaviour of the AOD (larger on July 14); at shorter wavelengths, where the RF decreases in magnitude due to the rapid intensification of the molecular scattering, the effect of the spectral aerosol behaviour is masked.

Dust particles are generally relatively large, with a mode in the size distribution centred at a few microns (e.g. *d'Almeida et al.* [1991]). Consequently, the asymmetry parameter is expected to be relatively large. In the following analyses we will keep g = 0.8; this value is representative of the three selected cases, and, in general, of desert dust. The values of ω_0 of the Saharan dust determined by different authors fall conversely in a relatively wide range of values.

The daily average TOA RFE on July 14 have been simulated varying ω_0 in the range 0.6-1.0, using both the lidar and the standard profiles (see Figure 5.3.6). The two curves indicate that the RFE decreases with ω_0; at a critical ω_0 a change from a heating to a cooling effect occurs. The critical ω_0 is 0.71 for the measured profile and 0.66 for the standard profile.

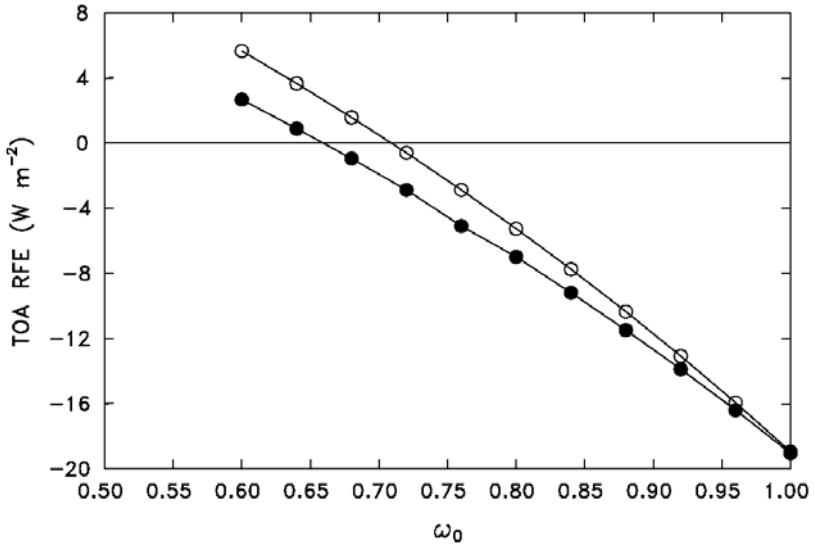

Figure 5.3.6. Radiative forcing efficiency (W m^{-2}) at the TOA as a function of ω_0 for July 14. Open and full symbols indicate the forcings obtained with the measured and with the standard aerosol profiles, respectively.

The visible RFE obtained with the observed profile is higher than the one calculated with the standard profile for all values of ω_0. This behaviour may not be in general true, since it may also depend on the value of *g* [see e.g. the results by *Haywood and Shine*, 1997 for sulphate aerosols]. The difference between the RFEs obtained with the two dust profiles is about 4 W m^{-2} for ω_0<0.7. Assuming that the visible spectral range contributes by 40% to the shortwave band, this difference corresponds to a shortwave RFE of about 10 W m^{-2}. It is interesting to note that for $\omega_0 \sim 0.67$ the use of the observed vertical profile produces a change of the sign of the forcing.

Liao and Seinfeld [1998] examined the daily average shortwave RF by mineral dust at the surface and at the TOA, focusing on the role of some key variables, like the imaginary part of the refractive index, size distribution, optical depth and vertical distribution. They found that, for cloud-free conditions, the RF both at the surface and at the TOA are not sensitive to the altitude of the dust layer, while the dependence on the AOD is nearly linear.

To further study the effect of relatively high absorbing dust, the Saharan dust outbreak on 18 May, 1999 has been examined, when the measured AOD around 60° SZA was 0.49, and the aerosol optical properties were derived from measurements and application of RT simulations. Three distinct layers were identified from the lidar profile, and the aerosol size distribution for each layer was three mode lognormal, as described in paragraph 4.2.3; the complex refractive index retrieved in the UV and assumed wavelength-independent in the visible and near infrared, and constant with altitude, was 1.536-0.0044*i*. Calculations based on the Mie theory gave values of ω_0 in the range 0.78-0.80, and of *g* around 0.76-0.77 at 532 nm, depending on the aerosol layer. The instantaneous and daily average RFs at the surface

and at the TOA have been estimated using both the lidar-derived and the standard aerosol profiles: the results are reported in Table 5.3.4.

Table 5.3.4. Instantaneous and daily average aerosol RF (W m^{-2}) at the surface and at the TOA for 18 May, 1999 calculated using the measured and the standard profiles.

SZA	Measured profile		Standard profile	
	surface	TOA	surface	TOA
20°	-56.6	-6.0	-55.7	-6.7
30°	-56.9	-6.8	-55.9	-7.4
40°	-56.9	-7.5	-55.8	-8.0
50°	-56.6	-8.6	-55.5	-9.0
60°	-53.3	-8.2	-52.2	-8.5
70°	-44.8	-7.5	-44.0	-7.7
80°	-23.5	-2.9	-23.2	-3.0
daily average	-27.6	-3.6	-27.1	-3.9

The coupled effect of a high AOD and a low ω_0 leads to a strong attenuation of the radiation at the surface, with the maximum RF at 30-40° SZA. At the TOA the daily average aerosol RF is comparable to that estimated for the case of July 14, 2002, although AOD and ω_0 are sensibly different: this is a consequence of the stronger aerosol absorption, that produces a lower RFE, which is –7.4 W m^{-2}, that is about 50% of the RFE for July 14. The strongest aerosol RF at the TOA occurs at 50° SZA.
The daily average RFE at the surface is –55.8 W m^{-2}, nearly doubled with respect to the RFE of July 14.
The percent difference between the RFs obtained with the standard and the measured profiles is small at the surface (-1.8% on the daily average), and large at the TOA, with a 11.6% difference at 20°.
The daily average atmospheric RF is 24 W m^{-2}, respectively 8 and 3 times larger than that of 14 and July 16, 2002.
The estimated RFD at the surface is very large (40.9 W m^{-2}), indicating a strong role of the scattered radiation. However, the RFD for a unit AOD at 500 nm on 18 May, 1999 is the lowest (82.7 W m^{-2}) among the considered cases (153.7 W m^{-2} for July 14, 130.1 W m^{-2} for July 16, and 103.6-108.3 W m^{-2} on the same dates when assuming $\omega_0 = 0.75$).

5.4. CONCLUSIONS

The two studies presented in this chapter investigate the impact of aerosols and ozone profiles on the vertical distribution of the actinic fluxes, and on the instantaneous and daily average aerosol radiative forcing at the surface and at the TOA.

The first study (paragraph 5.2) examines the impact of aerosols of different origins and loading, and of tropospheric ozone, on the vertical distribution of the actinic fluxes relevant for the photodissociation of NO_2 and ozone (to produce O^1D), respectively $F(NO_2)$ and $F(O^1D)$. The analysis is based on the comparison of measured and modelled actinic flux profiles. The measurements were carried out with filter actinometers (upward and downward facing) installed aboard an ultralight aircraft; data from three flights (on May 18, 25 and 27) performed at Lampedusa during the PAUR II campaign, have been used. Only cloud-free

cases were selected. The model calculations are performed using different aerosol and ozone vertical profiles, derived from the measurements and from the climatology.
During the three selected days the aerosol conditions were extremely different. In one case desert dust was present over Lampedusa, the layer of mineral particles extended up to 7 km, and the aerosol optical depth at 415 nm was 0.51. In the other two cases the airmass originated from Europe, the aerosol layer was confined below approximately 3 km, and the AOD at 415.6 was between 0.16 and 0.23. Both airborne measurements and model simulations show a dependence of the actinic radiation on the different aerosol conditions.
The actinic flux profiles estimated with the RT model initialised with a large set of observed parameters are in good agreement with the measurements in all three selected cases, i.e. for very different aerosol properties and distributions. A good agreement is found, in particular, also for the desert dust event.
The use of standard aerosol profiles, instead of measured profiles, produces minor effects on the surface values of $F(NO_2)$ and $F(O^1D)$, in all the selected cases. In the cases of airmasses originating from Europe, i.e. for low to moderate aerosol load, and when the aerosol vertical profile appears similar to the standard distribution, the actinic flux profiles obtained with standard instead of measured aerosol profile are close to the measurements, and the differences remain below ±3%. In the desert dust case the use of a standard aerosol vertical distribution produces significant (up to 19%) overestimates of both $F(NO_2)$ and $F(O^1D)$, throughout the lower and middle troposphere, except at the surface.
The use of a climatological ozone profile significantly affects the behaviour of $F(O^1D)$, due to the different overhead ozone amounts and the enhanced absorption by tropospheric ozone induced by the strong radiation scattering in the troposphere. The largest effect is observed at the surface for the case with a SZA of about 37° and for airmasses of European origin: $F(O^1D)$ is 7.7% higher when the climatological ozone profile, instead of the measured profile, is used in the calculations. The overestimate of $F(O^1D)$ decreases with altitude. A smaller effect (2.5%) is observed during the desert dust event, for a solar zenith angle of about 55°.
Calculations at fixed SZA show that during the desert dust event $F(NO_2)$ is reduced up to 24% in the lower and middle troposphere, with respect to the continental/marine aerosol cases. The actinic flux reduction increases with SZA, and the largest reduction occurs at the aerosol peak. Profiles of $F(O^1D)$ are largely determined by total ozone and its vertical distribution.
In conclusion, the derivation of actinic fluxes at the surface does not require a detailed knowledge of the aerosol vertical distribution. The aerosol profile is conversely needed for an accurate description of the photochemistry in the middle troposphere in cases of severely perturbed aerosol profiles, and in particular during desert dust events. In these cases the aerosol climatology does not provide a reliable description of the vertical particles' distribution.
The knowledge of the ozone vertical profile is needed for an accurate estimate of $F(O^1D)$ at the surface; the influence of the ozone vertical profile on $F(O^1D)$ decreases with altitude, and reliable estimates of the actinic flux may be derived in the middle troposphere by means of a climatological profile.

The impact of the dust vertical distribution, for several values of aerosol optical depth and single scattering albedo, on the instantaneous and daily average visible (400-700 nm) direct RF at the surface and at the TOA, have been studied in paragraph 5.3 through the application of the RT model and the use of measured dust vertical profiles. The simulations refer to July 14 and 16, 2002 and to 18 May, 1999.
The aerosol radiative forcing at the surface shows a very small dependency on the aerosol vertical profile. The instantaneous forcing at the surface varies with the solar zenith angle,

reaching a maximum (in absolute value) between 50° and 70°. The angle of the maximum forcing decreases as the aerosol absorption increases (i.e. for decreasing single scattering albedo), and for increasing optical depth.
At the TOA the radiative forcing by particles characterized by low absorption depends weakly on the vertical profile (different profiles produce up to 10% variation on the daily average forcing). The radiative forcing at the surface and at the TOA varies almost linearly with the optical depth.
The vertical distribution of absorbing particles, conversely, strongly affects the estimated radiative forcing at the TOA: variations of the daily forcing up to 100% are found when the standard profile is used in the simulation instead of the measured profile. The TOA visible radiative forcing efficiency produced by dust having single scattering albedo <0.7 is higher by 4 W m^{-2} when the observed vertical profile instead of the standard profile is used in the calculations (i.e. dust produces a lower cooling). For values of the single scattering albedo around 0.67 the sign of the forcing depends on the vertical profile. The influence of the vertical distribution on the radiative forcing is largest at small SZA, and at short wavelengths. Thus, a correct estimate of the radiative forcing of absorbing particles, as is often the case of desert dust, requires the knowledge of the aerosol vertical distribution. These results find a particular application in satellite remote sensing for two main reasons: firstly because the overpass time for most of the operative space-borne sensors corresponds to small solar zenith angles, when the influence of the vertical aerosol distribution on the radiative forcing is more important; second because the inversion algorithms of satellite observations use climatological aerosol profiles, which may significantly different from those occurring, for example, during desert dust outbreaks.

CONCLUDING REMARKS

Aerosols represent one of the largest uncertainties in climate forcing assessments, due to the lack of detailed knowledge of their optical properties. Monitoring of atmospheric aerosols is a fundamentally difficult problem. First, compared to atmospheric gases, aerosols are highly inhomogeneous and variable both in time and space; that is, aerosol observations have to be global and continuous. Second, the available accuracy of aerosol characterization is often not sufficient. Thus, detailed knowledge of the optical properties of the key aerosol types is needed to clarify the mechanisms of aerosol radiative forcing.

Modelling the aerosol effects on atmospheric radiation, by solving the radiative transfer equation, requires the following aerosol optical properties: aerosol optical depth (i.e. loading), phase function (angular dependence of light scattering), and single scattering albedo ω_0 (ratio of scattering to extinction). The sensitivity of radiative forcing to observed natural and anthropogenic variations of the above-listed optical properties characterizes the impact of the atmospheric aerosol on climate change. Present radiative models are particularly uncertain concerning values of the single scattering albedo. The magnitude of ω_0 is mostly dependent on the complex part of the refractive index and particle size. For example, ω_0 of desert dust simulated according to a number of models [*Shettle*, 1989; *d'Almeida et al.*, 1991; *Hess et al.*, 1998] has a wide range of variability. Such uncertainty is unacceptable, since even small changes of ω_0 would change the radiative forcing of desert dust from cooling to warming.

According to *IPCC* [2001] the global, annual mean radiative forcing for the mineral dust aerosol of anthropic origin is estimated to range between –0.6 and +0.4 W m^{-2}; the level of scientific understanding is however defined "very low", since estimates of the aerosol direct radiative forcing are affected by uncertainties deriving from an inadequate knowledge of the aerosol composition and associated optical properties.

In the Mediterranean basin transport of mineral dust from the Sahara desert is rather common and is modulated by the synoptic meteorological conditions. Because of its latitude, the Mediterranean Sea is located in a transitional zone where mid-latitude and tropical variability are both important. The Southern part of the region is mostly under the influence of the descending branch of the Hadley cell, while the Northern part is more linked to the mid-latitude variability, characterized by the North Atlantic Oscillation (NAO) and other mid-latitude teleconnection patterns. As a consequence, the basin is part of the time reached by airmasses from Europe, mainly carrying continental/polluted aerosols, and part of the time exposed to air coming from Africa, especially in spring/early summer, carrying high amounts of desert dust.

At the island of Lampedusa, in the Southern sector of the Central Mediterranean, the ENEA Laboratory for Climate Observations performs continuous measurements of ozone, solar radiation, and aerosols since 1998, with the aim of monitoring their long-term changes and of

studying the effects that different aerosol types can exert on the radiation levels. The station hosts the aerosol lidar from the University of Rome "La Sapienza", measuring vertical distributions of tropospheric aerosols since 2002.

The aim of this research was the retrieval of the aerosol properties over the Central Mediterranean using a combination of measurements performed at Lampedusa by instruments deployed at ground level, aboard aircraft and satellite. The collected data allow the characterization of some aerosol properties (spectral optical depth and vertical distribution), the ozone content, and the levels of ultraviolet and visible radiation at different altitudes in the atmosphere. A detailed radiative transfer model (UVSPEC), initialised with the observations, is applied to simulate the measured radiation levels: this "closure" approach allows to determine the unknown parameters and to isolate effects attributable to different factors. The model is also a useful tool to calculate the aerosol direct radiative forcing, simulating the irradiance with and without aerosols.
The main objectives of the work were:

1) to retrieve the aerosol optical properties, such as single scattering albedo and asymmetry factor, and to estimate the aerosol direct radiative forcing at the surface and at the top of the atmosphere;
2) to study the influence of the aerosol and ozone vertical distribution on radiation levels and on the radiative forcing at the surface, in the troposphere, and at the top of the atmosphere.

The approach to these aspects of the aerosol problem is the same, based on the reproduction of the measurements by means of the radiative transfer model. The differences among the various studies described in this thesis are in the fact that not all kind of measurements (from ground-based, airborne and spaceborne instruments) are always available, so that each analysis is based on the available data. Moreover, it will be shown that measurements from various instruments collected in a short time period (for example during intensive field campaigns) allowed to retrieve detailed information about the aerosol properties, while measurements carried on during a longer time period allow to derive the average aerosol properties, without focusing on single episodes.

The first of the two goals has been achieved in three studies described in Chapter 4.

In the first study cloud-free days during the PAUR II campaign with dust from the Saharan desert (May 18, 1999) and continental/maritime aerosols from Europe (May 25 and 27, 1999) have been selected, when a large set of ground-based measurements were available. The radiative transfer model was initialised with all the measured parameters, allowing for a detailed comparison of the observed and the simulated irradiances in the UV and visible. The estimated ω_0 and asymmetry factor g at 500 nm for the desert dust are in the range 0.73-0.84 and in the range 0.75-0.79, respectively. Radiative transfer calculations show that differences of the surface ultraviolet irradiance larger than 10% may arise from the lack of a detailed knowledge of the aerosol size distribution. Aerosols may also increase or reduce the absorption effectiveness of tropospheric ozone, depending on the characteristics of the particles. Estimates of the direct aerosol radiative forcing in the spectral range 300-800 nm and of the radiative forcing in the range 400-700 nm per unit optical depth at the surface and at the top of the atmosphere were also derived. At the surface aerosols produce a decrease of the instantaneous downward irradiance with respect to an aerosol-free atmosphere by 70.8, 37.2 and 39.1 W m^{-2}, for May 18 (the aerosol optical depth is 0.511 at 415.6 nm), 25 (0.165)

and 27 (0.224), respectively. The radiative forcing per unit optical depth at the surface is largest for aerosol of continental/marine origin, transported from North. The forcing at the top of the atmosphere is negative, thus producing a cooling, in the desert dust case, and close to zero or positive for aerosol originating from North.

The second study describes a closure experiment, when ground-based measurements were combined with simultaneous space-borne observations from the Multi-angle Imaging Spectro-Radiometer (MISR), to derive column-integrated aerosol optical properties, ω_0 and g, on two days of July 2002, 14 and 16, when airmasses originating from Africa and loaded by a moderate amount of desert dust reached Lampedusa. Large, irregular particles were present in the atmospheric layers between 2 and 6 km on July 14, and between 1 and 5 km on July 16. According to backtrajectory analysis, the airmasses arriving at Lampedusa spent a large fraction of the previous days over Central Sahara on July 14, while passed over Northern Africa on July 16. The different trajectories influence the value of the Ångström exponent, depolarisation, and backscattering produced by aerosols. A significant increase of the aerosol optical depth in the ultraviolet is observed, and is attributed to steep variations of the particles' refractive index. The radiative transfer model is used to reconstruct the observed radiative fluxes at the surface and the radiance at the satellite altitude, and to estimate the direct aerosol radiative forcing in the 290-800 nm and in the visible spectral range. Best agreement between measured and modelled radiative fluxes is found for values of the single scattering albedo of 0.96-0.97 (July 14) and 0.88-0.89 (July 16), and of the asymmetry factor of 0.79-0.80 (July 14) and 0.81-0.82 (July 16), indicating that significantly different optical properties pertain to dust particles of different origin. The instantaneous direct radiative forcing per unit optical depth over the 400-700 nm spectral interval is –(39-79) W m^{-2} at the surface, and –(5-20) W m^{-2} at the top of the atmosphere: the cooling effect of the desert dust at the top of the atmosphere, already observed in the first analysis, is confirmed. Although desert dust is the dominant aerosol type on both days, large differences, as large as a factor of 2 in the forcing efficiency at the surface, and a factor of 3 at the top of the atmosphere, are found. Calculations were also performed to study the effect of non-spherical aerosol shapes by using different scattering phase functions, and comparing modelled and measured reflectivities at the nine observation angles of MISR. The different phase functions match the observed wavelength dependence of the aerosol optical depth, and produce similar reflectance patterns for a scattering angle <150°. The effect of non-spherical particles becomes important mainly at scattering angles in the 150-180° interval. This effect should be taken into account in the derivation of radiation fluxes from satellite radiance measurements.
In the third study measurements of direct and diffuse irradiance performed by a multi-filter rotating shadowband radiometer (MFRSR) at 415.6 nm and 868.7 nm at Lampedusa in the period July 2001-September 2003 were used to classify various aerosol types carried by airmasses of different origin: among them, biomass burning-urban/industrial aerosols mostly from the European continent, and desert dust from the Saharan region. The radiative transfer model has been applied to reproduce the MFRSR diffuse-to-direct ratio (DDR), using the measured aerosol optical depth (AOD) as model input, to retrieve the single scattering albedo at the two wavelengths. Sensitivity studies were performed in order to check how the uncertainties of the measured AOD and DDR, and of the assumed asymmetry factor and surface albedo influence the retrieved ω_0 values. The results show that a 3% variation in the AOD or DDR gave a change in ω_0 of about 0.02 at 415.6 and 868.7 nm; when varying the asymmetry factor within the interval $g \pm 0.06$ ω_0 varies by no more than 0.04 at 415.6 nm and 0.06 at 868.7 nm; finally, increasing the assumed surface albedo of 0.05 gave very small changes in the ω_0 values (0.01-0.02). The calculations show that ω_0 of desert dust (DD)

increases with λ from 0.81±0.05 at 415.6 nm to 0.94±0.05 at 868.7 nm; on the contrary, ω_0 of urban/industrial (UN) aerosols decreases from 0.96±0.02 at 415.6 nm to 0.87±0.07 at 868.7 nm; for biomass burning (BB) particles ω_0 is 0.82±0.04 at 415.6 nm and 0.80±0.05 at 868.7 nm. Episodes of UN aerosols occurred in June and July, while those of BB with the largest AOD and duration are observed in July and August, generally the driest months of the year, when the development of fires is favoured.
The analyses in Chapter 4 evidence how the knowledge of the aerosol optical properties is a complex problem, not only for the variability of the aerosol types, but also because cases of occurrence of the same aerosol type present a high variability in particles amount, dimensions and composition, reflected in their properties.

The influence of the vertical ozone and aerosol distributions on the radiation levels and on the aerosol radiative forcing has been studied by means of radiative transfer simulations at the surface and at various altitudes in the atmosphere, in the lower troposphere and at the top of the atmosphere. Two analyses, described in Chapter 5, were devoted to this goal.

During PAUR II UV and visible actinic fluxes and ozone have been measured in the troposphere during aircraft flights performed on May 18, 25 and 27, 1999. The profiles of actinic fluxes in cloud-free days with desert dust and continental/maritime aerosols were reproduced with the model using both measured and model default ozone and aerosol vertical distributions and the differences with respect to observations have been explained. A good agreement between measurements and model results is obtained in all the examined cases. Calculations at fixed solar zenith angle show that during the desert dust event the actinic flux in the band of NO_2 photodissociation is reduced up to 24% in the lower and middle troposphere, with respect to the continental/marine aerosol cases. The actinic flux reduction increases with solar zenith angle, and the largest reduction occurs at the aerosol peak. To identify the influence of the aerosol vertical distribution, that in the desert dust case is extremely different from the generally assumed climatological profiles, model calculations were performed with the observed and the climatological distributions. The vertical distribution of aerosol particles does not influence the modelled fluxes at the surface, that basically depend on the aerosol column amount. Its detailed knowledge is conversely important to obtain accurate model results in the lower and middle troposphere: when the climatological instead of the measured profile is used, the actinic fluxes are within ±3% of the measurements in the days of low-to-moderate optical depths; the modelled fluxes largely overestimate, up to 19%, the measurements in the desert dust case. The sensitivity of the actinic fluxes in the $O_3 + h\nu \rightarrow O_2 + O(^1D)$ photodissociation region on the ozone distribution was studied by performing model calculations with the measured and the climatological profile. The ozone profile appears to affect the actinic fluxes in the O_3 photodissociation region, particularly at small solar zenith angles and near the surface. Due to an increase of the radiation scattering caused by aerosols in the troposphere, the model fluxes at the surface obtained with the climatological profile are 7.7% higher than those obtained with the measured profile for a zenith angle of about 37°; differences are smaller (2.5%) at 55°, and decrease with altitude.

In the second study the radiative transfer model has been used to estimate the visible direct radiative forcing due to desert dust at the surface and at the top of the atmosphere using different vertical aerosol profiles measured at Lampedusa (on May 18, 1999 and July 14 and 16, 2002) and model default as input. The discrepancies have been highlighted and discussed, and the impact of the aerosol optical depth and of the single scattering albedo on the

computed radiative forcing was also examined. The aerosol radiative forcing at the surface shows a very small dependency on the aerosol vertical profile, as already found in the previous analysis. At the top of the atmosphere, the radiative forcing is weakly dependent on the vertical profile (up to 10% variation on the daily average forcing) for low absorbing particles; conversely, it shows a strong dependency (the daily radiative forcing may vary up to 100%) for absorbing particles. The top of the atmosphere visible radiative forcing efficiency produced by dust having $\omega_0<0.7$ is higher by 4 W m^{-2} when the observed vertical profile instead of the climatological profile is used in the calculations (i.e. it produces a lower cooling). For values of ω_0 around 0.67 the sign of the forcing depends on the vertical profile. The influence of the vertical distribution on the radiative forcing is largest at small values of the solar zenith angle, and at short wavelengths.
The results achieved in Chapter 5 find a particular application in satellite remote sensing for two main reasons: firstly because the overpass time for most of the operative space-borne sensors corresponds to small solar zenith angles, when the influence of the vertical aerosol distribution on the radiative forcing is more important; second because the inversion algorithms of satellite observations use climatological aerosol profiles, which may significantly different from those occurring, for example, during desert dust outbreaks. Moreover, in all the cases when the radiation at any level in the troposphere has to be studied in detail, the aerosol and ozone vertical profiles have to be known. Conversely, the knowledge of the aerosol vertical profile is not necessary when the radiation at the surface is taken into account.

The achieved results constitute the first estimates of the aerosol radiative impact in the Central Mediterranean and point out the need of a thorough analysis of the wide and complicated aerosol problem. For example, the aerosol optical properties in the IR should be studied in order to evaluate the aerosol impact on the Earth-atmosphere radiative balance. The study of the optical properties of hygroscopic aerosols with changing relative humidity should be relevant for many aspects, such as the estimate of the aerosol semi-direct effects, i.e. their ability to inhibit the cloud formation, and indirect effects, i.e. their impact on the microphysical and radiative properties and lifetime of clouds. Moreover, further efforts should be devoted to understand the heterogeneous chemistry of important gases, such as ozone, occurring on the surface of some aerosol particles. Finally, a complete experiment, with the simultaneous measurements from ground-based, airborne and spaceborne instruments would evidence the relative importance of each instrument when trying to retrieve information on atmospheric properties.

APPENDIX A

THE DISCRETE ORDINATE METHOD

The discrete ordinate method was first developed by *Chandrasekhar* [1960]. It applies to resolve the radiative transfer (RT) problem in a plane-parallel atmosphere constituted of non-homogeneous and non-isotherm, absorbing, emitting and anisotropically scattering layers. The basic characteristic of the method is the discretization of the basic RT equation and the solution of a set of first-order differential equations.

Recall the RT equation for azimuthally-dependent diffuse intensity I_ν (equation 1.6.32)

$$\mu \frac{\mathrm{d}I_\nu}{\mathrm{d}\tau_\nu} = -I_\nu + \frac{\omega_{0\nu}}{4\pi} F_{0\nu} P_\nu(\mu, \varphi, \mu_0, \varphi_0) \exp(-\tau_\nu/\mu_0) + \\ + \frac{\omega_{0\nu}}{4\pi} \int_0^{2\pi} \int_{-1}^{1} I_\nu(\mu', \phi') \, P_\nu(\mu, \varphi, \mu', \varphi') \, \mathrm{d}\mu' \mathrm{d}\varphi'. \tag{A.1}$$

The azimuthally-independent diffuse intensity is (the suffix ν will be omitted)

$$\mu \frac{\mathrm{d}I(\tau, \mu)}{\mathrm{d}\tau} = -I(\tau, \mu) + \frac{\omega_0}{4\pi} F_0 P(\mu, \mu_0) \exp(-\tau/\mu_0) + \frac{\omega_0}{2} \int_{-1}^{1} I(\tau, \mu') \, P(\mu, \mu') \, \mathrm{d}\mu' . \tag{A.2}$$

For isotropic scattering, the phase function is 1, hence

$$\mu \frac{\mathrm{d}I(\tau, \mu)}{\mathrm{d}\tau} = -I(\tau, \mu) + \frac{\omega_0 F_0}{4\pi} \exp(-\tau/\mu_0) + \frac{\omega_0}{2} \int_{-1}^{1} I(\tau, \mu') \, \mathrm{d}\mu' . \tag{A.3}$$

If the Gauss formula is applied to replace the integral in equation (A.2) the result is

$$\mu_i \frac{\mathrm{d}I(\tau, \mu_i)}{\mathrm{d}\tau} = -I(\tau, \mu_i) + \frac{\omega_0 F_0}{4\pi} \exp(-\tau/\mu_0) + \frac{\omega_0}{2} \sum_{j=-n}^{n} a_j I(\tau, \mu_j) \tag{A.4}$$

where $i = -n, \ldots, n$ ($2n$ terms), a_j are the Gauss weights (constants), and μ_j are quadrature angles (or points).

Equation (A.4) is a system of $2n$ inhomogeneous differential equations, for which the solution is the sum of a general and a particular solution; the general solution is a solution of the homogeneous part of equation (A.4), that is

$$\mu_i \frac{\mathrm{dI}(\tau,\mu_i)}{\mathrm{d}\tau} = -\mathrm{I}(\tau,\mu_i) + \frac{\omega_0}{2}\sum_{j=-n}^{n} a_j \mathrm{I}(\tau,\mu_j)\,. \tag{A.5}$$

Denoting $I_i = I(\tau,\mu_i)$ the general solution of (A.5) can be found as

$$I_i = g_i \exp(-k\tau)\,. \tag{A.6}$$

Inserting (A.6) into (A.4) it becomes

$$g_i(1+\mu_i k) = \frac{\omega_0}{2}\sum_{j=-n}^{n} a_j g_j\,. \tag{A.7}$$

The terms g_i can be found in the form

$$g_i = L/(1+\mu_i k) \tag{A.8}$$

where L is constant to be determined. Substituting this expression for g_i into (A.7), we have

$$1 = \frac{\omega_0}{2}\sum_{j=-n}^{n}\frac{a_j}{1+\mu_j k} = \omega_0\sum_{j=1}^{n}\frac{a_j}{1-\mu_j^2 k^2}\,. \tag{A.9}$$

Equation (A.9) gives 2n solutions for $\pm k_j$ (j=1, …, n).
The general solution is

$$I_i = \sum_j \frac{L_j}{1+\mu_i k_j}\exp(-k_j\tau) \tag{A.10}$$

where L_j are constants.
The particular solution can be found as

$$I_i = \frac{\omega_0 \mathrm{F}_0}{4\pi} h_i \exp(-\tau/\mu_0) \tag{A.11}$$

where h_i are constants.
Inserting (A.11) into equation (A.4) we have

$$h_i(1+\mu_i/\mu_0) = \frac{\omega_0}{2}\sum_{j=-n}^{n} a_j h_j + 1\,. \tag{A.12}$$

From equation (A.12) h_i is found as

$$h_i = \gamma/(1+\mu_i/\mu_0) \tag{A.13}$$

where γ is determined from

$$\gamma = 1\Big/\left[1 - \frac{\omega_0}{2}\sum_{j=1}^{n}\frac{a_j}{1-\mu_j^2/\mu_0^2}\right]. \tag{A.14}$$

Adding the general solution (A.10) to the particular solution (A.11), we have the solution

$$I_i = \sum_j \frac{L_j}{1+\mu_i k_j}\exp(-k_j\tau) + \frac{\omega_0 \mathrm{F}_0 \gamma}{4\pi(1+\mu_i/\mu_0)}\exp(-\tau/\mu_0) \tag{A.15}$$

where L_j are constants to be determined form the boundary conditions.
Equation (A.15) gives a simple solution for the semi-infinite isotropic atmosphere.

Let's consider the atmosphere with non-isotropic scattering.
The diffuse intensity can be expanded in the cosine series

$$\mathrm{I}(\tau,\mu,\varphi)=\sum_{m=0}^{\mathrm{N}}\mathrm{I}^{m}(\tau,\mu)\cos m(\varphi_0-\varphi)\,. \tag{A.16}$$

By virtue of their unique mathematical properties, the Legendre polynomials have been extensively used in the analysis of RT problems.
The phase function can be expresses in terms of Legendre polynomials, in the form

$$\mathrm{P}(\cos\Theta)=\sum_{l=0}^{\mathrm{N}}\varpi_l\mathrm{P}_l(\cos\Theta) \tag{A.17}$$

or, using the relation between Θ and (μ,φ)

$$\mathrm{P}(\mu,\varphi,\mu',\varphi')=\sum_{m=0}^{N}\sum_{l=m}^{N}\varpi_l^m\mathrm{P}_l^m(\mu)\mathrm{P}_l^m(\mu')\cos m(\varphi'-\varphi) \tag{A.18}$$

where P_l^m denotes the associated Legendre polynomials and

$$\varpi_l^m=(2-\delta_{0,m})\varpi_l\frac{(l-m)!}{(l+m)!}\,. \tag{A.19}$$

Substituting (A.16) and (A.17) into (A.1) the equation of transfer splits into N+1 independent equations of the form

$$\begin{aligned}\mu\frac{\mathrm{dI}^m(\tau,\mu)}{\mathrm{d}\tau}=&-\mathrm{I}^m(\tau,\mu)+(1+\delta_{0,m})\frac{\omega_0}{4}\sum_{l=m}^{N}\varpi_l^m P_l^m(\mu)\times\int_{-1}^{1}P_l^m(\mu')\mathrm{I}^m(\tau,\mu')\mathrm{d}\mu'+\\&+\frac{\omega_0}{4\pi}\sum_{l=m}^{N}\varpi_l^m\mathrm{P}_l^m(\mu)\mathrm{P}_l^m(-\mu_0)\mathrm{F}_0\exp(-\tau/\mu_0).\end{aligned} \tag{A.20}$$

To proceed with the solution of (A.20) first of all the discretization of the equation is performed as in (A.4), by replacing μ with μ_i (i= -n, …, n) and the integral with the sum with the weights a_j.
The homogeneous solution for the set of first-order differential equations can be written as

$$I^m(\tau,\mu_i)=\sum_{j=-n}^{n}L_j^m\phi_j^m(\mu_i)\exp(-k_j^m\tau) \tag{A.21}$$

where ϕ_j^m and k_j^m denote the eigenvectors and eigenvalues, respectively, and L_j^m are coefficients to be determined from appropriate boundary conditions. Substituting (A.21) into the homogeneous part of (A.20) the eigenvectors can be expressed by

$$\phi_j^m(\mu_i)=\frac{(1+\delta_{0,m})\omega_0}{4(1+\mu_j k_j^m)}\sum_{l=m}^{N}\varpi_l^m P_l^m(\mu_i)\sum_{\alpha=-n}^{n}a_\alpha\mathrm{P}_l^m(\mu_\alpha)\phi_j^m(\mu_\alpha)\,. \tag{A.22}$$

The particular solution may be written in the form

$$I_p^m(\tau,\mu_i)=Z^m(\mu_i)\exp(-\tau/\mu_0)\,. \tag{A.23}$$

From equation (A.20)

$$\begin{aligned}Z^m(\mu_i)=&\frac{\omega_0}{4(1+\mu_i/\mu_0)}\sum_{l=m}^{N}\varpi_l^m P_l^m(\mu_i)\times\sum_{\alpha=-n}^{n}a_\alpha\mathrm{P}_l^m(\mu_\alpha)Z^m(\mu_\alpha)+\\&+\mathrm{P}_l^m(-\mu_0)\frac{\mathrm{F}_0}{\pi}.\end{aligned} \tag{A.24}$$

Equations (A.22) and (A.24) are linear equations in ϕ_j^m and Z^m and may be solved numerically. The complete solution for equation (A.1) is the sum of the general (A.21) and the particular (A.23) solution

$$I^m(\tau,\mu_i) = \sum_{j=-n}^{n} L_j^m \phi_j^m(\mu_i)\exp(-k_j^m\tau) + Z^m(\mu_i)\exp(-\tau/\mu_0)\,. \qquad \text{(A.25)}$$

In order to determine the unknown coefficients L_j^m, boundary conditions must be imposed.

At the top of the atmosphere we have no downward diffuse intensity

$$I^{m=0}(0,-\mu_i) = 0\,. \qquad \text{(A.26)}$$

Assuming that there are no external radiation sources from above and below a layer with an optical depth τ_m, at the layer's boundary upward and downward intensities must be continuous

$$I^m(\tau_m,\mu_i) = I^{m+1}(\tau_m,\mu_i)\,. \qquad \text{(A.27)}$$

At the bottom of the atmosphere, assuming a Lambertian surface with albedo r_{surf}

$$I^{m=N}(\tau_N,\mu_i) = \frac{r_{surf}}{\pi}\left[F^{\downarrow}(\tau_N) + \mu_0 F_0 \exp(-\tau_N/\mu_0)\right]. \qquad \text{(A.28)}$$

Equations (A.26) to (A.28) provide necessary conditions to find the unknown coefficients for i=1, …, n and m=0, …, N.

REFERENCES

Ackerman, S. A., and H. Chung, Radiative effects of airborne dust on regional energy budgets at the top of the atmosphere, *J. Appl. Meteor.*, *31*, 223-241, 1992.

Anderson, G. P., S. A. Clough, F. X. Kneizys, J .H. Chetwynd, and E. P. Shettle, AFGL Atmospheric Constituent Profiles (0-120 km), AFGL-TR-86-0110, AFGL (OPI), Hanscom AFB, MA 01736, 1986.

Bais, A. F., C. S. Zerefos, and C. T. McElroy, Solar UVB measurements with the double- and single- monochromator Brewer ozone spectrophotometer, *Geophys. Res. Lett.*, *23*, 833-836, 1996.

Bais, A. F., S. Kazadzis, D. Balis, Zerefos, and M. Blumthaler, Correcting global solar ultraviolet spectra recorded by a Brewer spectroradiometer for its angular response error, *Appl. Opt.*, *37*, 6339-6344, 1998.

Balis, D. S., V. Amiridis, C. S. Zerefos, E. Gerasopoulos, M. Andreae, P. Zanis, A. Kazadzis, and A. Papayannis, Raman lidar and sunphotometric measurements of aerosol optical properties over Thessaloniki, Greece during a biomass burning episode, *Atmos. Env.*, *37*, 4529-4538, 2003.

Bergametti, G., A.-L. Dutot, P. Buat-Ménard, R. Losno, and E. Remoudaki, Seasonal variability of the elemental composition of atmospheric aerosol particles over the northwestern Mediterranean, *Tellus*, *41B*, 353-361, 1989.

Bergstrom, R. W., P. B. Russell, and P. Hignett, Wavelength dependence of the absorption of black carbon particles: predictions and results from the TARFOX experiment and implications for the single scattering albedo, *J. Atmos. Sci.*, *59*, 567-577, 2002.

Bergstrom, R. W., P. Pilewskie, B. Schmid, and P. B. Russell, Estimates of the spectral aerosol single scattering albedo and aerosol radiative effects during SAFARI 2000, *J. Geophys. Res.*, *108*(D13), 8474, doi:10.1029/2002JD002435, 2003.

Bhartia, P. K., D. Silberstein, B. Monosmith, and A. J. Fleig, Standard profiles of ozone from ground to 60 km obtained by combining satellite and ground based measurements, in *Atmospheric Ozone*, edited by C. S. Zerefos and A. Ghazi, pp. 243-247, Reidel Publishing Company, Dordrecht, The Netherlands, 1985.

Blumthaler, M., and W. Ambach, Solar UVB albedo of various surfaces, *Photochem. Photobiol.*, 48, 85-88, 1988.

Boucher, O., et al., Intercomparison of models representing direct shortwave radiative forcing by sulfate aerosols, *J. Geophys. Res.*, *103*, 16979-16998, 1998.

Bowker, D. E., R. E. Davis, D. L. Myrik, K. Stacy, and W. T. Jones, Spectral reflectance of natural targets for use in remote sensing studies, *NASA Ref. Publ.*, 1985.

Bruegge, C. J., D. J. Diner, R. P. Korechoff, and M. Lee, MISR Level 1 radiance scaling and conditioning algorithm theoretical basis, Jet Propul. Lab., Pasadena, CA, JPL D-11507, Rev. E, 1999.

Brühl, C., and P. J. Crutzen, On the disproportionate role of tropospheric ozone as a filter against solar UV-B radiation, *Geophys. Res. Lett.*, *16*, 703-706, 1989.

Bucholtz, A., Rayleigh-scattering calculations for the terrestrial atmosphere, *Appl. Opt.*, *34*, 2765-2773, 1995.

Burrows, J. P., A. Dehn, B. Deters, S. Himmelmann, A. Richter, S. Voigt, and J. Orphal, Atmospheric remote-sensing reference data from GOME: 2. Temperature-dependent absorption cross sections of O_3 in the 231-794 nm range, *J. Quant. Spectrosc. Radiat. Transfer, 61*, 509-517, 1999a.

Burrows, J. P., et al.., The Global Ozone Monitoring Experiment (GOME): Mission Concept and First Scientific Results, *J. Atmos. Sci.*, *56*, 151-175, 1999b.

Cachorro V. E., P. Utrillas, R. Vergaz, P. Durán, A. M. de Frutos, and J. A. Martinez-Lozano, Determination of the atmospheric-water-vapor content in the 940-mm absorption band by use of moderate spectral-resolution measurements of direct solar irradiance, *Appl. Opt.*, *37*, 4678-4689, 1998.

Cattrall, C., K. L. Carder, and H. R. Gordon, Columnar aerosol single-scattering albedo and phase function retrieved from sky radiance over the ocean: Measurements of Saharan dust, *J. Geophys. Res.*, *108* (D9), 4287, doi: 10.1029/2002JD002497, 2003.

Chester, R., E. J. Sharples, G. D. Sanders, and A. C. Saydam, Saharan dust incursion over the Tyrrhenian sea, *Atmos. Envoron.*, *18*, 929-935, 1984.

Conant, W. C., An observational approach for determining aerosol surface radiative forcing: Results from the first field phase of INDOEX, *J. Geophys. Res.*, *105*, 15347-15360, 2000.

Conant, W. C., J. H. Seinfeld, J. Wang, G. R. Carmichael, Y. Tang, I. Uno, P. J. Flatau, K. M. Markowicz, and P. K. Quinn, A model for the radiative forcing during ACE-Asia derived from CIRPAS Twin Otter and R/V *Ronal H. Brown* data and comparison with observations, *J. Geophys. Res.*, *108*(D23), 8661, doi:10.1029/2002JD003260, 2003.

d'Almeida, G. A., P. Koepke, and E. P. Shettle, *Atmospheric Aerosols Global Climatology and Radiative Characteristics*, A. Deepak, Hampton, Va, 1991.

Di Iorio, T., A. di Sarra, W. Junkermann, M. Cacciani, G. Fiocco, and D. Fuà, Tropospheric aerosols in the Mediterranean: 1. Microphysical and optical properties, *J. Geophys. Res.*, *108*(D10), 4316, doi:10.1029/2002JD002815, 2003.

di Sarra, A., M. Cacciani, M. Campanelli, P. Chamard, C. Cornwall, J. DeLuisi, L. De Silvestri, T. Di Iorio, P. Disterhoft, G. Fiocco, D. Fuà, P. Grigioni, W. Junkermann, F. Marenco, D. Meloni, F. Monteleone, and B. Olivieri, Radiation, ozone, and aerosol measurements at Lampedusa during the PAUR II Campaign, in *IRS 2000: Current Problems in Atmospheric Radiation*, edited by W. L. Smith and Yu. M. Timofeyev, pp. 1193-1196, A. Deepak Publishing, Hampton, Virginia, 2001a.

di Sarra, A., T. Di Iorio, M. Cacciani, G. Fiocco, and D. Fuà, Saharan dust profiles measured by lidar at Lampedusa, *J. Geophys. Res.*, *106*, 10335-10348, 2001b.

di Sarra, A., M. Cacciani, P. Chamard, C. Cornwall, J. J. DeLuisi, T. Di Iorio, P. Disterhoft, G. Fiocco, D. Fuà, and F. Monteleone, Effects of desert dust and ozone on the ultraviolet irradiance at the Mediterranean island of Lampedusa during PAUR II, *J. Geophys. Res.*, *107*(D18), 8135, doi:10.1029/2000JD000139, 2002.

Dahlback, A., and K. Stamnes, A new spherical model for computing the radiation field available for photolysis and heating at twilight, *Planet. Space Sci.*, *39*, 671-683, 1991.

Díaz, J. P., F. J. Expósito, C. J. Torres, V. Carreño, and A. Redondas, Simulation of mineral dust effects on UV radiation levels, *J. Geophys. Res.*, *105*, 4979-4991, 2000.

Díaz, J. P., F. J. Expósito, C. J. Torres, F. Herrera, J. M. Prospero, and M. C. Romero, Radiative properties of aerosols in Saharan dust outbreaks using ground-based and satellite data: Applications to radiative forcing, *J. Geophys. Res.*, *106*, 18403-18416, 2001.

Diner, D. J., et al., Multi-angle Imaging SpectroRadiometer (MISR) instrument description and experiment overview, *IEEE Trans. Geosci. Rem. Sens.*, *36*, 1072-1087, 1998.

Diner, D. J., L. Di Girolamo, and E. E. Clothiaux, MISR Level 1 cloud detection algorithm theoretical basis, Jet Propul. Lab. Pasadena, CA, JPL D-13397, Rev. B, 1999.

Doda, D. D., and A. E. S. Green, Surface reflectance measurements in the UV from an airborne platform. Part 1, *Appl. Opt.*, *19*, 2140-2145.

Draxler, R. R., and G. D. Rolph, HYSPLIT (HYbrid Single-Particle Lagrangian Integrated Trajectory) model, *http://www.arl.noaa.gov/ready/hysplit4.html*, NOAA Air Resour. Lab., Silver Spring, MD, 2003.

Drummond, A. J., and M. P. Thekaekara, *The Extraterrestrial Solar Spectrum*, Eds. Institute of Environmental Sciences, Mount Prospect Illinois, 1973.

Dubovik, O., B. N. Holben, Y. J. Kaufman, M. Yamasoe, A. Smirnov, D. Tanré, and I. Slutsker, Single-scattering albedo of smoke retrieved from the sky radiance and solar transmittance measured from ground, *J. Geophys. Res.*, *103*(D24), 31903-31923, 1998.

Dubovik, O., B. Holben, T. F. Eck, A. Smirnov, Y. J. Kaufman, M. D. King, D. Tanré, and I. Slutsker, Variability of absorption and optical properties of key aerosol types observed in worldwide locations, *J. Atmos. Sci.*, *59*, 590-608, 2002.

Duncan, B. N., and I. Bey, A modelling study of the export pathways of pollution from Europe: Seasonal and interannual variation (1987-1997), *J. Geophys. Res.*, *109*, D08301, doi:10.1029/2003JD004079, 2004.

Early, E. E., E. A. Thompson, and P. Disterhoft, Field calibration unit for ultraviolet spectroradiometers, *Appl. Opt.*, *37*, 6664-6670, 1998.

Eck, T. F., B. N. Holben, J. S. Reid, O. Dubovik, A. Smirnov, N. T. O'Neill, I. Slutsker, and S. Kinne, Wavelength dependence of optical depth of biomass burning, urban, and desert dust aerosols, *J. Geophys. Res.*, *104*, 31333-31349, 1999.

Eck, T. F., B. N. Holben, D. E. Ward, O. Dubovik, J. S. Reid, A. Smirnov, M. M. Mukelabai, N. C. Hsu, N. T. O'Neill, and I. Slutsker, Characterisation of the optical properties of biomass burning aerosols in Zambia during the 1977 ZIBBEE fields campaign, *J. Geophys. Res.*, *106*, 3425-3448, 2001.

Eck, T. F. et al., Variability of biomass burning aerosol optical characteristics in southern Africa during the SAFARI 2000 dry season campaign and a comparison of single scattering albedo estimates from radiometric measurements, *J. Geophys. Res.*, *108*(D13), 8477, doi:10.1029/2002JD002321, 2003a.

Eck, T. F., B. N. Holben, J. S. Reid, N. T. O'Neill, J. S. Shafer, O. Dubovik, A. Smirnov, M. A. Yamasoe, and P. Artaxo, High aerosol optical depth biomass burning events: A comparison of optical properties for different source regions, *Geophys. Res. Lett.*, *30*(20), 2035, doi:10.1029/2003GL017861, 2003b.

Estupiñán, J. G., S. Raman, G. H. Crescenti, J. J. Streicher, and W. F. Barnard, Effects of clouds and haze on UV-B radiation, *J. Geophys. Res.*, *101*, 16807-16816, 1996.

Farman, J. C., B. G. Gardiner, and J. D. Shanklin, Large losses of total ozone in Antarctic reveal seasonal ClO_x/NO_x interaction, *Nature*, *315*, 207-210, 1985.

Feister, U., and R. Grewe, Spectral albedo measurements in the UV and visible region over different types of surfaces, *Photochem. Photobiol.*, *62*, 736-744, 1995.

Formenti, P., et al., STAAARTE-MED 1998 summer airborne measurements over the Aegean Sea. 2. Aerosol scattering and absorption, and radiative calculations, *J. Geophys. Res.*, *107*(D21), 4451, doi :10.1029/2001JD001536, 2002.

Fouquart, Y., B. Bonnel, G. Brogniez, J. C. Buriez, L. Smith, J. J. Morcrette, and A. Cerf, Observations of Saharan Aerosols: Results of ECLATS Field Experiment. Part II: Broadband Radiative Characteristics of the Aerosols and Vertical Radiative Flux Divergence, *J. Climate Appl. Meteor.*, *26*, 38-52, 1987.

Fu, Q., and K. N. Liou, On the correlated-k distribution method for radiative transfer in nonhomogeneous atmospheres, *J. Atmos. Sci.*, *49*, 2139-2156, 1992.

Fu, Q., and K. N. Liou, Parametrization of the radiative properties of cirrus clouds, *J. Atmos. Sci.*, *50*, 2008-2025, 1993.

Gilman, C., and C. Garrett, Heat flux parametrizations for the Mediterranean sea: The role of atmospheric aerosols and constraints from the water budget, *J. Geophys. Res.*, *99*, 5119-5134, 1994.

Hallett. J., W. P. Arnott, M. P. Bailey, and J. T. Hallett, Ice crystals in cirrus, in *Cirrus*, edited by D. K. Lynch et al., Oxford Univ. Press, 2002.

Halthore, R. N., M. A. Miller, J. A. Ogren, P. J. Sheridan, D. W. Slater, and t. Stoffel, Further developments in closure experiments for surface diffuse irradiance under cloud-free skies at a continental site, *Geophys. Res. Lett.*, *31*, L07111, doi:10.1029/2003GL019102, 2004.

Harrison, L., J. Michalsky, and J. Berndt, Automated multifilter rotating shadow-band radiometer: an instrument for optical depth and radiation measurements, *Appl. Opt.*, *33*, 5118-5125, 1994a.

Harrison, L., and J. Michalsky, Objective algorithms for the retrieval of optical depths from ground-based measurements, *Appl. Opt.*, *33*, 5126-5132, 1994b.

Haywood, J. M., K. P. Shine, Multi-spectral calculations of the direct radiative forcing of tropospheric sulfate and soot aerosols using a column model, *Q. J. R. Meteorol. Soc.*, *123*, 1907-1930, 1997.

Henyey, L. G., and J. L. Greenstein, Diffuse radiation in the galaxy, *Astrophys. J.*, *93,* 70–83, 1941.

Herman, B. M., R. S. Browning, and J. J. DeLuisi, Determination of the effective imaginary term of the complex refractive index of atmospheric dust by remote sensing: the diffuse-to-direct radiation method, *J. Atmos. Sci.*, *32*, 918-925, 1975.

Herman, J. R., N. Krotkov, E. Celarier, D. Larko, and G. Labow, Distribution of UV radiation at the Earth's surface from TOMS-measured UV-backscattered radiances, *J. Geophys. Res.*, *104*, 12059-12076, 1999.

Hess, M., P. Koepke, and I. Schult, Optical properties of aerosols and clouds: The software package OPAC, *Bull. Amer. Meteor. Soc.*, *79*, 831-844, 1998.

Hignett, P., J. P. Taylor, P. N. Francis, and M. D. Glew, Comparison of observed and modeled direct aerosol forcing during TARFOX , *J. Geophys. Res.*, *104*, 2279-2287, 1999.

Hofzumahaus, A., A. Kraus, A. Kylling, and C. S. Zerefos, Solar actinic radiation (280-420 nm) in the cloud-free troposphere between ground and 12 km altitude: Measurements and model results, *J. Geophys. Res.*, *107*(D18), 8139, doi:10.1029/2001DJ900142, 2002.

Höller, R., K. Ito, S. Tohno, and M. Kasahara, Wavelength-dependent aerosol single-scattering albedo: Measurements and model calculations for a coastal site near the Sea of Japan during ACE-Asia, *J. Geophys. Res.*, *108*(D23), 8648, doi:10.1029/2002JD003250, 2003.

Horvath, H., L. Alados Arboledas, F. J. Olmo, O. Jovanović, M. Gangl, W. Kaller, C. Sánchez, H. Sauerzopf, S. Seidl, Optical characteristics of the aerosol in Spain and

Austria and its effect on radiative forcing, *J. Geophys. Res.*, *107*(D19), 4386, doi :10.1029/2001JD001472, 2002.

Hsu, N. C., J. R. Herman, O. Torres, B. N. Holben, D. Tanre, T. F. Eck, A. Smirnov, B. Chatenet, and F. Lavenu, Comparisons of the TOMS aerosol index with Sun-photometer aerosol optical thickness: Results and applications, *J. Geophys. Res.*, *104*, 6269-6279, 1999.

Hsu, N. C., J. R. Herman, and C. Weaver, Determination of radiative forcing of Saharan dust using combined TOMS and ERBE data, *J. Geophys. Res.*, *105*, 20649-20661, 2000.

Intergovernmental Panel on Climate Change (IPCC), *Climate Change 2001, The Scientific Basis: Contribution of Working Group I to the Third Assessment Report of the International Panel of Climate Change*, edited by J. T. Houghton et al., Cambridge Univ. Press, New York, 2001.

Jayaraman, A., D. Lubin, S. Ramachandran, V. Ramanathan, E. Woodbridge, W. D. Collins, and K. S. Zalpuri, Direct observations of aerosol radiative forcing over the tropical Indian Ocean during the January-February 1996 pre-INDOEX cruise, *J. Geophys. Res.*, *103*, 13827-13836, 1998.

Joseph, J. H., W. J. Wiscombe, and J. A. Weinman, The delta-Eddington approximation for radiative flux transfer, *J. Atmos. Sci.*, *33*, 2452-2459, 1976.

Junkermann, W., An ultralight aircraft as platform for research in the lower troposphere: system performance and first results from radiation transfer studies in stratiform aerosol layers and broken cloud conditions, *J. Atmos. and Ocean. Tech.*, *18*, 934-946, 2001.

Junkermann, W., Measurements of the $J(O^1D)$ actinic flux within and above stratiform clouds and above snow surfaces, *Geophys. Res. Lett.*, *21*, 793-796, 1994.

Junkermann, W., An ultralight aircraft as platform for research in the lower troposphere: system performance and first results from radiation transfer studies in stratiform aerosol layers and broken cloud conditions, *J. Atmos. and Ocean. Tech.*, *18*, 934-946, 2001.

Kahn, R., R. West, D. McDonald, B. Rheingans, and M. I. Mishchenko, Sensitivity of multiangle remote sensing observations to aerosol sphericity, *J. Geophys. Res.*, *102*, 16861-16870, 1997.

Karyampudi, V. M., et al., Validation of the Saharan dust plume conceptual model using lidar, Meteosat, and ECMWF data, *Bull. Amer. Meteor. Soc.*, *80*, 1045-1075, 1999.

Kato, S. t. P. Ackerman, J. H. Mather, and E. E. Clothiaux, The k-distribution method and correlated-k approximation for a shortwave radiative transfer model, *J. Quant. Spectrosc. Radiat. Transfer*, *62*, 109-121, 1999.

Kaufman, Y. J., et al., Smoke, Clouds and Radiation-Brazil (SCAR-B) experiment, *J. Geophys. Res.*, *103*, 31783-31808, 1998.

Kaufman, Y. J., D. Tanré, O. Dubovik, A. Karnieli, and L. A. Remer, Absorption of sunlight by dust as inferred from satellite and ground-based remote sensing, *Geophys. Res. Lett.*, *28*, 1479-1482, 2001.

Kourtidis, K., et al., Regional levels of ozone in the troposphere over Eastern Mediterranean, *J. Geophys. Res.*, *107*(D8), 8140, doi:10.1029/2000JD000140, 2002.

Kouvarakis, G., Y. Doukelis, N. Mihalopoulos, S. Rapsomanikis, J. Sciare, and M. Blumthaler, Chemical, physical, and optical characterization of aerosols during PAUR II experiment, *J. Geophys. Res.*, *107*(D18), 8141, doi:10.1029/2000JD000291, 2002.

Kratz, D. P. The correlated-k distribution technique as applied to the AVHRR channels, *J. Quant. Spectrosc. Radiat. Transfer*, *53*, 501-517, 1995.

Krekov, G. M., Models of atmospheric aerosols, in *Aerosol Effects on Climate,* S. G. Jennings, Ed. Tucson, AZ, Univ. of Arizona Press, 1993.

Kubilay, N., T. Cokacar, and T. Oguz, Optical properties of mineral dust outbreaks over the northeastern Mediterranean, *J. Geophys. Res.*, *108*(D21), 4666, doi: 10.1029/2003JD003798, 2003.

Kurucz, R. L., *Synthetic infrared spectra, in Infrared Solar Physics*, IAU Symposium 154, edited by. D.M. Rabin and J.T. Jefferies, pp. 523-531, Kluwer, Dordrecht, 1992.

Kylling, A., A. F. Bais, M. Blumthaler, J. Schreder, C. S. Zerefos, and E. Kosmidis, Effect of aerosols on solar UV irradiances during the Photochemical Activity and Solar Ultraviolet Radiation campaign, *J. Geophys. Res.*, *103*, 26051-26060, 1998.

Kylling A., and B. Mayer, libRadtran, library for radiative transfer calculations, edition 1.0 for libRadtran version 0.99, 2001.

Léon, J. –F., P. Chazette, J. Pelon, F. Dulac, and H. Randriamiarisoa, Aerosol direct radiative impact over the INDOEX area based on passive and active remote sensing, *J. Geophys. Res.*, *107*(D19), 8006, doi:10.1029/2000JD000116, 2002.

Liao, H., and J. H. Seinfeld, Radiative forcing by mineral dust aerosols: sensitivity to key variables, *J. Geophys. Res.*, *103*, 31637-31645, 1998.

Liao, H., Y. L. Yung, and J. H. Seinfeld, Effects of aerosols on tropospheric photolysis rates in clear and cloudy atmospheres, *J. Geophys. Res.*, *104*, 23697-23707, 1999.

Martonchik, J. V., D. J. Diner, R. A. Kahn, T. P. Ackerman, M. M. Verstaete, B. Pinty, and H. R. Gordon, Techniques for the retrieval of aerosol properties over land and ocean using multiangle imaging, *IEEE Trans. Geosci. Rem. Sens.*, *36*, 1212-1227, 1998.

Mayer, B., G. Seckmayer, and A. Kylling, Systematic long-term comparison of spectral UV measurements and UVSPEC modelling results, *J. Geophys. Res.*, *102*, 8755-8767, 1997.

Meador, W. E., and W. R. Weaver, Two-stream approximation to radiative transfer in planetary atmosphere: a unified description of existing methods and a new improvement, *J. Atmos. Sci.*, *37*, 630-643, 1979.

Mishchenko, M. I., A. A. Lacis, B. E. Carlson, and L. D. Travis, Nonsphericity of dust-like tropospheric aerosols: Implications for aerosol remote sensing and climate modeling, *Geophys. Res. Lett.*, *22*, 1077-1080, 1995.

Mishchenko, M. I., L. D. Travis, R. A. Kahn, and R. A. West, Modeling phase functions for dustlike tropospheric aerosols using a shape mixture of randomly oriented polydisperse spheroids, *J. Geophys. Res.*, *102*, 16831-16847, 1997.

Moulin, C., C. E. Lambert, F. Dulac, and U. Dayan, Control of atmospheric export of dust from north Africa by the north Atlantic oscillation, *Nature*, *387*, 691-694, 1997.

Moulin, C., et al., Satellite climatology of African dust transport in the Mediterranean atmosphere, *J. Geophys. Res.*, *103*, 13137-13144, 1998.

Moulin, C., H. R. Gordon, V. F. Banzon, and R. H. Evans, Assessment of Saharan dust absorption in the visible from SeaWiFS imagery, *J. Geophys. Res.*, *106*(D16), 18239-18249, 2001.

Müller, D., I. Mattis, U. Wandinger, A. Ansmann, D. Althausen, O. Dubovik, S. Eckhardt, and A. Stohl, Saharan dust over a central European EARLINET-AERONET site: Combined observations with Raman lidar and Sun photometer, *J. Geophys. Res.*, *108* (D12), 4345, doi: 10.1029/2002JD002918, 2003.

Pace, G., A. di Sarra, D. Meloni, S. Piacentino, and P. Chamard, Optical properties of aerosols over the Central Mediterranean. 1. Influence of transport and identification of different aerosol types, *Atmos. Chem. Phys. Discuss.*, submitted, 2004.

Payne, R. E., Albedo of the sea surface, *J. Atmos. Sci.*, *29*, 959-970, 1972.

Petters, J. L., V. K. Saxena, J. R. Slusser, B. N. Wenny, and S. Madronich, Aerosol single scattering albedo retrieved from measurements of surface UV irradiance and a radiative transfer model, *J. Geophys. Res.*, *108*(D9), 4288, doi:10.1029/2002JD002360, 2003.

Podgorny, I. A., W. Conant, V. Ramanathan, and S. K. Satheesh, Aerosol modulation of atmospheric and surface solar heating over the tropical Indian Ocean, *Tellus*, *52B*, 947-958, 2000.

Procopio, A. S., L A. Remer, P. Artaxo, Y. J. Kaufman, B. N. Holben, Modeled spectral optical properties for smoke aerosols in Amazonia, *Geophys. Res. Lett.*, *30*, 2265, doi:10.1029/2003GL018063, 2003.

Prodi, F., and G. Fea, A case of transport and deposition of Saharan dust over the Italian peninsula and southern Europe, *J. Geophys. Res.*, *84*, 6951-6960, 1979.

Rajeev, K., and V. Ramanathan, Direct observations of clear-sky aerosol radiative forcing from space during the Indian Ocean Experiment, *J. Geophys. Res.*, *106,* 17221-17235, 2001.

Reagan, J. A., M. P. McCormick, and J. D. Spinhirne, Lidar sensing of aerosols and clouds in the troposphere and stratosphere, *Proc. IEEE*, *77*, 433-447, 1989.

Redemann, J., R. P. Turco, K. N. Liou, P. V. Hobbs, W. S. Hartley, R. W. Bergstrom, E. V. Browell, and P. B. Russell, Case studies of the vertical structure of the direct shortwave aerosol forcing during TARFOX, *J. Geophys. Res.*, *105,* 9971-9979, 2000.

Reid, J. S., T. F. Eck, S. A. Christopher, P. V. Hobbs, and B. N. Holben, Use of the Angstrom exponent to estimate the variability of optical and physical properties of aging smoke particles in Brazil, *J. Geophys. Res.*, *104*, 27473-27489, 1999.

Rosen, J. M., R. G. Pinnick, and D. M. Garvey, measurement of extinction-to-backscatter ratio for near-surface aerosols, *J. Geophys. Res.*, *102*, 6017-6024, 1997.

Ruggaber, A., J. Reuder, H. Schwander and P. Koepke, Spectral ground albedo in the UV-range, paper presented at European Conference on Atmospheric UV Radiation (ECUV), Helsinki, Finland, 1998.

Russell, P. B., et al., Pinatubo and Pre-Pinatubo Optical Depth Spectra: Mauna Loa Measurements, Comparison, Inferred Particle Size Distributions, Radiative Effects, and Relationship to Lidar data, *J. Geophy. Res.*, *98*, 22969-22985, 1993.

Russell, P. B., et al., Comparison of aerosol single scattering albedo derived by diverse techniques in two North Atlantic experiments, *J. Atmos. Sci.*, *59*, 609-619, 2001.

Sasano, Y., and E. V. Browell, Light scattering characteristics of various aerosol types derived from multiple wavelength lidar observations, *Appl. Opt.*, *28*, 1670-1679, 1989.

Satheesh, S. K. and V. Ramanathan, Large differences in tropical aerosol forcing at the top of the atmosphere and Earth's surface, *Nature*, *405*, 60-63, 2000.

Schmid, B, and C. Wehrli, Comparison of Sun photometer calibration by use of the Langley technique and the standard lamp, *Appl. Opt.*, *34*, 4500-4512, 1995.

Schoeberl, M .R., L. R. Lait, P. A. Newman, and J. S. Rosenfiled, The structure of the polar vortex, *J. Geophys, Res.*, *97*, 7859-7882, 1992.

Schwander, H., P. Koepke, and A. Ruggaber, Uncertainties in modeled UV irradiances due to limited accuracy and availability of input data, *J. Geophys. Res.*, *102*, 9419-9429, 1997.

Shettle, E. P., Models of aerosol, clouds and precipitation for atmospheric propagation studies, paper presented at *Conference on Atmospheric Propagation in the UV, Visible, IR and mm-Region and Related System Aspects*, NATO Adv. Group for Aerosp. Res. and Dev., Copenhagen, 1989.

Silva, A. M., M. L. Bugalho, M. J. Costa, W. von Hoyningen-Huene, T. Schmidt, J. Heintzenberg, and S. Henning, Aerosol optical properties from columnar data during the second Aerosol Characterization Experiment on the south coast of Portugal, *J. Geophys. Res.*, *107*(D22), 4642, doi:10.1029/2002JD002196, 2002.

Smirnov, A., B. N. Holben, O. Dubovik, N. T. O'Neill, L. A. Remer, T. F. Eck, I. Slutsker, and D. Savoie, Measurement of atmospheric optical parameters on U.S. Atlantic coast sites, ships, and Bermuda during TARFOX, *J. Geophys. Res.*, *105*, 9887-9901, 2000.

Sokolik, I., A. Andronova, and T. C. Johnson, Complex refractive index of atmospheric dust aerosols, *Atmos. Environ.*, *27A*, 2495-2502, 1993.

Sokolik, I. N., and O. B. Toon, Direct radiative forcing by anthropogenic airborne mineral aerosols, *Nature*, *381*, 681-683, 1996.

Sokolik, I. N., and O. B. Toon, Incorporation of mineralogical composition into models of the radiative properties of mineral aerosol from UV to IR wavelengths, *J. Geophys. Res.*, *104*, 9423-9444, 1999.

Spinhirne, J. D., J. A. Reagan, and B. M. Herman, Vertical distribution of aerosol extinction cross section and inference of aerosol imaginary index in the troposphere by lidar technique, *J. Appl. Meteorol.*, *19*, 426-438, 1980.

Stamnes, K., S.-C. Tsay, W. J. Wiscombe, and K. Jayaweera, Numerically stable algorithm for discrete-ordinate-method radiative transfer in multiple scattering and emitting layered media, *Appl. Opt.*, *27*(12), 2502-2509, 1988.

Tanré, D., Y. J. Kaufman, B. N. Holben, B. Chatenet, A. Karnieli, F. Lavenu, L. Blarel, O. Dubovik, L. A. Remer, and A. Smirnov, Climatology of dust aerosol size distribution and optical properties derived from remotely sensed data in the solar spectrum, *J. Geophys. Res.*, *106*, 18205-18217, 2001.

Tegen, I., and I. Fung, Contribution to the atmospheric mineral aerosol load from land surface modification, *J. Geophys. Res.*, *100*, 18707-18726, 1995.

Thuillier, G., M. Hersé, P. C. Simon, D. Labs, H. Mandel, and D. Gillotay, Observation of the solar spectral irradiance from 200 nm to 870 nm during ATLAS 1 and ATLAS 2 missions by the SOLSPEC spectrometer, *Metrologia*, *35*, 689-695, 1998.

Torres, O., P. K. Bhartia, J. R. Herman, Z. Ahmad, J. Gleason, Derivation of aerosol properties from satellite measurements of backscattered ultraviolet radiation: Theoretical basis, *J. Geophys. Res.*, *103*, 17099-17110, 1998.

Webb, A. R., I. M. Stromberg, H. Li, and L. M. Bartlett, Airborne spectral measurements of surface reflectivity at ultraviolet and visible wavelengths, *J. Geophys. Res.*, *105*, 4945-4948, 2000.

Webb, A. R., A. Kylling, M. Wendish, and E. Jäkel, Airborne measurements of ground and cloud spectral albedos under low aerosol loads, *J. Geophys. Res.*, *109*, D20205, doi:10.1029/2004JD004768, 2004.

Weber, A., S. P. S. Porto, L. E. Cheesman, and J. J. Barrett, High resolution Raman spectroscopy of gases with cw-laser excitation, *J. Opt. Soc. Am.*, *57*, 19-28, 1967.

Weihs, P., and A. R. Webb, Accuracy of spectral UV model calculations, 1. Consideration of uncertainties in input parameters, *J. Geophys. Res.*, *102*, 1541-1550, 1997.

Wendish, M., P. Pilewskie, E. Jäkel, S. Schmidt, J. Pommier, S. Howard, H. H. Jonsson, H. Guan, M. Schröder, and B. Mayer, Airborne measurements of areal spectral suface albedo over different sea and land surfaces, *J. Geophys. Res.*, *109*, D08203, doi:10.1029/2003JD004392, 2004.

West, R. A., L. R. Doose, A. M. Eibl, M. G. Tomasko, and M. I. Mishchenko, Laboratory measurements of mineral dust scattering phase function and linear polarization, *J. Geophys. Res.*, *102*, 16871-16881, 1997.

World Climate Programme WCP-112, *A Preliminary Cloudless Standard Atmosphere for Radiation Computation,* IAMAP, Boulder, CO, 1984.

Yu, S., V. K. Saxena, B. N. Wenny, J. J. DeLuisi, G. K. Yue, and I. V. Petropavlovskikh, A study of the aerosol radiative properties needed to compute direct aerosol forcing in the southeastern US, *J. Geophys. Res.*, *105*, 24739-24749, 2000.

Zerefos, C. S., et al., Photochemical Activity and Solar Ultraviolet Radiation Modulation Factors (PAUR): An overview of the project, *J. Geophys. Res.*, *107*(D18), 8134, doi:10.1029/2000JD000134, 2002.

LIST OF ACRONYMS AND ABBREVIATIONS

AOD	Aerosol Optical Depth
ATLAS	ATmospheric Laboratory for Applications and Science
ATSR	Along Track Scanning Radiometer
DDR	Diffuse-to-Direct Ratio
ESA	European Space Agency
GHG	Greenhouse Gases
IPCC	Intergovernmental Panel on Climate Change
IR	Infrared
LIDAR	LIght Detection And Ranging
LWC	Liquid Water Content
MFRSR	Multifilter Rotating Shadowband Radiometer
MISR	Multi-angle Imaging Spectro-Radiometer
MODIS	Moderate Resolution Imaging Spectroradiometer
PAUR	Photochemical Activity and solar Ultraviolet Radiation
RF	Radiative Forcing
RFD	Radiative Forcing for Diffuse radiation
RFE	Radiative Forcing Efficiency
RT	Radiative Transfer
SW	ShortWave
SZA	Solar Zenith Angle
TOA	Top Of the Atmosphere
TOMS	Total Ozone Mapping Spectrometer
UV	Ultraviolet Radiation